1-1-2010

Effect of micro vibration from two space platform on liquid mixture during thermodiffusion experiment

Amirhossein Ahadi
Ryerson University

Effect of micro vibration from two space platform on liquid mixture during thermodiffusion experiment

By

Amirhossein Ahadi

B.Sc. in Aerospace Engineering, KNTU, Tehran, Iran, 2010

A thesis

Presented to Ryerson University

in partial fulfillment of the

requirement for the degree of

Master of Applied Science

In the Program of

Mechanical Engineering

Toronto, Ontario, Canada, 2012

AUTHOR DECLARATION

I hereby declare that I am the sole author of this thesis or dissertation.

I authorize Ryerson University to lend this thesis or dissertation to other institutions or individual for the purpose of scholarly research.

I further authorize Ryerson University to reproduce this thesis or dissertation by photocopying or by other means, in total or in part, at the request of other institutions or individuals for the purpose of scholarly research.

ABSTRACT

Effect of vibration from two space platform on thermodiffusion experiment

Amirhossein Ahadi

Master of Applied Science

Mechanical and Industrial Engineering, 2012

Ryerson University, Toronto, On, M5B 2K3, Canada

In the present study, a two-dimensional numerical simulation was carried out for binary mixture. The influence of micro gravity vibration or acceleration on board Iinternational Space Station and FOTON-M3, influence of different cavities size as well as the effect of the sign of the Soret coefficient (fluid flow, heat and mass transfer and concentration) in the solvent were investigated in detail. It must be noted that based on previous experiences with this investigation using the same mixture and cavity by Saghir and Parsa [**1**] the CFD modeling was performed up to 8500s. By this time the quasi-steady state has been reached in most of the mixtures. This thermodiffusion experiment using binary mixture at low pressure condition on the ISS cases shows higher error value for concentration profile at the end of the experiment; compare to FOTON-M3 satellite. However, it should be mentioned that all the errors are significant and more than 25 percent; thus, this kind of investigation should be considered for experiments on all of space vehicles.

BORROWER

Ryerson University requires the signatures of all persons using or photocopying this thesis. Please sign below, and give address and date.

ACKNOWLEDGEMENTS

Author would like to sincerely thank Prof. Saghir of Ryerson University not only for his helpful assistance, guidance and encouragement throughout the completion of this thesis which is mostly fulfilled by supervisor, but also because of his sympathy, endeavor and providing a quite intimate scientific atmosphere which were unique for author to fulfill this investigation. Without his help, it was impossible for the author to complete this thesis. The author also acknowledges the financial support by the Canadian Space Agency and the useful suggestions of his colleagues Mr. Parsa and Mr. Abdur Rahman, PhD candidates at Ryerson University.

This thesis is dedicated to my family, specially my parents who sacrificed everything for me, as well as my kind sisters, Faezeh and Faeghe.

TABLE OF CONTENT

LIST OF TABLES

LIST OF FIGURES

NOMENCLATURE

A Area

C,c Fluid Concentration

C_p Specific heat of liquid at constant pressure

D_M Molecular diffusion coefficient

D_T Thermal diffusion coefficient

d_i Diameter of component i

E Energy

f Body force, Frequency

g Gravitational acceleration

J Mass flux

H Height of cavity in horizontal *y*-direction

L_{iv} Phenomenological coefficient

L_{qi} Phenomenological coefficient

k Conductivity of the fluid

L Length of cavity in horizontal *x*-direction

m_i Segment number

M_W molecular weight of pure component

P pressure

Q Heat flux

Q_k^* Net heat of transport

R Gas constant

S_T Soret coefficient

t time

T Temperature

Δc Initial concentration difference

ΔT Temperature difference between lateral wall

U Velocity magnitude

u Velocity component in the x direction

V Volume

v Velocity component in the y direction

w Velocity component in the z direction

x variable

Greek Symbols

α Thermal diffusivity

α_T Soret effect

τ_D Diffusive characteristic time

τ_{th} Thermal characteristic time

μ Dynamic viscosity

λ Kinematic viscosity

Φ Dissipation function

ρ Density of the fluid

σ Stress

$\dot{\sigma}$ Entropy production

σ_{ii} Segment diameter

ε_{ii} Interaction energy parameter

Subscripts

C Cold

H Hot

Chapter 1 : Introduction to Thermodiffusion and Literature Review

1.1 Introduction

Thermodiffusion results in the Soret effect, the chemical separation which is obtained by the thermal gradient in non reacting mixtures, and is quantified by the Soret coefficients when there is no convection. Thermodiffusion was introduced by Ludwis (1856) and Soret (1879), and is thus, known as the Soret effect. The Soret coefficients are known to be difficult to measure on ground conditions because of technical constraints in the control of spurious thermal and liquid convection and convective instabilities. Thermodiffusion is the diffusive coupling between heat transport and mass transport. By knowing the isothermal diffusion coefficients, thermodiffusion is determined by the corresponding Soret coefficients, the experimental quantities that relate the solute gradient to the thermal gradient in a cavity without convection or reaction and a closed system at a steady state. The thermal diffusion plays a vital role in the investigation of hydrodynamic stability in fluid mixture, movement of mineral, mass transport modeling in organ matters, and the compositional variation in hydrocarbon reservoirs[**2**].

1.2 Literature Review

In the late twentieth century, the basic theoretical approaches to studying and analyzing thermodiffusion have been developed. Some of these important theories were irreversible thermodynamics by Hasse [**3**]; the kinetic theory of irreversible thermodynamics by Raderford (1963), and the same theory by Dougherty and Drickmer [**4**]. After that, there was a gap in these investigations until the last two decades of the twentieth century. During this period of time, the new range of theories and investigations in this area can be observed such as the elementary transition state theory by Mortimer and Eyring [**5**], the kinetic theory of dense hard spheres and its revisions by Lopez de Haroal [**6**], and the partial excess enthalpy and activity coefficient by Guy and the maximization of the partition function of the idealized bulb by Kempers [**7**]. In this

literature review, the details of the main important investigation between 1990 and 2010 in this field are considered. Our goal is to study the thermodiffusion in different micro vibrational conditions. Thus, in this review the major researches in different aspects of thermodiffusion experiments are taken into accounts.

One can see that the first investigation on instability of a fluid in a vibration field in microgravity and weightlessness was performed by Gershuni and Zhukhovitskii[**8**]. In their study, the conditions of equilibrium were discussed, and the boundaries of vibration instability were determined for some equilibrium states. They modeled the convection problem with an infinite circular cylinder with transverse and mutually perpendicular directions of the temperature gradient and the vibration axis. They assumed a cavity filled with an incompressible fluid with a temperature distribution specified on the boundary on condition of weightlessness, so they ignored the static gravitational field. In the presence of high-frequency vibration, the vibration period was much shorter than the characteristic hydrodynamic times; the secondary motions can be examined by means of the equations found by the method of averaging from the complete convection equations. The method of averaging was used to investigate the influence of high frequency vibrations on the occurrence of convection in a static gravity field. The result showed the dependence of the minimal critical Rayleigh number on the angle for perturbations. In other words, they surveyed the stability of equilibrium in a cavity of dimensions bounded by the directions of the temperature gradient and the vibration axis.

They extended their last investigation for considering a more complicated subject, namely the vibrational convective instability of a mixture layer with Soret effect [**9**]. In this paper Gershuni and his coworkers investigated the stability of the mechanical equilibrium of a plane horizontal binary mixture layer vibration theoretically. One of the main strong points in this study was considering the Soret effect with a high frequency static gravity field. They simulated an endless plane horizontal layer of binary mixture with Soret effect locked up between two rigid walls; the temperature was maintained constant and equal for both walls. They assumed to have two dimensional disturbances for the reason that such kind of a disturbance was the most harmful by analogy with the case of a one-component fluid. The two different cases were surveyed according to following characteristics. In the first case, the longitudinal vibration, in the presence of thermo-gravitational and thermo-vibrational convective instability, was considered. In the

other one, the transversal vibrations mechanism wasn't operative, and the vibration took part in a purely stabilizing role. Their numerical solution of the eigenvalue problem was found by using the Runge-Kutta-Merson method in combination with the shooting procedure gradually.

Savino and his team [**10**] worked on thermo vibration convection. This paper deals with the three-dimensional numerical simulation, by means of a finite difference method of the steady flow regimes in a fluid cell subjected to periodic accelerations with a relatively high frequency as well as influence of gravity modulation on the onset of convective instability, with more details. It can be claimed that an initial linear temperature distribution and a g-jitter orthogonal to the density gradient, in a fluid layer heated from above or from below, was carried out. The 3D numerical results presented here in terms of velocity and temperature fields are helpful to design microgravity experiments and to evaluate the range of validity of the two-dimensional simulation. In the present work, they consider an oscillatory acceleration vector along the direction perpendicular to the applied temperature gradient. They assumed the cavity with a homogeneous Newtonian fluid as well as the frequency of the vibration was large enough that the acceleration period was very small compared with the characteristic momentum and energy diffusion times. The displacement amplitude was very small compared with the characteristic length. The problem was solved using an explicit formula and the QUICK scheme. Although the two approaches are completely different, there was a qualitative agreement between the results in this work and those obtained by other researchers in this field. They presented the differences between 2D and 3D results evaluated by parameters. They carried out the analysis of the general case of quasi steady residual g-levels superimposed to high frequency-small amplitude g-disturbances by means of a time-averaged formulation. They numerically analyzed the thermo-fluid-dynamic distortions as a function of the classical Rayleigh number for steady and of the vibrational Rayleigh number. The same investigation on the fluid cell was conducted by Chacha and Saghir[**11**]; they performed a three-dimensional numerical simulation on a fluid cell subject to periodic accelerations of relatively high frequencies orthogonal to the density gradient. The main point in this article was time averaged convective motion arising from thermo-vibrational effects. Their results revealed the vector plots and the isotherms were placed in the mid-section of the cell. The 3D results approach those obtained under 2D assumptions when the aspect ratio increases. Larger value of the aspect ratio was necessary at large Rayleigh numbers to obtain a

good description of the field in the mid-section using a 2D formulation as the influence of the side walls increases with the vibrational Rayleigh number.

The last investigation of Gershuni's team [**12**], on this field, was investigation of the same problem with regarding Soret effect under transversal high frequency vibration. The stability of the mechanical equilibrium of a plane horizontal binary mixture layer with Soret effect in the presence of high frequency transversal vibration was studied, so they added the effects of Soret phenomenon to their investigation and other assumptions were the same as their last works. The critical disturbances and values of Rayleigh number were obtained in this work. The effect of longitudinal high frequency vibration on a plane horizontal layer of the mixture with rigid and isothermal boundaries was studied. It was found that convective instability was caused by both mechanisms of excitation thermo gravitational and thermo vibrational. Contrary to the last Gershuni's works, they simulated the case where the axis of vibration was vertical transversal with respect to the layer. Thus, the situation was quite different from that one physically. It had been proven that the equilibrium was absolutely stable if the axis of vibration was parallel to the temperature gradient. Consequently, one expects that for a binary mixture the mechanical equilibrium will be stable if the axis of vibration and the density gradient were mutually parallel. There was a static gravity in this investigation. Therefore they assumed that the standard Boussinesq approximations were valid in this case. It was shown that the effect of vibration was purely stabilizing at arbitrary values of binary mixture parameters: the critical Rayleigh number decreases monotonously with decreasing vibrational parameter. At the end, the critical characteristics of the critical disturbances were determined.

One of the most important theoretical diffusion models was developed by Shukla and Firoozabadi [**13**]. This model was presented for the prediction of thermal diffusion coefficients in binary mixtures of reservoir fluids using the thermodynamics of irreversible processes in one of Firoozabadi's recent researches. The model can be used by having equilibrium properties of mixtures and energy of viscous flow. Equilibrium properties were obtained from the volume translated Peng-Robinson equation of state, and the energy of viscous flow was estimated from viscosity. The model applied to forecasted thermal diffusion coefficients of several mixtures. The thermal diffusion coefficient sign obtains the direction of the thermal diffusion.

As mentioned before by some author such as Eslamian and Saghir that, in liquids, energetic interactions, the size and shape of the molecules, and thermodynamic conditions play important roles in diffusion process. Three models were applied to describe thermal diffusion coefficients in some hydrocarbon mixtures qualitatively. The assumptions for these simulations were the absence of convection and gravity segregation with zero mass flux, steady state condition and in one dimensional simulation. Their results indicated a consistent and systematic study of the thermal diffusion coefficients in binary mixtures. Another approach in this study was Kinetic approach of determining that was based on irreversible thermodynamics and has been exploited by several workers. The specific heats of transport were obtained from the activation energy of molecular motion.

They found that the consequence of the nonequilibrium part in the model was accounted for incorporating the energy of viscous flow, which can be determined from the viscosity of the mixture components. They showed that the energy of viscous flow can be obtained from the viscosity data of the components. In other words, they have modified the previously available models, the Kempers model [**7**], the Haase model [**3**], and the Rutherford model, based on phenomenological and kinetic approaches, and after that they compared their results, theoretical result, with experimental data.

After this theory, Firoozabadi and his coworkers [**14**] expanded their theory into modeling multicomponent diffusion and convection in porous media. In this work, numerical investigations of diffusion and convection in multicomponent hydrocarbon mixtures in two-dimensional cross sectional porous media were performed applying the finite volume method, with second order centered scheme spatial discretization. Results from several conditions of composition, temperature, and pressure were compared with previous results obtained in the binary mixture C1 /nC4. The temperature field was assumed to be a linear one. In their study, the main difference between the experimental apparatus and the numerical simulations was the use of different model geometry. In the real experiment, a cylindrical column was used, but they represented it numerically as a rectangular column. The molecular diffusion coefficients were obtained using Kooijman and Taylor's correlation [**15**]. In this work the authors assumed that molecular pressure and thermal diffusion coefficients were constant in the whole cross section. This assumption was justified by the fact that the mixture was far from the critical point. In this

paper the Peng-Robinson equation [**16**] of state was used to relate density to other property of the mixture.

Their results showed that in all the cases there was more compositional variation of methane than ethane. It was concluded that when steady-state convection was governed by the horizontal temperature gradient, the measurement of horizontal temperature variation was a vital parameter. There was no convection at steady state when they didn't have horizontal temperature variation. They showed that there were various features of compositional variation in hydrocarbon reservoirs depending on composition.

Demirel and Sandler [**17**] developed the linear-nonequilibrium thermodynamics theory for coupled heat and mass transport in the beginning of the twenty century. It observes that the analysis of LNET[1] defines the correct forces and flows involved in an irreversible process because the entropy production depends on the flows and forces. LNET was used to present dissipation functions and the entropy generation. The forces and flows for heat and mass transport in a multicomponent fluid were introduced into the phenomenological equations to formulate the coupling phenomenon between heat and mass flows. The local thermodynamic equilibrium holds for derivation on the formula in this work; thus, LNET deals with rate processes and the transport which were irreversible. Thus the specific internal and entropy energy were estimated as in a system at equilibrium, and the Gibbs and the Gibbs-Duhem relation are applicable in each volume element. They expressed the phenomenological equations with the resistance coefficients. The conjugate forces and flows of the processes were defined by the dissipation function. These flows were related to the forces in a linear form with the PCs[2] through PEs[3]. In this theoretical study, DPE[4] approach was used. Someone can use this approach when there are no large temperature and concentration gradient in a system. They mentioned that the volumes must contain a sufficient number of molecules for a macroscopic theory to be applicable. Consequently the main purpose of this study was to determine the role of the PEs

[1] Linear-nonequilibrium thermodynamics

[2] phenomenological coefficients

[3] phenomenological equations

[4] dissipation-phenomenological equation

with true transport coefficients and the relations between the flows and forces. This role was formulated in this study.

Saghir and his coworker's have performed many researches in this field in last decade. It is obvious that one of the pioneers and basic researches in microgravity condition for binary mixture was done by Chacha and Saghir [**11**] at that time. This work categorizes among the first articles that deals with investigating the flow due to thermal diffusion for different oscillatory g-jitters. The model considered was a rectangular rigid cavity filled with a binary mixture of methane and normal butane subject to a temperature difference on its end walls and radiation heat transfer on the lateral ones. They used the finite element technique for solving the problem. It was among the first results that showed the thermal diffusion was affected by a strong convection. Convection was enhanced, and therefore temperature and species profiles distortion from purely diffusive condition increased when a parallel g-jitter was added to the residual gravity. Their numerical study indicates that both residual gravity and g-jitter may be detrimental but also beneficial to achieve purely diffusive conditions. The g-jitter was found to reduce compositional variation. They found that if the temperature fluctuation at a given point remained small, the compositional variation due to residual g-jitter convection was not negligible. They considered a finite two-dimensional binary mixture of methane and n-butane (C1/nC4) subject to lateral temperature gradient including the Soret effect in two different orientations of the gravity acceleration (parallel and perpendicular to the thermal gradient). They assumed a single-phase fluid and all physical properties, except the fluid density, were constant with the assigned values obtained at mean temperature; however, according to the investigations by Saghir and Seshasai [**18**] maybe this assumption wasn't accurate enough to affect the final result. In their method, the time integration was performed using a first-order implicit scheme. The solution convergence was achieved at each time step, and the iteration obtained once the relative error in the unknowns u, v, c and T for two successive iterations was less than one over thousand in recent work of Saghir and coworkers; this error reduced to ten to the power of minus six [**19**].

In the first case, zero gravity condition was adopted; in the second case, the g-jitter and/or residual gravity in x direction was applied, and finally in the third case, the g-jitter and/or residual gravity in y direction was studied. Three frequencies were investigated: f = 0.1, f = 1 and f = 10 Hz. In the condition that there was no g-jitter in the system, by comparing the butane

distribution at two difference levels, it was found that as they got closer to the cavity wall, more butane was located due to the loss of heat by radiation. The amount of butane on the cold end was however higher than that of the hot end. Unlike the last two works of Saghir and coworkers, two convection rolls were observed sustaining the presence of a minimal temperature cross-section. In the case of zero gravity, the density variation was very smooth and was monotonically increasing from the hot end to the cold end. Variation of density at the two special locations was minimal. After, they repeated their investigation in presence of residual gravity. In this case, the density increased to a maximum value situated at around 3/4 of the cavity length, and then decreased to an intermediate value at the cold wall. The butane segregates towards the radiating walls while the methane migrates towards the central part of the cavity because of the fact that the Soret number was positive. They found that the convective flow was stronger. In presence of gravity, the centre line was no more than a line of symmetry for species distribution; they believed this was due to the fact that Soret effect was more pronounced in a zero gravity environment and was overcome by convection when the residual gravity was present. And at the end, they surveyed the influence of the frequency of the g-jitter Soret effect. They were interested in studying the effect of large frequency spectrum on the thermal diffusion. Their result showed that for the temperature, the frequency variation effect was negligible, but for the butane concentration, it was indicated that low frequency g-jitter will have a tremendous effect on the butane distribution in the cavity. Thus, they came to the conclusion that for low and high frequency, g-jitter affects the Soret diffusion process in microgravity. When they considered the horizontal g-jitter at the same frequency on the system, they observed symmetry for the butane concentration between the upper and the lower part of the cavity.

Chacha and Saghir [**20**] continued their research on solutal thermo diffusion convection in a vibrating rectangular cavity. As well as their last research on this area, they simulated methane (20%) and normal butane (80%) mixture subject to a temperature difference on its lateral walls and radiation heat transfer on the horizontal walls. This time they used the control volume technique to solve numerically. It was assumed that thermal coefficient is variable, but other thermodynamics property would be constant and was calculated based on average temperature. They studied the effect of vertical g-jitter and residual gravity on mass-thermo-fluid dynamics in a fluid mixture by performing a direct numerical simulation of the time-varying processes using the control volume method. To put it in another way, a finite two-dimensional binary mixture of

methane and n-butane (C1/nC4) subject to lateral temperature gradient was considered, including the Soret effect under the influence of vibration instability in micro-gravity environment. Their model was accounted for the fluid density variation as well as the variation of species diffusion and thermal diffusion coefficients with the temperature and the fluid composition. The vibration was applied to a model by a harmonic contribution to the body force. They assumed both the residual gravity and the g-jitter were applied perpendicular to the thermal gradient. The cavity was allowed to exchange heat with its environment through radiation process at its horizontal walls. They assumed that most of the liquid properties are variable, so they calculated them mathematically using the thermodynamics of irreversible processes in Firoozabadi works. The other assumption for this study was that the dynamic viscosity was varying in the cavity as a function of the local pressure, temperature and composition. They used the Peng–Robinson equation [**16**] of state (PR-EOS) as well as governing equation to find the main parameters. The boundary condition of this problem was left vertical wall which imposed a constant temperature Th[5] while the right vertical wall was at Tc[6] and difference between these two temperatures was ten degrees. They explained the importance of having the diffusion coefficients to vary in the numerical calculation rather than assuming a constant parameter by observing the migration which was less pronounced near the cold wall when the coefficients are kept constant.

They have seen in the first case that gravity causes the mixing in the fluid cavity leading to a uniform mass distribution of the butane. The results show that even with such low residual gravity, buoyancy starts to affect the mass diffusion as less butane was migrating toward the cold end of the cavity. As the residual-gravity level increases, the convection cell becomes more significant, and a deformed butane profile indicates the effect that buoyancy convection has on the Solutal diffusion in the cavity, and buoyancy effect reduces the butane diffusion toward the cold wall. In the last part of this work they considered effects of the amplitude variation and Frequency variation on mass diffusion. They found as the amplitude of the g-jitter increases, the oscillation amplitude changes very slowly while the difference between the initial value and the average value of the concentration was significantly reduced. Also increasing the amplitude on the g-jitter enhances the mixing of the fluid in the cavity, and therefore reduces species

[5] Temperature of the hot wall

[6] Temperature of the cold wall

differentiation. Their results indicate the amplitude of fluctuations of the butane concentration increases with the frequency, with a slight change in the average value.

Jue and Ramaswamy[**21**] have published on a similar subject. According to the importance of thermo solutal flows in cavities with a g-jitter effect, this study was among the first researches that provided an understating for the effect of gravity modulation in flow evolution as well as heat and mass transfer phenomena. Two-dimensional convection flow, under a sinusoidal gravity modulation (g-jitter) field, was studied to determine the influence of the periodic source on flow field, as well as heat and mass transfer mechanisms. A semi-implicit projection finite element method was used to solve the transient Navier-Stokes, energy and species concentration equations. Distribution of unstable responses for the singly unstable condition was in agreement with the literature predicted. The results show that heat and mass transfer rates are affected by the response type.

In this study, the flow considered to be laminar and the fluid was Newtonian with variable density. Incompressibility of the fluid follows Boussinesq's assumption and changes with concentration as well as temperature. The weakness in assumption was removing the Soret, Dufour and viscous dissipation effects in this model. Considering the effect of g-jitter in model made this model strong and helpful. The unstable flow field for the solutal and thermal driving forces in opposite direction was classified into two kinds for fingering and diffusive regimes. However, the increase in gravity modulation frequency makes larger heat and mass transfer rates in fingering regime, but results were opposite in the diffusive regime. The last part of this study was about this effect on the crystal material; they observed that in the augmenting status for a low-gravity environment, there was a different distribution of the flow variation response. The results showed a simultaneous response in the higher modulation frequency and a sub-harmonic response in the lower ones.

Parallel to Chacha and Saghir [**11**][**20**], Galliéro [**22**] worked on thermal diffusion sensitivity to the molecular parameters based on a non-equilibrium molecular dynamics approach. In this work, molecular dynamics simulations, a systematic study of the thermal diffusion factor behavior with the molecular parameters in a binary mixture, has been performed. The main purpose of this study was to find how the thermal diffusion procedure was dependent on molecular parameters when describing a fluid mixture. Validity of this model was checked to

estimate thermal diffusion factor for simple Alkane mixtures, by finding the results for sufficient number of particles and long enough simulations. Then, using various mixing rules, the separate influences of the mass, the moment of inertia, the atomic diameter and the interaction strength have been studied. Same molar binary mixtures of simple molecules have been used because of easiness in CPU time. They investigated the effect of the cross-interaction parameters and explained how strongly these parameters have an effect on the magnitude of the separation. The positive sign of thermal diffusion factor means that methane, or in other word, second component prefers, more than the other species, migrates toward the hot areas.

The results indicate a strong increase of thermal diffusion factor with the mass ratio. They got to the point that the lightest component prefers more than the heaviest, hot regions of the simulation box. The component with the highest potential strength was more willing in generating the density gradient, for the reason that they were more attractive and thus drag more particles into their neighborhoods. They noticed that thermal diffusion factor reduces with the atomic diameter ratio whatever the mixing rule. For influence of the cross-interaction parameters clearly results shows a strong dependence of the thermal diffusion factor on the cross-parameters and for coupling between contributions, it indicated that couplings exist, especially for the atomic diameter case. They showed that the molar fraction of the component, having the smallest mass and moment of inertia as well as the biggest radius and the strongest potential, tends to immigrate to the hot area as well as the species with the biggest mass and moment of inertia, with the strongest potential and the smallest volume, tends to migrate more than the other component, toward the cold areas. In addition, it was found that, as expected, the thermal diffusion was strongly dependant on the interactions between unlike particles. The two cross-interaction parameters have a large and opposite effect on the computed thermal diffusion factor.

Lyubimova [**23**] deal with the numerical simulation of the influence of static and vibrational acceleration in low gravity conditions on the measurement of diffusion and Soret coefficients in binary mixtures. The modeling was made for a rectangular cavity subjected to static acceleration (normal gravity) and/or vibrational accelerations with different levels and orientations. In their last work, the vibration period was assumed to be small in comparison with hydro dynamical time scales and the product of their amplitude; the influence of acceleration level on transient process and steady-state characteristics was identified for various binary mixtures that were

candidates for space experiments. Numerical investigation of high frequency vibration in a closed cavity has two different aspects. The first one was vibration influence on separation in the presence of temperature gradient, and the second one was about vibration influence on diffusion in isothermal regime. Gravity field and vibrations with linear polarization applied in the direction of the unit vector. They assumed that the vibration frequency was such high that the thickness of the dynamical Stokes boundary layer was small in comparison with the cavity size. For high frequencies, it was convenient to decompose all variables into the sum of slowly variable. The above decomposition was efficient if vibration amplitude was small enough that non-linear terms in the pulsation equations can be neglected.

Finally, if their conditions were satisfactory, they could describe the flows and heat/mass transfer in the binary mixture using the following average equations for thermo-solutal vibrational convection that was introduced by Gershuni and Lyubimov, 1998. Their work like other studies in this field was on first level simulation corresponding to the unsteady process of mass separation due to the Soret effect under imposed temperature gradient and allows determining the Soret coefficient and after that performing same procedure corresponds to the diffusion under isothermal external conditions. It allows determination of the diffusion coefficient. For the case they found when gravity field was absent and vibration was applied in the direction of imposed temperature gradient an equilibrium state was possible since this fact was in agreement with their numerical calculations. The behavior of a binary mixture in such conditions was the same as in purely diffusive regime. They explained the effect of micro gravity by the damping of buoyancy convection by vibrations which resulted in a weaker mixing; an equilibrium state was impossible. At small vibrational Grashof numbers the flow was a single-vortex due to the dominating role of buoyancy convection. In summary, the effect of vibrations applied in both directions, normal and tangent to the imposed temperature gradient, has been investigated by numerical simulation in the framework of the average approach.

Myznikov and Smorodin [**24**] considered nonlinear evolution of two-dimensional convection pattern for an incompressible binary mixture with Soret coupling in a horizontal layer. Their analysis was based on the nonlinear stage of convection driven by a temperature gradient across a horizontal layer of a mixture. The system was subjected to finite-frequency vertical vibration of arbitrary amplitude. They surveyed the effect of vibration amplitude on the evolution of

convection patterns corresponding to different resonance regions in the parameter space and revealed hysteretic transitions between nonlinear oscillations at the fundamental and sub harmonic frequencies.

The property of the fluid found their mean values at every point. The spatial distributions of these variables at a certain instant are represented. The critical Grashof numbers predicted by linear theory and nonlinear computations in this study, the error for this prediction was less than right persent. It was observed that the outcome of pattern formation in a modulated field was qualitatively different from that in the limit of high-frequency vibration in a different situation. Simulation of thermo-gravitational convection in a vertical porous column was important enough in diffusion process to Saghir and his team to concentrate on diffusion in porous column filled with a binary fluid mixture. Thus Jiang [**25**] considered the 2D numerical simulation, the convection effect in a vertical cavity having an aspect ratio of 10 and subject to a lateral heating condition based on the irreversible thermodynamics theory of Shukla and Firoozabadi [**13**]. The diffusion system was a vertical porous media combined with natural convection flow over a range of permeability from 0.001 to 10000 md.

Their results show that the lighter fluid component migrates to the hot side of the cavity, and when the permeability increases, the Soret process at first increased, when reached its peak, and then decreases. The numerical result in this investigation was the best result because it was the first time that the Soret coefficient has not been fixed in the computational domain but rather calculated at each point of the grid as a function of the temperature, pressure and the composition of the fluid mixtures. According to their assumptions the Darcy equation was applied to their CFD simulation. On the horizontal walls, a linear temperature gradient was applied. All the walls are assumed solid walls, so zero velocities are maintained. The mixture inside the cavity consists of 20%methane and 80% *n*-butane. Since the Peng–Robinson Equation [**16**] was used to calculate the density variation, as well as other fluid properties, the flow was assumed to be compressible. The thermal conductivity was considered constant in the model; the viscosity of the mixture was obtained with a method proposed by Herning and Zipperer[**26**]. There wasn't any heat generation or chemical reaction. The convergence criterion the pressure *P*, the temperature *T* and the concentration *c*, respectively were checked in each iterative. The Soret process begins by assuming the initial pressure, temperature and concentration in the mixture.

The viscosity and all three diffusion coefficients were evaluated for each control volume based on a given temperature, pressure and composition at each time iteration. For these calculations they used the Firoozabadi's model [**13**]. The convergence of the steady state was achieved when the absolute relative error of the concentration was found to be less than ten to the power of minus eight between successive time step iterations at each control volume. For validation of this numerical investigation, they compared their numerical results and experimental data and issued some journal papers.

It is seen that a uniform density distribution in the vertical direction with and without considering the Soret effect. In the case of low permeabilities, the flow was weak and did not noticeable effect on the linear horizontal temperature distribution. There wasn't any difference between the vertical density distributions with and without the Soret effect, so they got to the point that convection was too weak. When they neglected the Soret effect, a linear decrease in the density was due to the lateral heating condition. However with presence of the Soret effect, the results indicated the lighter component of the mixture, in this case the methane migrates towards the hot side of the cavity. When the permeability increases, convection had more influence in the cavity. They got to the point that Soret effect in porous media was mainly affected by the convection flow. One of the most important results of this study was that the convection effect on the thermal diffusion in a hydrocarbon binary system could be explained in terms of the characteristic times, and the other one was that if the thermal diffusion was faster than convection information transfer; then it would contribute to the Soret effect. After this work, Saghir focused on the low frequency G-jitter and its influence of the thermal diffusion. As result of this goal Yan *et al* [**27**] published a paper with this name. In this research the author has surveyed the effect of g-jitters on thermal diffusion. The mixture water-Isopropanol with ten percent mass fraction of Isopropanol bounded in a cubic cell was simulated with a lateral heating and different vibration conditions. The thermodynamics properties of fluid were thoroughly analyzed for different g-jitter scenarios. In earlier studies, it had been approved that low frequency vibrations exhibit a more dangerous effect on diffusion measurements with respect to high frequency vibrations.

According to their previous studies, Saghir and his coworker Yan focused on applying the low frequency on their CFD simulation model. Thus one of the important objectives of this study was

to evaluate the g-jitter effect on thermal diffusion with a focus on low frequency g-jitters. They considered the binary water Isopropanol (90:10 wt%) during the thermal diffusion process in a cubical cell in the presence of g-jitters ranging from 0.001Hz to 0.025Hz and a three-dimensional numerical model has also been introduced within the framework of a finite volume method to solve the Boussinesq approximated governing equations. They used same formulation as Shukla and Firoozabadi [**13**] and Patankar [**28**], in order to find thermo diffusion coefficient as well as solving the governing equations with the SIMPLE algorithm.

Since they just applied the static residual gravity, the buoyancy force constantly acted on the mixture without changing direction and the linear concentration profile did not change very much at amplitude vibration equal to ten to the power of six times less than gravity at sea level. When the gravity increased one thousand times, a boundary layer structure became visible in the concentration profile. When the static residual gravity increases at the time needed for establishing, the mass equilibrium reduces significantly. In zero gravity and microgravity conditions, the mass transport was only due to thermal diffusion as a result of the temperature difference between hot and cold wall. In the presence of high gravity condition, the convection far overcomes the diffusion and speeds up the fluid remixing noticeably. When the frequency increases from a few thousandths of Hz, the output oscillations become much weaker. In the case that they combined static and oscillatory gravities, the amplitude of the velocity oscillation increases noticeably compared to the one in the pure oscillatory g-jitter case. It can also be improved in the variation of the fluid flow and force stronger vibrations than the pure g-jitter alone. It has been detected that in pure oscillatory g-jitter cases and combined g-jitter cases, the instability of the fluid flow intensifies as the g-jitter frequency decreased. So they got to the fact that the consequence of low frequency g-jitters was significant either alone or in a combination with static and/or high frequency g-jitter components. In all the g-jitter cases simulated, the velocity field oscillates in a frequency equal to that of the driving g-jitters. The results show that with the presence of the oscillatory g-jitter component, the water distribution has been more distorted in comparison with the case that only the static residual gravity exists, and the degree of such distortion decreases as the frequency of the oscillatory g-jitter increases. They concluded that a stronger vibrational convection has been made by the lower frequency g-jitters than by the higher frequency ones. This investigation shows when the static residual gravity exists, both temperature and concentration fields oscillate in a frequency equal to that of the driving g-jitter

excitation. The flow field was enhanced when the static residual gravity exists simultaneously with the oscillatory g-jitter component in the direction perpendicular to the temperature gradient.

So far, the gap between experimental results and theoretical predictions of the thermal diffusion factor has been so large that the importance of the comparison work between theoretical and experimental results of the Soret coefficient of the binary mixture was completely clear. So in a new effort, Jiang and Saghir [**29**] investigated the results of both methods in the same paper. Water-methanol and water-ethanol mixtures were a vital challenge. Water was a very special fluid in terms of thermodynamic properties, and the association term was necessary in the equation of state for water property calculation. They applied Firoozabadi's thermal diffusion model[**13**] to calculate the Soret coefficient, as well as the molecular diffusion and coefficient thermal diffusion coefficient for methanol-water and ethanol-water mixtures at 310 K temperature and 1 bar pressure with 10% water mass fraction. The results were compared with Platten's [**30**] experimental data as well as theoretical predictions with other models. The author found better agreement with the experimental data by using Firoozabadi's model. In this investigation, the most important goal was to calculate the molecular and thermal diffusion coefficients for water-ethanol and water-methanol mixtures and the main purpose was to compare the results obtained using the Firoozabadi's approach with the experimental data. In addition to Firoozabadi's model the CPA [7] equation of state was used to find the Soret coefficient.

To calculate the thermal and the molecular diffusion coefficients, they need to calculate the density of the mixture of water-ethanol and water-methanol and compare the results with the experimental data for the water-methanol case; an excellent agreement between the two methods was evident. A difference of less than 0.04% between the two values was detected which was suitable. The calculation was repeated for the water-ethanol case with a 1.25% error. It should be noted that for both density variation curves with temperature results were similar variations but different in values. For the mass density of the water-methanol mixtures as a function of water concentration, the slope differs between the two data, but the results were still close to each other. Although author observed a difference between the experimental and numerical results for

[7] Cubic Plus Association

water-ethanol mixture as a function of temperature and water concentration, the slopes were identical. They came to an acceptable agreement on the water-methanol mixture with a difference of 0.35%, but this agreement for water-ethanol mixtures was not as good as water-methanol. There was a 6.5% difference between the prediction and experimental data. Results show that there was a problem in mass expansion. They suggested that maybe it was because of the numerical side; the CPA approach was an approximation technique, so we could expect some inaccuracy. On the other hand, the experimental results of Platten [**30**] had an uncertainty of approximately 5%. In both methanol-water and ethanol-water mixtures, the molecular diffusion coefficients were predicted.

The effect of vibration on diffusion experiment was considered by Mathiak1*et al* in 2005[**31**]. In this survey author relates his previous results with the steady state case, and if the Rayleigh criterion for convection was met, numerical simulations of the convection velocity with parallel acceleration can be significantly higher than with perpendicular acceleration which developed a new study on the effect of vibration on the diffusion experiment. The goals were to measure the mixing effect of vibration on transport and to examine the effect of frequency and direction. They had to use analogy between diffusive mass transport and heat transport, as result of the short term effect of a parabola. The temperature gradient between hot and cold wall was raised to 60flC. The temperature was measured by thermocouples with a rate of 4.5Hz. Their equipment could be rotated up to 45 degree and 296 Microgravity. The amplitude of the vibration was between 3 and 10cm; with the nominal frequency of 1Hz. They could decline the acceleration amplitudes between 0.120g and 0.40g.

The experiments with the 10mm capillary showed strong mixing as a consequence of the sheer process opposite to the experiments in the 4 mm capillary. Another result which was found was that the temperature symmetry interface was shifted. When the frequency was more than 1 Hz, the oscillation was easily detectable with the thermocouples close to the shear interface.

For oscillation amplitude of 100mm, as long as incensement in the frequency up to 1 Hz, they observed a slight increase of the additional transport. They had additional transport up to fifty percent in the case study of 1.7 Hz. The influence of the angle between the capillary and the acceleration vector was in the order of the error. The experimental results were completely overlapped with the calculation that was made by Langbe[**32**], especially for frequencies higher

than 1 Hz. As a result of increase in the frequency, they observed increases in the tolerable level of residual accelerations alternatively. For the conclusion, we can say that the importance of active vibration damping for liquid diffusion experiments in space vehicles has to be proved.

Another attempt on instability of the flow of a binary mixture was performed by Gnevanov and Smorodin[**24**] in 2006. The main difference of this study in comparison to other instability investigations was consideration of the effect on vibration and thermal diffusion on the fluid. Gnevanov and Smorodin studied the vibrational convective instability of an upward–downward flow of binary mixture by considering the thermal diffusion effect in a vertical layer in the presence of longitudinal high-frequency harmonic vibrations. The fluid assumed to be an incompressible and the axis of vibrations was directed along the layer. The case assumed to be rigid and isothermal boundaries of the layer impermeable for the mixture. The effects of thermal diffusion on the mixture and the thresholds of flow stability were considered. The survey was carried out on the basis of equations for averaged fields. Author applied an asymptotic method with the use of perturbation wave number as a small parameter in the long-wave limit. The main goal of this literature was investigation of the interaction with vibrational and gravitational mechanisms of convective instability.

In 2008, the influence of the diffusion in the Cristal was discovered. Asaro, Farkas and Kulkarni [**33**] studied this effect. The main goal of this research was studying the Soret effect that occurs in the diffusion of solutes in crystals. This analysis was performed by using the principle of microscopic reversibility. Their attempt was to interpret and compute Q* as well as the heat of transport for such crystal materials. To compute the transport of energy during the diffusion process, and after that Q*, the procedures of thermal activation to the transition state were assumed to be inverses, so the net process was compacted to the investigation of the purely mechanical decay process. They simulate the decay process, suggesting the molecular statics and dynamics. Carbon diffusion in body-centered cubic a-iron was investigated. It was observed that for the case heat of transport, the activation energy for carbon diffusion was in agreement with experimental results. This team forecasted the magnitude and sign of heat of transport correctly. They studied different cases such as the diffusion of substitution solutes and vacancies. There are huge amounts of literature in diffusion in crystals, but we don’t want to spend time to describe

more about the details and results because our effort will be diffusion in microgravity environment.

Then, Saghir and Yan [**34**] surveyed the effect of sinusoidal low frequency on the thermodiffusion process. The main purpose on this investigation was simulating the coupled phenomenon of diffusion–thermodiffusion–convection or Double diffusion. The numerical simulation for a binary mixture of water–Isopropanol (90:10) was carried out. They considered a dependence of the Soret separation on g-jitter frequency and amplitude. Two scenarios, low frequency low amplitude, and low frequency high amplitude have been studied for this binary mixture. Under the same amplitude, the fluctuation of local properties was found as result of decrease of the g-jitter frequency. When they considered oscillatory g-jitter and static residual gravity, the diffusion process was affected by the non-linear interaction between individual g-jitters. When the amplitude decreases to 1g, this nonlinearity becomes less significant in comparison with the high-amplitude scenario.

At low frequencies, the nonlinear interaction between different g-jitter components has a dependency on the amplitude. As a result, g-jitter amplitude increases, and the g-jitter frequency decreases; the Soret separation was found to decrease and the temperature deformation was enlarged. As a static residual gravity was super imposed on an oscillatory g-jitter, the overall effect of these vibrations on diffusion exhibits a characteristic of nonlinearity between each individual effect induced by the static residual gravity and the oscillatory g-jitter, separately. It was observed that the nonlinearity was very significant when the g-jitters have high amplitude and low-frequency. Moreover, it becomes less noticeable as the g-jitter frequency and amplitude decrease.

The last two years of the first decade of new century were years of working hard for this scientific field and specially Saghir and his team. Different theoretical models and investigations were performed by Eslamian and Abbasi in these years. One of the great important factors in estimating the thermodiffusion coefficient for associating and non-associating fluid mixtures is evaluation of the activation energy in Eyring's viscosity theory [**4**]. They applied several methods to estimate the activation energies of pure components, and then extended them to complex hydrocarbon mixtures. So Saghir and Abbasi[**35**] in this study worked on this issue and they presented the activation energy model using alternative forms of Eyring’s viscosity theory[**4**] to

estimate the thermodiffusion coefficient values for hydrocarbon binary. The kinetics approach and phenomenological approach are two different approaches in modeling thermodiffusion coefficients. The kinetics approach is based on the irreversible thermodynamics theory and thermodiffusion coefficients are based on the specific heat of transport of the two components in a binary mixture. Based on the results of Dougherty and Drickamer[**4**] which believed a good approximation for calculating the energy was required to detach a molecule by using Eyring viscosity theory [**4**], they continued this method to find accurate thermodiffusion coefficient. In their model, the activation energy of each component in a mixture was simulated as a function of its molecular size. In this paper, they performed a comparative study between the measured thermodiffusion coefficients with those forecasted using various methods of estimating the activation energy of viscous flow in order to find the best way to estimate the values of the thermodiffusion coefficients. The other goal of this study was evaluating the effect of the molecular size on the activation energy. It was shown that the results of the proposed models for predicting the thermodiffusion coefficients were in very nice agreement with the experimental data. Comparing two components such as C10, C12 in their mixtures with C5 and C6 and C18 shows that the lighter component, C6, has smaller thermodiffusion coefficient than the lighter component C5 in the mixtures. It was shown that Shukla and Firoozabadi's model [**13**] was very sensitive to the ratio of the evaporation energy to the activation energy; recently this result was shown by other authors.

Later Abbasi and Saghir [**36**], based on free volume theory which explains the diffusivity in diffusion-limited systems, estimated the Soret coefficient for binary mixture of toluene and hexane, and following that they compared their results with experimental data. The proposed model combined with Shukla and Firoozabadi's model [**13**] was applied to predict the Soret coefficient. The perturbed chain statistical associating fluid theory equation of state (PCSAFT-EoS [**16**]) was used to calculate the related thermodynamic properties. In their model both equilibrium and nonequilibrium properties of mixtures were incorporated. Equilibrium properties were obtained from a proper equation of state, while nonequilibrium properties were determined using the energy of viscous flow estimated from viscosity data. The viscous energy of each component was corrected by its molecular size.

It has been found that in non-associating solutions, the choice of $\tau = 4$ proposed by Shukla and Firoozabadi for hydrocarbon mixtures along with Dougherty and Drickamer's[**4**] work did not coordinate with experimental results. Results showed that the size of the molecule was not the only condition to have more viscous energy. They concluded that the viscous energy increases by quenching temperature and the ratio of evaporation energy to viscous energy, τ has inverse behavior. The τ value for bigger molecules increases as the percentage of bigger molecule inside the mixture was decreased; however, τ value of smaller molecules increases. Their new model results were in good agreement with the experimental results.

Eslamian and Saghir[**37**] based on their pervious theoretical investigation in this area, presented a new dynamic model to emulate thermodiffusion process and proposed expressions for estimating the thermal diffusion factor in binary nonassociating liquid mixtures in 2009. They correlate the net heat of transport in thermodiffusion with parameters such as the mixture temperature and pressure, the size and shape of the molecules, and mobility of the components. This modeling approach was different from that of Haase[**3**] and Kempers's[**7**], in which thermodiffusion was presented as a function of the thermostatic properties of the mixture like enthalpy along with Haase-Kempers[**3**] [**7**]and Drickamer-Firoozabadi[**4**][**13**] models related with the Peng-Robinson equation of sate were evaluated. Although the model prediction wasn't very accurate, the model was simple and easy to use, physically justified, and predicts the experimental data very good in comparison with the existing models. According to the Gibbs-Duhem equation, the gradients of chemical potential or concentration, temperature, and pressure were interrelated; they neglected the mass diffusion due to a pressure gradient because in typical applications, pressure diffusion compared to other effects was negligible. In this study Eslamian combined two methods to find a better approach with weight factor ½ for both methods. However, both Drickamer and Firoozabadi [**4**][**13**] considered a constant for all liquids with a value equal to 4.0. This assumption, in fact, turns this model from a dynamic model to a static model. In this investigation Effect of temperature and concentration, Effect of number of carbon atoms, and Effect of pressure were presented in different conditions. The second attempt in this study was the estimation of the thermal diffusion factor, where an equal weight was assigned to the constant parameters; this way the model was essentially applicable to both non-associating and associating molecules. They observed that even though the Haase-Kempers's [**3**][**7**] model was the least accurate model for liquid mixtures studied under the atmospheric pressures and

moderate temperatures, it was capable of predicting experimental data of highly condensed gaseous mixture of methane-n-butane. Finally, they suggested the approach to estimate the thermal diffusion factor in a binary mixture with minimum effort and without using an equation of state and just based on the viscosity data.

Investigation about the thermodiffusion in associating mixtures is one of the most complex processes performed by Eslamian and Saghir [**38**]. This complexity is a result of the strong relation between the molecular structures of mixtures with concentration. They illuminated a qualitative mechanism for the separation of components in binary associating mixtures. The author found the connection between the sign change in the thermal diffusion factor and a change in the molecular structure, mixture viscosity, and the excess entropy of mixing in such mixtures. They modified developed dynamic model according to the Drickamer[**4**] non equilibrium thermodynamic approach to compute this connection. The results were examined against the experimental data. The theoretical expressions were self-contained and forecast a sign change in the thermal diffusion factor in associating mixtures. They mentioned that the main problem was the coupled heat and mass diffusion due to a temperature gradient or thermodiffusion or Soret effect. The molecular or Fickian mass diffusion coefficients and thermal diffusion coefficients were assumed as input parameters. It was found that the concentration at which a significant change in the structure of mixture occurs, the mixture viscosity reaches a maximum, and the excess entropy of mixing attains its minimum value close to the concentration at which the sign of the thermal diffusion factor changes. It was observed that since a temperature difference was applied across the mixture, it was easier for the molecules to migrate in the mixture toward either the hot side or the cold side. The thermal diffusion factor and its sign change were predicted in this study accurately.

The other study of Eslamian and Saghir [**39**] in 2009 was Role and Significance of the Heat of Transport and the Activation Energy of Viscous Flow. In this paper, thermodiffusion models developed to estimate the thermal diffusion factor in non-ideal liquid mixtures are reviewed; the merits and demerits of each model are discussed in detail. Their focus here was on binary mixtures; however most of these models are multicomponent in principle. Two rather different models are identified: models needing a matching parameter to be obtained usually from the outside of thermodynamics, and the self-contained or independent models. Derivation of the

matching parameter models using linear non-equilibrium thermodynamics and the details of how to find the matching parameters are investigated. The physical meaning of parameters such as the net heat of transport and the activation energy of viscous flow was elucidated, as the literature was overwhelmed with confusing and misleading information. The so-called dynamic and static models and their relations to the matching and non-matching parameter models are also discussed. They concluded that modeling the net heat of transport by the activation energy of self-diffusion may provide better results than approximating it by the activation energy of viscous flow. Nonetheless, the matching parameter models, which use the activation energy of viscous flow, are more dynamic and predict the thermal diffusion factor better than the non-matching parameter or static models. A spatial concentration or chemical potential difference within a solution or mixture was the most common driving force for mass diffusion. In a homogeneous solution, temperature or pressure gradients may also cause mass diffusion. They mention some details of the sequence of the development of the matching parameter methods and the reaction rate theory. They got to specific conclusions that in summary are listed below.

First one all the thermodiffusion process can be considered to be a function of the mixture equilibrium properties such as enthalpy and/or the dynamic and non-equilibrium properties. The second one was the net heat of transport of various components which was assumed to be related to the activation energy of viscous flow, but there was a difference between the movements of liquid molecules in a viscous flow and the movement and separation of different components in thermodiffusion that should be considered. After they concluded that the entire concepts of the reaction rate theory and the activation energy of viscous flow are debatable. Matching parameter models predicts the experimental data rather better than the independent models. This was because of their dynamic nature. The prediction ability of the matching parameter methods will be improved by using more sophisticated models for the net heat of transport. Their sensitivity analysis showed that, in general, matching parameter methods are sensitive to the choice of the matching parameter used. Using variable matching parameters corresponding to the actual mixture temperature and pressure was helpful, as using a constant matching parameter turns the dynamic model into a static model. The non-matching parameter models seem to be promising, as they are self-contained. At last, it was found that a discontinuity and lack of understanding and interaction was found among the thermodiffusion models. This study has provided a rather

comprehensive and critical review of the existing thermodiffusion models, which was a prerequisite to developing new models.

Recently, Eslamian *et al* [**40**] have tended to publish a journal paper on the Role of the Velocity Frame of Reference. This paper deals with modeling and formulation of thermodiffusion in binary and multicomponent liquid mixtures investigated. The focus of this work was on the nonequilibrium thermodynamics models although some other models are considered and were explained briefly. One of the most important notes that could be concluded was that while in binary mixtures the transformation does not affect the sign and magnitude of the thermodiffusion coefficients, in multicomponent mixtures (ternary and higher), even the sign of the thermodiffusion coefficients may change. Nonequilibrium thermodynamics seems to be the best approach to model thermodiffusion because of good prediction of thermodiffusion coefficient as well as it providing a general and rather satisfactory description and practicable expressions.

In this work lots of complex aspect of the Soret effect were determined clearly such as, velocity frame of reference in thermodiffusion modeling and the importance of that, defined thermodiffusion based on the mole or mass fractions of the species and difference between these two definitions, validation of assuming a constant local pressure or zero pressure gradient within the non-isothermal mixture. Define quantity net heat of transport in nonequilibrium thermodynamics and some explanations about how to calculate this quantity. In thermodiffusion modeling, usually three frames of references are employed: mass, molar, and volume frames. They show whereas the pressure gradients were assumed zero, they have shown that the dissipation functions were invariant and independent of the velocity frame of reference. They briefly explained how switching between mass and mole-based definitions of the diffusion coefficients acts. His results indicated the magnitude and even the sign of the predicted thermodiffusion coefficients in a ternary mixture. In methane and n-butane, mole fraction variations, the DT sign change of n-butane appears in the mole-based definition only. However, the magnitude of the D_T of both methane and n-butane changes significantly when the definition is changed.

The role of the velocity frame of reference in the development of various models was discussed. Thermodiffusion coefficients were considered using mole-based and mass-based

definitions and also it was shown how to switch between definitions. In the case study of work Eslamian show that the choice of the mole-based or mass-based definitions for the thermodiffusion coefficients can significantly affect the estimated results of a ternary mixture. However it should be mentioned that this effect on the binary mixture was negligible.

The next goal of Saghir and Srinivasan was [**19**] the thermal simulation of thermodiffusion in ternary hydrocarbon mixtures at high pressure. The sign of the thermal diffusion coefficient for a given component in more than two components mixture cannot be related to the segregation of that component to the cold top end or the hot bottom end. Thus, an approach to determine the mass and thermodiffusion coefficients is necessary for the governing equations. Because of this, a critical part of modeling the thermodiffusion is estimating an accurate estimation of the net heat of transport. This was defined as the amount of energy transported across a given reference plane per mole of the i^{th} component in the absence of a temperature gradient minus the partial molar enthalpy of the i^{th} component in the mixture. They used the Firoozabadi's formulation for the net heat of transport (in molar average velocity frame). The thermodiffusion model has been coupled with the PR EOS. The model has been implemented in a FORTRAN-based CFD code and has been validated against the experimental data of Platten[**30**]. Five different ternary hydrocarbon mixtures of methane, n-butane, and n-dodecane have been investigated in a microgravity environment. While the mole fraction of methane was kept constant, the mole fraction of n-dodecane was changed. Results of the measured concentration difference and the applied temperature gradient were used to determine the thermal diffusion factor. It was shown that in all mixtures methane and n-dodecane immigrate to the hot and cold sides. In addition, n-butane at low concentrations is separated to the hot side, but at higher concentrations, a large majority of the molecules are separated to the cold side. This sign change was discussed by the relatively intermediate density of n-butane and the amount of interaction with either methane or n-dodecane. The author showed that the model performed well only for certain compositions. More precisely, the sign change behavior of n-butane was not accurately captured.

In this year, Influence of vertical vibrations on the separation of a binary mixture in a horizontal porous layer was studied by Elhajjar *et al* [**41**]. They surveyed the influence of vertical high-frequency and small-amplitude vibrations on the separation of a binary mixture saturating a shallow horizontal porous layer heated from below. In their survey, they consider Soret-driven

convection and thermo vibrational convection in a porous medium. In this modeling they used the formulation of Charrier and Mojtabi *et al*[**42**] for a shallow porous cavity saturated by a binary mixture and heated from below. Their results show that it is possible to find the species separation of a binary mixture in this geometrical configuration, and that the vibrations can be used to delay the loss of stability of the mono cellular flow, which allows separation at a higher Rayleigh number. They applied the case of high-frequency, small-amplitude vibrations, so that a formulation using time-averaged equations was used.

The condition in this study was the cavity with a porous medium saturated by a binary fluid for which the Soret effect was taken into account. The impermeable horizontal walls are kept at different, uniform temperatures. The vertical walls are impermeable and adiabatic. All the boundaries are assumed rigid. The porous medium was subjected to linear harmonic oscillations in the vertical direction. The averaged equations in the limiting case of high-frequency and small-amplitude vibrations, was proper and used in this model. The numerical method in this survey was a finite element with 150×30 and 120×20 mesh resolution for spectral method. It was observed that vertical high-frequency vibrations had a stabilizing effect on the convective flow as well as this fact that vibrations could be used to decrease the value of the separation ratio beyond which the flow at the onset of convection became mono cellular, allowing separation of the components in the horizontal cell for a wide range of positive separation-ratio binary mixtures.

Grcar and Bell [**43**] simulated the Soret effect in naturally propagating, premixed, lean, hydrogen–air flames. They considered lean, premixed, hydrogen– air flames that circulate unreservedly and are consequently non-planar and unsteady. They compared the mixture-averaged diffusion model and the multicomponent model with Dufour and Soret effects; the Soret effect was the most significant for the flames of interest. Earlier computational investigations of this kind of flame have abandoned thermal diffusion. For cellular flames, including Soret effects the predicted flame speed was increased by 20% globally and by up to 170% locally compared to the planar case of Bongers and de Goey[**44**] and to the conical case of Ern and Giovangigli[**45**]. Their simulations were based on the low Mach number algorithm, with adaptive mesh refinement. The inventive algorithm was according to the mixture averaged model, discredited by Crank–Nicolson approximation. The simulation in this word was two

dimensional. They observed a number of differences which were noticeable between the multicomponent transport model, with Dufour and Soret effects, and the mixture-averaged approximation without cross-diffusion. In these studies this dissimilarity was mentioned, but based on our main topic of this project, we don't want to state all of them.

Tai and Char [**46**] surveyed the effects of diffusion thermo and thermal diffusion on heat and mass transfer by free convection flow. The laminar free convection flow with presence of thermal radiation and mass transfer of non-Newtonian power-law fluids along a vertical plate within a porous medium was considered. The influence of Soret and Dufour diffusion and thermal radiation and power-law fluid index was applied in this study. The DQM[8] was applied to solve this convective heat and mass transfer problem. The quasi steady state condition was the maximum change between the current and the previous iterations in all the dependent variables satisfying 10^{-5}.

In the results, thermal and concentration fields and local Sherwood number for different values of the controlling parameters were discussed. They indicated that if the buoyancy ratio of concentration to temperature is positive, the local Nusselt number decreases with a decrease in the power-law index and the Soret number or an increase in the radiation parameter and the Dufour number. The results show that the Dufour number enhanced the local Sherwood number; however it reduced the local Nusselt number. They mentioned that an increase in Soret number leads to a reduction in the local Sherwood number, but it makes an increase in the local Nusselt number.

The effects of Soret and Dufour on free convection along a vertical wavy surface were investigated by [**47**]. Free convection of heat and mass transfer along a vertical wavy surface in a Newtonian fluid saturated Darcy porous medium was studied by considering cross Dufour and Soret diffusion in the medium. Under the large Darcy–Rayleigh number assumption a similarity solution to this problem was presented.

The results were prepared for a range of the flow governing parameters such as the diffusivity ratio parameter, the buoyancy ratio parameter, the Soret parameter, the Dufour parameter, and

[8] Differential quadrature method

the amplitude of the wavy surface. It was observed that the Sherwood number becomes negative as the Soret number increases. It was found that as the amplitude of the wavy surface increases, the heat and mass transfer coefficients decrease while the thermal and solutal boundary layer thicknesses increase. The effect of the Dufour parameter was to increase the heat transfer coefficient. The mass transfer coefficient increases with the Dufour parameter up to a certain critical value of the Soret parameter. In the case when the solutal buoyancy opposes the thermal buoyancy, the heat transfer coefficient decreases with increasing values of the Soret parameter. In the aiding buoyancy case, increasing the Soret parameter increased the heat transfer coefficient while a reduction in heat transfer coefficient occurs with this parameter for the opposing buoyancy case.

A review of Experimental Approaches to Study Thermodiffusion was done by Srinivasan[**48**]. Our purpose in this review is numerical and theoretical, but because of the results of this study, that showed the significant role of vibration on the diffusion process, it is necessary to be present here. This paper deals with a detailed review of the experimental investigations of the thermodiffusion process in liquid and gaseous mixtures as well as experiments in the laboratories on earth and studies in a microgravity environment in space have been described. Experiments performed in the microgravity environment are also discussed.

They classified the techniques of the experimental approaches to understand the thermodiffusion process in mixtures of gases, liquids, and polymer solutions into two types: the optical methods and the non-optical methods. These methods of experiment were 1.Classical Soret Cell 2.Soret Cell with Beam Deection (BD) Technique. 3. Thermogravitational Column (TGC) 4. Two-Chamber Thermodiffusion Cell 5. Thermal Diffusion Forced Rayleigh Scattering (TDFRS) 6.Thermal Lens Method 7. Microuidic Fluorescence Method 8.Thermal Field-Flow Fractionation (ThFFF). These methods are discussed along with their advantages and disadvantages. For each approach its advantages and disadvantages are presented. They stated that a wide variety of experimental techniques have been employed to study thermodiffusion. Author after reviewing the experimental method of Soret effect has presented some details about microgravity experiments.

For advantages and disadvantages of performing microgravity experiments, they mentioned that there was a significant reduction in the convection issues discussed earlier and the results

can serve as benchmark values if the microgravity experiments are successful. However, costs involved in these experiments are very high. Another issue was the vibrations the experimental apparatus experience in a space fight and the consequent impact on the thermodiffusion process. They got some details that show us there was a significant increase in the heat transport due to the g-jitters when compared to the results from a purely diffusive behavior. Their study shows that optical techniques are more sophisticated such as Soret cell with beam detection; thermal diffusion forced Rayleigh scattering, thermal lens method. Convection was viewed differently for different methods because of the fact that in some cases convection was to be avoided completely in a Soret cell. Besides, convection was used to enhance separation in a thermo gravitational column. Dyeing in order to enhance the absorption of light must be done with caution after proper investigation of the impact of the dye on the thermodiffusion process. They mentioned that inclination of the thermodiffusion column can impact the separation; accurate values of inclination must be used in the theoretical analysis; also it's important that experiments in a microgravity environment can mitigate the drawbacks of convection. However, these investigations are very expensive. They concluded that availability of power was generally an issue on the space platforms. Hence, mixtures with very large diffusion times cannot be investigated at present. The platform of satellite and International Space Station provide the best environments to do experiment in weightlessness. While these platforms are extremely good at isolating the earth gravitational effects, there still exist some residual gravity that can impact the experiments. Theoretical investigations have been conducted by several researchers to study the effects of these g-jitters presented by author. Totally, in this study, there are three other review articles. The first review focuses on the author's experimental investigations on the Soret effect; the second article purely on the optical techniques that have been used to investigate liquid mixtures and polymer solutions. And at last the experiment that deals with microgravity forces is presented as well as thermophoresis in colloidal suspensions.

The other works of this author with Saghir in this year was Thermo-solutal-diffusion in high pressure liquid mixtures in the presence of micro-vibrations [**49**]. This work was a simulation of ternary hydrocarbon mixtures of methane, n-butane and n-dodecane subject to micro-vibrations at reduced gravity for high pressure mixture. The results indicated a formation of a single convective cell in all the mixtures due to a steady static micro-gravity in all two dimensions. It showed a stronger velocity component orthogonal to the direction of the temperature gradient.

The separation behavior mixture in terms of the concentration profiles and the thermodiffusion coefficients matched with the experimental trends. They also predicted the change of the sign of thermodiffusion correctly. The experimental and simulation model just had a small difference in the concentration profile of n-butane and the displacement of small traces of n-butane via the bulk flow of n-dodecane.

Their simulation confirmed that the heaviest component separated to the cold side and the lightest species moved to the hot side. And they saw that the separation direction of the species with an intermediate molecular weight at low concentrations, it moved to the hot side and at higher concentrations it moved to the cold side. The most important objective of this investigation was to simulate these experiments on FOTON-M3 to understand the fluid separation and flow behavior in the thermodiffusion apparatus via the numerical results, as well as investigating on the board of FOTON-M3 to determine whether this satellite Appropriate for micro-gravity experiment or not. They used data that was obtained from the satellite by the onboard accelerometer (DIMAC) for the source of vibration that affected the experiment. Their simulations as well as the experiment were made in a same dimensions rectangular cavity, so the actual micro-gravity environment was taken in to account. They assumed that the thermal conductivity of the mixture was constant as well as no internal heat generation in the mixture. In addition to the basic conservation law in this study, they employed Penge-Robinson Equation of state (PR EOS) that presented the mixture density at any location in the cavities which was a function of the temperature, species concentration and pressure.

The numerical solution was based on finite volume method to discretization of the governing equation. The problem was solved using the Semi-Implicit Pressure Linked Equation (SIMPLE) algorithm as outlined by Patankar. They used National Institute of Standard's Database, work of Yan *et al* [**34**]as well as models of Firoozabadi and co-workers to obtain density, viscosity, heat capacity, molecular, and thermodiffusion coefficients.

All simulations were made more than 50 hours. This time was enough to the approximate diffusion time of the mixture. They observed the phenomenon that has been studied by Yan *et al*, where the authors found that with an increase in the molecular weight of the second component of the mixture, the DT values of Octadecane decreased. As a result, whether it interacted with C1 or C12, the disparity in their molecular weights was smaller leading to weaker separation

strengths. They explained the negative value of DT by mentioning the point that in all mixtures methane tends to separate towards the hot side. It was in agreement with the experimental study. Their results showed that opposite to C1, C12, there was a positive thermodiffusion coefficient for all mixtures and were in agreement with the experimentally observed separation tendencies. They saw in their plots, near the walls the velocity in the y direction was two orders of magnitude larger than the velocity in the x direction, it was first observed by Chacha. They concluded all of these form the concentration profiles as well as the sign of the thermodiffusion coefficients of the two species. They concluded that FOTON missions provide a suitable platform to conduct the investigations of purely diffusive processes with minimal hindrance. And they mentioned that the most important reason for this was that because FOTON-M3 satellite was unmanned and the micro gravity accelerations along the direction of the temperature gradient were in a way that the velocities in this direction were not large enough to enhance the separation.

Recently, Srinivasan and Saghir [**50**] investigated Impact of the vibrations on Soret separation in binary and ternary mixtures. According to last article that was simulating vibration on the FOTON satellite, Saghir and his teammate in this study provided CFD simulations of the vibrations on the thermodiffusion process, but in this survey, they simulated two ternary hydrocarbon mixtures and one binary associating mixture that were methane (nC1)/n- butane (nC4)/n-dodecane (nC12) and nC12/isobutylbenzene (IBB)/tetralin (THN), and a binary mixture of isopropanol/water. One of the tendary mixtures was assumed to be a pressure of 35 MPa and the other mixtures were at a pressure of 0.101325 MPa. The vibrations were recorded by the accelerometers onboard the international space station. Based on their previous model, the thermal gradient was applied in the horizontal direction of a two-dimensional domain. At first, they simulated environment corresponding to an ideal zero-gravity or purely diffusive scenario, and after that they focused on case (ISS), the demeaned Root Mean Squared (RMS) values of the acceleration. Their assumption was a constant thermal conductivity and no internal energy generation. As well as pervious work, they used a finite volume method which was used for discretization of the governing equation to solve the problem. All simulations have been made in about 18.5 hours. This duration time was sufficient because the experimental duration corresponding to this study was shorter than this duration. This duration of time was selected for these investigations because about 18 hours a quasi steady state was reached. In the Ideal case

the velocities in both directions were seen very weak with order of magnitudes about 1×10^{-50} m/s. However, in the both cases the velocities are higher than magnitudes of the order of 1×10^{-6} m/s. The result of this study shows that the vibrations were too strong for all three mixtures which made a significant amount of mixing in the cell that minimized the Soret separation. It can be concluded that performing diffusion investigations for liquid mixtures on the ISS was prone to non-negligible errors that arise due to the vibrations of the platform. In addition, they mentioned that while the error decreases for fluids at high pressure, there was still assigning amount of convective disturbance that will destroy the small separations that are obtained via the Soret effect, so they proved that in order to experiment on the board of ISS, it was advisable to use the vibration isolation facility that was available on the ISS to conduct pure diffusion investigations. It can be stated that performing diffusion experiment for liquid mixtures on the ISS was not reliable. The results of analysis showed that unlike the purely diffusive scenario, imposing the ISS vibrations had a profound effect on the Soret effect in all three systems. More precisely, in all three mixtures, a single convective cell was observed to make a mixing effect; this phenomenon destroyed most of the Soret separation. The influence of vibrations to remove the Soret effect on the low pressure mixture was more than high pressure mixture. And this happened as a result of the fact that in lower pressure the fluids respond occur more easily to the applied vibrations.

The last research that is presented here was done by Parsa and Saghir in 2011. In this study Parsa and Saghir [**1**] simulated the double-diffusive thermal convection with the Soret effect process presented to different vibration conditions when the steady gravity was assumed to be zero. A square shape cavity was subjected to a lateral thermal gradient filled with a binary mixture of ninety percent mass fraction of water and Isopropanol put under the influence of different levels of vibrations. The thermal gradient was applied to cavity perpendicular to the vibration. One of the most important characteristics of this work that made this research to be unique was that all physical properties including density, mass diffusion, and thermodiffusion coefficients were assumed variable as a function of temperature and concentration using PC-SAFT equation of state. PC-SAFT equation was used in this study to make a relation between density change and concentration and temperature. The concentrations were set equal to the initial concentrations and the velocities in the computational domain were set equal to zero for

initial condition. For the initial value of pressure author used the average temperature to calculate that. The analysis was performed at viscous time and thermal time. It should be noted that at the thermal time, the thermal equilibrium is reached. Moreover, mass separation occurs along the temperature gradient; however, it is much slower than the thermal process.

The thermal properties of the fluid as well as the concentration profiles were scrutinized on a long time scale, during thermal time. The system was subjected to the three different levels of Rayleigh vibrations by using different frequencies, amplitudes and temperature gradients. The results showed that using variable properties from PC-SAFT make the outcomes more reasonable in comparison with the model with constant properties. It is observed that a strong mixing was found in cases with high Rayleigh vibrations.

1.3 Research Objectives

Thermal diffusion, or Ludwig-Soret Effect, plays a vital role in mass transport in multicomponent mixtures, especially hydrocarbon mixtures, such as is found in old reservoir investigations. Theoretical studies have reached a certain level with several models proposed to explain the mechanism involved in this essential process, and experimental results have been accumulated to help researchers to widen their investigation. However, to have a clear comparison between pure thermodiffusion in a mixture that is the result of theoretical investigation, and the experimental data, the vibration effect on the experiment result should be considered. In some cases, the consequence of this vibration may be induced by strong convection cell in the sample mixture so that the diffusion pattern in the mixture is removed completely by convection.

The main objectives of this research are:

1- To simulate a thermodiffusion experiment when it is subjected to gjitter acceleration as well as to understand the quality of the microgravity environment on FOTON-M3 and ISS[9];

[9] International Space Station

2- To simulate these experiments and understand the fluid separation and flow behaviour in the thermodiffusion apparatus via the numerical results by applying the vibration result to the system;

3-To conduct the computational fluid dynamics simulations of the thermodiffusion in atmospheric pressure binary mixtures of water and isopropanol subject to micro-vibrations at reduced gravity;

4-To compare ISS and FOTON-M3 as suitable vehicle for operating the thermodiffusion experiments;

5-To perform result comparison between different cavities based on their dimensions,

1.4 Thesis Organization

This thesis consists of four chapters and an appendix which are organized as follows:

Chapter One presents an introduction to thermodiffusion and a literature review.

In Chapter Two, the results of the microgravity condition on board of international space station and FOTON-M3, as well as different presentation techniques of these vibrations in order to apply an axial vibrational acceleration field to our problem were analyzed.

Chapter Three displays governing equations which are used to solve the problem. These equations are the Navier-Stokes equations, continuity, energy and mass transport equations as well as the different equations of state. Also, the numerical scheme of the problem as well as the SIMPLE method is discussed to solve the problem.

In Chapter Four, first the mathematical and boundary conditions of the problem are mentioned. After that, the results and discussion of different effects of microgravity vibration on board ISS and FOTON-M3 in the cavity with lateral temperature gradient are presented. Finally the conclusion of this study is given.

In the appendices, different subroutines to calculate the vibration results as applied to the CFD code and other subroutines for presenting the result of the CFD code are presented.

Chapter 2 : Accelerometer Data Analysis

2.1 Abstract

The goal of the detailed analysis is to use all available vibration raw data in our simulation model. The reasons that this analysis is needed are as follows; first, the time step of the raw data is too short to apply to our CFD code. Thus an appropriate method is required to change the raw data to acceleration with our chosen time step. Secondly, in the raw data, there is no reference. As a result of this issue, before making any change, it is necessary to calculate the mean data over each given interval. Detailed analysis requires developing estimates of the frequency of the vibration signal. Analytical techniques for solving vibration problems are difficult and the technology frequently advances. Therefore, the approach presented in this chapter focuses on the key steps usually taken by a professional in the field.

The MMAP[10] at the NASA[11] LeRC[12] controls the Space Acceleration Measurement System and the Orbital Acceleration Research Experiment instruments to measure the microgravity environment on orbiting space laboratories. These laboratories include the Spacelab payloads on the shuttle, the SPACEHAB module on the shuttle, the middeck area of the shuttle, Russia's Mir space station and the International Space Station. Experiments are carried out in these laboratories to study scientific principles in the near-absence of gravity.

The microgravity environment that would be ideal for most experiments would have zero acceleration diagonally for all frequency bands or a true weightless condition. This condition cannot be attained in actual space flight, where there are numerous things which provide accelerations to the environment.

This chapter does not deal to present an overview of the major microgravity environment disturbances of these laboratories; however, few sources of these vibrational accelerations are

[10] Microgravity Measurement and Analysis Project

[11] The National Aeronautics and Space Administration

[12] Lewis Research Centre

mentioned. These disturbances are characterized by their source, their magnitude, frequency and duration, and their effect on the microgravity environment.

2.2 Introduction

Materials science, combustion science, low temperature microgravity physics, fluid physics, biotechnology and life sciences experiments are performed on the NASA Lab Orbiters and on Russians Mir Space Station to take benefit of the reduced gravity environment consequential from the continuous weightlessness state of low earth orbit. Accelerometer systems are flown with these experiments to record the microgravity environment to which the experiments were exposed. This microgravity environment is a multifaceted combination of vibrations and accelerations produced by orbital mechanics, vehicle maneuvers, experiment equipment, vehicle subsystems, flight attitude and the crew.

Two common accelerometer systems flown to carry experiments are the SAMS[13] and the OARE[14]. These accelerometer systems are managed by the MSD[15] at NASA Glenn Research Center. These accelerometer systems are flown by the MRD [16] of the NASA Headquarters Office of Life and Microgravity Science and Applications. Other accelerometer systems are infrequently flown in support of these and other science experiments.

The Principal Investigator Microgravity Services project in the MMAP[17] supports principal investigators of microgravity science experiments as they evaluate the effects of varying acceleration levels on their experiments.[**51**]

The residual acceleration environment of an orbiting spacecraft in a low earth orbit is a very complex observable phenamena. Many reasons such as experiment operation, life-support systems, equipment operation, aerodynamic drag, gravity gradient, crew activities, and rotational effects as well as the vehicle structural resonance frequencies[18] contribute to form the overall

[13] Space Acceleration Measurement System

[14] Orbital Acceleration Research Experiment

[15] Microgravity Science Division

[16] Microgravity Research Division

[17] Microgravity Measurements and Analysis Project

[18] Structural modes

reduced gravity environment. Weightlessness is an ideal condition which cannot be assessed in practice as a result of the various sources of acceleration present in an orbiting spacecraft. Because the environment in which experiments are performed is not zero gravity; consequently, experiments can be affected by the residual acceleration due to their relation with acceleration magnitude, orientation and duration, frequency. Hence, experimenters must know what the environment was when their experiments were executed in order to analyze and correctly interpret the consequence of their experimental data.

The NASA GRC Principal Investigator Microgravity Services project has the responsibility for practicing and archiving acceleration measurements, analyzing these measurements, characterizing the reduced gravity environment in which the measurements were taken, and providing expertise in reduced gravity environment assessment for a range of carriers platforms and facilities such as the Space Shuttle, parabolic aircraft, sounding rockets, drop towers and the ISS[19] in support of the NASA's PSD PIs[20]. The PIMS[21] project supports PIs from various science disciplines for example biotechnology, fluid physics, combustion science, material science and fundamental physics. The PIMS project is funded by the NASA Headquarters and is part of the NASA Glenn Research Center's MMAP[22] which integrates the analysis and interpretation component of PIMS with the various NASA sponsored acceleration.

The NASA PSD[23] sponsors science experiments on different reduced-gravity carriers or platforms and facilities such as the STS[24] , parabolic aircraft, sounding rockets, drop towers and the ISS. The NASA Glenn Research Center Principal Investigator Microgravity Services project supports NASA’s Microgravity Research Division Principal Investigators by providing acceleration data analysis and interpretation for a range of microgravity carriers including the International Space Station, the Space Shuttle, the Russian Mir Space Station, parabolic aircraft, sounding rockets, and drop towers. The PIMS project is funded by the NASA Headquarters

[19] International Space Station

[20] Principal Investigators

[21] Principal Investigator Microgravity Services

[22] Microgravity Measurement and Analysis Project

[23] Physical Science Division

[24] Space Transportation System

OBPR [25] which is part of the NASA Glenn Research Center's Microgravity Environment Program. It integrates the analysis and interpretation component of PIMS with the various NASA sponsored acceleration measurement systems. For the ISS, these acceleration measurement systems include the Space Acceleration Measurement System-II and the Microgravity Acceleration Measurement System. In the next section we discuss more about ISS vibration measurement.

During ISS operations, the PIMS project is responsible for receiving, processing, displaying, distributing, and archiving the acceleration data from SAMS-II[26] and MAMS[27]. These tasks are accomplished by utilizing various ISS resources and by utilizing custom software components developed by PIMS. Detailed capabilities of the PIMS custom software components related to PI support are provided in PIMS-ISS-001 [**52**].

2.3 Background and Scope

This chapter is intended, as a reference document, to describe the PAD[28] file format employed by the PIMS project to archive the acceleration data from the SAMS-II and MAMS ISS payloads and the GSE[29] telemetry packet data required by PIMS to support offline analysis of the MAMS data. Another main objective of this data is to inform developers of future ISS acceleration measurement hardware on the information of the PAD file format and its associated directory hierarchy. The final goal of this education process is to have such future ISS acceleration measurement systems to adopt the PIMS Acceleration Data format and directory hierarchy utilized by PIMS for the SAMS-II and MAMS acceleration measurement systems in order to be used with their own acceleration measurement system. In this fashion, all acceleration statistics obtained from the ISS would be archived in an identical format, in that way microgravity PI's straightforward access is granted to ISS acceleration data regardless of the position of their experiment or the acceleration measurement system supporting their experiment[**53**].

---

[25] Office of Biological and Physical Research

[26] Space Acceleration Measurement System-II

[27] Microgravity Acceleration Measurement System

[28] PIMS Acceleration Data

[29] Ground Support Equipment

2.3.1 Acceleration Measurement System Description

The general microgravity acceleration environment includes two separate regimes: the quasi steady environment and the vibratory/transient environment. Each part of the general microgravity environment has distinctive measurement requirements that necessitate the development of multiple acceleration measurement systems. The SAMS-II and MAMS acceleration measurement systems are briefly described here because we used them in this project. Reference [**54**] provides further information of the two acceleration regimes.

2.3.1.1 MAMS

The MAMS system includes two different acceleration measurement systems called MAMS Orbital Acceleration Research Experiment[30] Sensor Subsystem and MAMS High Resolution Accelerometer Package, each with a distinct measurement objective. The purpose of the MAMS OSS data is to evaluate the quasi-steady accelerations on the ISS. MAMS OSS data are gained at a rate of 10 samples per second and are low-pass filtered with a cutoff frequency of 1 Hz. Each MAMS OSS[31] data packet encloses 16 seconds of MAMS OSS acceleration data and is transmitted in real-time at a rate of one data packet every 16 seconds. MAMS can store 25.6 hours of MAMS OSS data on board. Activated at MAMS power up or via ground command, this on board storage ability permits capturing of vital quasi-steady acceleration events for later downlink. These stored acceleration data can be send out to the ground at a ground commanded rate between 20 and 200 kbps.

The MAMS HiRAP[32] data are obtained at a fixed rate of 1000 samples per second and low pass filtered with a cutoff frequency of 100 Hz. The purpose of the MAMS HiRAP data is to measure the vibratory and transient accelerations on the ISS. Each MAMS HiRAP data packet contains 192 acceleration readings and is transmitted at a rate of one data packet every 0.192 seconds. MAMS does not have any capability to store MAMS HiRAP data on board.

---

[30] Orbital Acceleration Research Experiment

[31] Orbital Acceleration Research Experiment Sensor Subsystem

[32] Resolution Accelerometer Package

2.3.1.2 SAMS-II

The SAMS-II system includes two major elements, scattered as required throughout the ISS to measure the vibratory/transient acceleration environment. The Interim Control Unit is a Portable Computer System laptop configured to carry the SAMS-II system. The ICU[33] provided as a collection point for all SAMS-II acceleration data and all SAMS-II housekeeping data. Any authorities intended for the SAMS-II and its parts are routed through the ICU. The second section is termed the Remote Triaxial Sensor Subsystem and consists of an Electronics Enclosure and up to two Sensor Enclosures. The RTS[34] is placed throughout the International Space Station to provide a distributed, localized measurement of the vibratory/transient microgravity acceleration environment. The SE [35] contains the actual accelerometers and transmits its acceleration data to the EE[36] and next to the ICU for downlink to the ground. Each SAMS sensor can be controlled to measure and downlink acceleration data at one of five sampling rates, with five corresponding cutoff frequencies. Since the SAMS sampling rate can be varied, the number of readings per packet and the number of packets per second varies as a function of the SAMS sampling rate. Table 1 shows the connection amongst sampling rate, cutoff frequency, acceleration readings per packet, and acceleration data packets per second for the SAMS sensors.

Table 2-1 SAMS Sampling Rates

Sampling Rate[Hz]	Cutoff Frequency [Hz]	Readings Per Packet	Packets Per Second
62.5	25	31 or 32	2
125	50	62or 63	2
250	100	74 or 51	4
500	200	74 or 28	8
1000	400	74 or 56	14

[33] The Interim Control Unit

[34] Triaxial Sensor Subsystem

[35] Sensor Enclosures

[36] Electronics Enclosure

2.4 International Space Station

2.4.1 Configuration at Assembly Complete

The ISS represents a global partnership of sixteen nations. This project is an engineering, scientific and technological awesome sight guiding in a new era of human exploration in space. Assembly of the ISS began in late 1998 and will continue until completion of some of its tasks. During its assembly and over its nominal ten-year lifetime, the ISS will be used as an orbital platform for the United States and its International Partners to make benefits in microgravity, space, life, and earth sciences as well as in engineering research and technology development. The completed space station will have nearly fourteen payload racks or experiment storage facilities, six fully equipped laboratories and more than fifteen external payload locations for conducting experiments in the free space. The six main laboratories which will house research facilities, are: Destiny (US), the Centrifuge Accommodations Module (CAM-US), Columbus (ESA), Kibo (NASDA) and two Russian Research Modules. Its gigantic solar arrays will generate the electricity needed. An initial crew of three, increased to seven when assembly is complete, is living aboard the ISS. The space station represents a quantum leap in our ability to perform research on orbit and explore basic questions in a variety of disciplines such as biomedical, fundamental biology, biotechnology, fluid physics, advanced human support technology, material science, combustion science, fundamental physics, earth science and space science[**55**].

2.4.2 Space Station Analysis Coordinate System

Another important aspect is the adoption of a coordinate system for appearance of the acceleration data. Since the sensor heads itself, it can be oriented in arbitrary, non-orthogonal orientations relative to other coordinate systems; comparison of acceleration data between various accelerometers would be hard without first transforming data into a common coordinate system. For this goal, PIMS has made a choice for the Space Station Analysis coordinate system as the common coordinate system. Figure 1 shows the SSA[37] coordinate system relative to the ISS configuration at flight 6A (April, 2001) and illustrates the relationship between the MAMS

[37] Space Station Analysis

OSS, the MAMS HiRAP, and the SSA coordinate systems. MAMS is physically located within the United States laboratory, Destiny [**56**].

2.4.3 AOS and LOS Considerations

Communication from the ISS is broken. A time interval where real time data downlink is available is referred to as an Acquisition of Signal interval. Similarly, the lack of real time data downlink availability is referred to as a Loss of Signal interval. Prior to generating any acceleration data archive, both SAMS and MAMS acceleration data must have AOS[38] data and LOS[39] data merged.

LOS data is stored on board the ISS by the Medium-rate Communication Outage Recorder. Both SAMS and MAMS will measure and transmit acceleration data constantly throughout a given increment. As a result, real time acceleration data is available on the ground at some stage in AOS periods and acceleration data are stored on the MCOR[40] during LOS periods for eventual downlink.

When acceleration data are send out to the ground, either real time data downlink or data transmitted from a dump of the MCOR memory, data packets are routed from Marshall Space Flight Center to the GRC Telescience Support Center where the PIMS GSE stores each received pack into a database table devoted to each accelerometer supported by PIMS. Consequently, a separate database table is presented for MAMS OSS, MAMS HiRAP, and the five SAMS sensors. The primary function of the database tables is to automatically merge AOS and LOS data packets for each accelerometer.

The merging of the AOS and LOS streams is made probable by examining the timestamp that is put out as part of each acceleration data package received by SAMS or MAMS. As there exists overlap between the AOS and LOS acceleration data packets received, each sensor's dedicated database table overwrites any redundant data packet by checking these timestamps and the

[38] Acquisition of Signal

[39] Loss of Signal

[40] Medium-rate Communication Outage Recorder

packets themselves resulting in a table including a contiguous set of acceleration data sachets ready for the archival process[**56**].

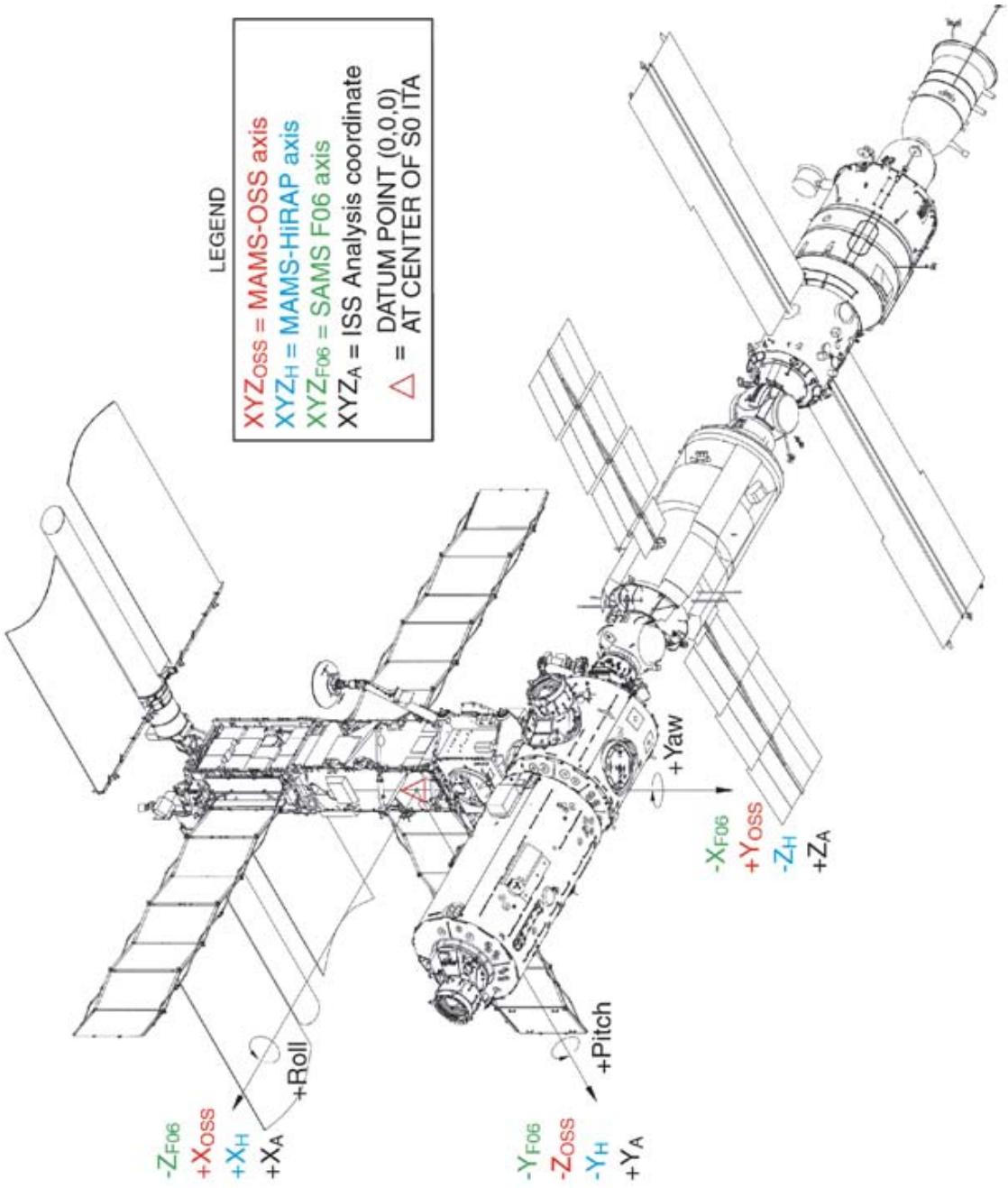

Figure 2-1 Space Station Analysis Coordinate System[**51**]

2.5 PAD File Descriptions and Directory Hierarchy

A discussion of the PAD directory hierarchy and PAD file format is provided at this point in time. Regardless of the acceleration data type, each acceleration data archive will actually consist of two files. In general, the first file (binary format) is referred to as the data file and includes the acceleration data itself, consisting four columns in the form of time, x-acceleration, y-acceleration, and z-acceleration. The second file (Extensible Markup Language (XML) format is referred to as the header file and contains ancillary data that explains the circumstances under which the data was attained. The binary format data files are stored in little endian 32-bit IEEE floating point format.

The MAMS raw acceleration data contains two additional columns in addition to the acceleration data which are the OSS base temperature and the OSS status bytes necessary for determining bias activity from the raw data stream. Each of the current acceleration data file types is described briefly in next section.

2.5.1 Acceleration Data File Types

2.5.1.1 Four Column Acceleration Data File

The four-column acceleration data file type is employed to archive acceleration data for each SAMS sensor, the MAMS HiRAP sensor, and the MAMS OSS best available TMF data types. The output from a sample acceleration data file is provided below. Per the header files discussed previously in section 4, the binary data saved in the acceleration data files are stored in binary 32 bit IEEE float little endian format. This format is specified in the ‘GData format’ header file parameter. Twenty sample records from a four-column acceleration data file are provided below. To verify the proper operation of file reading software, the following result should be obtained from the first twenty records of the data file:

2001_12_01_00_05_27.462+2001_12_01_00_15_27.464.121f02

Table 2-2 Four-Column Example

Time	X-Acceleration	Y-Acceleration	Z-Acceleration
0.00E+00	9.837032E-04	-4.740996E-04	-4.150363E-04
2.00E-03	-2.270368E-04	1.804806E-04	1.510161E-04
4.00E-03	-3.432796E-04	7.942862E-04	-1.494198E-05
6.00E-03	8.387887E-04	-3.459106E-04	-3.441011E-06
8.00E-03	1.415047E-04	-7.893521E-04	7.512448E-04
1.00E-02	-1.019951E-03	2.896064E-04	-8.919730E-05
1.20E-02	6.460590E-04	-1.200642E-04	-2.890266E-04
1.40E-02	4.568079E-04	-1.107866E-03	8.468466E-04
1.60E-02	-1.196886E-03	1.798459E-04	6.793907E-05
1.80E-02	7.237342E-04	9.244012E-04	-7.356259E-04
2.00E-02	1.297818E-03	-6.380729E-04	1.977606E-04
2.20E-02	-7.137657E-04	-2.843878E-04	4.605404E-04
2.40E-02	-4.200042E-04	1.093102E-03	-6.532240E-04
2.60E-02	1.044050E-03	-1.322112E-04	2.121586E-04
2.80E-02	-8.959807E-05	-8.211969E-04	1.130929E-03
3.00E-02	-1.082437E-03	5.247764E-04	-9.678888E-04
3.20E-02	8.361743E-04	2.773062E-04	-9.347146E-04
3.40E-02	6.122881E-04	-8.240640E-04	1.250753E-03
3.60E-02	-1.076711E-03	2.808300E-04	2.774833E-04
3.80E-02	3.359845E-04	5.769318E-04	-1.140098E-03

2.5.1.2 Six Column Acceleration Data File

The six-column acceleration data file type is utilized to archive acceleration data for each MAMS OSS raw data only. The output from a sample acceleration data file is provided below. Per the header files discussed previously, the binary data stored in the acceleration data files is saved in binary 32 bit IEEE float little *endian* format. This format is specified in the 'GData format' header file parameter. Twenty sample records from a six-column acceleration data file are provided below. To verify the proper operation of file reading software, the following result should be obtained from the first twenty records of the data file:

2001_12_01_01_00_29.547+2001_12_01_03_00_42.531.ossraw

Table 2-3 Six-Column Example

Time	X-Acceleration	Y-Acceleration	Z-Acceleration	MAMS Temperature	MAMS Status Byte
0.000000E+00	-4.595947E-06	1.519775E-05	5.799866E-06	3.962188E+01	8.923682E+06
1.000000E-01	-5.850220E-06	9.017945E-06	1.968384E-06	3.962188E+01	8.923682E+06
2.000000E-01	-6.192017E-06	3.474426E-06	-3.753662E-07	3.962188E+01	8.923682E+06
3.000000E-01	-5.538941E-06	2.471924E-07	-1.281738E-06	3.962188E+01	8.923682E+06
4.000000E-01	-4.421997E-06	-8.148193E-07	-7.324219E-07	3.962188E+01	8.923682E+06
5.000000E-01	-3.283692E-06	-1.208496E-06	1.419067E-06	3.962188E+01	8.923682E+06
6.000000E-01	-1.971435E-06	-2.947998E-06	4.417419E-06	3.962188E+01	8.923682E+06
7.000000E-01	-1.831055E-07	-7.781982E-06	7.044983E-06	3.962188E+01	8.923682E+06
8.000000E-01	1.962280E-06	-1.624145E-05	8.427429E-06	3.962188E+01	8.923682E+06
9.000000E-01	3.738403E-06	-2.723236E-05	9.017945E-06	3.962188E+01	8.923682E+06
1.000000E+00	4.553223E-06	-3.824158E-05	1.031342E-05	3.962188E+01	8.923682E+06
1.100000E+00	4.632569E-06	-4.673309E-05	1.301880E-05	3.962188E+01	8.923682E+06
1.200000E+00	4.531860E-06	-5.131073E-05	1.582947E-05	3.962188E+01	8.923682E+06
1.300000E+00	4.891968E-06	-5.192413E-05	1.695099E-05	3.962188E+01	8.923682E+06
1.400000E+00	5.905151E-06	-4.969482E-05	1.591186E-05	3.962188E+01	8.923682E+06
1.500000E+00	7.131958E-06	-4.622040E-05	1.347198E-05	3.962188E+01	8.923682E+06
1.600000E+00	7.830810E-06	-4.235229E-05	1.016235E-05	3.962188E+01	8.923682E+06
1.700000E+00	7.562256E-06	-3.816376E-05	5.863953E-06	3.962188E+01	8.923682E+06
1.800000E+00	6.661987E-06	-3.296356E-05	1.107788E-06	3.962188E+01	8.923682E+06
1.900000E+00	5.902099E-06	-2.623901E-05	-2.705383E-06	3.962188E+01	8.923682E+06

Included in this section is a clarification of what constitutes to a file break or file closure. A file break can happen for one of the three following reasons. The first cause is based on the archival software detecting a time gap when generating the PAD file. A time gap can occur for a couple of reasons. The basic reason of time gaps results from the reality that data packages are broadcasted from MSFC to the GRC TSC via User Datagram Protocol; UDP [41] does not guarantee successful delivery of each data package.

If the network transmission loses a data packet, the resultant time gap closes the current file and opens a new file. This products in the file name are marked as not append able. Time gaps can also result from operational troubles with the MCOR. If the MCOR doesn't successfully

[41] User Datagram Protocol

store data packages during an LOS interval, those data packets may be eternally lost, and would therefore result in a time gap when the data archives are produced. A second reason is derived from the time period covered by a given file. When the PAD archival software is started, the user presents a maximum file size in time for the especial acceleration data type. Characteristically for SAMS and HiRAP data, the file sizes are limited to 10 minutes in duration. Because of the lower sampling rate, the file sizes for MAMS OSS data are classically on the order of hours. If contiguous data is obtained for the maximum file size specified, the present file is closed and a new file is opened. These results in the file name scored as append able.

The third reason is when one of the ancillary parameters varies value. The intention of the ancillary data is to explain each data point included in the associated binary data file. Consequently, when an ancillary data parameter changes value, it is essential to close the existing data file and open a new file reflecting the change in the ancillary data[**56**].

2.6 Directory Hierarchy for Data Archives

The directory structure for the data archives is found over the time which the data was taken and processed. Figure 2-2 exemplifies the various intensities of the directory structure, starting with the year, month, and day designations. Each individual sensor type as described in pervious section will have its own branch from the basic time based structure.

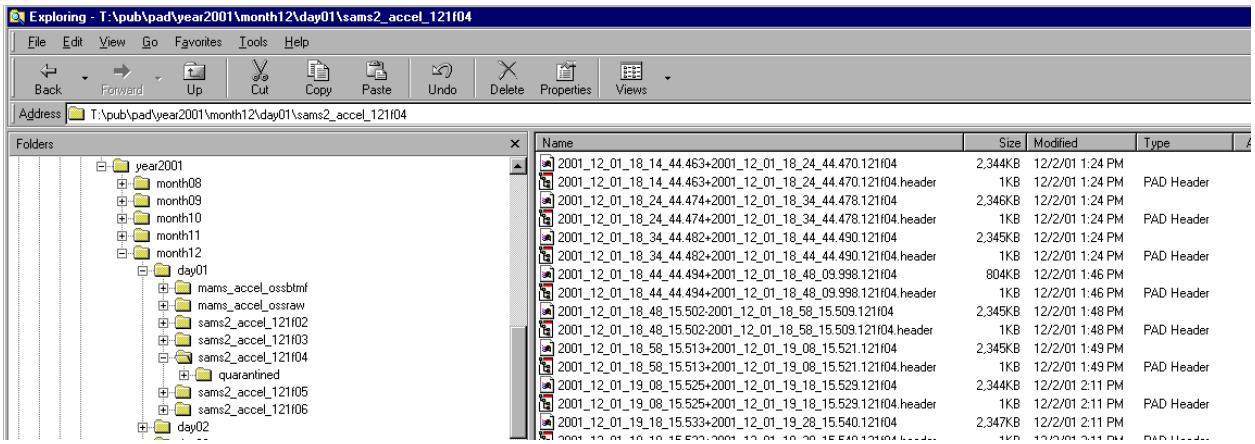

Figure 2-2 PAD File Directory Structure[**51**]

2.6.1 Filename Description

The filename convention for the data archives is explained below. The XML header file consists of the same file name convention with a ".header" appended to the end of the base filename.

Filename: YYYY_MM_DD_hh_mm_ss.sss±YYYY_MM_DD_hh_mm_ss.sss.<SensorID>

Fields: start time is Appendable stop time sensor

The fields are defined as follows:

Start time: GMT for timestamp of first record in the data file

Is Append able: "+" if this data file is append able to previous; otherwise "–"

Stop time: GMT for timestamp of last record in the data file

Sensor: sensor ID

The naming convention for the directory for each of the data types available is described in Table 2-4. The Append able designation means the data from consecutive files is truly consecutive in time with no missing acceleration readings.

Table 2-4 Data Type and Sensor ID

Data Type	Data Description	Directory Name
MAMS OSS raw data	10 sample per second OSS data	mams_accel_ossraw
MAMS OSS best available trimmean filter (TMF) data	OSS data filtered to one data point every 16 seconds	mams_accel_ossbtmf
MAMS GSE data	ISS body rates and body angles data necessary to mathematically map OSS data to alternate locations	iss_rad_radgse
MAMS OSS final bias data	Bias data obtained from the OSS sensor	mams_accel_ossfbias
MAMS HiRAP data	1000 sample per second HiRAP data	mams_accel_hirap
SAMS-II data	yyy sample per second SAMS-II data, where yyy=sampling rate of a particular SAMS-II sensor	sams2_accel_121xxx, where xxx=serial number of a given SAMS-II sensor

Again, data gaps and changes in the ancillary data restrained in the header file trigger generating a new file, the first of which will have **isAppendable** set to "–". With this convention, a series of files that constitute a contiguous slice of data will have **isAppendable** set to "–"in the first file of the series and a "+" in the remaining files in the series.

2.6.2 PIMS Acceleration Data (PAD) File Format

The details of the PAD header files and binary files are provided in this section. Again, the PAD file format exists in file pairs.

Table 2-5 Ancillary Data Parameters and Acceleration Measurement Systems

Ancillary Parameter	Parameter Applicable to SAMS	Parameter Applicable to MAMS HiRAP	Parameter Applicable to MAMS OSS
Time Zero	YES	YES	YES
Sampling Rate	YES	YES	YES
Cutoff Frequency	YES	YES	YES
Sensor ID	YES	YES	YES
Gain	YES	NO	NO
Data Quality Measure	YES	YES	YES
Bias Coefficients	YES	YES	NO
Scale Factor	YES	YES	YES
Station Configuration	YES	YES	YES
Sensor Coordinate System	YES	YES	YES
Data Coordinate System	YES	YES	YES
g Data Format	YES	YES	YES

2.6.2.1 Binary File Format

The binary format data files are saved in little endian 32-bit IEEE floating point format. Each of the current acceleration data binary file types is explained shortly in pervious.

2.6.3 Description of Header File Ancillary Data Parameters

The current set of ancillary data parameters contained in each archive file is explained in the sections that follow. Each ancillary parameter may not be applicable to a special sensor for different reasons. Some examples of this are supplied in the following sections. Table 2 summarizes the connection between ancillary data factor and acceleration measurement system. However, even where the ancillary parameter does not apply, a dummy value is supplied in the ancillary file for reliability between each sensor.[**56**]

2.7 Accelerometer Systems' Description and Locations

One of the major goals of ISS is to make a quiescent reduced gravity environment available to execute fundamental scientific research. However, small interruptions aboard the Space Station impact the overall environment in which experiments are being executed. Such small disturbances should be considered in order to evaluate their potential impact on the experiments. Two accelerometer systems built up by NASA's Glenn Research Center in Cleveland, Ohio, are being employed aboard the ISS to acquire such measurements. These two systems were flown to ISS on April 19, 2001 aboard the space shuttle flight STS-100 [**56**].

2.7.1 Microgravity Acceleration Measurement System (MAMS)

MAMS measures acceleration provided by aerodynamic drag created as the space station orbits the earth. It also measures accelerations are generated as the vehicle rotates and vents water. MAMS consists of two sensors. MAMS-OSS, a low frequency range sensor that covers up to 1 Hz, is used to illustrate the quasi-steady environment for payloads and the vehicle itself. MAMS-HiRAP [**57**] is used to characterize the ISS vibratory environment up to 100 Hz. For Increment-2, MAMS is placed in a double middeck locker.

2.7.2 Space Acceleration Measurement System

SAMS determines accelerations caused by vehicle, crew and equipment disturbances. SAMS measures the vibratory/transient accelerations, which take place in the frequency range of 0.01 to 300 Hz. For Increment-2, there are five SAMS sensors along with experiments located in the EXPRESS Racks 1 and 2. The sensors measure the accelerations electronically and transmit the measurements to the Interim Control Unit placed in an EXPRESS Rack drawer. Data is collected

from all the sensors and down linked to Glenn Research Center's Telescience Support Center. The PIMS project analyzes processes, and then illustrates the data on the PIMS' Web site for ready access by the microgravity scientific community.

2.8 Vibratory Regimes

The frequency response of the accelerometer systems employed to pull together vibratory data may extend below 0.01 Hz down to DC, but those instruments are not optimized for making quasi-steady or DC measurements. The MAMS-OSS instrument is specialized for this goal. As a result, unless otherwise noted, it is assumed that the vibratory data has been demeaned for plots and analyses of vibratory data which is, for the time interval under consideration, the mean value is calculated and then subtracted off of each data point on a per axis basis.

2.8.1 Interval Statistics

A plot of acceleration interval statistics in units of g versus time gives some information about acceleration variations as a function of time. This display type permits relatively long times to be showed on a single plot. There are three of such interval statistic plots that are employed for this and other reasons as described below: (1) interval average, (2) interval root-mean-square, or (3) interval minimum/maximum. One can see the raw acceleration in Figure 2-3.

2.8.1.1 Interval Average

Interval average plots demonstrate net accelerations which last for a number of seconds (it depents on the interested time step) equal to or greater than the interval parameter used. Short period, high amplitude accelerations can also be sensed with this kind of plot, however, the precise timing and magnitude of specific acceleration events cannot be extracted. This type of display is useful for identifying general effects of extended thruster firings and other activities that have a tendency to cause the average acceleration levels to shift. Figure 2-4 shows the sample of this method over ten minutes [**51**].

It should be noted that decrease in levels starting at 450 seconds in figure 2-4 was caused by cycling off of LSLE refrigerator/freezer compressor.

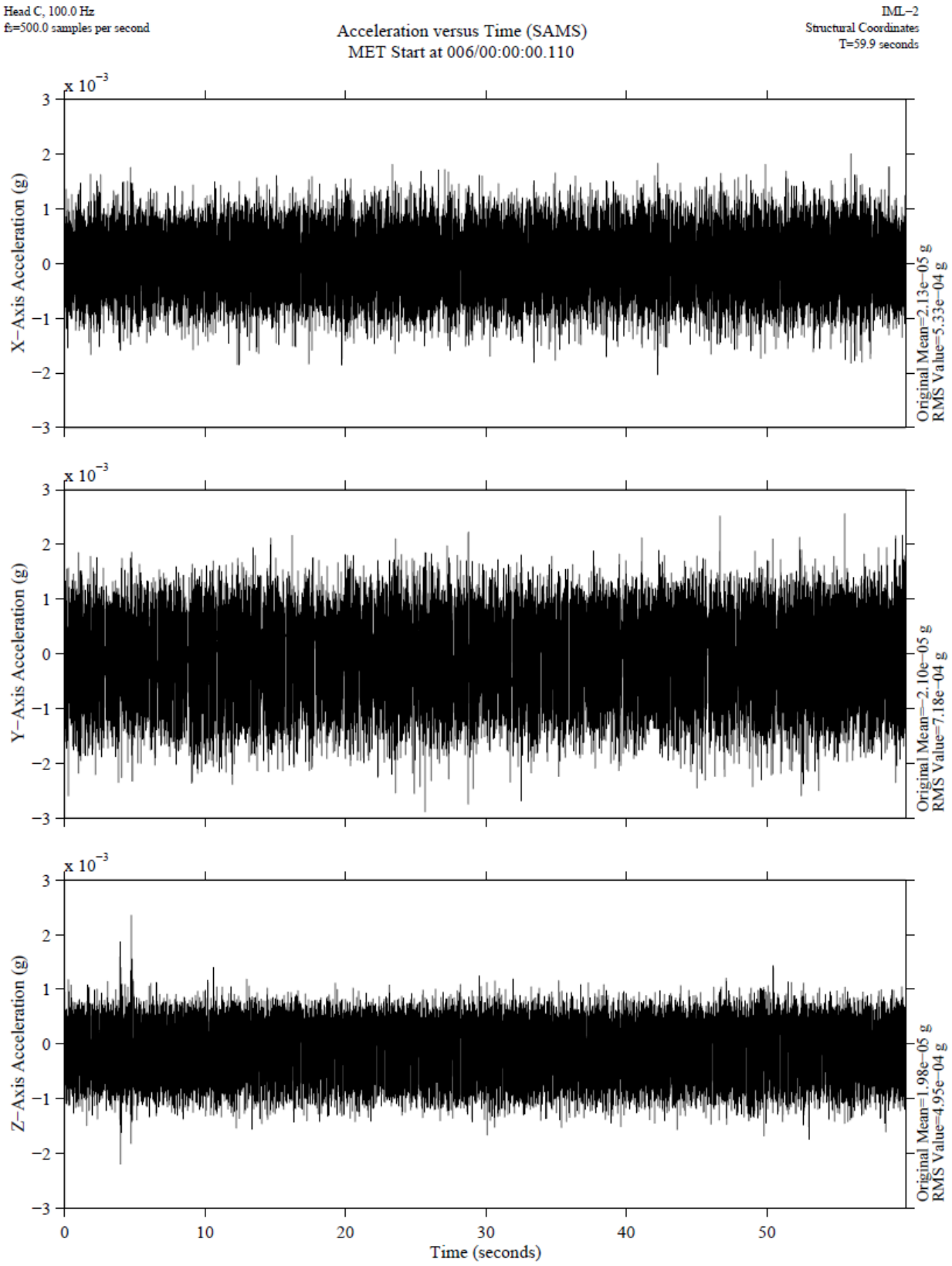

Figure 2-3 SAMS acceleration versus time plot. One minute's worth of data[**51**].

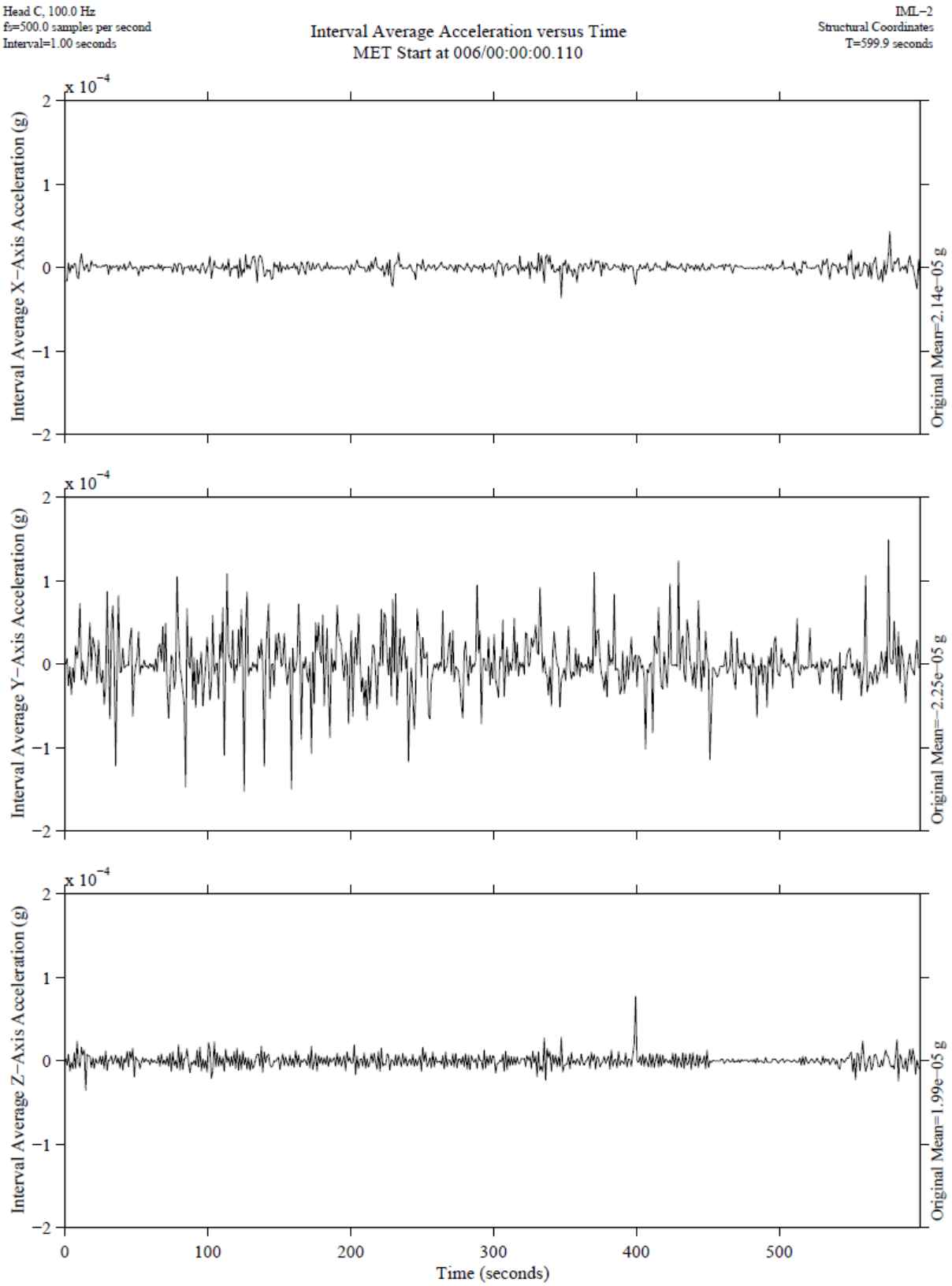

Figure 2-4 SAMS data with one-second interval average applied[**51**].

2.8.1.2 Interval Root-Mean-Square

The basic definition of Root-Mean-Square is the square root of the average of the squares of a variable quantity. The first usage of this phrase was in terms of voltage, the root mean square voltage is called the effective voltage, as opposed to the peak voltage which corresponds to the maximum AMPLITUDE of the voltage variations. RMS power (in watts) is similarly called the effective power since for an AMPLIFIER; for example, it represents its real POWER. The following relationships hold between peak, RMS and average voltage. Note that the so-called peak-to-peak voltage is twice the peak voltage.

Table 2-6 RMS statistic result

rms voltage = 0.707 peak voltage	rms voltage = 1.11 average voltage
peak voltage = 1.414 rms voltage	peak voltage = 1.57 average voltage
average voltage = 0.637 peak voltage	average voltage = 0.9 rms voltage

RMS[42] is a mean value and not an instantaneous measurement. It is very simple to describe the root-mean-square acceleration, sometimes written as GRMS or Grms or grms or Grms value as just the square root of the area under the ASD versus frequency curve, which it really is, but to physically interpret this concept, we need to consider Grms in a different way. The easiest way to think of the Grms[43] is to first observe the mean square acceleration [**58**].

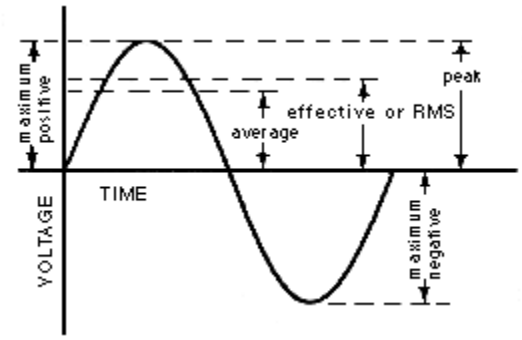

Figure 2-5 Relative levels of average, RMS and peak voltages in a sine wave signal[**58**]

[42] The root-mean-square

[43]The root-mean-square acceleration

Using the mean square value keeps everything positive. If the accelerometer time past is a pure sinusoid with zero mean value, e.g., a steady-state vibration, the RMS acceleration would be 0.707 times the peak value of the sinusoidal acceleration (if just a plain average was used, then the average would be zero)[**59**].

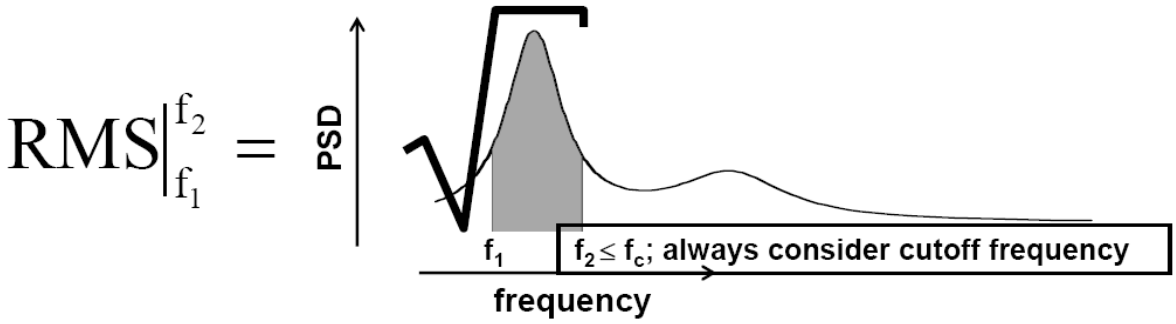

Figure 2-6 Root Mean Square illustration[**51**]

The equation of RMS was provided in the following.

$$X_{RMS} = \sqrt{\frac{\sum_{i=1}^{n} x_i^2}{n}} \tag{2-1}$$

It should be noted that equation 2-1 is used for a discrete distribution.

2.8.1.2.1 Position RMS

The position RMS provides means of determining the error associated with a reported position. This value is considered over time and consequently not representative of the error of any particular position value. It makes a statistical measure of the magnitude of the possible error in 3 dimensions available. The position RMS value is presented in term of meters.

2.8.1.2.2 Attitude RMS

The attitude RMS provides a means of determining the error associated with a reported attitude. This value is quantified over time and therefore not representative of the error in any particular attitude value. It gives a statistical measure of the magnitude of the probable error.

2.8.1.2.3 Velocity RMS

The velocity RMS provides a means of determining the error associated with a reported speed. This value is measured over time and representative of the error associated with the

manner in which speed is recorded and reported. It provides a statistical measure of the magnitude of the possible error.

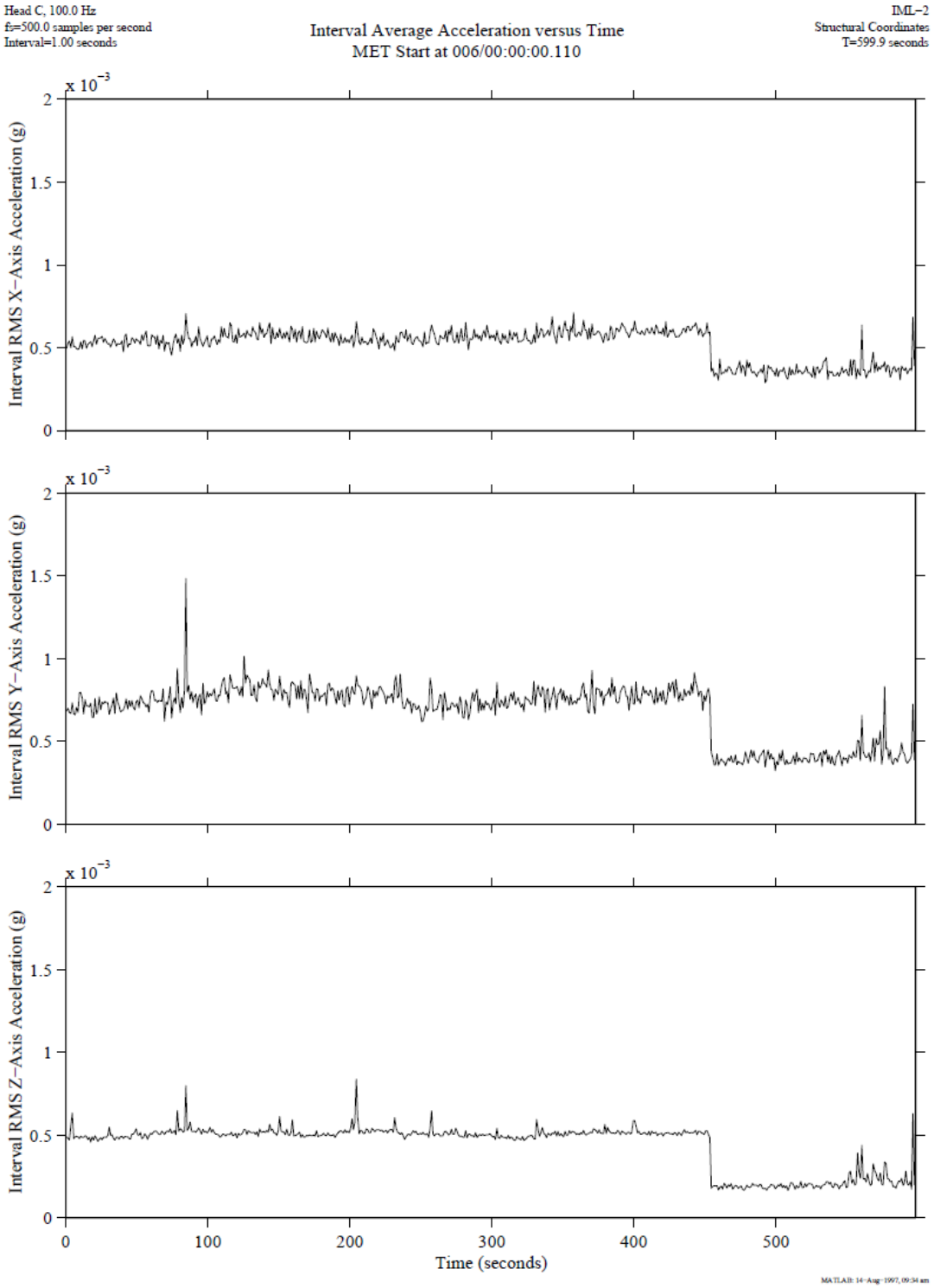

Figure 2-7 SAMS RMS data with one-second interval same ten minutes as Figure 2-4[**51**].

2.8.1.2.4 Presence Vector

JAUS is provided for variable length messages. These messages either have repeating data or have a mixture of required and optional data fields. The Presence Vector is used to indicate which of the optional data fields are included.

2.8.1.2.5 Data Validity

The Data Validity field in JAUS messages shows whether the originator of the message had sufficient information to populate the fields specified accurately. This field is not dependent on the Presence Vector. This field characteristically uses an identical mapping as the Presence Vector when a Presence Vector is described. Interval root-mean-square plots show oscillatory content in the acceleration data. For the period of time considered, this quantity gives a measure of the variance of the acceleration signal. This data representation is helpful for identifying gross changes in acceleration levels usually caused by the initiation or cessation of activities such as crew exercise or equipment operations [**51**].

2.8.1.3 Interval Minimum/Maximum

An interval minimum/maximum plot shows the peak-to-peak variations of the acceleration data. For each interval, this plot type indicates both the minimum and maximum values, and thereby shows the acceleration data envelope. This type of display is another way to track gross changes in acceleration, but it is not very accurate, in this thesis, we used primarily the RMS method, and in some special cases, to have a good comparison between different methods of applying vibration data, an average method was employed.

2.8.2 Numerical Procedure to Provide Vibrational Acceleration from Raw Data

Based on the previous section, to calculate the RMS acceleration for ISS, we need to divide the acceleration data files, which comprise to two hours and twenty minutes, the duration of the experiment, into 14 files of ten minutes each. The following outlines the analysis performed on each ten-minute data file as follows:

- Extract the files based on the file name

- Read each ten minute binary file and store data (x, y, z accelerations) and time into lists
- Convert the date to GMT date
- Record start and end times of the data in the file
- Plot the **raw data** contained in the file
- Calculate the overall mean of this data and include in the plot
- Calculate the overall RMS value of this data and include in the plot
- Demean the ten-minute data using the mean calculated above

The procedure for analyzing a 60-minute or 8-hour period is similar to the one outlined above. All of these steps are perform by the MATLAB Code given in Appendix 1. We need only put the raw data in the folder that contains that code and insert the selected time step. By running the code, all results and plots will be generated automatically.

2.9 Accelerometer Data Analysis and Presentation Technique on board FOTON

Similar to ISS acceleration, in this part we want to analyze and present acceleration of a micro satellite in the name of FOTON series. Unmanned recoverable capsules of the Foton type were introduced in 1985 by the Soviet Union. Foton (or Photon) is the project name of two types of Russian science satellite and re-entry vehicle programs. Foton was imagined as a microgravity platform for physics and materials science to complement the very similar Bion capsules that were intended for materials science studies, but some missions have also contained experiments for other fields of investigation like biology. The Foton series included 12 launched from the Plesetsk Cosmodrome from 1985 to 1999. The participation of ESA[44] began in 1991 with a single protein crystallization experiment on Foton-7, continued in 1992 by the qualification flight of Biopan on Foton-8. This was a significant step for a series of significant ESA contributions on Foton-9, -10, -11 and -12. Nowadays, the key part of the Foton payload is provided by ESA. The second series, under the name Foton-M, incorporates many design developments over the original Foton, and is still in use. So far, there have been three launch attempts of the Foton-M. The first was in 2002 from the Plesetsk Cosmodrome, which ended in failure due to a problem in

[44] European Space Agency

the launch vehicle. The last two were from the Baikonur Cosmodrome, one in 2005 and one in 2007; both were successful [**60**].

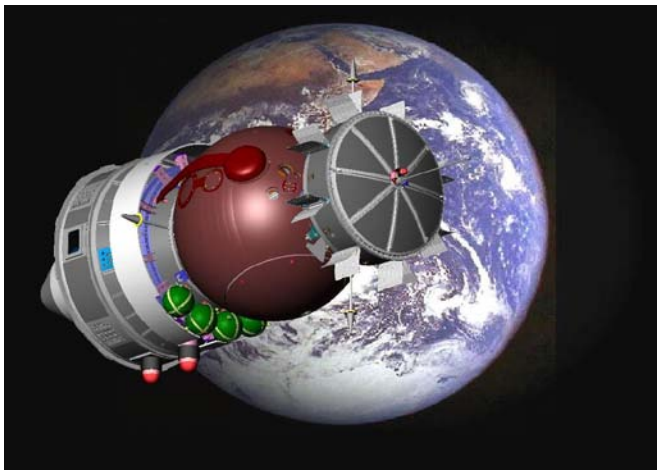

Figure 2-8 Three Dimensional modeling of the FOTON [**60**].

Table 2-7 FOTON Flight History [61**]**

	Launch Date	Flight Duration (Days)	ESA Payload	Launch Site
Foton-1	16 April 1985	12.6		Plesetsk
Foton-2	21 May 1986	13.6		Plesetsk
Foton-3	24 April 1987	13.6		Plesetsk
Foton-4	14 April 1988	13.6		Plesetsk
Foton-5	26 April 1989	14.6		Plesetsk
Foton-6	11 April 1990	15.6		Plesetsk
Foton-7	4 October 1991	15.6	x	Plesetsk
Foton-8	8 October 1992	15.6	x	Plesetsk
Foton-9	14 June 1994	17.6	x	Plesetsk
Foton-10	16 February 1995	14.6	x	Plesetsk
Foton-11	9 October 1997	13.6	x	Plesetsk
Foton-12	9 September 1999	14.6	x	Plesetsk
Foton-M1	15 October 2002	launch failure	x	Plesetsk
Foton-M2	31 May 2005	16.0	x	Baikonur
Foton-M3	Autumn 2006	13.0	x	Baikonur

2.9.1 FOTON Mission

Foton is competent of carrying a scientific payload of up to five hundred kilograms, with an average daily power budget of four hundred watt (on a typical 2-week mission) and power consumption peaks of 700 W (for a few hours). The residual acceleration levels are $10^{-4} - 10^{-6}$ g. Foton-12 was launched on 9 September 1999 from the Plesetsk Cosmodrome, about thousand km north of Moscow, entering a 225x405 km orbit with an inclination of 62.8°. It remained slowly rotating in space for 14.6 days before its descent module was ordered from the ground to re-enter. It landed successfully on 24 September in a desert area close to the city of Orenburg in Russia, close to the Kazakhstan border. All the payloads were retrieved at the landing site and within a couple of days, the experiment samples and the recorded flight data were made available to the researcher teams in different universities and research institutes engaged in the project [**61**].

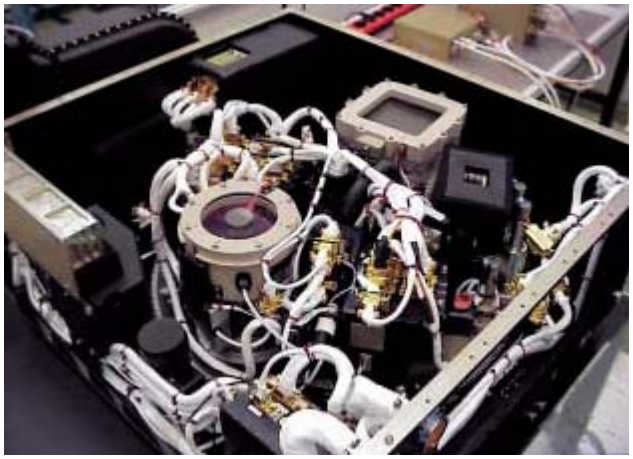

Figure 2-9 The three Experiment Containers installed on FluidPac's rotating carrousel [**61**].

ESA has been using Foton and the Bion life sciences counterpart since 1987 for its microgravity experiments. Foton-12 saw the debut of the difficult FluidPac fluid physics facility and its TeleSupport Unit in addition to the fourth flight of Biopan and three autonomous experiments.

Table 2-8 ESA's payload on Foton-12[61**]**

Facility	Mass
Fluid Pac	182 kg
Tele Support	24 kg
Biopan-3	27 kg
Autonomous	4.5 kg
Experiments	0.2 kg
Total Mass	240 kg

2.9.2 ESA facilities and experiments

ESA's principal fields of scientific investigation on Foton-12 were bordered to space biology in past missions, as well as fluid physics and materials science. ESA's payload includes all the experiment collect about 240 kg, the largest so far in this series of missions.

2.9.3 Fluid Package

FluidPac is a new-generation facility for studding fluids in weightlessness. It was designed and built by Verhaert (Belgium); Alcatel-Space (Switzerland) and Kayser Italia (Italy) were subcontractors responsible for the data management system software and part of the electronics, the Microgravity Research Centre of the Université Libre de Bruxelles took care of the diagnostics idea and optics layout.

FluidPac is proposed for examination and measurement of thermo-capillary phenomena along with free liquid-gas interfaces. Other types of fluid physics experiments can also be performed. The reusable instrument offers multipurpose diagnostics and can accommodate three complex experiment containers, see Figure 2-9. The optical diagnostics consist of observation along three different axes; two Electronic Speckle Pattern Interferometers, for free surface deformation and transmitted modulation, correspondingly, and one Infrared Camera, working at 8–12 μm, figure 2-10 shows this apparatus. The fluid sample can be clarified either by diffuse light or by two adjustable light sheets to make the experiment volume visible and to measure the velocity field in two orthogonal planes. High-resolution digital cameras attain the relevant images which are

then saved as filtered Fourier coefficients, calculated by an Image Compression Algorithm. The experiments require the application of thermal gradients. The temperature on the hot side, directly corrected within the experiment cavity itself, is regulated by a liquid loop. The boundary conditions on the cold side of each experiment are controlled by a foton-12 mission thermal control loop capable of removing up to thirty watt net heat. A hydraulic pump pushes pre-cooled water into the cold core of the active experiment container, removing the heat flux generated by the internal heater.

The Experiment Box and the Electronic Box Assembly, lying on the lower and upper part of the attachment structure, respectively (Figure 4). FluidPac's main characteristics are given in Table 2.

Table 2-9 FluidPac characteristics[61**]**

Experiment Box Mass	125.7 kg
Electronic Box Mass	47.6 kg
Experiment Box Size (W, H, L)	$800 \times 560 \times 940 \ mm^3$
Electronic Box Size (W, H, L)	$800 \times 560 \times 940 \ mm^3$
Handled Electrical	400 W

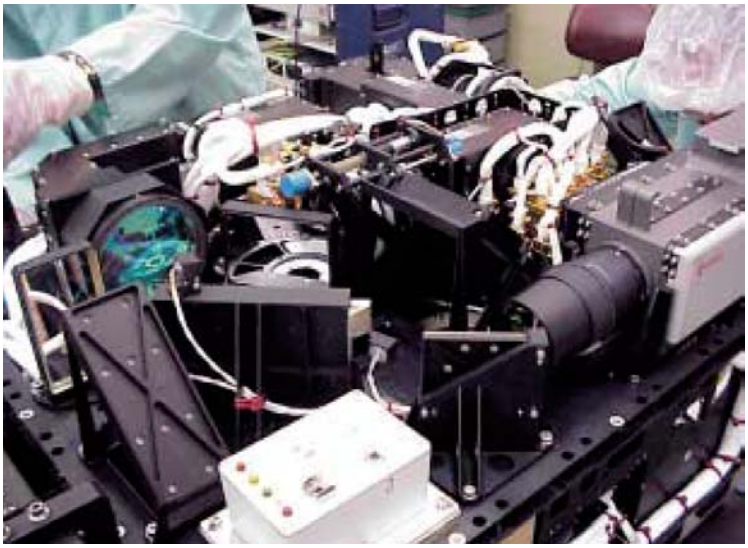

Figure 2-10 FluidPac's optical diagnostic[**61**]

2.9.4 FluidPac experiments

The experiments chosen for FluidPac's maiden flight were Magia, Bambi and Tramp. Magia (Marangoni- rown Instabilities in an Annulus) was designed to investigate thermo capillary flows, particularly their typical motions and structures, and their time-dependent behaviour.

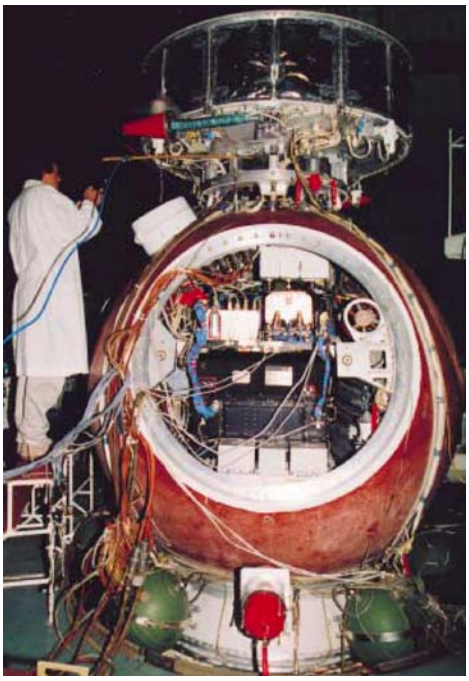

Figure 2-11 The FluidPac Experiment Box and the Electronic in front of FluidPac[**61**]

Bambi (Bifurcation Anomalies in Marangoni-Benard Instabilities) examined the behaviour of convective motions near the threshold of instabilities occurring in a flat liquid layer when heated from below. The Bambi's primary objective was the determination of the critical Marangoni number Mac, at which this instability effect is triggered. The transport of the liquid changes its speed as a function of the heat flux and the distance from the lateral walls of the cell. The liquid flows can be made visible with the help of two CCD cameras observing the dispersed tracers from two perpendicular directions Figure 2-10[**61**].

2.9. 5 FOTON-M3

Dr. Saghir and his team developed digital simulators for the petroleum sector. These make it easier to determine the quality of oil in a given well and how long the reserves will last. The

SCCO[45] experiment made it possible to forecast the behaviour of various components in an oil well—specifically, how a well is affected by the heaviest components, which push up and displace the gaseous top layer of a well. This top layer of gas is an important indication of the presence of oil. But since it shifts constantly, it's difficult to establish exactly where the well is and how big it is. The experiment first flew aboard a 16-day Russian Foton M3 recoverable satellite in 2005.

After orbiting the Earth for 12 days, it re-entered the atmosphere, and landed in a desert near the border of Russia and Kazhakstan. Then the experiments were retrieved and analyzed, with science results anticipated about one year afterwards. The CSA flew OSTEO on the same mission (an experiment to study bone loss in space), and participated in satellite operations. The CSA provided the European Space Agency with the control software and electronics hardware for SCCO. The CSA also supported the activities of Dr. Saghir, the sole Canadian scientist involved in the SCCO experiment [**62**]. Thus with the cooperation of the European Space Agency and the Canadian Space Agency, SCCO examined the influence of temperature gradients on oil wells. A gradient is the difference in temperature between two points beneath the Earth's surface, divided by the distance between them.

2.9.6 Presentation technique for FOTON acceleration

For both the FOTON and ISS acceleration, there is a computer archive of the vibration versus time, but there are two main differences between these two cases; the first one is that the time step for FOTON is about 32 seconds while this parameter for ISS is about 0.002 second, and based on the physics of our problem, we need to interpolate between each two steps for FOTON acceleration. According to previous experience with different time steps on the main CFD simulation code, the time step should be less than 0.1 second. The second difference is for the FOTON vibration. We do not need to calculate the RMS for the Average Interval because the exact amount of vibration is supposed to be applied to the problem.

[45] Soret Coefficient in Crude Oil

2.9.7 Curve Fitting

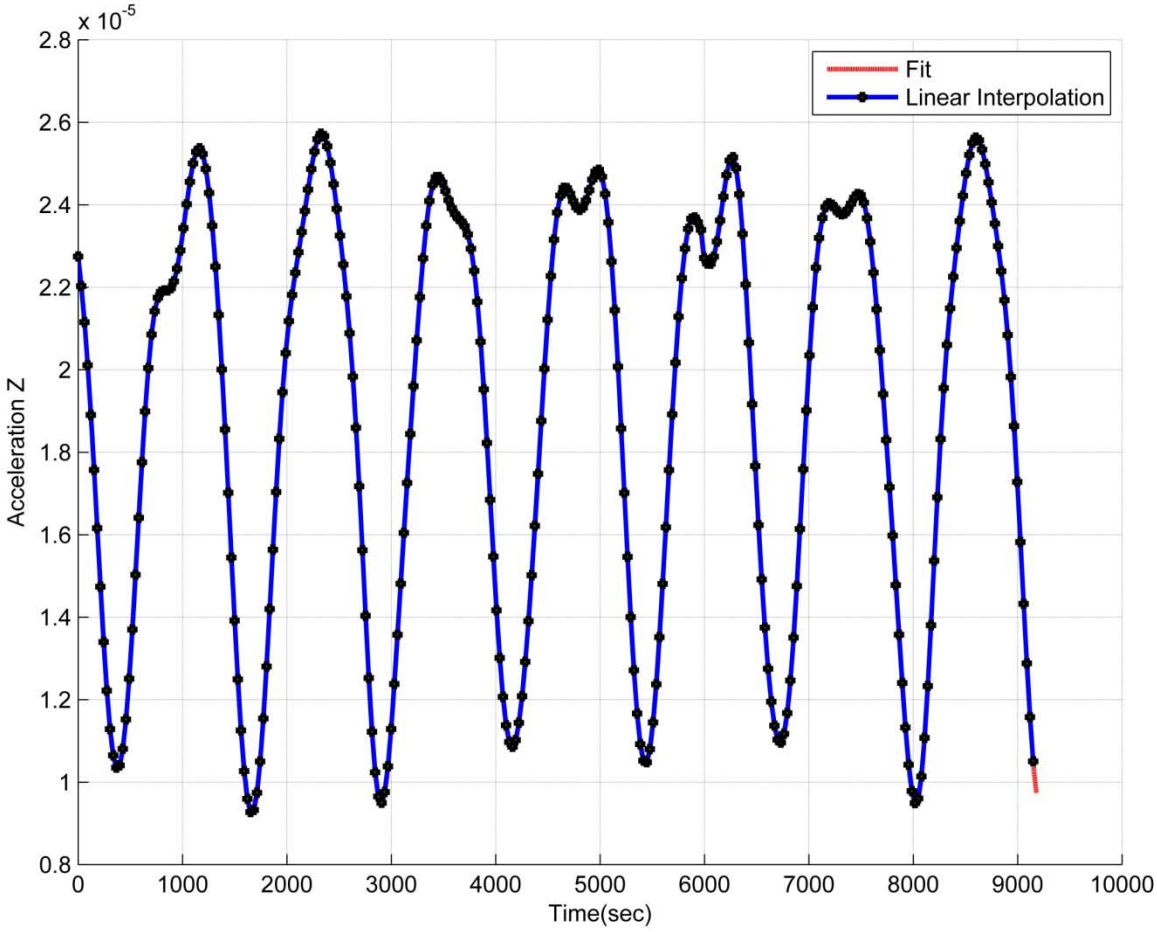

Figure 2-12 Acceleration along z direction presentation by two different interpolation

We are often presented with discrete data for which we desire a more continuous representation. For instance, given a set of empirical measurements, we might predict some sort of functional relationship between the relevant parameters of the experiment by fitting a curve to the points. As such, we are more interested in capturing the overall trend in the data rather than capturing the actual values of each and every point in the data set. The most common approach to curve fitting is least-squares regression, and the process of fitting a curve to discrete data is often referred to as a regression analysis. Regression is generally a highly statistical endeavour.

The more traditional sources of numerical error like rounding off are not as important in regression analyses since bigger issues exist with regards to the suitability of the functions to fit.

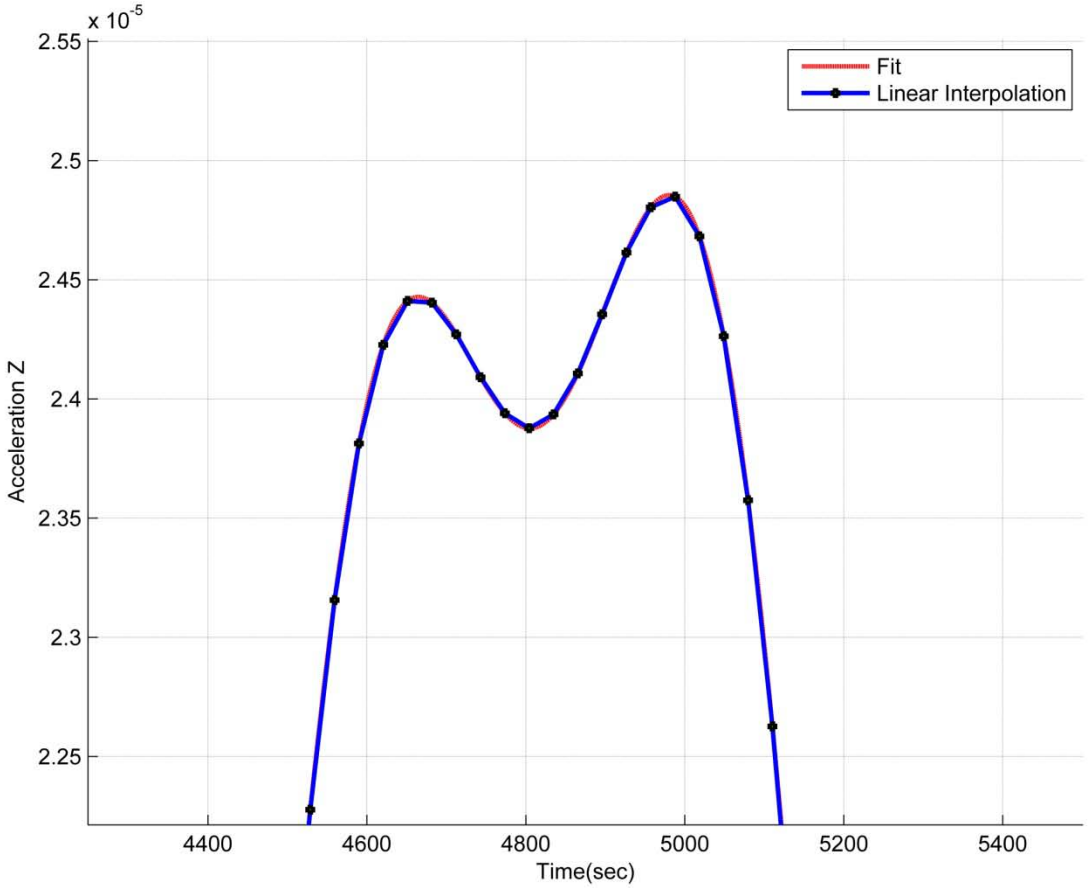

Figure 2-13 Acceleration along z direction for special duration

There are some previous similar attempts to apply the acceleration to the main CFD simulation code by interpolating between two points. We can find similar work in some studies by Saghir and his team [**50**][**19**]. They used linear interpolation between each two steps and found the amount of acceleration that must be applied in the system between two continual step times. In the current study, we used a different methods to interpolate data because in the linear interpolation, the data are not continues and do not resemble natural vibration. Consequently, a higher level of interpolation was employed in this model. For this part of problem, as in the case of ISS, the simulation was carried out for about 2.4 hours, yielding about three hundred points to interpolate.

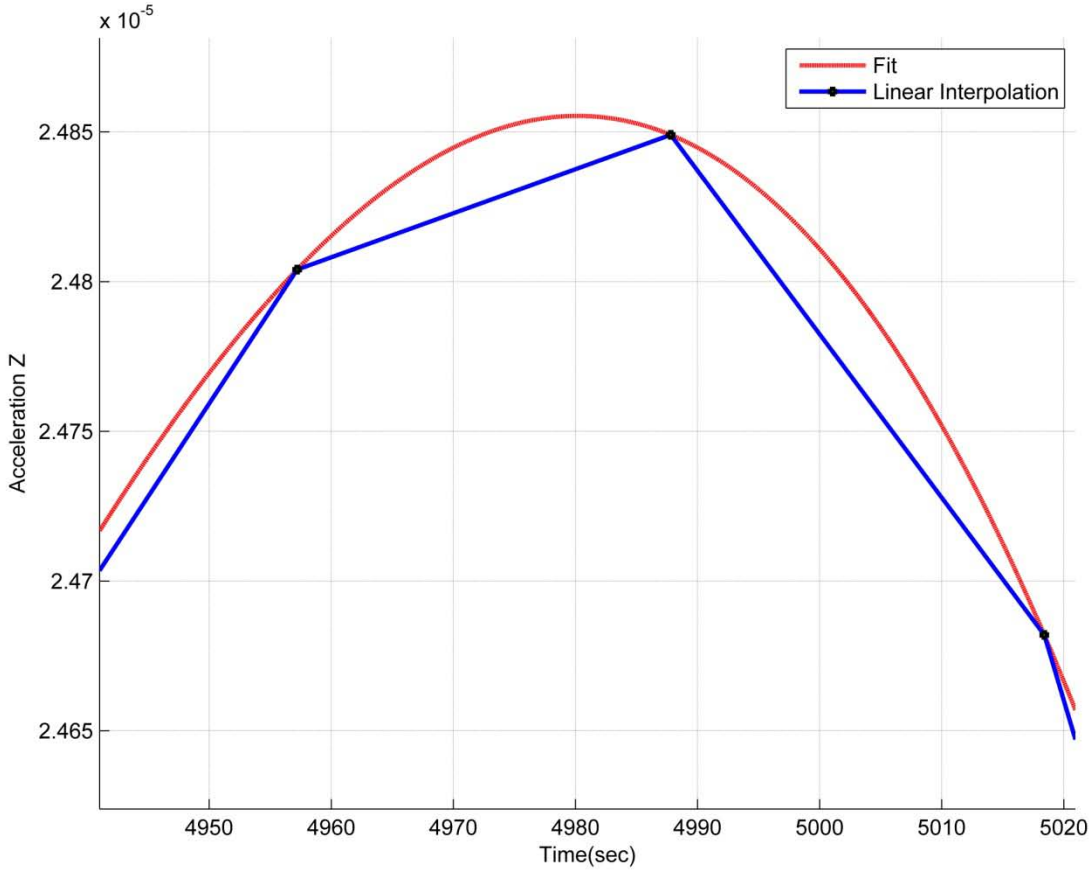

Figure 2-14 Acceleration along z direction over very small time

Interpolation between all points a single polynomial function is almost impossible. To solve this issue, we chose several adjacent points and fitted the curve to them. We when repeated the procedure for next several points. However, the same problem occurs in this method between each level of interpolation from one step to another. To remove this issue, in each level of the procedure, the MATLAB code reads one point before the first point of each level and one after the last point of that specific level and fits the curve which is two orders larger than the total number of the points at that level of the procedure. In Figures 2-12 to 2-14, one can see the curves versus time, where the first one is fitted to the points by the MATLAB code and the second one is a linear interpolation. For more detail of the code refer to Appendix 2.

Chapter 3 : Governing Equations and Numerical Scheme

3.1 Introduction and Theoretical Background

There are various fields in which compositional variations have been observed. The application of this idea encompasses a variety of areas, from oceanography, chemistry, metallurgy and material science to geology, geophysics and petroleum engineering (Turner, 1974, 1985). A number of authors have looked at compositional variation in hydrocarbon reservoirs with a view to improving the characterization of such reservoirs. The relevant literature comprises research on natural convection, double-diffusive phenomena and multicomponent convection in porous media in terms of both numerical solutions and stability analysis.

3.2 Natural and Double-Diffusive Convection

Natural convection can be defined as the flow induced by density gradients caused by temperature differences. Double-diffusive convection is flow due to simultaneous heat and mass transfer. For this phenomenon to occur, the minimum requirements are:

1. The fluid must contain at least two components with different molecular diffusivities.

2. These components must make opposing contributions to the vertical density gradient (Turner, 1974).

This study seeks to investigate the interaction between convection and diffusion in a cavity subjected to a micro-gravity environment and their effects on compositional variation. In this chapter, these processes are described with their governing equations; the techniques used to solve the problem are also presented.

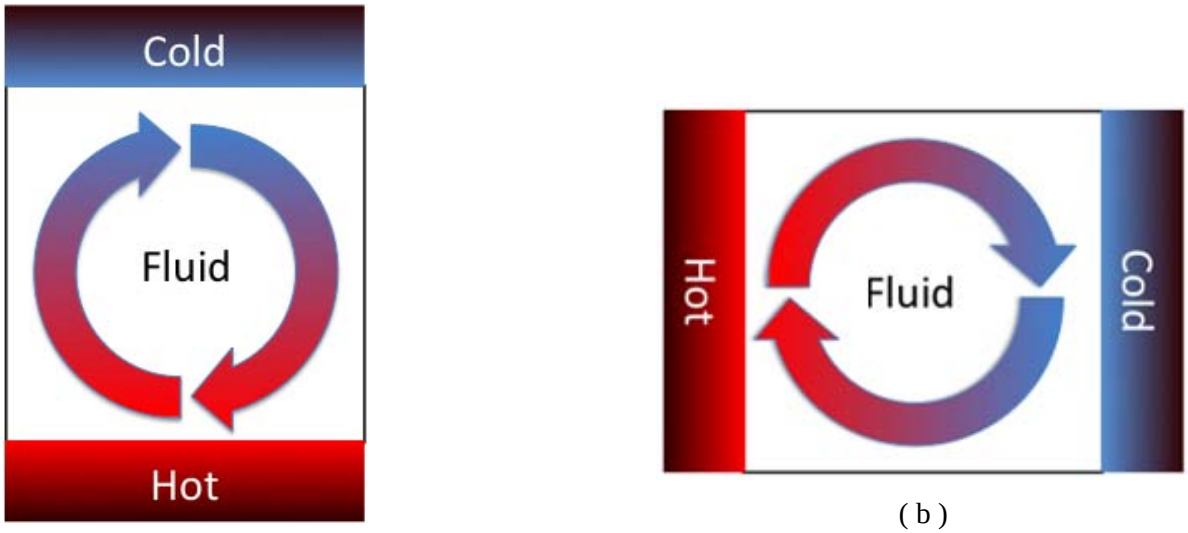

(a) (b)

Figure 3-1 Convection pattern between hot and cold wall[**63**]

3.3 Convection

Convection is a fluid movement due to density differences. Free convection is due to buoyancy differences, and the fluid will remain static when the temperature is uniform. Thermal convection is heat transfer through fluid motion. The Rayleigh-Bernard problem, describes convection in a fluid layer heated from below, see Figure 3-1.

3.4 Stability Analysis

Because of the complex equations of convection and diffusion in a fluid cavity, except in very simple case, analytical solutions in terms of velocity and composition profiles in the reservoir as a function of position are impossible. Stability analysis may be used to determine the limit on certain parameters or variables at which convection occurs. For this, the continuity, energy, mass balance and species mass transfer equations as well as an equation of state are solved. The fluid is compressible and can be represented with PC-SAFT or the Peng-Robinson equation of state in different solutions; however, depending on the mixture, either PC-SAFT or the Peng-Robinson equation of state is used. This essentially means, with respect to this section, that either changes of fluid density or the buoyancy terms of the governing equations are not ignored.

3.4.1 Gravity Segregation

In common, reservoirs are assumed to have uniform temperature distribution. If gravity is a main force, the components of the fluid will be distributed in a way to maintain local thermodynamic equilibrium in the reservoir. For example, Figure 3-2 shows composition in a reservoir with a uniform temperature field as a function of depth in a ternary system (methane, ethane and butane). Reservoirs with areal and vertical compositional variations generally have existing temperature gradients; see Figure 3-3 that shows a temperature profile with both vertical and horizontal gradients, which influences significantly the distribution of fluid components. A reservoir with a uniform temperature field will have fluid components distributed in order to keep the equilibrium condition under the prevailing gravitational force. Vertical temperature gradients alone may be not enough to produce multicomponent convection and would result in a redistribution of the fluids under equilibrium conditions.

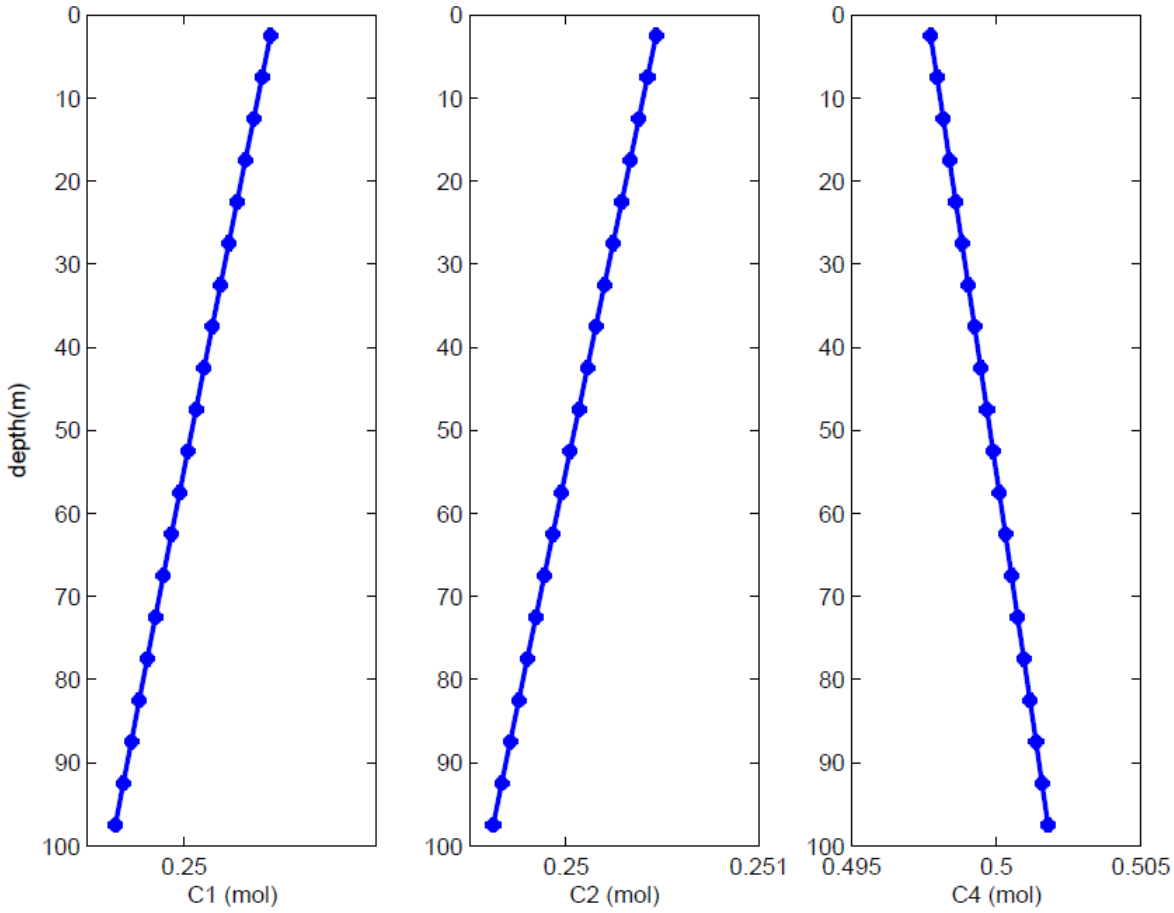

Figure 3-2 Depth composition in a reservoir with a uniform temperature field [**64**].

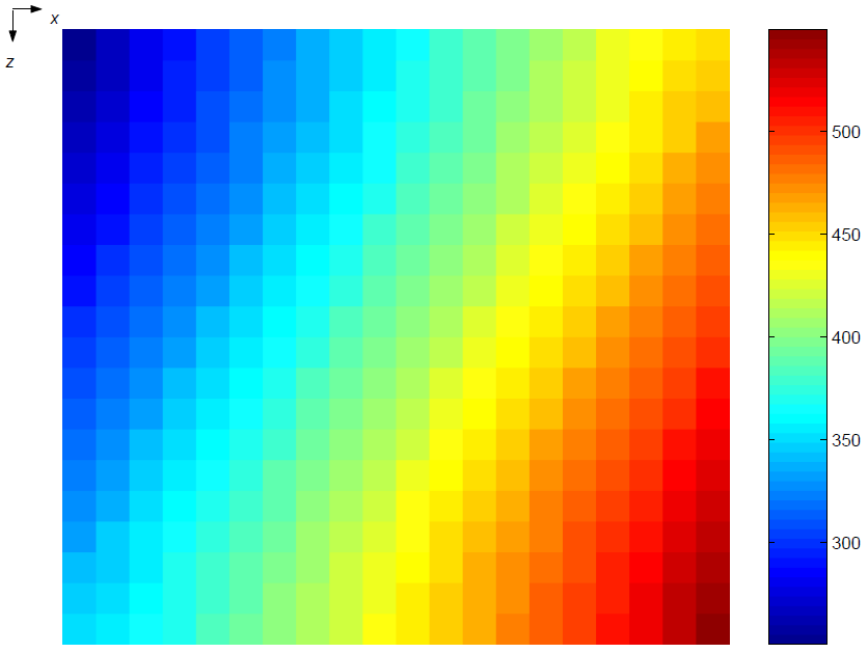

Figure 3-3 Vertical and horizontal temperature gradients [**64**]

There are some observations in a way that when the gradient is small enough and collinear with the gravity direction, convection is so weak that isn't observable. In the last case, horizontal temperature differences make horizontal density differences which induce fluid movement. Although, this slow process occurs over geologic time, the perfect understanding of convection and fluid motion are vital to the distribution of the chemical species in a reservoir. There are also diffusive influences that are dependent on the other property of the fluid like pressure, temperature and molar gradients present in the reservoir, which also force to have different fluid distributions [**64**].

3.5 Diffusion

Diffusion is the thermal motion of all fluid molecules at temperatures above absolute zero. Diffusion rate is a function of only temperature, and is not affected by concentration. Under a normal situation, molecular diffusion depends only on length scales between nanometer and millimeter. On larger length scales, transport in liquids and gases usually happens as a result of convection. As a result of this narrow misunderstanding of diffusion in the fluid, some often

usual examples of diffusion are wrong: if perfume is sprayed in one place, it will soon be smelled in the entire space or room, but a straightforward calculation demonstrates that this cannot be a consequence of diffusion; thus convection rules are the main part in this phenomenon. In contrast, heat conduction through solid media is an everyday occurrence, and it is not confusing. That is why the diffusion of heat was explained mathematically before the diffusion of mass. It leads to an equalization of concentrations within a phase. Temperature has an effect on the rate of diffusion since the kinetic energy of the molecules modifies a change in temperature. Diffusion that is maintained by concentration gradients is the most common form of diffusion recorded in the literature. Diffusion of species depends on composition difference that is called ordinary diffusion, on pressure gradients that is called pressure diffusion, and the last one on temperature gradients which is termed thermal diffusion; however there is another type of diffusion as a result of an external which occurs very rarely explained under name of forced diffusion. In particular situations, diffusion may cancel out gravitational effects. This occurs for the reason that gravity behavior like to segregate the heavier and lighter components while diffusion tends to make the mixture uniform. Consequently, at equilibrium condition of the mixture, it will not be homogeneous. The net motion in molecular diffusion will be from a region of high concentration to one of lower concentration. The diffusion of component *i* in a mixture of *j* is expressed as following:

$$J_i = -D_{ij}\frac{dC_i}{dx} \tag{3-1}$$

where J is the diffusion flux, C is the concentration, D is the diffusion coefficient or diffusivity and x is the distance. This is generally referred to as Fick's first law. This equation is true in an isobaric binary mixture, but there is another form of this type of equations, for component *i*, the diffusion term is given as;

$$J_i^m = -\rho^m\left(\sum_{j=1}^{n_c-1} D_{ij}^M \frac{\partial c_i}{\partial x} + D_i^P \frac{\partial p_i}{\partial x} + D_i^T \frac{\partial T_i}{\partial x}\right) \tag{3-2}$$

where D_{ij}^M , D_i^P and D_i^T are the molecular, pressure and thermal diffusion coefficients for more information on this formulation which is a result of the Firoozabadi and his coworker, see the first chapter.

Diffusion coefficients can be obtained either from experiments or from solving the constitutive equations. The diffusion coefficients are frequently assumed to be constant, while they are functions of pressure, temperature and composition. Their dependence on pressure, temperature and composition will be discussed in following section in this chapter. Thermal diffusion takes place when a uniform mixture is subject to temperature gradients, and results in the mixture that is not mixed itself. Diffusion, or the flow of material, in this case is not driven by the concentration gradient, but by the temperature gradient. Inter diffusion, which is the inverse effect of thermal diffusion, causes significant temperature differences. Thermal diffusion in liquids is referred to as the Soret effect. It must be mentioned that thermal diffusion also occurs in solids [**64**].

3.6 Governing equation of Fluid Mechanics and Heat Transmission

In this section, the governing equations of fluid mechanics and heat transfer (i.e., fluid dynamics) will be described. Since the reader is assumed to have some background in this field, a complete derivation of the governing equations is not included. For the most part, only the classical forms of the equations are given. Other forms of the governing equations, which have been simplified primarily for computational purposes, are not presented. The fundamental equations of fluid dynamics are based on the following; universal laws of conservation:

- Conservation of Mass
- Conservation of Momentum
- Conservation of Energy
- Conservation of Species
- Equation of State

The equation that results from applying the Conservation of Mass law to a fluid flow is called the continuity equation. When Newton's Second Law is applied to a fluid flow, it yields a vector equation known as the momentum equation. The Conservation of Energy law is identical to the First Law of Thermodynamics, and the resulting fluid dynamic equation is named the energy equation. In addition to the equations developed from these universal laws, it is necessary to establish relationships between fluid properties in order to close the system of equations. An example of such a relationship is the equation of state which relates the thermodynamic variables pressure p, density p, and temperature T. Basically, there have been two different approaches

taken to derive the equations of fluid dynamics: the phenomenological approach and the kinetic theory approach. In the phenomenological approach, certain relations between stress and rate of strain and heat flux and temperature gradient are postulated, and the fluid dynamic equations are then developed from the conservation laws. The required constants of proportionality between stress and rate of strain and heat flux and temperature gradient must be determined experimentally in this approach. In the kinetic theory approach, the fluid dynamic equations are obtained with the transport coefficients defined in terms of certain integral relations, which involve the dynamics of colliding particles.

3.6.1 Continuity Equation

The Conservation of Mass law applied to a fluid passing through an infinitesimal, fixed control volume yields the following equation of continuity:

$$\frac{\partial \rho}{\partial t} + \frac{\partial}{\partial x_j}\left(\rho u_j\right) = 0 \tag{3-3}$$

where ρ is the fluid density and u_j is the fluid velocity. This equation expresses the mass conservation in on the tensor notation; however we can represent this equation as following in the Lagrangian approach. So, the changes to the properties of a fluid element are recorded by an observer moving with the fluid element.

$$\frac{\partial \rho}{\partial t} + \frac{\partial(\rho u)}{\partial x} + \frac{\partial(\rho v)}{\partial y} + \frac{\partial(\rho w)}{\partial z} = 0 \tag{3-4}$$

where ρ is the fluid density and u, v and w are the fluid velocity in x, y and z direction for a Cartesian coordinate system. The first term in this equation represents the rate of increase of the density in the control volume, and the rest terms represent the rate of mass flux passing out of the control surface which surrounds the control volume per unit volume.

3.6.2 Momentum Equation

Newton's Second Law applied to a fluid passing through an infinitesimal, fixed control volume. The principle of conservation of momentum is an application of Newton’s second law

of motion to an element of fluid. That is, when considering a given mass of fluid in a Lagrangian frame of reference, it is stated that the rate at which the momentum of the fluid mass is changing is equal to the net external force acting on the mass. Thus the mathematical equation which results from imposing the physical law of conservation of momentum is:

$$\rho \frac{\partial u_j}{\partial t} + \rho u_k \frac{\partial u_j}{\partial x_k} = \frac{\partial \sigma_{ij}}{\partial x_i} + \rho f_i \tag{3-5}$$

where the left-hand side represents the rate of change of momentum of a unit with the volume of fluid. The first term is the familiar temporal acceleration term while the second term is a convective acceleration and allows for local accelerations (around obstacles) even when the flow is steady. This second term is also nonlinear since the velocity appears quadratically. On the right hand side are the forces which are causing the acceleration. There are two types of fluid forces;

- surface forces (proportional to area)
- body forces (proportional to volume)
- Surface forces are usually expressed in terms of stress σ which defines force per unit area.

The major surface forces are;

- Pressure p: always acts normal to a surface
- Viscous stresses σ_{ij}: frictional forces arising from relative motion of fluid layers.

The main body forces are:

- Gravity: the force per unit volume that is ρg
- Coriolis forces: the force as a result of rotating reference frames

Separating surface forces determined by a stress tensor and body forces (f per unit Volume), the integral equation for the i^{th} component of momentum may be written:

$$\frac{d}{dt}\int_V \rho u_i dV + \oint_{\partial V} \rho u_i \cdot dA = \oint_{\partial V} \sigma_{ij} dA_j + \int_V f_i dV \tag{3-6}$$

where the first term in right hand side is surface force and second term is body forces that are explained.

The equation of momentum conservation together with the constitutive relation for a Newtonian fluid yield the famous Navier-Stokes equations which are the principal conditions to be satisfied by a fluid as it flows:

$$\rho\frac{\partial u_j}{\partial t}+\rho u_k\frac{\partial u_j}{\partial x_k}=-\frac{\partial p}{\partial x_j}+\frac{\partial}{\partial x_j}\left(\lambda\frac{\partial u_k}{\partial x_k}\right)+\frac{\partial}{\partial x_i}\left[\mu\left(\frac{\partial u_i}{\partial x_j}+\frac{\partial u_j}{\partial x_i}\right)\right]+\rho f \tag{3-7}$$

Equation of motion in the x-direction:

$$\frac{\partial\rho u}{\partial t}+\frac{\partial(\rho uu)}{\partial x}+\frac{\partial(\rho vu)}{\partial y}+\frac{\partial(\rho wu)}{\partial z}=-\frac{\partial p}{\partial x}+\frac{\partial}{\partial x}\left[2\mu\frac{\partial u}{\partial x}-\tfrac{2}{3}\mu(\nabla\bullet\underline{u})\right]+ \frac{\partial}{\partial y}\left[\mu\left(\frac{\partial u}{\partial y}+\frac{\partial v}{\partial x}\right)\right]+\frac{\partial}{\partial z}\left[\mu\left(\frac{\partial u}{\partial z}+\frac{\partial w}{\partial x}\right)\right]+S_u \tag{3-8}$$

3.6.3 Energy Equation

The First Law of Thermodynamics applied to a fluid passing through an infinitesimal, fixed control volume. The principle of conservation energy amounts to an application of the first law of thermodynamics to a fluid element as it flows. When applying the first law of thermodynamics to a flowing fluid the instantaneous energy of the fluid is considered to be the sum of the internal energy per unit mass and the kinetic energy per unit mass. In this way the modified form of the first law of thermodynamics which will be applied to an element of fluid states that the rate of change in the total energy (intrinsic plus kinetic) of the fluid as it flows is equal to the sum of the rate at which work is being done on the fluid by external forces and the rate on which heat is being added by conduction. In this way the mathematical expression becomes:

$$\frac{D}{Dt}\int_V (\rho e + \frac{1}{2}\rho u \cdot u)dV = \int_S uPdS + \int_V u\rho\, fdV - \int_S q \cdot ndS \tag{3-9}$$

The basic conservation laws discussed in the previous section represent five scalar equations which the fluid properties must satisfy as the fluid flows. The continuity and the energy equation are scalar equations while the momentum equation is a vector which represents three scalar equations, but our basic conservation laws have introduced seventeen unknowns: the scalars ρ and e, the density and internal energy respectively, the vectors u_j and q_j, the velocity and heat flux respectively, each vector having three components and the stress tensor σij, which has in general nine independent components.

In order to obtain a complete set of equations the stress tensor σij and the heat-flux vector q_j must be further specified. This leads to so-called "constitutive equations" in which the stress tensor is related to the deformation tensor, and the heat-flux vector is related to the temperature gradients.

The stress tensor is supposed to satisfy the following condition: when the fluid is at rest the stress is hydrostatic and the pressure exerted by the fluid is the thermodynamic pressure.

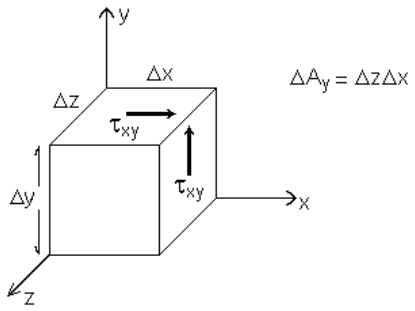

Figure 3-4 Stress Acting on a Small Cube

The above figure represents stress acting on a small cube, where τ_{ij} are the components of the shear-stress tensor which depends upon the motion of the fluid only. Using that condition the constitutive relation for stress in a Newtonian fluid becomes:

$$\sigma_{ij} = -p\delta_{ij} + \lambda\delta_{ij}\frac{\partial u_k}{\partial x_k} + \mu\left(\frac{\partial u_j}{\partial x_i} + \frac{\partial u_i}{\partial x_j}\right) \tag{3-10}$$

The nine elements of the stress tensor have now been expressed in terms of the pressure and the velocity gradients and two coefficients λ and μ. These coefficients cannot be determined analytically and must be determined empirically. They are the viscosity coefficients of the fluid.

The second constitutive relation is Fourier's Law for heat conduction:

$$q_j = -k\frac{\partial T}{\partial x_j} \tag{3-11}$$

where q_j is the heat-flux vector, k is the thermal conductivity of the fluid and T is the temperature. Collecting terms, the final form of the energy equation can be expressed as follows:

$$\frac{\partial(\rho E)}{\partial t}+\frac{\partial(\rho u_j E)}{\partial x_j}= -\frac{\partial(pu_j)}{\partial x_j}+\frac{\partial(u_j\tau_{ij})}{\partial x_i}+\frac{\partial}{\partial x_j}\left(k\frac{\partial T}{\partial x_j}\right)+S_E \tag{3-12}$$

where;

$$E = e+\tfrac{1}{2}\left(u^2+v^2+w^2\right) = e+\tfrac{1}{2}U^2 \tag{3-13}$$

Thus at the end, we can achieve popular form of the Energy Equation as follow:

$$\rho\frac{\partial e}{\partial t}+\rho u_k\frac{\partial e}{\partial x_k} = -p\frac{\partial u_k}{\partial x_k}+\frac{\partial}{\partial x_j}\left(k\frac{\partial T}{\partial x_j}\right)+\lambda\left(\frac{\partial u_k}{\partial x_k}\right)^2+\mu\left(\frac{\partial u_j}{\partial x_i}+\frac{\partial u_i}{\partial x_j}\right)\frac{\partial u_j}{\partial x_j} \tag{3-14}$$

Equation for Energy with the Newtonian model for viscous stresses:

$$\frac{\partial(\rho\varepsilon)}{\partial t}+\frac{\partial(\rho u_j e)}{\partial x_j}=-p\frac{\partial u_j}{\partial x_j}+\frac{\partial}{\partial x_j}\left(k\frac{\partial T}{\partial x_j}\right)+\Phi+S_e \tag{3-15}$$

where;

$$\Phi = \mu \frac{\partial u_i}{\partial x_j}\left(\frac{\partial u_i}{\partial x_j}+\frac{\partial u_j}{\partial x_i}\right)-\frac{2}{3}\mu\left(\frac{\partial u_k}{\partial x_k}\right)^2 \tag{3-16}$$

where e is the internal energy per unit mass and Φ is customarily called the *dissipation function* and represents the rate at which mechanical energy is expended in the process of deformation of the fluid due to viscosity [**65**].

3.6.4 Mixture compositions and species fluxes

A mixture of different chemical species shows its own density, molecular weight, and other overall thermodynamic properties. These properties depend on the types and relative amounts of the component substances, which may vary from point to point in the mixture. To verify the local properties of a mixture, we must identify the local amount of each species composing the mixture. One way to explain the amount of a particular species in a mixture is by the mass of that species per unit volume, called as the partial density. The mass of species i in a small volume of mixture, in kg, divided by that volume, in m^3, is the partial density, ρ_i, for that species, in kg of i per m^3. The composition of the mixture may be shown by stating the partial density of each of its components. The mass density of the mixture itself, ρ, is the entire mass of all species per unit volume; therefore,

$$\rho = \sum_i \rho_i \tag{3-17}$$

The relative amount of species i in the mixture is described by the mass of i per unit mass of the mixture, which is simply $\rho_i \big/ \rho$, partial density over total density. This ratio is called the mass fraction, m_i:

$$m_i = \frac{\rho_i}{\rho} \tag{3-18}$$

where ρ_i presents the $mass\,of\,species\;i$. This definition guides to the following two results:

$$\sum_i m_i = \sum_i \frac{\rho_i}{\rho} = 1 \qquad and \quad 0 \le m_i \le 1 \tag{3-19}$$

The molar concentration of species i in $\mathrm{kmol/m^3}$, c_i, states concentration in terms of moles more than mass. However, M_i is the molecular weight of species i in [kg/kmol], then;

$$c_i = \frac{\rho_i}{M_i} = \frac{mole\,of\,species\ i}{volume} \tag{3-20}$$

The molar concentration of the mixture, c, is the total number of moles for all species per unit volume; thus,

$$c = \sum_i c_i \tag{3-21}$$

The mole fraction of species i, x_i , is the number of moles of i per mole of mixture:

$$x_i = \frac{c_i}{c} = \frac{moles\,of\,species\ i}{mole\,of\ mixture} \tag{3-22}$$

Just as for the mass fraction, it follows for mole fraction that;

$$\sum_i x_i = \sum_i \frac{c_i}{c} = 1 \qquad and \quad 0 \le x_i \le 1 \tag{3-23}$$

The molecular weight of the mixture is the number of kg of mixture per k.mol of mixture: $M = \rho/c$. By using above equation respectively, M may be written in terms of either mole or mass fraction

$$M = \sum_i x_i M_i \quad or \quad \frac{1}{M} = \sum_i \frac{m_i}{M_i} \tag{3-24}$$

Mole fraction can be changed to mass fraction using the following relations:

$$m = \frac{x_i M_i}{M} = \frac{x_i M_i}{\sum_k x_k M_k} \quad and \quad x_i = \frac{M m_i}{M_i} = \frac{m_i / M_i}{\sum_k m_k / M_k} \tag{3-25}$$

The mixture dynamic viscosity μ at each node is computed based on mass fraction average of the pure species viscosities:

$$\mu = \sum_{i}^{n} c_i \mu \tag{3-26}$$

where C_i is the mass fraction of each component at each node and μ_i is the pure component viscosities.

3.6.4.1 Diffusion fluxes and Fick's law

When the composition of a mixture is nonuniform, the concentration gradient in any species, i, of the mixture presents a driving potential for the diffusion of that species. It flows from regions of high concentration to regions of low concentration- similar to the diffusion of heat from regions of high temperature to region s of low temperature. We have already led the same equation including other source term in pervious sections that mass diffusion obeys Fick's law.

$$\vec{j}_i = -\rho D_{im} \nabla m_i \tag{3-27}$$

which is analogous to Fourier's law. The constancy of proportionality, ρD_{im}, between the local diffusive mass flux of species i and the local concentration gradient of i. engages a physical property named the diffusion coefficient, D_{im}, for species i diffusing in the mixture m. Like the thermal diffusivity, α, or the kinematic or momentum viscosity, υ, the mass diffusivity D_{im} has the units of m^2/s. In nature, the well known kinetic models are for binary diffusion. In binary diffusion, species one has the same diffusivity through species two as does species through species one.

3.6.4.2 Coupled diffusion phenomena

Mass diffusion can occur by factors other than concentration differences although the latter are of primary importance. For example, temperature differences can induce mass diffusion in a process recognized as thermal diffusion or the Soret effect for more information see first chapter. The diffusional mass flux consequential from both temperature and concentration gradients in a binary fluid mixture is then

$$\vec{j}_1 = -\rho D_{12} [\nabla m_1 + \frac{M_1 M_2}{M^2} D_T \nabla \ln(T)] \tag{3-28}$$

where D_T is known as the thermal diffusion ratio and is usually quite smaller than other diffusion coefficients. Thermal diffusion is infrequently used in chemical separation processes. Body forces acting unequally on the different species as well as pressure gradients and can also induced diffusion. Again, these effects are in general small. A related observable fact is the generation of a heat flux by a concentration incline named the diffusion-thermo or Dufour effect [**66**]. The more generalized form of this equation is following;

$$\vec{j}_i = -\rho(\sum_{j=1}^{n-1} D_{ij}\nabla x_j + D_{i,T}\nabla T) \tag{3-29}$$

In the above equation ρ is the total mole density, D_{ij} is the Fick's mass diffusion coefficients, and $D_{T,i}$ is the thermodiffusion coefficient of the i^{th} species.

Table 3-1 Typical diffusion coefficients for binary fluid mixture[66**]**

Gas Mixture	T [K]	$D_{12}\left[m^2/s\right]\times 10^9$
Ethanol-Banzene	288	2.25
Water-ethanol	298	1.24
Benzene-ethenol	298	1.81
Carbon dioxide- water	288	1.00
Methane- water	275	0.85
	333	3.55
Pyridine-water	288	0.58

3.6.4.3 Species conservation equations

In addition to the mass conservation equation, for the ternary mixtures, species conservation equations can bet employed. As a result of these above coefficients, we can have the species conservation equations. It should be noted for mixture including n different components, there n-1 equation on species and one equation for summation of all concentration which is always equal to one so for example for binary and ternary mixture the equation are as follows:

$$(\frac{\partial}{\partial t}(\rho c_1)+\frac{\partial}{\partial x}(\rho u c_1)+\frac{\partial}{\partial y}(\rho u c_1))=\frac{\partial}{\partial x}(\rho(D_{11}\frac{\partial c_1}{\partial x}+D_{12}\frac{\partial c_1}{\partial x}+D_{T,1}\frac{\partial T}{\partial x}))+\frac{\partial}{\partial y}(\rho(D_{11}\frac{\partial c_1}{\partial y}+D_{12}\frac{\partial c_1}{\partial y}+D_{T,1}\frac{\partial T}{\partial y})) \quad (3\text{-}30)$$

$$(\frac{\partial}{\partial t}(\rho c_1)+\frac{\partial}{\partial x}(\rho u c_2)+\frac{\partial}{\partial y}(\rho u c_2))=\frac{\partial}{\partial x}(\rho(D_{21}\frac{\partial c_2}{\partial x}+D_{22}\frac{\partial c_2}{\partial x}+D_{T,2}\frac{\partial T}{\partial x}))+\frac{\partial}{\partial y}(\rho(D_{21}\frac{\partial c_2}{\partial y}+D_{22}\frac{\partial c_2}{\partial y}+D_{T,2}\frac{\partial T}{\partial y})) \quad (3\text{-}31)$$

$$c_3=1-c_1-c_2 \quad (3\text{-}32)$$

$$(\frac{\partial}{\partial t}(\rho c_1)+\frac{\partial}{\partial x}(\rho u c_1)+\frac{\partial}{\partial y}(\rho u c_1))=\frac{\partial}{\partial x}(\rho(D_{12}\frac{\partial c_1}{\partial x}+D_{T,1}\frac{\partial T}{\partial x}))+\frac{\partial}{\partial y}(\rho(D_{12}\frac{\partial c_1}{\partial x}+D_{T,1}\frac{\partial T}{\partial y})) \quad (3\text{-}33)$$

$$c_2=1-c_1 \quad (3\text{-}34)$$

where equations, c_i is the mole fraction of respective species and T is the temperature of the mixture at the Cartesian location x and y at a particular time, t. D_{ii} and D_{ij} represent the main term and the cross term diffusion coefficients. Since these coefficients depend on the mixture concentration that is nonuniform when $t > 0$ s, and constantly changing will happen in the mixture, in this study, diffusion coefficients are treated as variables in computational domain. Consequently, the CFD code used in this investigation is equipped with models for computing these diffusion coefficients; see chapter one for more information about the first idea of this method [**50**].

3.7 Nonequilibrium Thermodynamics

Based on the nonequilibrium thermodynamics, there is another approach to find the mass flux in the mixture which will be present in this section. For a general small volume of the mixture, assuming the local equilibrium hypothesis in the mixture with two or more species in a temperature gradient with chemical reaction, the entropy per unit volume σ is depended on entropy generation rate $\dot{\sigma}$ and the entropy flux passing throw surface control on the element j_σ

may be expressed as equation (3-35). Basically, the equation (3-36) is considered for the energy flux j_v in a differential element of the system:

$$\frac{\partial \sigma}{\partial t} + \nabla . j_\sigma - \dot{\sigma} = 0 \tag{3-35}$$

$$\frac{\partial v}{\partial t} + \nabla . j_v = 0 \tag{3-36}$$

The energy flux j_v should be the summation of all energies transferred within the control surface or volume through convection and conduction fluxes. These energy fluxes induced in the system as a result of several components such as the kinetic, potential and internal energy. The following continuity equations lead between the mass flux of species *i*, j_i, and the concentration of component *i*, x_i; in addition one can add the other equation to the first one as a result of the local equilibrium which is assumed to exist which is an expression of the classical equilibrium thermodynamic which applies for a small element of the mixture;

$$\frac{\partial x_i}{\partial t} + \nabla . j_i = 0 \tag{3-37}$$

$$d\sigma = \frac{1}{T} de - \sum_{i=1}^{n} \frac{\mu_i}{T} dx_i \tag{3-38}$$

where μ_i is the chemical potential of component i, e is the mixture energy, and *T* is the local temperature. Based on equation (3-39), the entropy flux is related to the energy and mass flux via the following equation:

$$j_\sigma = \frac{1}{T} j_e - \sum_{i=1}^{n} \frac{\mu_i}{T} j_i \tag{3-39}$$

As a result of the equations (3-35) to (3-39), and then solving for the entropy production rate, one can reach the function of energy and mass fluxes that is:

$$\dot{\sigma} = \nabla\left(\frac{1}{T}\right) . j_v - \sum_{i=1}^{n} \left(\frac{\mu_i}{T}\right) . j_i \tag{3-40}$$

It can be seen that in above equation (3-40) there are two new introduced terms which are $\nabla(1/T)$ and $\nabla(\mu_i/T)$ as the thermodynamic forces in thermodiffusion, these forces cause mass transfer and entropy generation. Now it is possible to express the energy and mass fluxes in terms of forces, as forces are the mass transfer causes and the fluxes are the effects.

$$j_v = f\left(\nabla\left(\frac{1}{T}\right), \nabla\left(\frac{\mu_i}{T}\right)\right) \qquad i = 1..n \tag{3-41}$$

$$j_i = g\left(\nabla\left(\frac{1}{T}\right), \nabla\left(\frac{\mu_i}{T}\right)\right) \qquad i = 1..n \tag{3-42}$$

By using Taylor series and expanding j_v about the equilibrium state when removing the higher order terms and keeping just the first one, the result can be the following expression;

$$j_v = j_{v0} + \left(\frac{\partial j_v}{\partial \nabla\left(\frac{1}{T}\right)}\right)_0 \nabla\left(\frac{1}{T}\right) + \sum_{i=1}^{n}\left(\frac{\partial j_v}{\partial \nabla\left(\frac{\mu_i}{T}\right)}\right)_0 \nabla\left(\frac{\mu_i}{T}\right) \tag{3-43}$$

where j_{v0} is the energy flux under equilibrium when there are zero forces, and consequently will be equals to zero. To simplify this equation, we need to define some coefficients that are called the PCs[46]. These coefficients may be defined as the rate of change of fluxes with respect to forces in equilibrium state:

$$L_{vv} = \left(\frac{\partial j_v}{\partial \nabla\left(\frac{1}{T}\right)}\right)_0 \tag{3-44}$$

$$L_{iv} = \left(\frac{\partial j_v}{\partial \nabla\left(\frac{\mu_i}{T}\right)}\right)_0 \tag{3-45}$$

By substituting these coefficients in equation (3-43), it can be rewritten as follows:

$$j_v = L_{vv}\nabla\left(\frac{1}{T}\right) + \sum_{i=1}^{n} L_{iv}\nabla\left(\frac{\mu_i}{T}\right) \tag{3-46}$$

One of the main tasks in thermodiffusion and other similar phenomena is to somehow approximate the magnitude of the PCs from outside of the nonequilibrium thermodynamics.

[46] Onsager or phenomenological coefficients

Similarly, this equation can express the mass fluxes in terms of the forces by expanding j_i about the equilibrium state and retaining the linear terms:

$$j_i = -L_{vi}\nabla\left(\frac{1}{T}\right) - \sum_{j=1}^{n} L_{ji}\nabla\left(\frac{\mu_i}{T}\right) \tag{3-47}$$

Phenomenological coefficients in equation (3-46) are defined as follows:

$$L_{vi} = \left(\frac{\partial j_i}{\partial\nabla\left(\frac{1}{T}\right)}\right)_0 \tag{3-48}$$

$$L_{ji} = \left(\frac{\partial j_i}{\partial\nabla\left(\frac{\mu_j}{T}\right)}\right)_0 \qquad i \neq j \tag{3-49}$$

The above relations were gained based on the energy flux. Since the entropy-based heat flux j_q^s, can be related to the entropy flux j_σ through the absolute temperature T, $j_q^s = Tj_\sigma$, equation (3-47) expresses a relationship between the entropy-based heat and energy fluxes as follows:

$$j_v = j_q^s + \sum_{i=1}^{n} \mu_i j_i \tag{3-50}$$

Based on equation (3-47), in a double diffusive problem (system with coupled heat and mass transfer), the energy flux is evaluated with summation of the entropy-based heat flux and the chemical potential flux. In order to show the phenomenological equations and coefficients in terms of the heat flux, it's needed to state the entropy production rate in terms of the heat flux, instead of energy flux. Having expressed the entropy production rate in terms of the entropy-based heat and mass fluxes, one can rewrite the fluxes as a function of forces using new sets of phenomenological coefficients:

$$\dot{\sigma} = \nabla\left(\frac{1}{T}\right).j_q^s - \sum_{i=1}^{n} \nabla\left(\frac{1}{T}\nabla\mu_i.j_i\right) \tag{3-51}$$

$$j_q^s = L_{qq}\nabla\left(\frac{1}{T}\right) + \sum_{i=1}^{n} L_{iq}\frac{1}{T}\nabla\mu_i \tag{3-52}$$

$$j_i = -L_{qi}\nabla\left(\frac{1}{T}\right) - \sum_{k=1}^{n} L_{ki}\frac{1}{T}\nabla\mu_k \tag{3-53}$$

According to the Onsager reciprocal relation, it is right to mention equation (3-53). The same equation can be written for the energy flux phenomenological coefficients;

$$L_{qi} = L_{iq} \tag{3-54}$$

$$L_{ik} = L_{ki} \tag{3-55}$$

Heat flow may be defined based on the entropy balance or energy balance equations or other frames which also can be either interpreted as the pure heat conduction or heat transfer due to mass diffusion. It is shown that there is an alternative way which the entropy production rate is expressed in terms of conjugate forces and fluxes using various definitions for the heat flux. In this method using different heat fluxes cause a change in the conjugate thermodynamic forces. On the other hand, by using the definition of energy balance, the heat flux j_q may be represented as consisting of two terms, one term due to pure conduction heat flow j_q' as a result of a temperature difference and a second term due to the heat transfer associated with mass diffusion ($\sum_{i=1}^{n} h_k j_k$):

$$j_q' = j_q - \sum_{i=1}^{n} h_k j_k \tag{3-56}$$

Entropy production rate equation can be expressed in terms of the *n*-1 independent molar fluxes $\sum_{i=1}^{n} j_k = 0$ is written as follows bearing in mind that $\nabla(1/T) = -\nabla T/T^2$, where n is the number of component in the mixture.

$$\dot{\sigma} = -\frac{\nabla T}{T^2}.j_q' - \sum_{k=1}^{n-1}\frac{\nabla(\mu_k - \mu_n)}{T}.j_k \tag{3-57}$$

In the nonequilibrium thermodynamics literature, net heat of transport is defined as follows:

$$j_q' = \sum_{k=1}^{n} Q_k^* j_k \qquad @\nabla T = 0 \tag{3-58}$$

Thus;

$$Q_k^* = \left(\frac{\left(j_q^{'} \right)_k}{j_k} \right)_T \qquad @\nabla T = 0 \tag{3-59}$$

where $\left(j_q^{'} \right)_k$ means the component *k* heat flux associated. Heat flow per mole of the diffusing component *k*, should be absorbed by the local region to keep the temperature of the region constant. Interestingly, it may be concluded that Q_k^* used in equation (3-59) can be also expressed in terms of the PCs as follows:

$$Q_k^* = \sum_{i=1}^{n} L_{qi} L_{ik}^{-1} = \sum_{k=1}^{n} L_{ki}^{-1} L_{iq} \tag{3-60}$$

This equation can be reduced for binary mixture as follows;

$$Q_1^* = L_{q1} L_{11}^{-1} \tag{3-61}$$

As result of equations (3-58 and 3-59), the entropy production rate for a multicomponent mixture in terms of *n*-1 independent fluxes is expressed as follows:

$$\dot{\sigma} = -\sum_{k=1}^{n-1} \left[\left(Q_k^* - Q_n^* \right) \frac{\nabla T}{T^2} + \frac{\nabla \left(\mu_k - \mu_n \right)}{T} \right] . j_k \tag{3-62}$$

Consequently, the mass fluxes are expressed in terms of the net heat of transport and PCs L_{ik} as follows;

$$j_i = -\sum_{k=1}^{n-1} L_{ik} \left[\left(Q_k^* - Q_n^* \right) \frac{\nabla T}{T} + \nabla \left(\mu_k - \mu_n \right) \right] \tag{3-63}$$

The above equation is the final result of the linear nonequilibrium thermodynamics for the mass flux in terms of temperature and chemical potential gradients [**40**]. Consequently for binary mixture we have;

$$j_1 = -L_{11} \left[\left(Q_1^* - Q_2^* \right) \frac{\nabla T}{T} + \nabla \left(\mu_1 - \mu_2 \right) \right] \tag{3-64}$$

$$j_2 = -L_{21} \left[\left(Q_1^* - Q_2^* \right) \frac{\nabla T}{T} + \nabla \left(\mu_1 - \mu_2 \right) \right] \tag{3-65}$$

It can be used to obtain expressions for the thermodiffusion coefficients and factors. The mass and thermodiffusion coefficients can be expressed in terms of the phenomenological coefficients as;

$$D_{ij} = \frac{1}{\rho T}\sum_{k=1}^{n} L_{ik}\sum_{l=1}^{n-1}(\delta_{kl} + \frac{x_j}{x_n})\frac{\partial \mu_l}{\partial x_j} \tag{3-66}$$

$$D_{i,T} = \frac{L_{iq}}{\rho T^2} \tag{3-67}$$

Thus, to determine the mass and thermodiffusion coefficients solving for the above equations is required. In doing so, a main part of simulating the thermodiffusion process is in obtaining an accurate estimate of the net heat of transport. This is described as the amount of energy transported across a given reference plane per mole of the ith component in the absence of a temperature gradient without the partial molar enthalpy of the ith component in the mixture. In order to obtain this as well as using molar average velocity frame, in a multicomponent mixture the net heat of transport has been formulated:

$$Q_i^* = -\frac{U_i}{\tau_i} + (\sum_{j=1}^{n} x_j \frac{U_j}{\tau_j})\frac{V_j}{\sum_{k=1}^{n} x_k V_k} \tag{3-68}$$

where V_j and x_j are the partial molar volume and mole fraction that are determined by mixture properties. The nonequilibrium thermodynamic property of the ith component and τ_i has been assigned to be constant value of 4.0. Further, U_i is the partial molar internal energy and n is the number of components in the mixture.

The thermodiffusion and mass diffusion coefficients gained from pervious equations are used to determine the computational thermal diffusion factor $\alpha_{i,T}$ in an n component mixture as follows;

$$\begin{bmatrix} \alpha_{1,T} \\ \alpha_{2,T} \\ \vdots \\ \alpha_{n-1,T} \end{bmatrix} = T \begin{bmatrix} D_{1,1} & D_{1,2} & \cdots & D_{1,n-1} \\ D_{2,1} & D_{2,2} & \cdots & D_{2,n-1} \\ \vdots & \vdots & \ddots & \vdots \\ D_{n-1,1} & D_{1,2} & \cdots & D_{1,1} \end{bmatrix}^{-1} \begin{bmatrix} D_{1,T} \\ D_{2,T} \\ \vdots \\ D_{n-1,T} \end{bmatrix} \tag{3-69}$$

In the above equation $D_{i,T}$ and $D_{i,j}$ are again the thermodiffusion and molecular diffusion coefficients. In order to calculate $\alpha_{i,T}$ [47] of the n^{th} species, there is another equation in addition to the above equation that is as follows:

$$\sum_i x_i(1-x_i)\alpha_{i,T} = 0 \tag{3-70}$$

Thus, for binary mixture these two recent equations will be expressed as follows;

$$\alpha_{1,T} = T\frac{D_{1,T}}{D_{1,1}} \tag{3-71}$$

$$x_1(1-x_1)\alpha_{1,T} + x_2(1-x_2)\alpha_{2,T} = 0 \tag{3-72}$$

For binary mixture we know $x_1 = 1-x_2$; thus these equations may be modified as follows [**67**];

$$\alpha_{1,T} + \alpha_{2,T} = 0 \tag{3-73}$$

$$\alpha_{1,T} = T\frac{D_{1,T}}{D_{1,1}} = -\alpha_{2,T} = -T\frac{D_{2,T}}{D_{2,2}} \tag{3-74}$$

3.8 Equation of State

In order to solve system of fluid dynamic equations, it is necessary to define relations between the thermodynamic variables *(p, ρ, T, e, h).*

3.8.1 Equation of State for Ideal Gas

For instance, consider a compressible flow without external heat addition or body forces and use the continuity equation, for the three momentum equations, as well as the energy equation. These five scalar equations contain seven unknown ρ, *p, e, T, u, v, w,* provided that the transport coefficients may be related to the thermodynamic properties in the list of unknowns. It is obvious that two additional equations are required to solve the system. These two additional equations can be obtained by shaping relations that exist between the thermodynamic variables. Relations of this kind are known as equations of state. Based on the state principle of thermodynamics, the

[47] The thermal diffusion factor

local thermodynamic state is fixed by any two independent thermodynamic variables provided that the chemical composition of the fluid is not changing owing to diffusion or finite-rate chemical reactions. For most problems in gas dynamics, it is possible to assume a perfect gas. A perfect gas is defined as a gas whose intermolecular forces are negligible. A perfect gas obeys the perfect gas equation of state,

$$P = \rho RT \tag{3-75}$$

where R is the gas constant. However, the intermolecular forces become important under conditions of high pressure and relatively low temperature. For these conditions, the gas doesn't obey the perfect gas equation of state, and an alternative equation of state must be used. An example is the Vander Waals equation of state,

$$(P + a\rho^2)(\frac{1}{\rho} - b) = RT \tag{3-76}$$

where a and b are constants which can be found for each type of gas. For problems involving a perfect gas at relatively low temperatures, it is good approximate assumption to behave the gas as a calorically perfect gas. A calorically perfect gas is described as a perfect gas with constant specific heats. Specific heat at constant volume C_v, the specific heat at constant pressure C_p and the ratio of specific heats γ all remain constant in a calorically perfect gas and the following relations exist:

$$e = \mathrm{C_v} T \tag{3-77}$$

$$h = \mathrm{C}_p T \tag{3-78}$$

$$\gamma = \frac{\mathrm{C}_p}{\mathrm{C_v}} \tag{3-79}$$

$$\mathrm{C_v} = \frac{R}{\gamma - 1} \tag{3-80}$$

$$\mathrm{C}_p = \frac{\gamma R}{\gamma - 1} \tag{3-81}$$

For example, in problem involving air as fluid, one can assume that air at standard conditions, $R = 287\ {\mathrm{m}^2}/{\mathrm{s}^2 K}$ and $\gamma = 1.4$. If we assume that the fluid in our problem is a calorically perfect gas, then we can use the following equations;

$$P = (\gamma - 1)\rho e \tag{3-82}$$

$$T = \frac{(\gamma - 1)e}{R} \tag{3-83}$$

For fluids that calorically perfect gas assumption is not accurate, the required state relations can be found in the form of tables, charts, or curve fits or the other complex form of equation of state had to be used [**65**]. It appears clear that particular attention should be paid to the choice of the model when trying to represent system including mixture of two or more components according to their properties.

3.8.2 Peng-Robinson equation of state

In 1967, Peng as PhD student of Prof. Robinson at the University of Alberta (Edmonton, Canada) introduced this well-known equation of state. When they used this equation for the gas/condensate systems, a slightly better performance around critical conditions was observed by the PR EOS. The Peng-Robinson EOS has become the most famous equation of state for natural gas systems in the petroleum industry. By having Peng-Robinson Equation of State, the parameters of state will be expressible in terms of the critical properties. This model has this ability to provide reasonable accuracy near the critical point, particularly for calculations of the compressibility factor and liquid density. This equation of state should be applicable to all calculations of all fluid properties in natural gas processes. It should be noted that in this model mixing rules shall not employ more than a single binary interaction parameter which should be independent of temperature pressure and composition.

For the most part the Peng-Robinson Cubic Equation of State exhibits performance similar to the Soave equation although it is generally superior in predicting the liquid densities of many materials, especially non polar ones. The Peng-Robinson Cubic Equation of State is formulated below;

$$P = \frac{RT}{V_m - b} - \frac{\alpha a}{V_m^2 + 2b_{\ m} - b^2} \tag{3-84}$$

where a, b, α and T_r are defined as following;

$$a = \frac{0.45724\mathrm{R}^2 T_c^2}{P_c} \tag{3-85}$$

$$a = \frac{0.07780\mathrm{R}T_c}{P_c} \tag{3-86}$$

$$\alpha = (1 + (0.37464 + 1.5226\omega - 0.2699\omega^2)(1 - \sqrt{\frac{T}{T_c}}))^2 \tag{3-87}$$

There is cubic expression in Z of Peng Robinson equation of state in polynomial form:

$$A = \frac{\alpha a P}{R^2 T^2} \tag{3-88}$$

$$B = \frac{bP}{RT} \tag{3-89}$$

$$Z^3 - (1 - B)Z^2 + (A - 2B - 3B^2)Z - (AB - B^2 - B^3) = 0 \tag{3-90}$$

where, ω is the acentric factor of the species, *R* is the universal gas constant and Z is defined compressibility factor as follow

$$Z = \frac{\mathrm{PV}}{\mathrm{RT}} \tag{3-91}$$

For the most part, the Peng-Robinson equation exhibits performance similar to the Soave equation although it is generally superior in predicting the liquid densities of many materials, especially no polar ones. The cubic Peng-Robinson equation of state is suitable for simple sphere-like molecules. Using Peng-Robinson EOS caused a correct representation of the ternary system behavior. It should be added to this information about PR EOS[48] that it behaves very accurately for non associating mixture, like hydrocarbons mixture. Consequently, it is strongly recommended to use more accurate EOS[49] to simulate the mixtures which are involved with water or other associating fluid. Even if good results have been obtained, cubic equations of state

[48] Peng-Robinson Equation of State

[49] Equation of State

are not the most suitable to represent phase equilibrium involving complex molecules, and this is often the case of micronization processes. From an engineering point of view, it is important to have an accurate model that can be taken into account. These differences, in industrial applications the model is considered useful if it is able to predict the system behavior, and not only if it can simulate experimentally tested conditions [**68**].

3.8.3 PC-SAFT[50] Equation of State

The perturbed chain statistical associating fluid theory equation of state has been developed to predict phase equilibria for chemical engineering separation processes. These processes include stripping, absorption and distillation columns. Each of these processes relies on some of the components existing primarily in the gas phase while others exist primarily in the liquid phase so that they can be separated. There is a huge variety of equations of state each specializing in specific kinds of mixtures. Many of these have difficulty with associating compounds such as water, electrolytes and polar molecules; see the last discussion about PR-EOS. Consequently, in PC-SAFT equation an association term in order to account for intermolecular forces is considered. By modeling these forces more accurately, the chance to having the better prediction of the conditions under situation which associating compounds will exist in a gas or liquid phase will be increased.

The Perturbed Chain SAFT [51] model is designed for modeling mixtures of all types of substances like gases, solvents and polymers. Perturbed-Chain SAFT is suitable for the calculation of thermophysical properties of pure components and mixtures. Its results has been checked with experimental data for numerous systems and found to give excellent outcomes. When compared to other equations of state, it was found that Perturbed-Chain SAFT is more precise for correlation of experimental data and more predictive when applied to mixtures. PC-SAFT is very reliable for extrapolations over the regions where parameters were fitted.

---

[50] Perturbed-Chain Statistical Associating Fluid Theory

[51] Statistical Associating Fluid Theory

In this part we intend to mention some theoretical aspect of PC-SAFT; however, it does not contain a full review of the theoretical background of the Perturbed-Chain SAFT equation of state. Large progress in simulating phase behavior of polymer systems and fluid mixture was made during the last years with use of equations of state. In many such theories chain-like molecules are modeled as chains of freely-jointed spherical segments, see Figure 3-5.

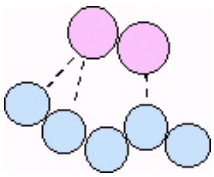

Figure 3-5 Modeling molecules as chains of freely-jointed spherical segments [**69**].

According to this model, molecules are determined by three pure component parameters. First of all, segment diameter (σ) which is the equivalent parameter to *s* is in the original SAFT model the segment volume (v^{00}) and the segment volume. Second, segment number (m), and finally attraction parameter ε. The parameter ε is in the original SAFT equation of state is termed u^0. This molecular model explains the essential characteristics of real molecules. Those characteristics are:

- non-spherical shape of molecules (chain formation)
- attractive interactions (dispersion)
- repulsive interactions

In the Perturbed-Chain SAFT equation of state, the dispersive forces are considered for applying a perturbation theory of second order, using an expression for the radial pair distribution function of a hard-chain reference fluid. This equation of state has been checked through computer simulation data of square-well chains, and excellent results are observed for mixtures of short chains. The PC-SAFT equation of state requires three pure component parameters and is applied to mixtures with one-fluid mixing rule. Comparison to the original SAFT equation of state reveals significant improvement for both, mixtures of small components and polymer solutions.

The Perturbed-Chain SAFT equation of state assumes a hard-sphere chain fluid as a reference fluid. The equation of state consists, thus, of a reference hard-chain equation of state and a perturbation contribution.

$$\frac{A}{NKT} = \frac{A^{hc}}{NKT} + \frac{A^{pert}}{NKT} \tag{3-92}$$

$$Z = \mathrm{Z}^{id} + \mathrm{Z}^{hc} + \mathrm{Z}^{disp} \tag{3-93}$$

where Z is defined as follows;

$$Z = \frac{\mathrm{PV}}{\mathrm{RT}} \tag{3-94}$$

Z is the compressibility factor, P is the pressure, v is the molar volume, R denote the gas constant, T is the absolute temperature, A is the Helmholtz free energy, N denote the total number of molecules, k is the Boltzmann constant, and superscripts hc, and pert are the hard-sphere chain reference equation of state, and the perturbation contribution, respectively. In this terminology the reference equation of state reduces to ideal-gas behaviour at the zero-density limit.

According to Wertheim's thermodynamic perturbation theory of the first order, the equation of state was developed, which for hard-sphere chains comprising m segments is given by,

$$\frac{A^{hc}}{NKT} - \frac{A^{ideal}}{NKT} = \overline{m}.\frac{A^{hc}}{N_s KT} - \sum_i x_i (m_i - 1).\ln(g_{ii}^{hc}(\sigma_{ii})) \tag{3-95}$$

$$\mathrm{Z}^{\mathrm{hc}} = 1 + \overline{m}(\mathrm{Z}^{\mathrm{hc}} - 1) - \sum_i x_i (m_i - 1).\rho \frac{\partial \ln(g_{ii}^{hc}(\sigma_{ii}))}{\partial \rho} \tag{3-96}$$

$$\overline{m} = \sum_i x_i m_i \tag{3-97}$$

where $\mathrm{x_i}$ indicates the mole fraction of chains of component i, $\mathrm{m_i}$ shows the number of segments in a chain of component i, ρ is the total density of molecules, g_{ii}^{hc} is the radial pair distribution function for segments of component i in the hard sphere system, and superscript hc indicates quantities of the hard-sphere system.

$$\frac{A^{hc}}{N_s KT} = \frac{1}{\zeta_0}\left[\frac{3\zeta_1\zeta_2}{(1-\zeta_3)} + \frac{\zeta_2^3}{\zeta_3(1-\zeta_3)^2} + \left(\frac{\zeta_2^3}{\zeta_3^3} - \zeta_0\right)\ln(1-\zeta_3)\right] \tag{3-98}$$

$$Z^{hc} = \frac{1}{(1-\zeta_3)} + \frac{3\zeta_1\zeta_2}{\zeta_0(1-\zeta_3)^2} + \frac{3\zeta_2^3 - \zeta_3\zeta_2^3}{\zeta_0(1-\zeta_3)^3} \tag{3-99}$$

$$g_{ij}^{hc} = \frac{1}{(1-\zeta_3)} + \frac{d_i + d_j}{d_i d_j}\frac{3\zeta_2}{(1-\zeta_3)^2} + \left(\frac{d_i + d_j}{d_i d_j}\right)^2 \frac{2\zeta_2^2}{(1-\zeta_3)^3} \tag{3-100}$$

where ζ_m is defined as follows;

$$\zeta_m = \frac{\pi}{6}\rho\sum_i x_i m_i d_i^m \qquad m = \{1, 2, ...\} \tag{3-101}$$

with d_i being a temperature dependent diameter segment of component i, based on the following relation,

$$d_i = \sigma_{ii}\left(1 - 0.12\exp\left(-3\frac{\varepsilon_{ii}}{kT}\right)\right) \tag{3-102}$$

In the above equations m_i, σ_{ii} and ε_{ii} are the pure component parameters, in order the first one segment number, second one segment diameter and the last one interaction-energy parameter. Pure components of all molecular weights are generally very well described with the Perturbed-Chain SAFT model, see Figure 3-6[**69**].

3.9 Numerical Solution

Numerical solutions are useful in calculating profiles of velocity, pressure, temperature, fluid composition, etc., especially when analytical solutions are not possible. In this study, a numerical solution to the set of partial differential equations that govern convection and diffusion in the cavity was sought.

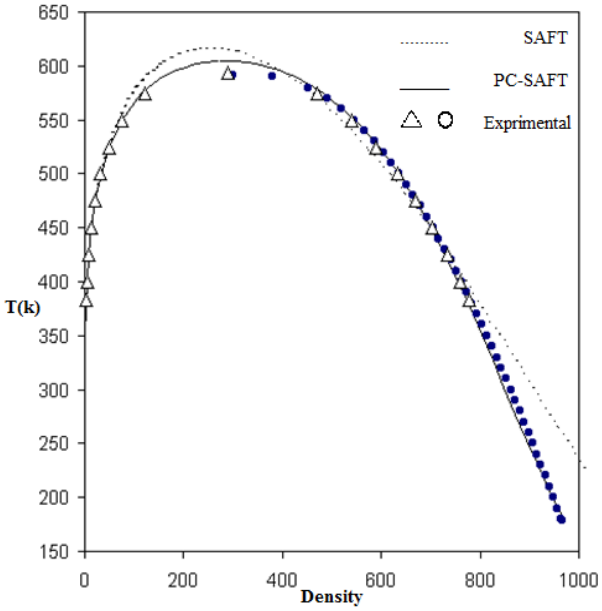

Figure 3-6 Comparison between PC-SAFT and SAFT model and Experimental [**69**]

3.9.1 SIMPLE Algorithm

The procedure for the calculation of the flow field was developed by Prof. Brian Spalding and his student Dr. Patankar at Imperial College, London in the early 1970s. It has been given under the name of SIMPLE[52], which stands for Semi-Implicit Method for Pressure-Linked Equations. In CFD[53], the SIMPLE algorithm is a widely used numerical procedure to solve the Navier-Stokes equations. The procedure is explained in following section.

3.9.1.1 The Pressure and Velocity Corrections

The basic idea behind the SIMPLE method is to guess the pressure of the system, then find the other properties of the fluid as a result of this guess, when making a correction to this guess, based on the previous result. The process is continued with next iteration which will be explained in the next section. For instance, our attempt in this part is to introduce a parameter to improve the guessed pressure $p*$ such that the resulting starred velocity field will progressively get closer to satisfying the continuity equation; however, more details about calculating this

[52] Short term of Semi-Implicit Method

[53] Computational Fluid Dynamics

parameter are provided by Patankar's Numerical Heat Transfer and Fluid Flow[**28**]. The correct pressure p, may be defined as the following equation;

$$p = p^* + p' \quad (3\text{-}103)$$

where p' is the pressure correction. After that the velocity components responding to this change in pressure should be found. The corresponding velocity corrections u', v', w'can be introduced in a similar manner;

$$u = u^* + u' \qquad v = v^* + v' \qquad w = w^* + w' \quad (3\text{-}104)$$

3.9.1.2 Chain of Operations

The main steps, in the order of their execution, are the following; first, estimate the pressure field p^* , for instance, the initial pressure of the fluid or mixture could be a close guess. Then solve the momentum equations, in order to obtain the velocity vector according to our estimation or u^*, v^* and w^*. After that, calculate the p' equation and correction term of pressure. To more details about the procedure for finding this parameter, see reference [**28**]. Next, add p' and p^* to find the current step pressure or p. Then, calculate *u*, *v*, *w* from their starred values using the velocity-correction formulas. After that, solve the discretization equation for other properties like temperature and concentration. Finally, for the next iteration, treat the corrected pressure *p* as a new guessed pressure p^*, when return to the first step of our iteration. It is necessary to repeat the whole procedure until a converged solution is obtained. In each step of this iteration process, the average relative error of u, v, p, T and concentration are computed as F_u, F_v, F_p, F_T and F_{c_i}, respectively, where F is defined as follows,

$$F_\phi = \frac{1}{n \times m} \sum_{i=1}^{m} \sum_{j=1}^{n} \left| \frac{\phi_{i,j}^{t,s+1} - \phi_{i,j}^{t,s}}{\phi_{i,j}^{t,s+1}} \right| \quad (3\text{-}105)$$

In the above equation, *t* is the time step, *s* is the iteration number and i and j are indices represent the cell on the grid. A convergence is achieved if the results of function F for all the

unknowns are below 10^{-6} in two continue successive iterations. The maximum number of iterations within each loop is five hundred, after which if convergence has not been reached, the time step increment is divided by a factor of two and the loop is begun again.

3.9.2 A Revised SIMPLER Algorithm

Although the SIMPLE algorithm results are good enough for all kinds of fluid, in order to improve its rate of convergence, a revised version has been worked out. It is called SIMPLER, which stands for SIMPLE Revised.

The approximation that is used in the derivation of the p' equation leads to rather exaggerated pressure corrections, and hence under relaxation becomes essential. Because the effect of the neighboring point velocity corrections is removed from the velocity correction formula, the pressure correction has the total load of correcting the velocities, and these result in a rather severe pressure correction field. If pressure correction is employed in the equation only for the task of correcting the velocities and providing some other means of obtaining an improved pressure field, then a more efficient algorithm is constructed. This explains the main idea behind the SIMPLER algorithm. The revised algorithm consists of solving the pressure equation to gain the pressure field and solving the pressure correction equation only to correct the velocities. It is observed that, for the one-dimensional problem discussed, the SIMPLER algorithm would at once give a converged solution. In SIMPLE, a guessed pressure field plays a vital role; however, SIMPLER does not use guessed pressures, but extracts a pressure field from a given velocity field. Although SIMPLER has been found to give faster convergence than SIMPLE, it should be recognized that each step of SIMPLER involves more computational effort. First, the pressure equation must be solved in addition to all the equations solved in SIMPLE; and second, the calculation of the velocity vector represents an effort for which there is no counterpart in SIMPLE. Consequently, SIMPLER requires fewer steps for convergence; however, the additional effort per iteration is more than compensated by the overall saving of effort.

3.10 Discretization of Equations

The discretization is carried out with respect to the primary variables, pressure, temperature and composition. The previous governing equations were obtained for each grid block using a

central finite-difference scheme in space on a Cartesian grid and a first-order finite-difference approximation for the derivative in the accumulations term, in time.

3.10.1 Mesh Sensitivity Analysis

Performing a mesh sensitivity analysis is an integral part of producing accurate, time-efficient and cost-effective results. For this study, we used the same mesh as used by Parsa and Saghir [**1**]. They used a mesh of 17 elements in the x-axis by 17 elements in the y-axis for the two-dimensional laterally heating conditions for a cavity one centimeter in length and height. Thus, for other cases with different sizes are smaller than the first cavity, at least the same resolution was used.

3.10.2 Time Step Control

In order to obtain sufficient accuracy, while maintaining optimal processing time, the value of the incremental time step must be chosen carefully. One of the major goals of this study is to find the best time step for our problem so that the accuracy and computational time remain optimal. The initial time step is set to 0.02 second.

3.11Brief description of main simulation code

For this investigation, several two-dimensional rectangular cavities with a different length and height, respectively, were chosen as the computational domains. Such a cavity is represents the experimental chamber when the valve is in the open position. This CFD simulation was developed in FORTRAN based on the Firoozabadi model. In this package of software, there are several source and input files. Figure 1 in Appendix C shows the flowchart of these subroutines.

Chapter 4 : Results and Discussion

4.1 Review of Research Objectives

Theoretical studies have reached a certain level with the several models proposed to explain the mechanism involved in this essential process, and the experimental results have been accumulated to help researchers to widen their investigation. However, to have a clear comparison between pure thermodiffusion in the mixture that is the result of theoretical investigation into the experimental data, the vibration effect on the experimental result should be considered. The main objectives of this research are the following:

- To simulate these experiments and understand the fluid separation and flow behaviour in the thermodiffusion apparatus via the numerical results by applying the vibration result on the system as well as understanding the quality of the microgravity environment on FOTON-M3 as well as ISS[54].
- To compare ISS and FOTON-M3 as suitable platform to operate the thermodiffusion experiments.
- To compare different cavities based on their dimensions.

4.2 Initial and Boundary Conditions

For component mole fractions, the small cavity used in the simulations is a two dimensional cross-sections (i.e. x-y); the effect of gravity should be taken into account. The component mole fractions may either be initialized uniformly across the cavity or according to Gibb's equation[**39**]. In this investigation we used uniform initial concentration on the domain. The effect of gravity on two different binary mixtures with different initial concentrations was investigated, where the first one has the same concentration for both components, and the second one in the ratio of nine part water to one part isopropanol to consider both negative and positive Soret effect.

[54]International Space Station

In most studies, the pressure field is initialized based on the depth of the gridlock centres with respect to the datum depth and the pressure at the datum depth. However, in this study, the pressure on the mixture is set to be approximate close to atmospheric pressure.

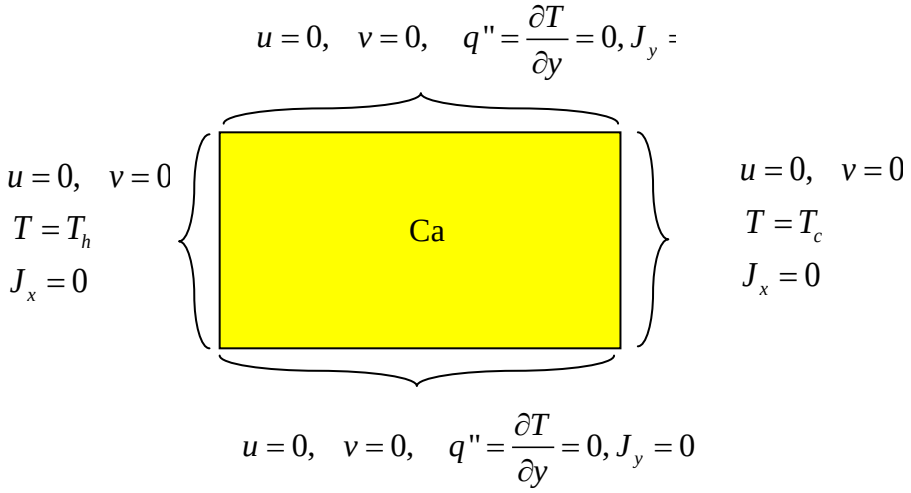

Figure 4-1 Problem Boundary Conditions

The temperature field is initialized as purely conductive pattern. The horizontal temperature gradients are defined on the two sides of the cavity so that the hot and cold wall temperatures are 303 and 293 K respectively. In other words, 10 K temperature gradient was applied to the cavity. The primary variables are initialized as being uniform across the vertical line but linear with respect to the horizon. Thus, on each wall of the cavity conditions of no-flow and no-slip have been applied. Consequently, the boundary condition can be expressed as follows;

@ $x = 0, \quad x = L$

$$u = 0, \quad v = 0 \tag{4-1}$$

$$T|_{x=0} = T_h, \; T|_{x=L} = T_c \tag{4-2}$$

$$J_x = 0 \tag{4-3}$$

@ $y = 0, \quad y = H$

$$u = 0, \quad v = 0 \tag{4-4}$$

$$\frac{\partial T}{\partial y} = 0 \tag{4-5}$$

$$J_y = 0 \tag{4-6}$$

where J_i shows the flux in the i^{th} direction. The positions in two perpendicular directions are x and y; L (in the x-direction) and H (in the y-direction) are the length and height of the cavity

respectively. They are the cavity dimensions. In this investigation, three different cavity sizes were considered with following dimensions and the depth of the cavity is assumed to be unit. See Figure 4-2;

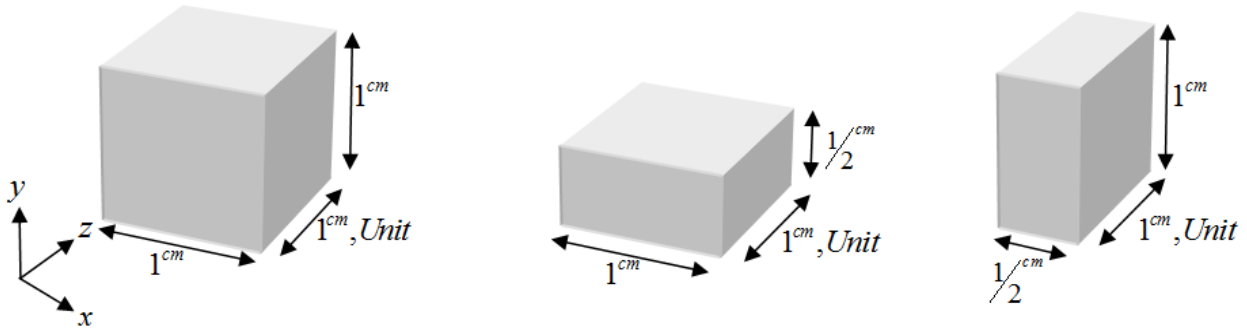

Figure 4-2 Three different cavities were simulate in this study

In all the simulations there is no velocity in the cavity at the beginning. Further, the mixture temperatures in all the cases have been initialized as a linear interpolation between the hot and cold sides of the cavity. Finally, the pressure in the cavity is set at atmospheric pressure at beginning.

4.3 Physical Fluid Properties

The fluid properties are found in several articles by Saghir and his team and are based on reservoir pressure and temperature as well as fluid composition [**1**,**49**,**19**,**50**].

Table 4-1 Fluid Properties

	Water	Isopropanol
viscosities of the pure components[g/(m.s)]	0.923	2.0553
Molar volume at the boiling $\left[\mathrm{cm}^3/mol\right]$	18.81	82.97
Critical Temperature [k]	647.29	508.30
Critical Pressure [MPa]	22.090	4.762
M_W [g / mol]	18.015	60.096
Mixture	10%Isopropanol, 90%water Mass Fraction	50%Isopropanol, 50%water Mass Fraction
Initial Density $\left[kg/m^3\right]$	984	905
Thermal Conductivity [w / m.K]	0.5220	0.2866

where M_W is molecular weight of pure component.

4.4 Results & Discussions

4.4.1 Vibration acceleration onboard FOTON-M3 and ISS

CFD simulations were performed for all the nine mixtures, four onboard FOTON-M3, four onboard ISS and the last one without any vibration (zero gravity). In order to accurately simulate the space vehicle environment, the vibrations experienced by the experiments during the space fight were applied to the governing equations. These acceleration profiles on the ISS in the x and y-directions are shown in Figure 4-3. In addition, the acceleration profiles onboard FOTON-M3 are shown in Figure 4-4.

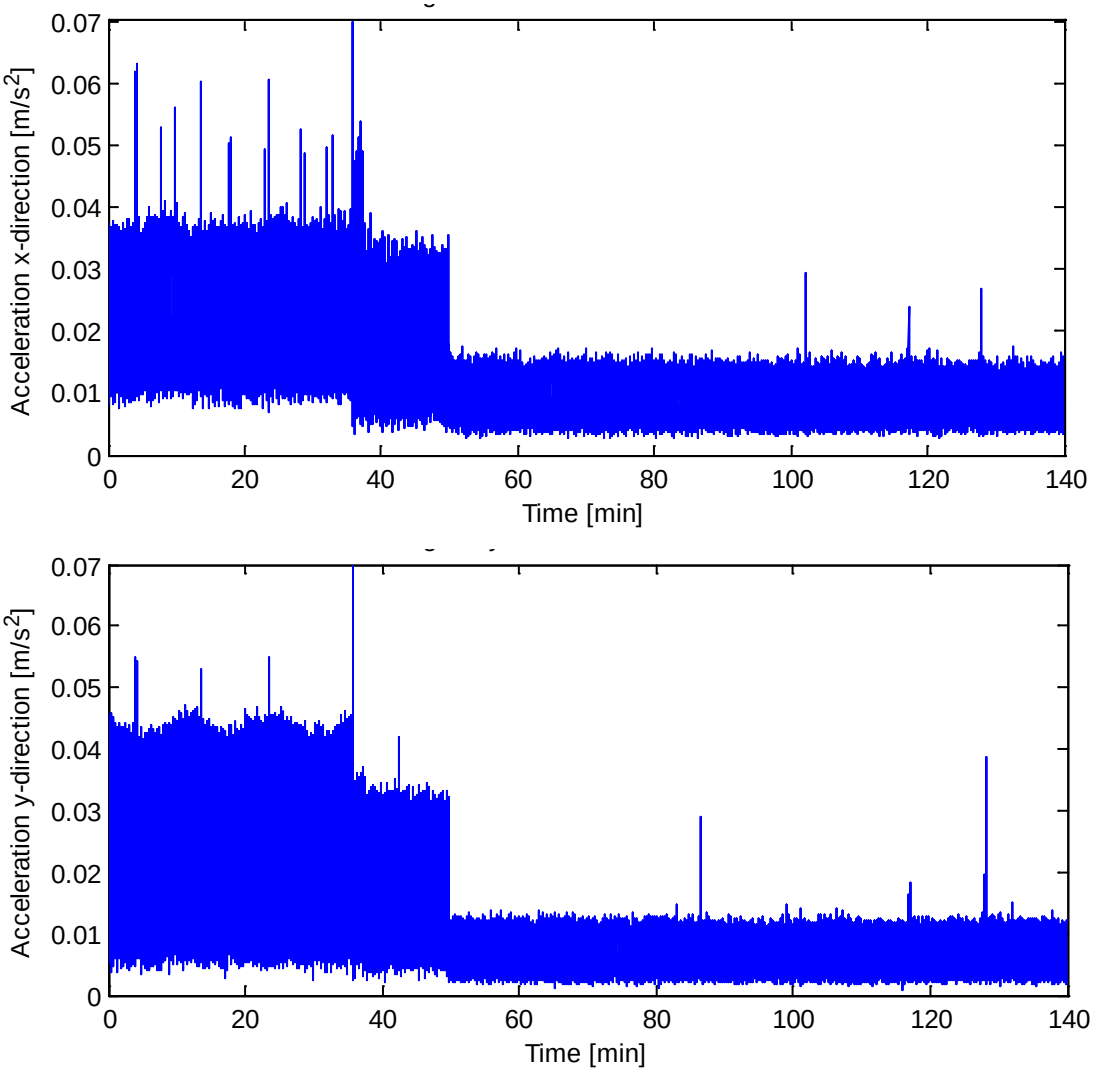

Figure 4-3 Acceleration along the x and y-directions due to the vibrations on ISS

In the next sections contained further details about the influence of these profiles on the final experimental results.

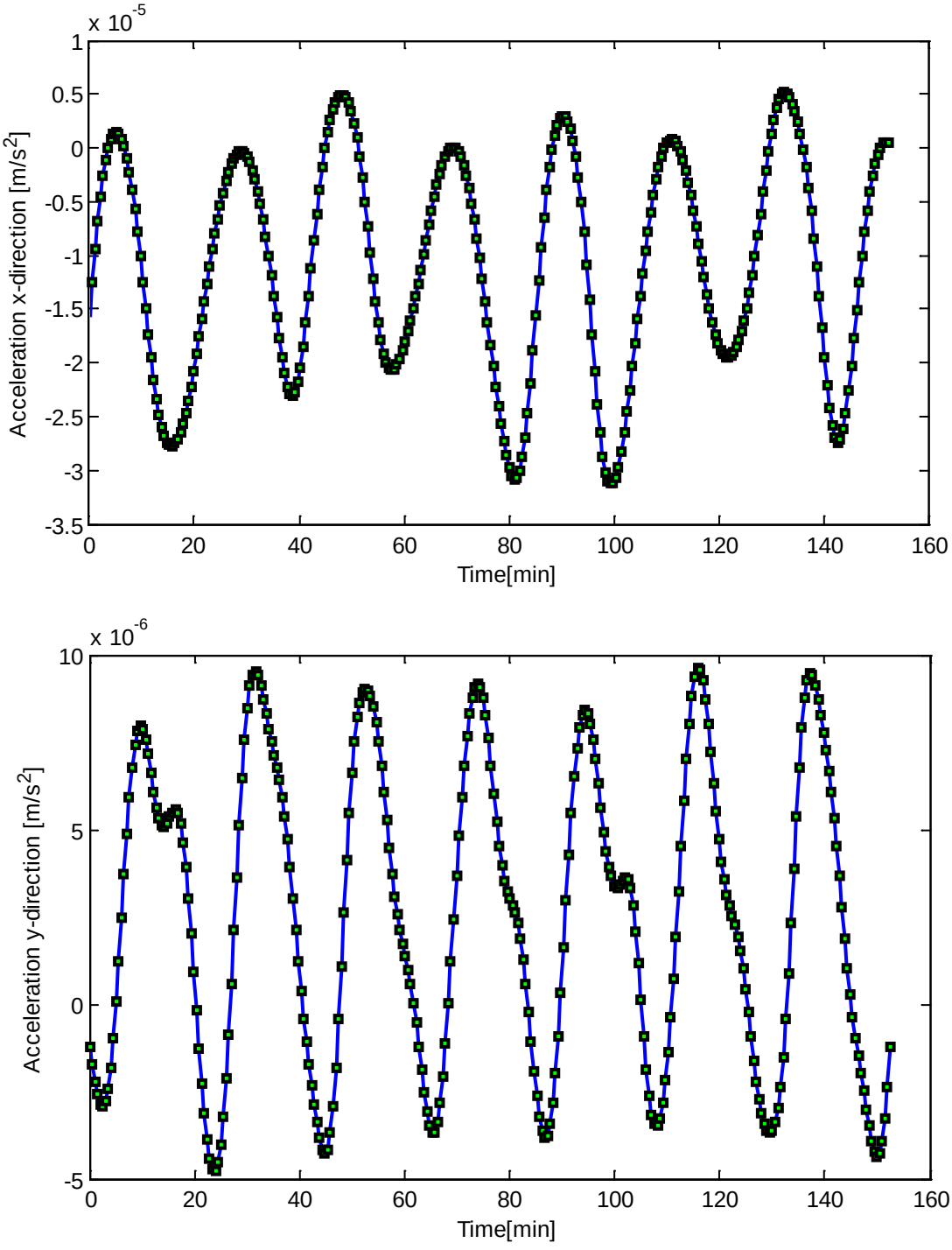

Figure 4-4 Acceleration along the x and y-directions due to the vibrations on FOTON-M3

From the above figures, it can be concluded that the average acceleration in the x- and y-directions onboard ISS is about $20\,mm/s^2$; however, in Figure 4.4, it is shown that this quantity for FOTON-M3 is less than $18\,\mu m/s^2$. Although these are both very small acceleration values, they have effects on the fluid mixture experiments. Another important point about these two values of acceleration is the ratio of their magnitude; the ISS vibrations are one thousand times stronger than the FOTON ones.

The different experimental cases which were simulated in this study are summarized in Table 4-2. For the CFD simulations, a mesh with 17×17 nodes in the both x- and y-directions, for the 1 cm by 1 cm cavity size was used, for the main case in this investigation. For the other cases with different cavity sizes, for instance, $1\,[cm] \times 0.5\,[cm]$ and $0.5\,[cm] \times 1\,[cm]$, simulation meshes with 32×17 and 17×32 nodes in the x- and y-directions, respectively were used. The initial and boundary conditions were as described in Section 4.2. It is required to mention again that an adiabatic cell was assumed for the top and bottom walls. All simulations were performed until a quasi-steady state was reached, that is, more than two hours for our experiments. This duration was used based on previous investigations that were performed by Saghir and his team [**49**][**1**][**50**][**19**].

Table 4-2 Mass fraction, Cavity size, Mesh Resolution and Experimental Board of each case.

Case	Plat Form	Isopropanol Mass Fraction	Water Mass fraction	Cavity Size	Mesh Resolution
1	ISS	0.10	0.90	$1\,[cm] \times 1\,[cm]$	17×17
2	FOTON-M3	0.10	0.90	$1\,[cm] \times 1\,[cm]$	17×17
3	ISS	0.50	0.50	$1\,[cm] \times 1\,[cm]$	17×17
4	FOTON-M3	0.50	0.50	$1\,[cm] \times 1\,[cm]$	17×17
5	ISS	0.10	0.90	$1\,[cm] \times 0.5\,[cm]$	32×17
6	FOTON-M3	0.10	0.90	$1\,[cm] \times 0.5\,[cm]$	32×17
7	ISS	0.10	0.90	$0.5\,[cm] \times 1\,[cm]$	17×32
8	FOTON-M3	0.10	0.90	$0.5\,[cm] \times 1\,[cm]$	17×32
9	Ideal	0.10	0.90	$0.5\,[cm] \times 1\,[cm]$	10×30

It was found that the separation in a mixture is dictated by the probability of an interaction between two molecules of different components[**48**]. The probability of these events is dictated by the activation energy, size of the molecules and the mole fractions of the individual components in the mixture. For more detail about this theory, see [**67**].

4.4.2. Spatial Analysis

All mixtures reached a quasi-steady state by about 8500 seconds. At this point, for all mixtures, almost a linear variation of the parameters such as the fluid temperature, species concentration etc., is established from the hot wall to the cold wall for FOTON cases, and this variation was observed to be similar, linear and completely overlapping for all horizontal property variations. For example, the nodes near the bottom ($y = -4.375\ [mm]$), at the middle of the cavity ($y = 0[mm]$,which corresponds to the locations at the centre of the domain in the direction of the applied thermal gradient) and top of the cavity ($y = 4.375\ [mm]$), are presented in part (a) of most of the figures from Figure 4-7 to Figure 4-20 for different properties like temperature, species concentration, diffusion coefficient, density and viscosity. However, the most important variations to be studied are those which correspond to the direction of the applied thermal gradient. In this investigation, the vertical variation which corresponds to the perpendicular direction of the applied thermal gradient is considered. For each of these variations, three different horizontal lines near the hot wall, near the cold wall and at the middle of the cavity were investigated. Unlike FOTON cases, for ISS cases this linear variation was not observed for fluid properties.

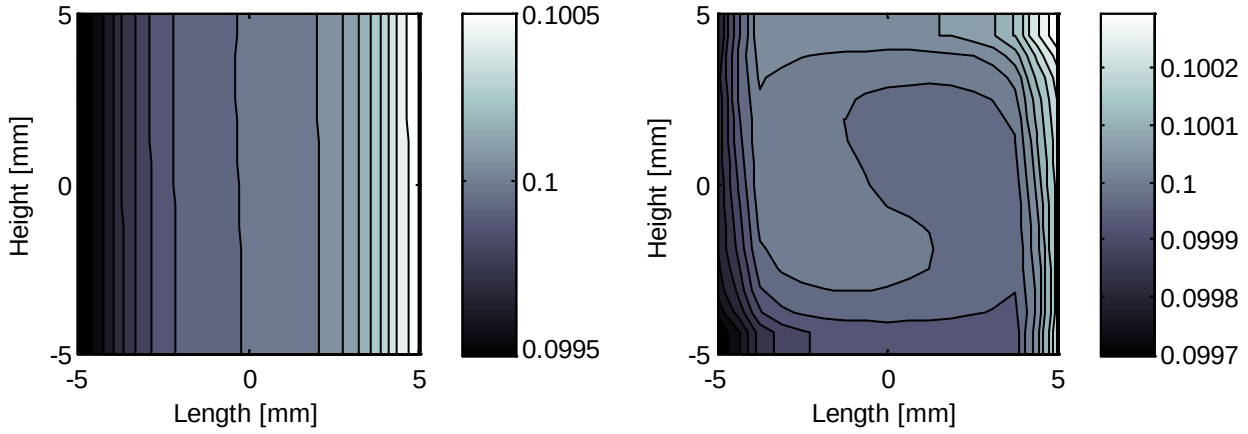

(a) FOTON-M3 **(b) ISS**

Figure 4-5 Isopropanol mass fraction distribution in cavity

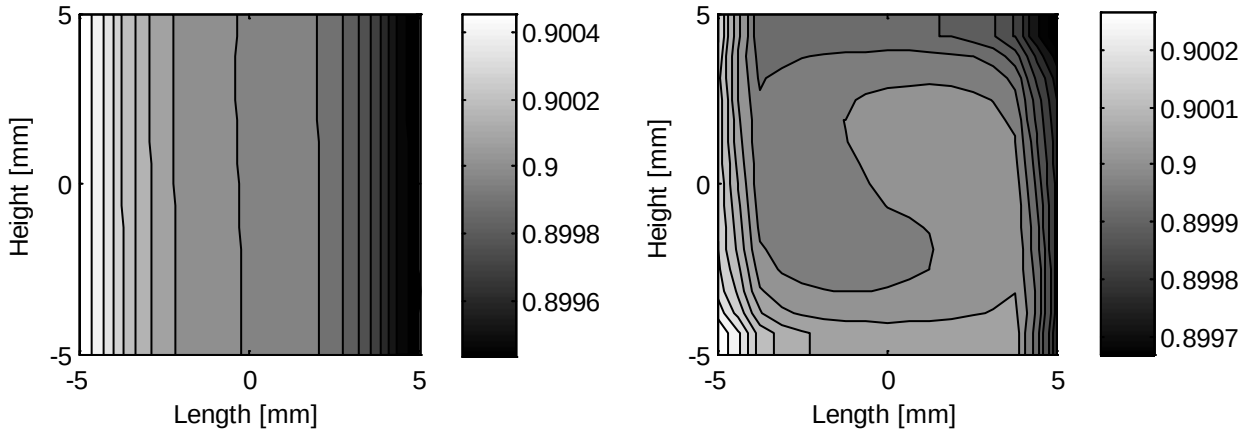

(a) FOTON-M3 **(b) ISS**

Figure 4-6 Water mass fraction distribution in cavity

Due to the Soret effect, generally isopropanol separates towards the cold wall and water moves to the hot wall. The concentration of the two components and the temperature in the domain along three different horizontal lines at about 2.5 hours is shown in Figures 4-7 and 4-14 for case 1. Once again, the ISS case is compared with the FOTON and ideal cases in Figure 4-20. Like other mixtures, we can see in these figures that in the ISS case there is a much weaker separation. As before, the disagreements between the ISS and the Ideal cases can be attributed to the ISS vibrations that delay this separation behaviour by inducing a convective flow in the domain. The strong mixing in the ISS cases is evident in the form of large velocities in the cavity

along the x and y-directions at about 2.5 hours in Figures 4-5b and 4-6b. Figures 4-5 and 4-6 part (a) show the mass fraction of isopropanol and water, respectively for FOTON; that means case 2 based on Table 4-2. Moreover, part (b) shows this fraction for the ISS, which is case 1, according to Table 4-2. As one can see in these figures, separation on FOTON-M3 occurred in a manner similar to the pure diffusion phenomena, while for the ISS case, not only was this phenomenon not visible, but also strong convection as a result of buoyancy forces made a strong mixing in the cavity. In the ISS case at the top of the cavity near the cold wall, the concentration of isopropanol reaches maximum, and there is a minimum isopropanol mass fraction at the bottom near the hot wall; however, the opposite is true for the water mass fraction. In comparison, for FOTON-M3 the fractions of components near each wall remained the same. Moreover, it must be added that for both cases, the mass fraction of water near the hot wall is less than that near the cold wall, while isopropanol was trapped near the hot wall.

Figure 4-7 shows the mass fraction of isopropanol along the three different horizontal lines at the bottom, middle and top of the cavity for cases 1 and 2. Despite a constant initial mass fraction of 0.1 for both cases, the separation in case 2 was more pronounced than the separation in the ISS case as a result of a strong convection cell in the ISS case. All lines overlapped for FOTON; that proves a smooth diffusion environment, while at the top of the cavity of case 1, a slightly higher mass fraction of isopropanol was seen. It should be added that although the mass fraction at the top of the cavity is higher than that at the bottom, the separation along both of these lines is the same. In other words, a small shift of mass fraction along the direction perpendicular to the temperature gradient is observed.

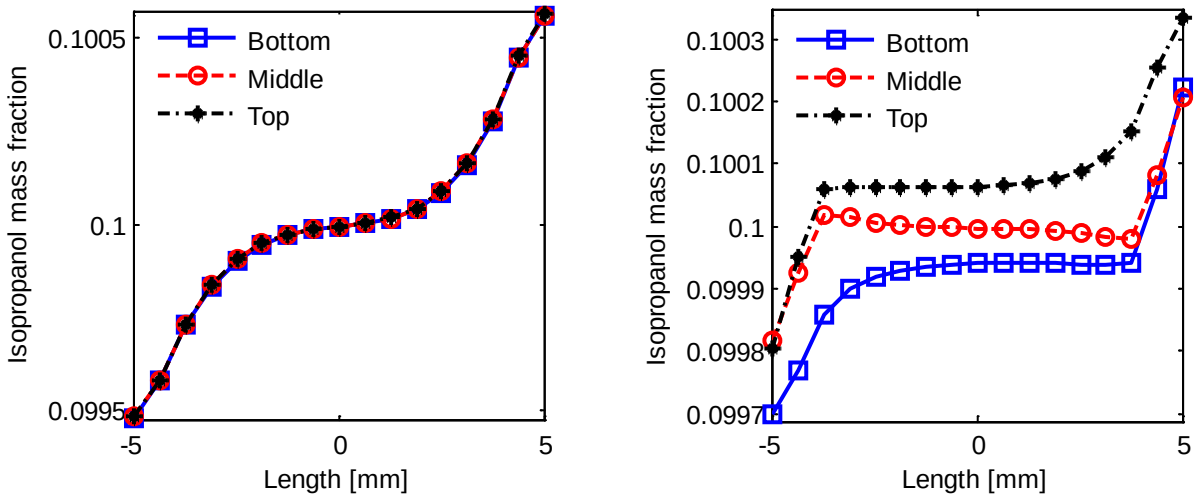

(a) FOTON-M3 **(b) ISS**

Figure 4-7 Isopropanol mass fraction variation along x-direction

Figure 4-8a illustrates the mass fraction of isopropanol, along the three different vertical lines (near the hot and cold walls and in the middle) for case 2; part b shows this variable for case 1. Again, despite a constant initial condition for both cases, the vertical separations are not similar to each other; in case 2, the concentration along the vertical lines remained constant, while this quantity changed very strongly in the ISS case. Two opposite curvatures were observed for the isopropanol mass fraction along the y-direction at the top and bottom of the cavity. We can claim that this behaviour at the centre of the cavity and the bottom half of it, is caused by the hot wall; however, the behaviour at the top half is caused by the cold one.

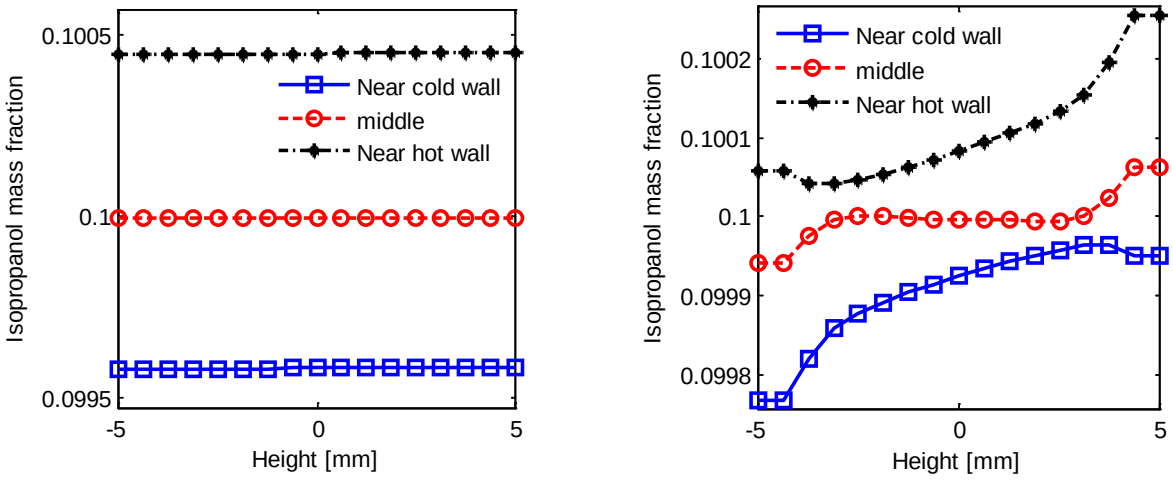

(a) FOTON-M3 **(b) ISS**

Figure 4-8 Isopropanol mass fraction variation along y-direction

4.4.3 Quasi-steady condition

4.4.3.1 Velocity field and Stream function

It was observed that at the quasi steady state a single convective cell was established as shown in Figure 4-9 for both ISS and FOTON cases. This is due to a dominant induced velocity in the cavity; however, these single cells are similar to each other; to have a better view of the strength of these convection cells, the magnitude of the fluid velocity is required. As mentioned in Figure 4-10, we used the average magnitude of the velocity to compare the strength of these cells. For the ISS cases, this was about $18\,\mu m/s$, and for the FOTON cases, close to $0.02\,\mu m/s$.

An important observation is that the logarithmic difference between vibration acceleration and average induced velocity was similar for all cases. This remains true even if we compare the result of ISS to FOTON, which results in logarithmic difference close to 3.

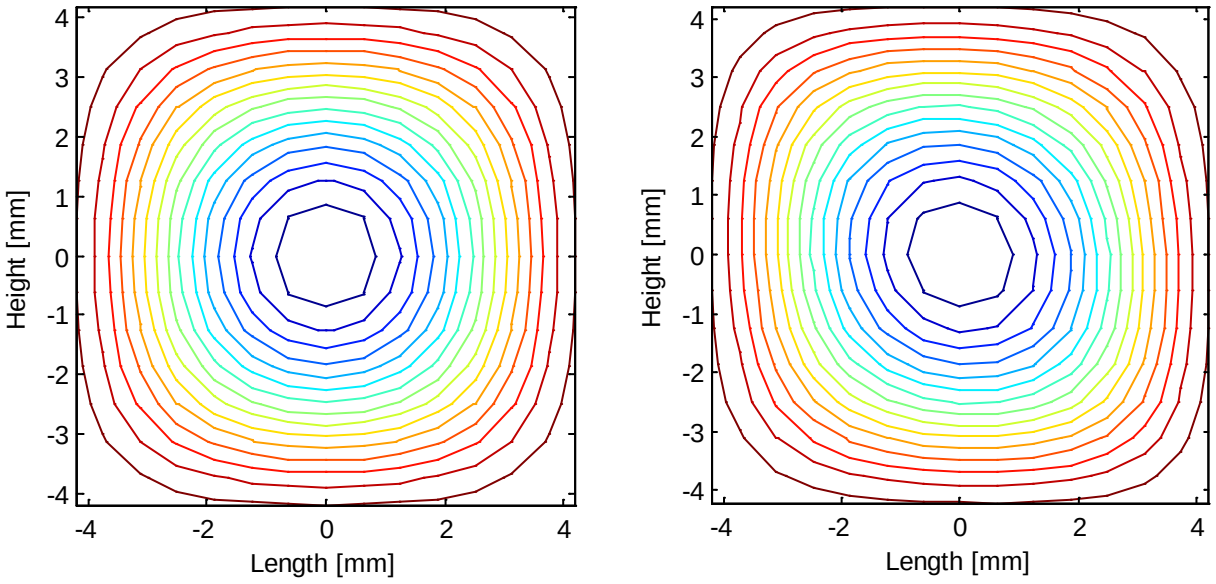

(a) FOTON-M3 **(b) ISS**

Figure 4-9 Cavity steam line

It also has to be mentioned that to prove these relations lots of researches and investigations are required, and we only claim that such a relation may exist between the velocity and acceleration patterns; this relation would be a function of other characteristics of the vibrational acceleration, like its frequency.

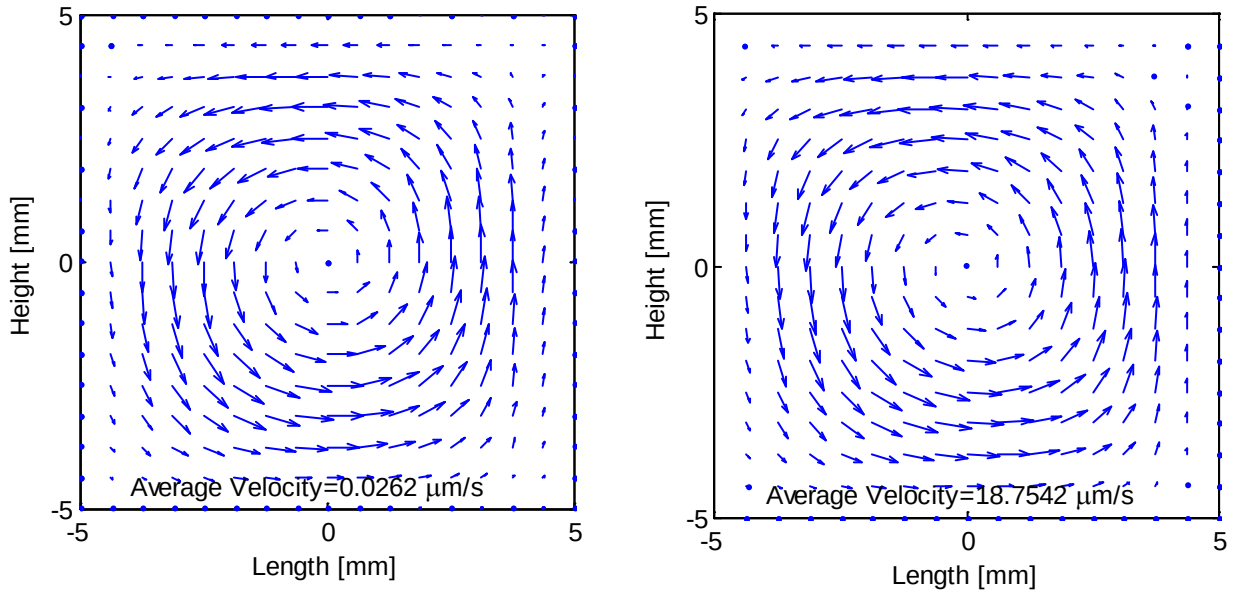

(a) FOTON-M3 **(b) ISS**

Figure 4-10 Velocity field in the domain at quasi-steady condition

As can be seen in Figure 4-11, near the walls, the velocity in the x-direction is two orders of magnitude larger than the velocity in the y-direction as a result of boundary condition.

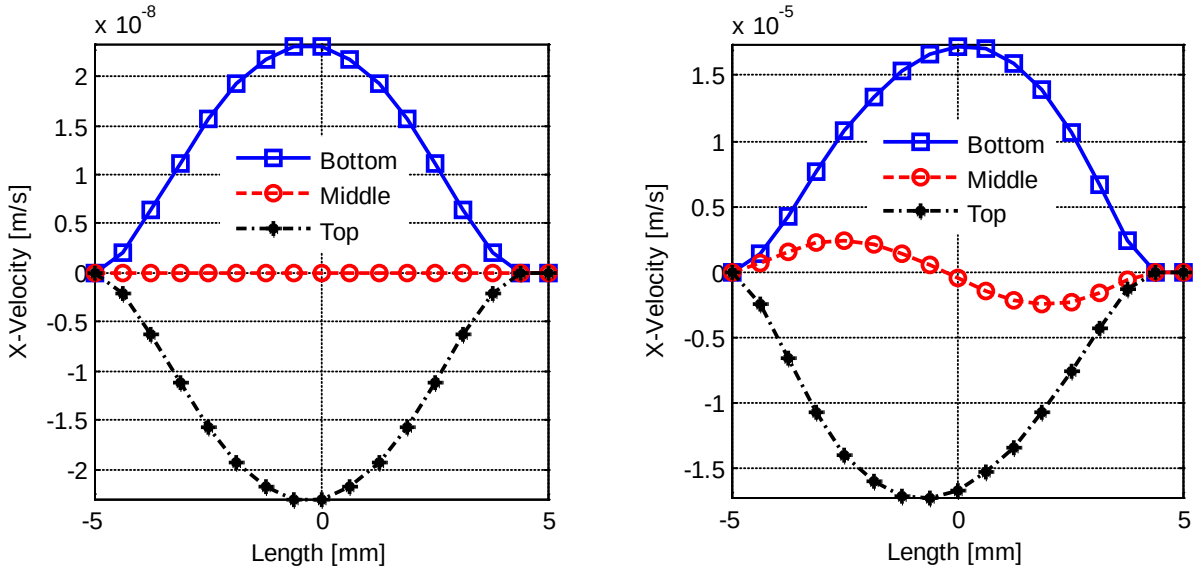

(a) FOTON-M3 **(b) ISS**

Figure 4-11 x-velocity variation along x direction

The velocity along the x-direction or parallel to the temperature gradient at the middle of the cavity was observed to be near zero for FOTON case (Figure 4-11a); however, for the ISS

(Figure 4-11b) the shape and pattern of the strong convection cell in the cavity cause a magnitude of the x-velocity along the middle of the cavity.

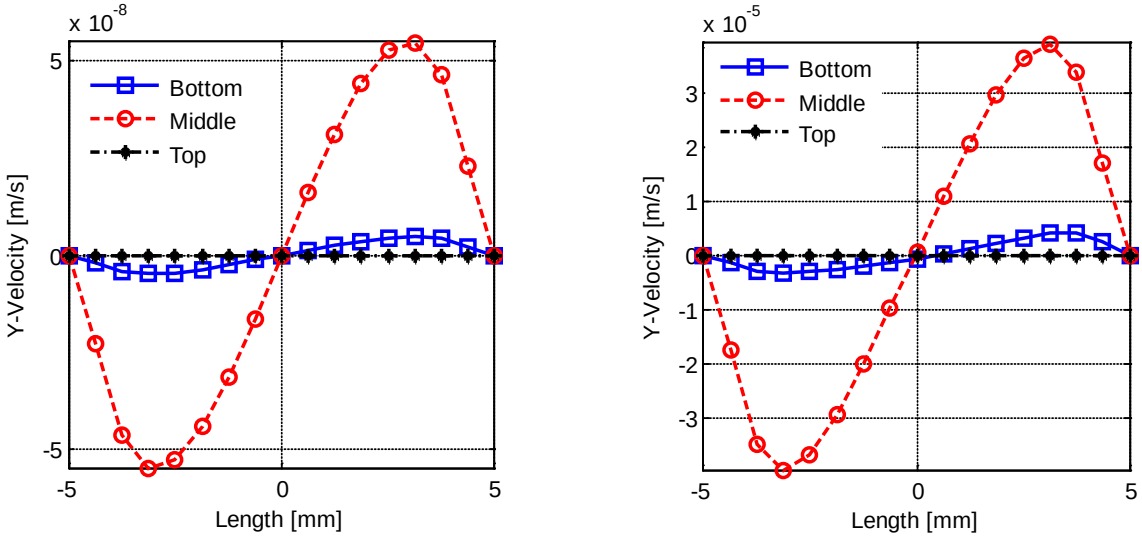

(a) FOTON-M3 **(b) ISS**

Figure 4-12 y-velocity variation along x direction

The component of velocity along the y-direction at the centre has the maximum magnitude (Figure 4-121 and b), while; the component in the x-direction has the minimum magnitude. For the y-velocity both ISS and FOTON-M3 behave completely like each other. The only difference is the order of the velocity, which is caused by the different vibrational acceleration magnitude on these two space vehicles.

4.4.3.2 Temperature distribution

Figure 4-13 shows the temperature contours in the cavity for the quasi steady state condition for both ISS and FOTON cases. From this figure, it can be seen that for the FOTON satellite cases, the temperature contours are almost vertically parallel. However, temperature in the ISS case was affected by the strong induced convection as a result of vibration on board ISS.

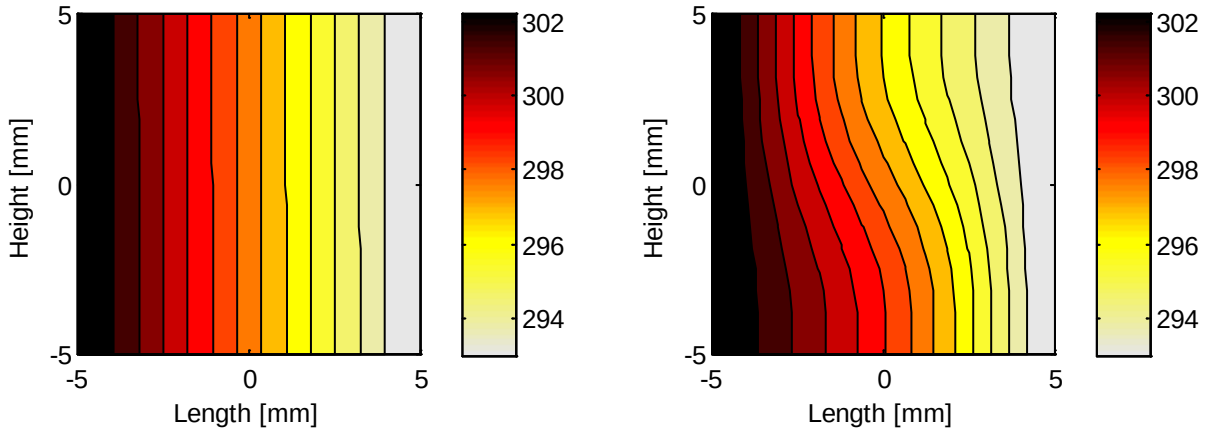

(a)T[K]; FOTON-M3 **(b) T[K]; ISS**

Figure 4-13Temperature distribution in domain

As can be observed in Figures 4-13 and 4-14 part (b), unlike the FOTON temperature, which has a similar variation for all horizontal lines, as a result of the convection cell at the top of the cavity the fluid experiences a colder regime than that at the bottom for the ISS cases, and the variation between the hot and cold walls is not linear except for the line at the middle of the cavity.

Figure 4-15a shows temperature variation along the y-direction or perpendicular to the direction of the temperature gradient. As was expected, a constant temperature for all vertical lines in the cavity was seen.

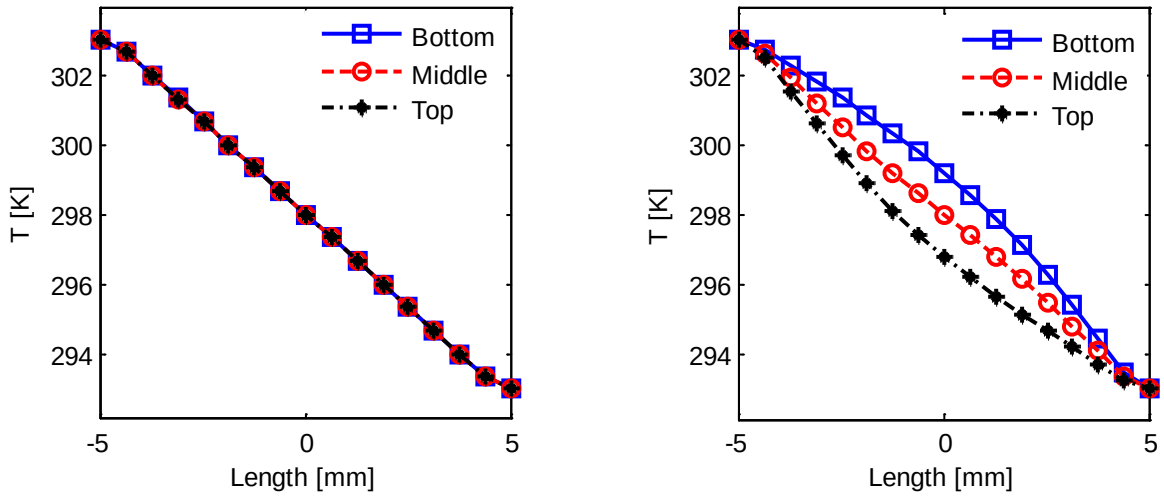

(a) FOTON-M3 **(b) ISS**

Figure 4-14 Temperature variation along x-direction

However, if this behaviour in Figure 4-15b is compared to the dashed lines which are parallel to the x-axis, it can be understood that the fluid temperature varies along the y-direction, even near the walls. The maximum variation was observed for the vertical line at the centre of the cavity for all ISS cases.

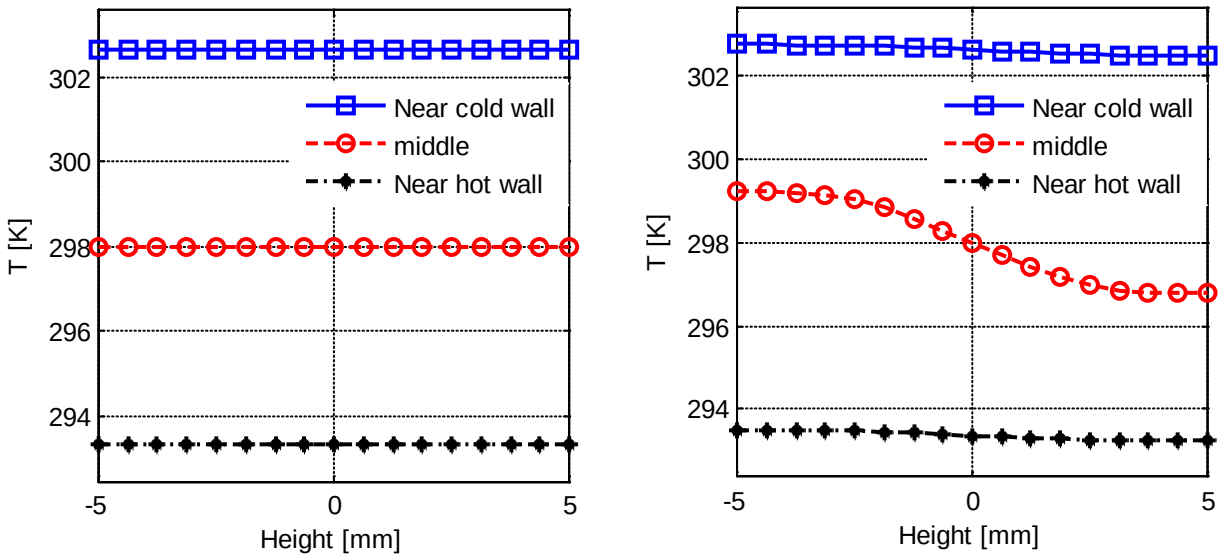

(a) FOTON-M3 **(b) ISS**

Figure 4-15 Temperature variation along y-direction

4.4.3.3 Diffusion coefficients

Figure 4-16 shows the molecular and thermodiffusion coefficients contour in the cavity. At least two important points can be observed from these figures. First, it is important to consider these coefficients in the cavity to be variable, because a wide range of variation can be seen for them. The second point is that the contour pattern for both of these coefficients is like the temperature contour; see Figure 4-13. It is common that thermodiffusion coefficient is a function of temperature over the domain, while more study is required to determine whether the similarity between the temperature contour and the molecular diffusion coefficient is accidental or not.

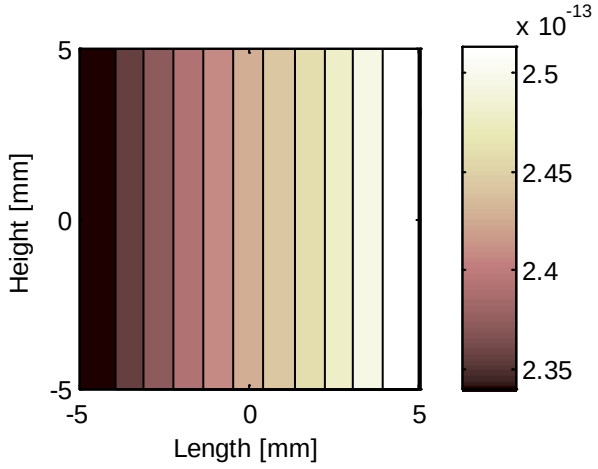

(a) $D_T[m^2/(K.s)]$**; FOTON-M3**

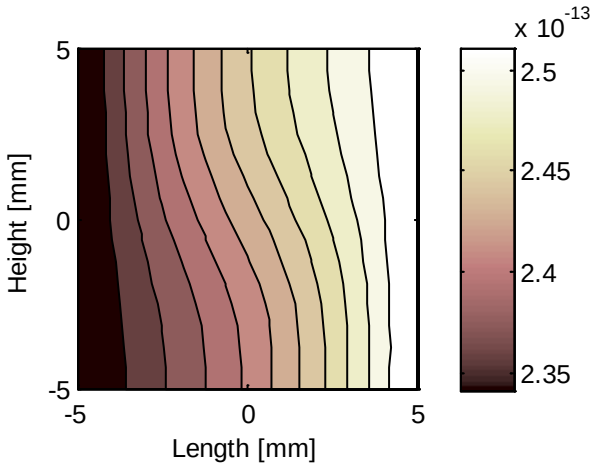

(b) $D_T[m^2/(K.s)]$**; ISS**

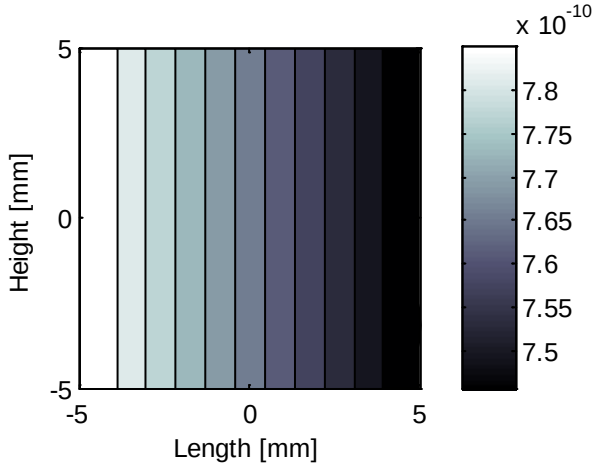

(a) $D_M[m^2/s]$**; FOTON-M3**

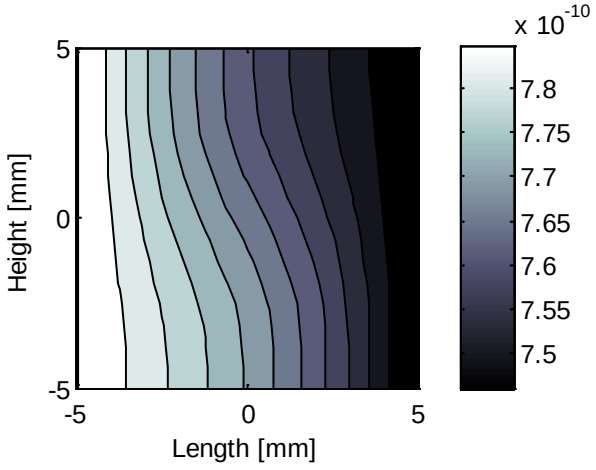

(b) $D_M[m^2/s]$**; ISS**

Figure 4-16 Diffusion coefficients distribution in domain

The variations of these coefficients are completely similar for both cases; while like the other parameters, these coefficients are vary linearly for the FOTON satellite, but for the ISS case, two opposite curvatures were observed for the horizontal lines at the top and bottom of the cavity. Another important observation is the opposite behaviour of these coefficients along the length of the cavity. In other words, D_M increased but D_T decreased along the length of the cavity, and in addition, the horizontal line with the maximum thermodiffusion coefficient had the minimum molecular diffusion coefficient.

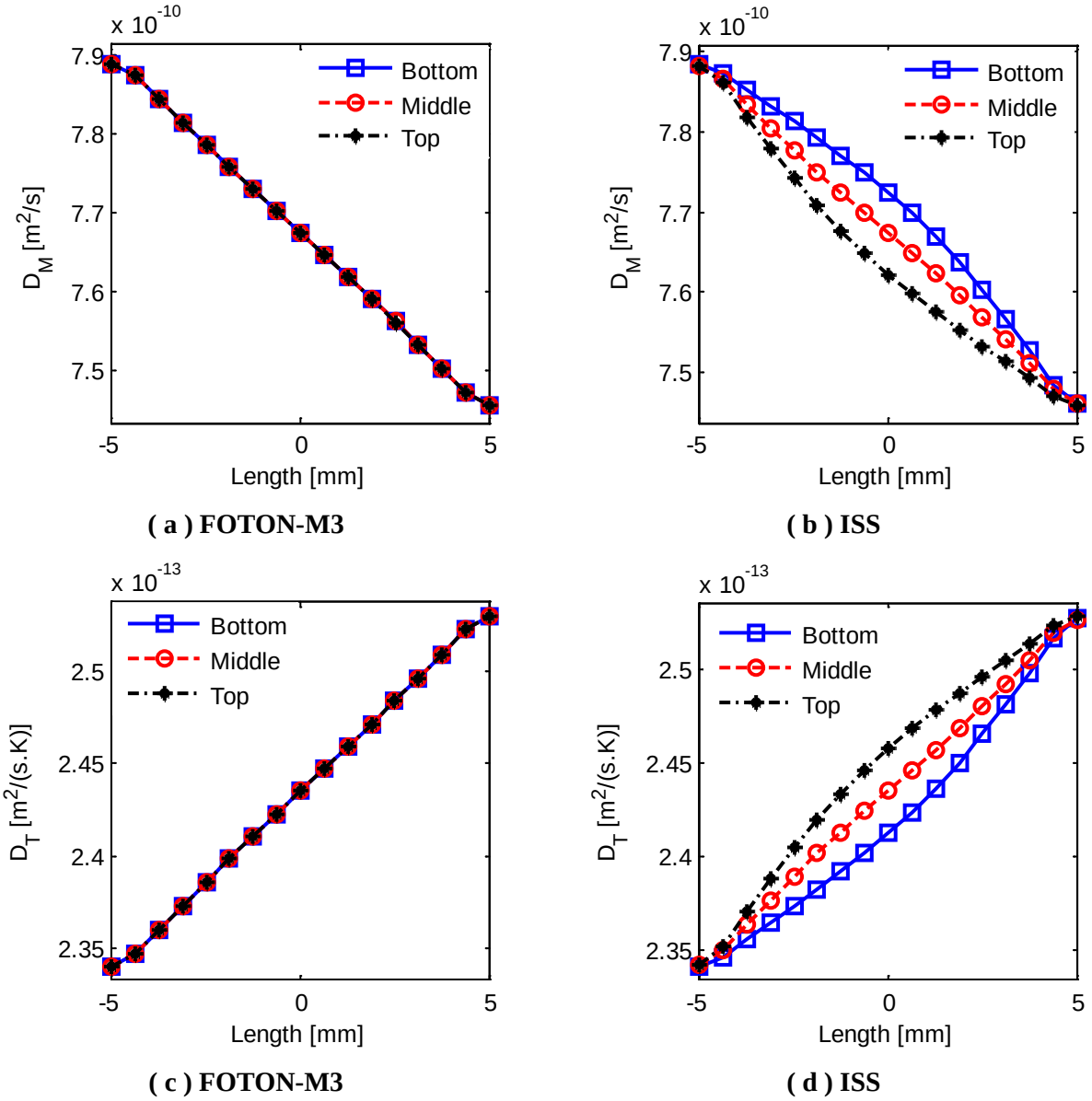

Figure 4-17 Diffusion coefficients variation along x-direction

4.4.3.4 Density and Viscosity

The last properties of the mixture which will be discussed are density and viscosity. As mentioned in the last chapter, density of the mixture at each node was found by using the PC-SAFT equation of state, which has good performance for associating mixtures like water isopropanol. The values of the density over the cavity illustrate that this property was a strong function of the temperature in this experiment, and because of the high initial mass fraction of the water in the mixture, the density values are mostly close to water density.

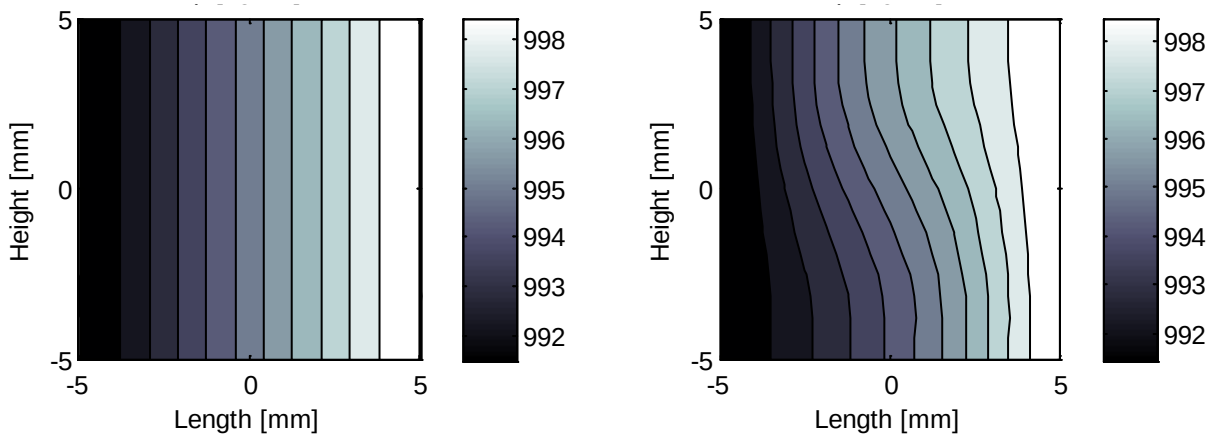

(a) $\rho[kg/m^3]$; FOTON-M3 (b) $\rho[kg/m^3]$; ISS

Figure 4-18 Density distribution in the domain

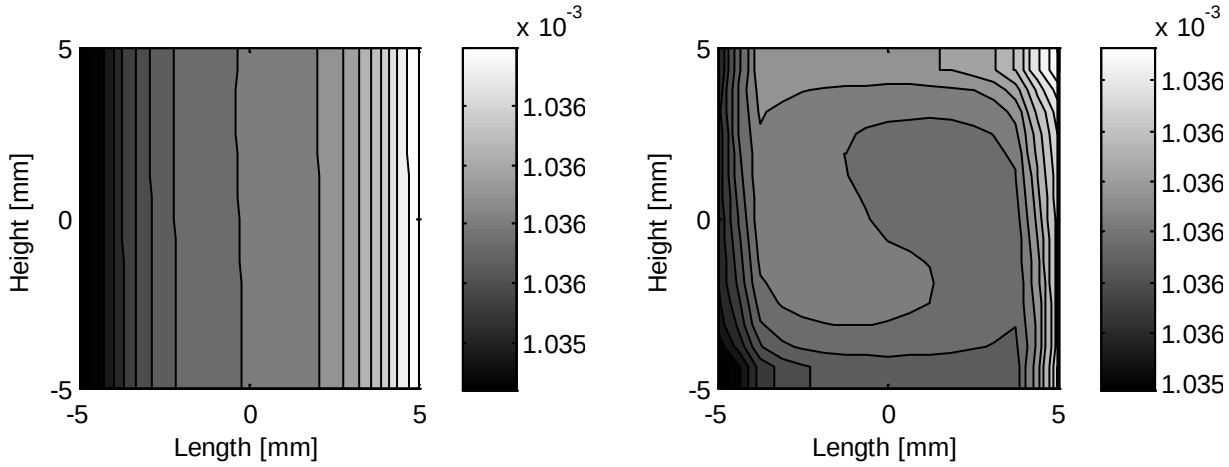

(a) $\mu[kg/(m.s)]$; FOTON-M3 (b) $\mu[kg/(m.s)]$; ISS

Figure 4-19 Viscosity distribution in the domain

In most of the previous researches in this field, the viscosity was assumed to be constant, but in this study we assumed it to be variable by special formulation which is explained in Chapter two. Unlike density, viscosity is a function of concentration and follows the same pattern as mass fraction of isopropanol in the mixture. It must be added that, although this variation for density and viscosity are less than one percent, the importance of considering these properties to be variable could be understood from Figures 4-18 and 4-19.

4.4.3.5 Comparison with Ideal case

To conclude the steady state discussion, a comparison among the zero gravity or ideal case, the ISS case and the FOTON case were performed with the result shown in Figure 4-20. All of these simulations used a binary mixture of isopropanol and water with initial mass fraction of 10:90 respectively, and filled the cavity, one centimeter high and half a centimeter long.

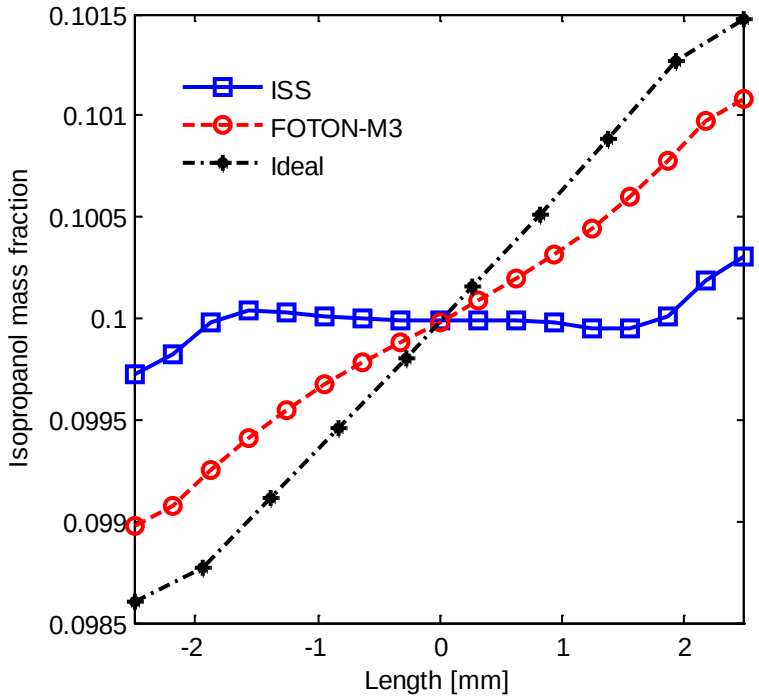

Figure 4-20 Isopropanol variation along x-direction for three different environment

One can see that the ISS case is strongly affected by the convection cell, and as a result of mixing, a weak separation of water toward the hot wall occurs. The observation is quite different for the ideal case, were the separation variation is linear from the hot to the cold wall with a high slope. Because of very weak vibration on board the unmanned satellite, we can see that it behaves mostly like the ideal case; however, the effect of the convection cell could be seen in Figure 4-20.

4.4.4 Transient Analysis

In order to understand the behaviour of the mixture during the course of the experiment, various quantities are examined at five specific locations in the domain, over a period of time. More precisely, the mole fraction of the individual species, the temperature, velocity and the diffusion coefficients were studied at Location 1; bottom and near the hot wall, Location 2; top and near the hot wall, Location 3; top and near the cold wall, and Location 4, centre of the cavity, top and near the cold wall.

4.4.4.1 Transient temperature

As we know from similar studies like this, the first four nodes may be considered for investigation because each one of these can explain the mixture behaviour at a special region in the cavity. But we must add that all of these nodes are affected as a result of boundary conditions and the geometry of the cavity. In other words, the first three nodes are very close to both walls, as a result of the no-slip boundary condition on the surface, are affected and their velocity will be less than the other velocity at other nodes in the domain.

It is true that Location 4 at the centre of the cavity is not influenced from boundary conditions. But base on our symmetric geometry of the problem and having one strong convection cell, the centre of the cavity and the centre of the convection cell overlap. And the velocity at the centre of the convection cell is always close to zero. Although we can claim that the velocity at this node is important to study, the node can't show the effect of vibration on our experiment.

As a result of all of these points, we chose Location 5 dynamically where "dynamically" is taken to mean having a complete view of the vibration effect of the cavity. In each step time the entire domain is searched for the node with maximum velocity and this point is taken as Location 5. This location with maximum velocity was used because in our problem the induced velocity in the system is the most important parameter that causes mixing in the cavity and it reduced separation. Moreover for studying the velocity field in the domain, the average of the velocity on

entire domain was used as shown in figure 4-21. The transient behaviors of the parameters at these locations are discussed next.

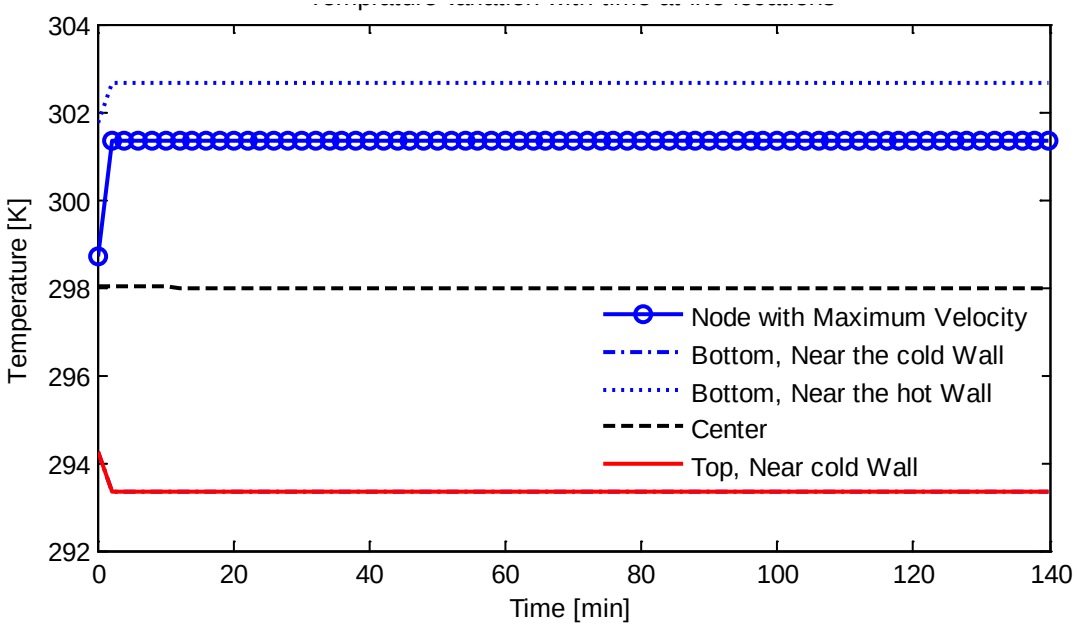

(a) FOTON-M3

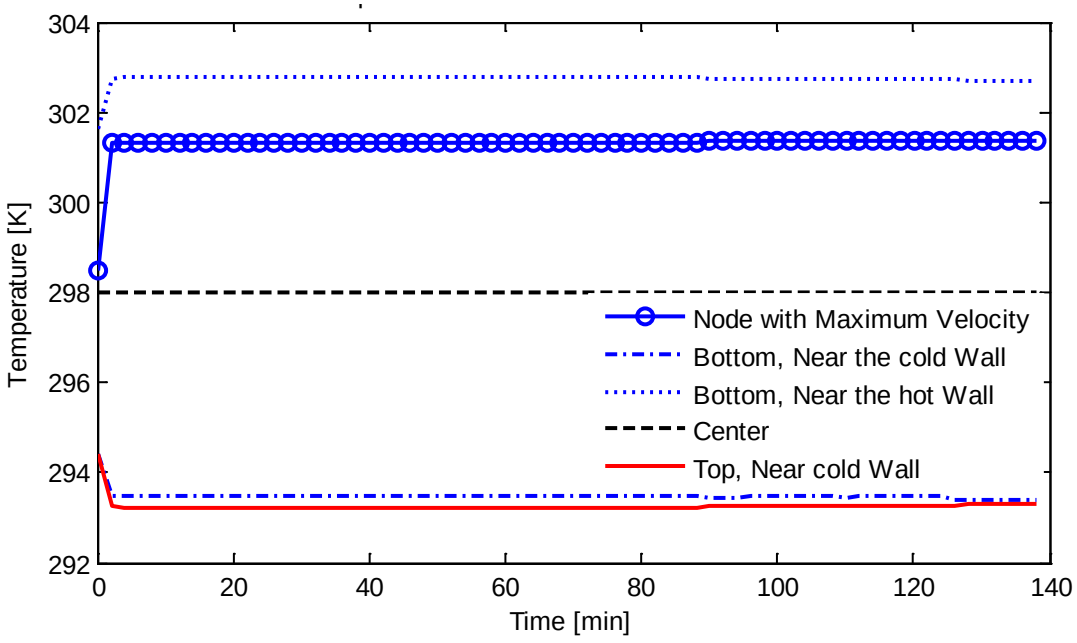

(b) ISS

Figure 4-21 Temperature variation over time at five locations

4.4.4.2 Transient mass fraction

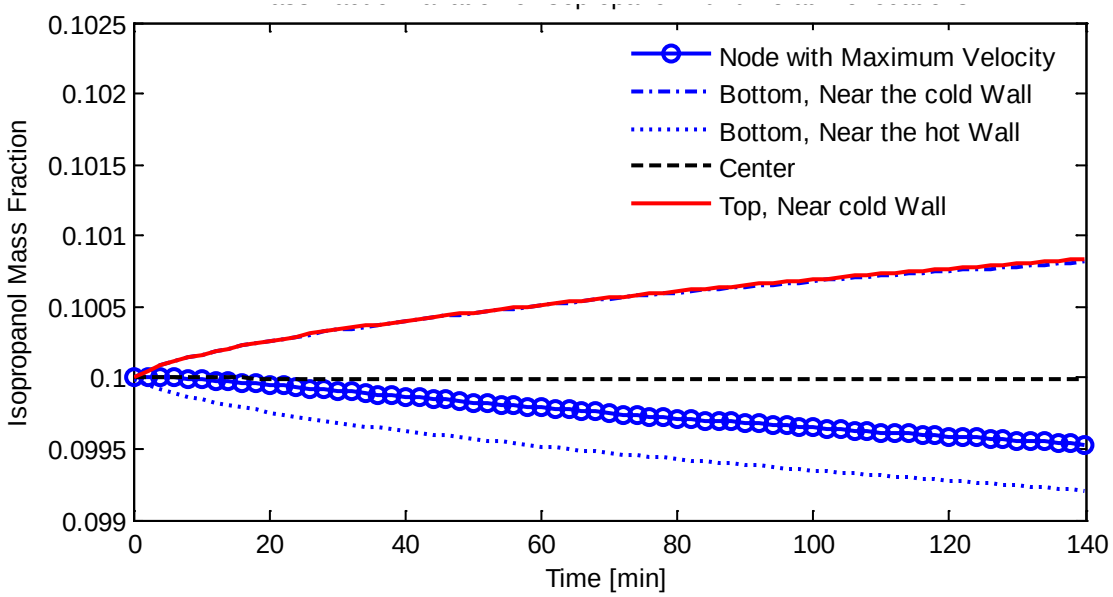

(a) FOTON-M3

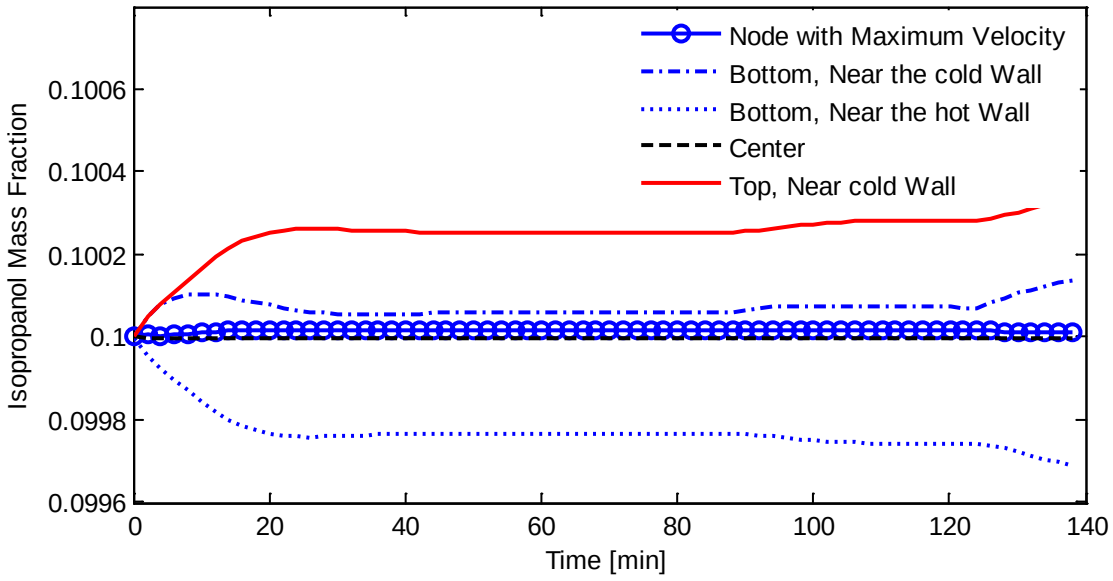

(b) ISS

Figure 4-22 Isopropanol mass fraction versus time at five locations

Figure 4-22, part (a) and (b) show the mole fraction of the first two mixtures isopropanol and water, on board FOTON-M3 and ISS respectively at the five locations. The corresponding

temperatures at these locations are given in Figure 4-21. As seen in these figures, the mole fraction of water begins to increase at the location near the hot wall. At the location near the cold wall there is a proportional decrease in the mole fraction.

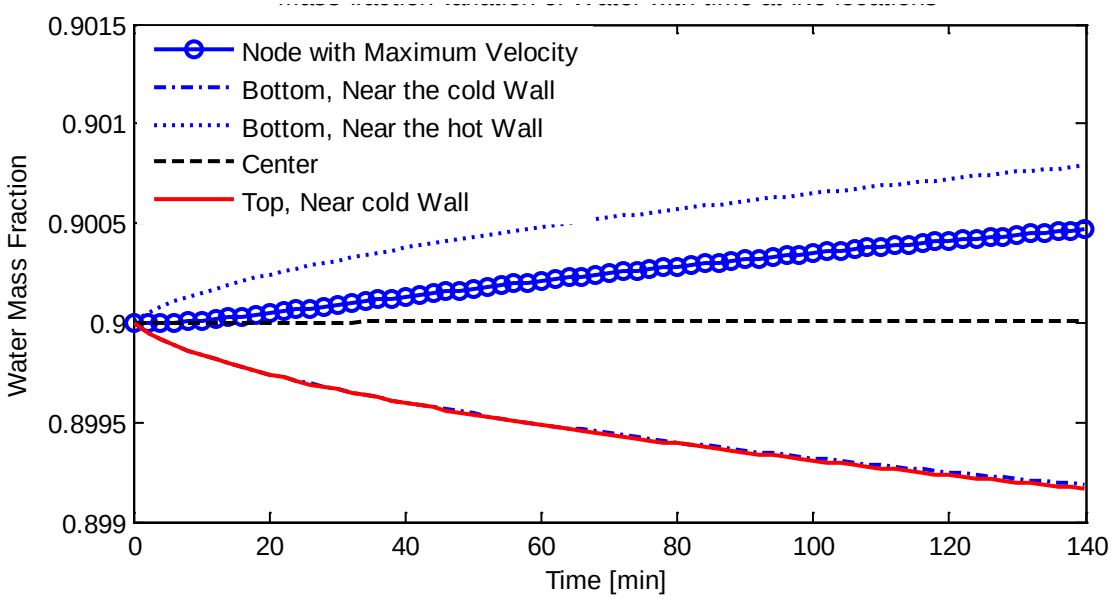

(a) FOTON-M3

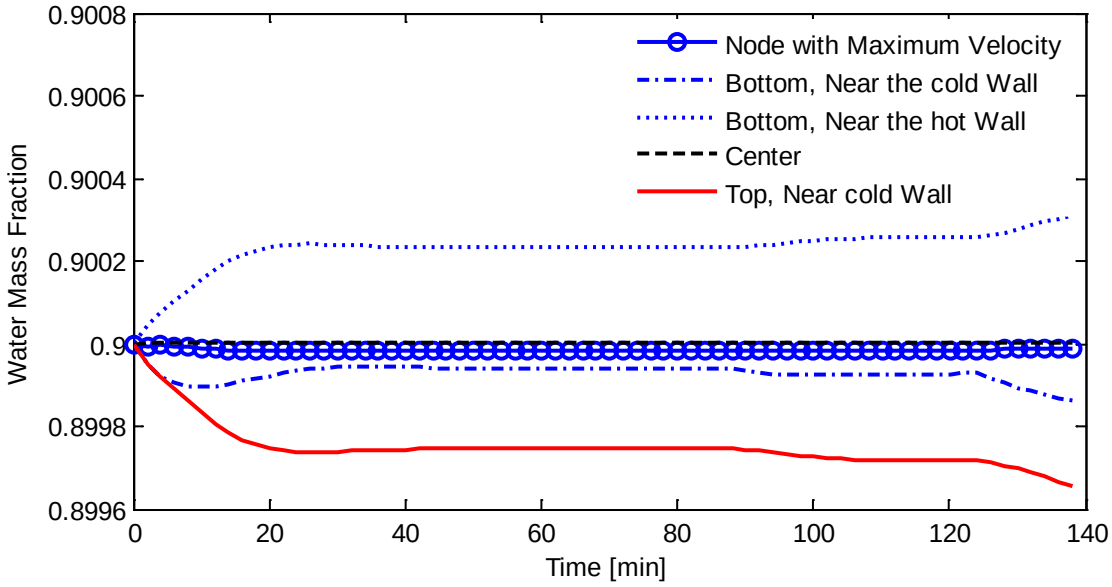

(b) ISS

Figure 4-23 Water mass fraction versus time at five locations

Isopropanol experiences a strong separation versus time for the FOTON case; however, the amount of separation for the ISS case at first increased, but at t=20 min, it achieved a special amount of separation and remained almost constant for the entire experiment after this critical time. Thus, a closer look at the scale on the y-axis indicates that the separation is extremely weak for the ISS case. However, for FOTON we can see that after two hours of experimentation, the separation continued.

There are two points that should be mentioned; first, the separation at centre of the cavity is almost nearly zero for both cases; and secondly, for both cases the magnitude of separation at the bottom near the hot wall and the top near the cold wall are the same but with different direction. It is likely that for both systems, the cavities have point asymmetric separation around their centres. However, it should be added that for the FOTON cases, separation is line symmetric corresponding to the horizontal line at the middle of the cavity. As a result, the mass fractions of the isopropanol at the top near the cold wall and at the bottom near the cold wall are identical. This observation could not be seen for ISS cases because of strong induced convection.

4.4.4.3 Transient diffusion coefficient

The thermodiffusion and molecular coefficients of the five locations in the first mixture is shown in Figures 4-24. Because of the identical behaviour of these coefficients for all mixtures, we did not investigate the other mixtures for this diagram. We can observe that the location with the maximum thermodiffusion coefficient has the minimum molecular diffusion coefficient and vice versa. At the centre of the cavity no changes in these coefficients was detected.

The result demonstrates that for these coefficients, such as concentration on the cavity there is a kind of a point a symmetric around the value at the centre of the cavity. Despite the sharp rate of change in these coefficients at the beginning, the rate of change remains near zero for thermo and molecular coefficients Figure 4.24. The gradient scales of these two coefficients are similar to each other.

Figure 4-21 shows the temperature profile over time in the cavity. In all the profiles discussed above, it has been seen that the variation of the parameters with time is very smooth. In a microgravity environment with vibrations, one can expect small instantaneous fluctuations of the

parameters with time. The absence of such fluctuations on FOTON-M3 was due to the fact that these vibrations were at a very small magnitude.

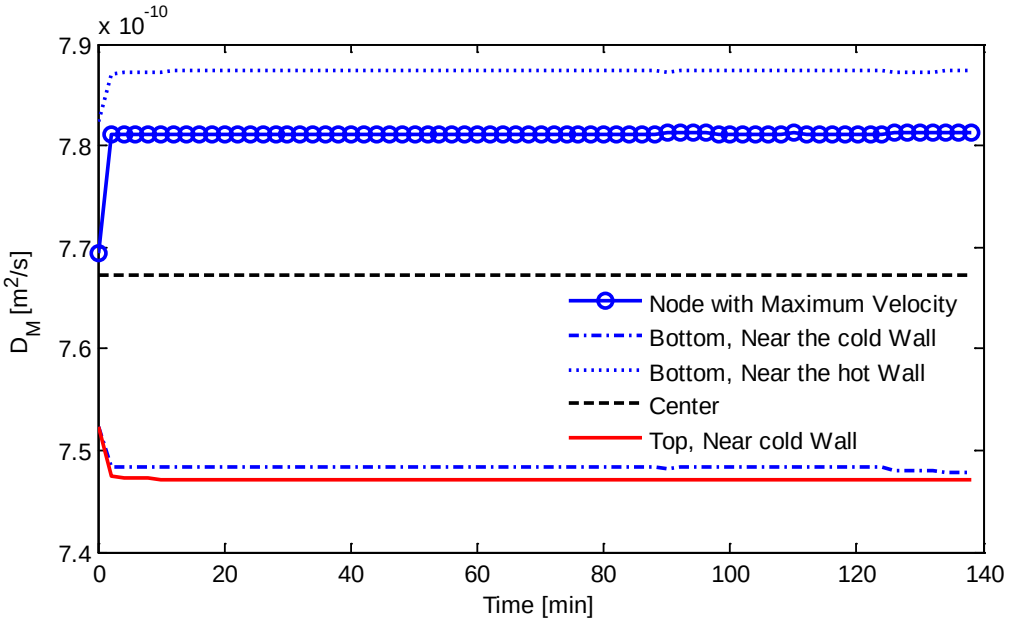

(a) FOTON-M3

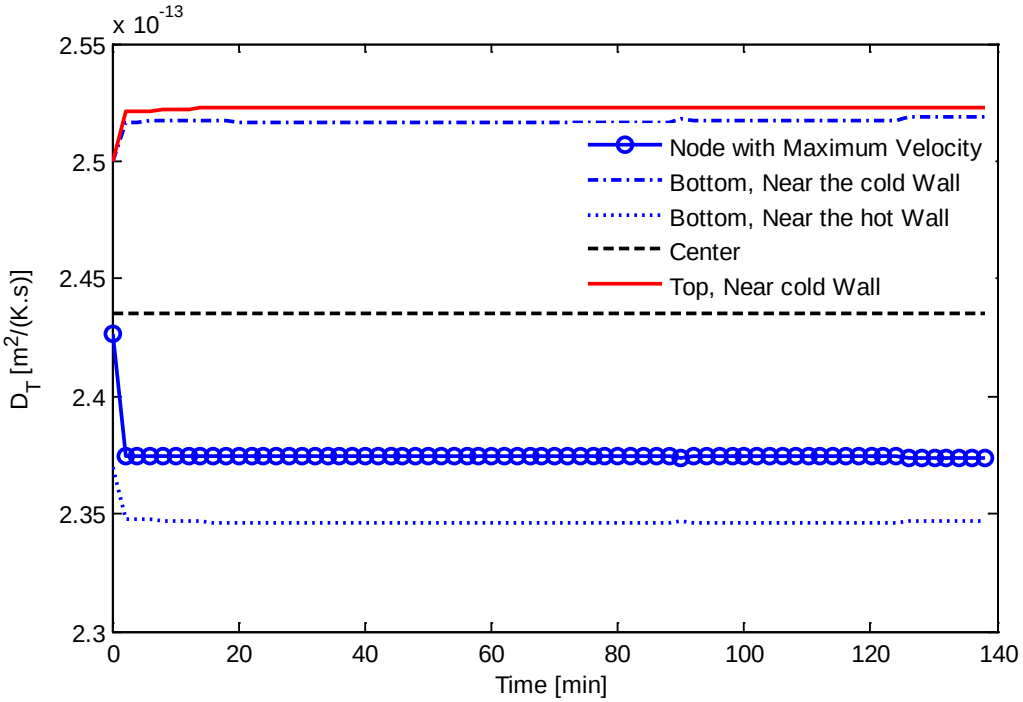

(b) ISS

Figure 4-24 Diffusion coefficients variation over time

4.4.4.1 Transient velocity

As expected, the velocity along the x-direction at the bottom near the cold wall, at the top near the hot wall and at the centre of the cavity was less than velocity at other nodes in the domains. While the interesting observation is that the component of the velocity at bottom near the hot wall is one order larger see Figure 4-25.

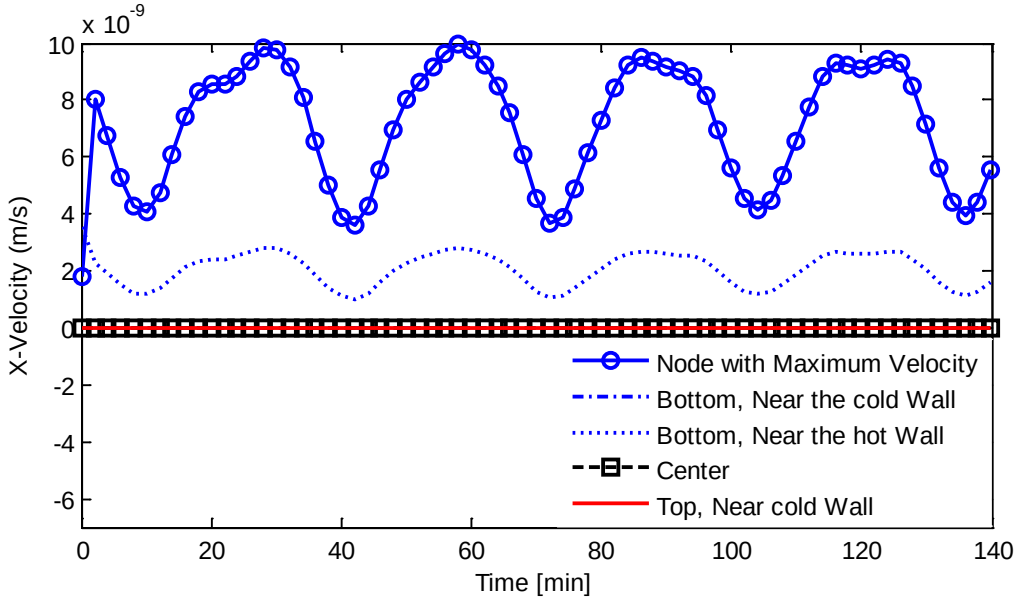

(a) FOTON-M3

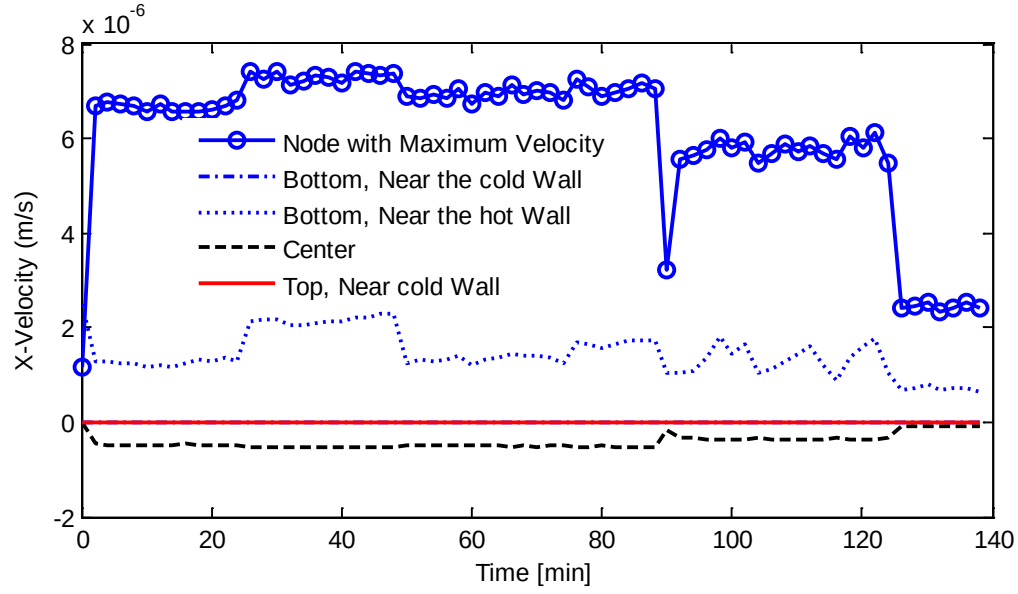

(b) ISS

Figure 4-25 x-velocity variation over time

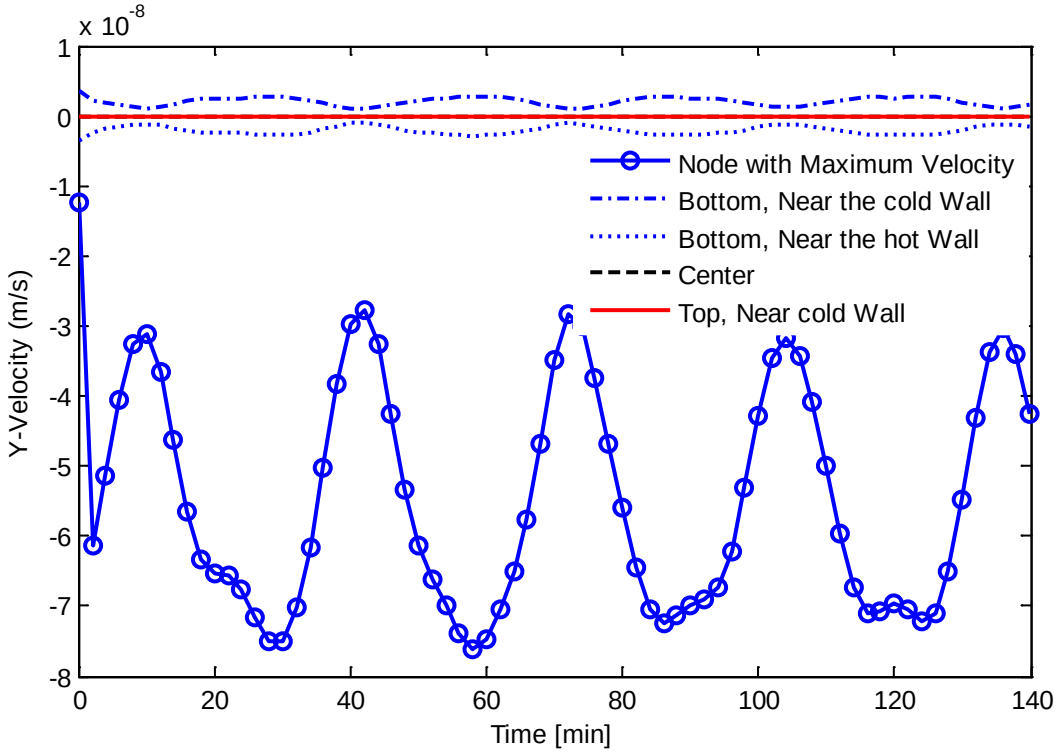

(a) FOTON-M3

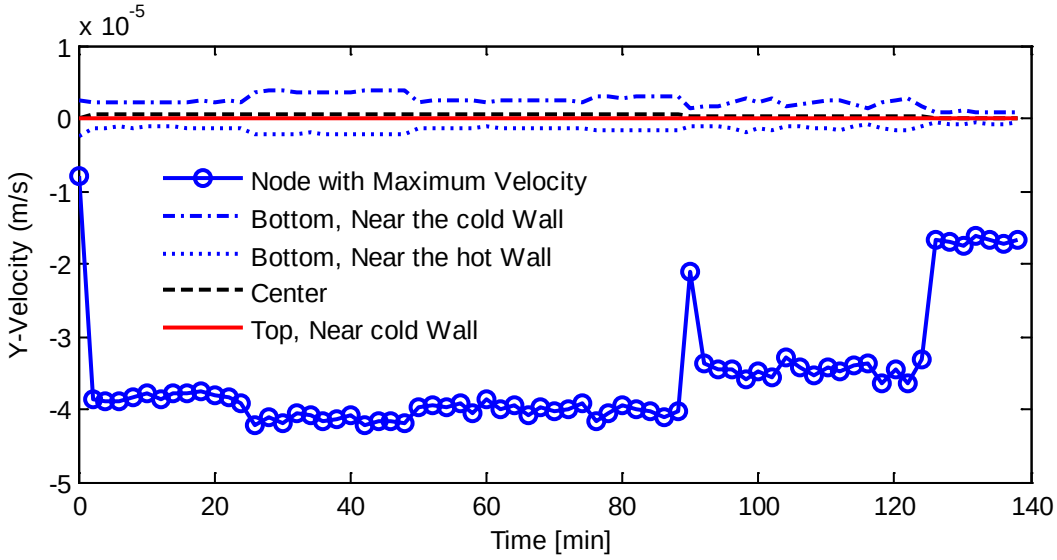

(b) ISS

Figure 4-26 x-velocity variation over time

It should be noted that velocity in all nodes has the same pattern with a different scale or opposite sign. For example, Figure 4-26 indicates the velocity at these locations along the y-

direction. As we can see in this figure, the node with maximum velocity has negative values; however, the trend and shape are the same as other nodes. In the next section we will have more discussion about this trend and pattern.

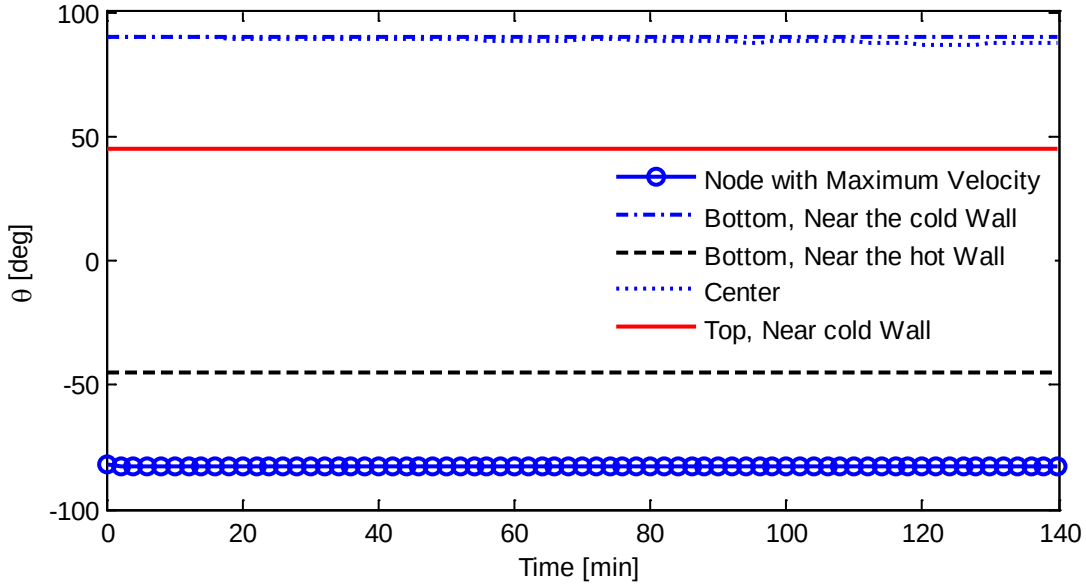

(a) FOTON-M3

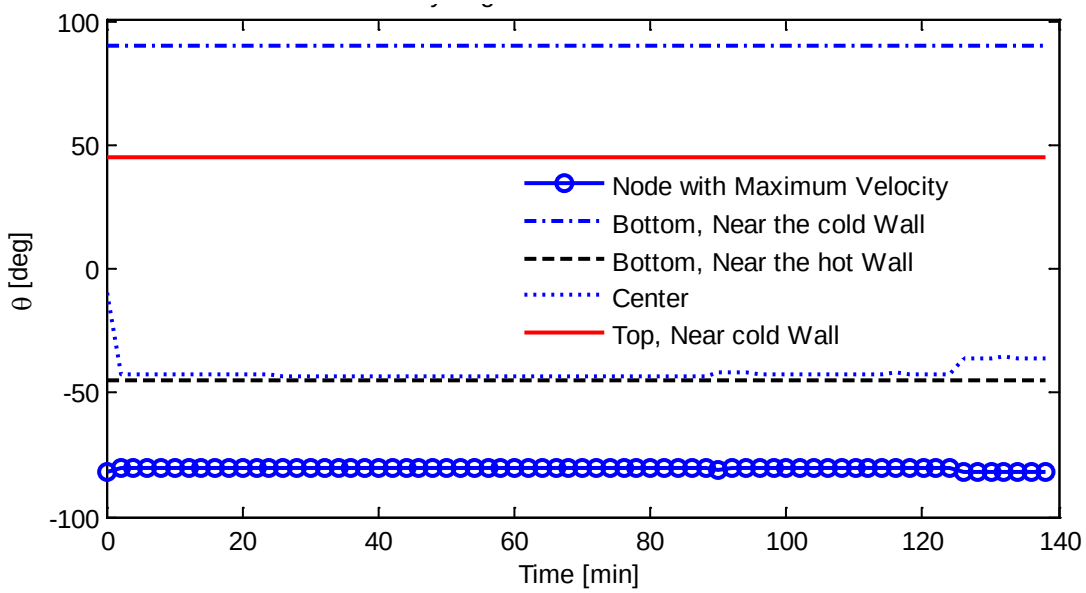

(b) ISS

Figure 4-27 velocity angle variation over time

Finally Figure 4-27 displays the angle of the velocity vector in the cavity. As expected, the curvature were symmetric while there were no big changes in these values over time except for the centre location that was sensitive to the vibration and shows small response to change of

vibration. The same result was seen for both cases in angle of velocity except for centre of the cavity that was 90 degrees for the FOTON case and -45 degrees for the ISS case.

Figure 4-28 shows the magnitude of the instantaneous velocities at five locations as well as average velocity in the cavity over time. As expected before, FOTON velocity has very small vibration values when compared to the accelerations that are experienced in a microgravity platform such as the ISS. This is because FOTON missions are commonly unmanned missions and do not have any activities of crew or disturbances such as external docking, that the ISS usually experiences.

As a result, it is normal to have small vibrations. As mentioned before, because of having no slip boundary condition near the walls, the velocity at those specific locations is smaller than the average velocity. In this figure, we can observe the importance of choosing the node with maximum velocity to investigate velocity in the cavity. Another interesting observation about the velocity field can be expressed as follows; the velocity near the hot wall is smaller than that near the cold wall. Moreover, the velocity at the centre of the cavity is at least two orders of magnitude smaller than the maximum velocity.

In addition to the different order of velocity, different trends and patterns are observed for the ISS and FOTON, which, if one compares them to their vibration acceleration, it is found that these shapes are quite similar to vibrational acceleration. Especially this observation is very clear for FOTON, which has smooth vibration trend.

Therefore, the acceleration along the x and y-directions and the induced velocity in the cavity over time were plotted in Figure 4-29, where the velocity field is considered from the node with maximum velocity in the domain. This figure could be one of the most important results of this study, and can open a new field of study in the thermodiffusion problem in the microgravity environment. it is obvious in this figure that the induced velocity in the cavity behaves quite similarly to its corresponding vibration that was applied in the system. This observation was seen by previous researchers. Therefore, we will avoid further investigation on these similarity which, based on our knowledge would required much investigation to achieve a complete result. Our goals in this study were to define some questions, find reasonable answers for them and, from these answers generate new questions and answers. We noted that the pattern of the velocity was similar to the pattern of its vibrational acceleration, based on this our first question was how

close is the similarity. Moreover, we attempted to find whether it was similar to vector summation of acceleration in both axis or like acceleration along either of the x or y direction. The next question is, what can we say about its frequency and shifted time on these two similar plots?

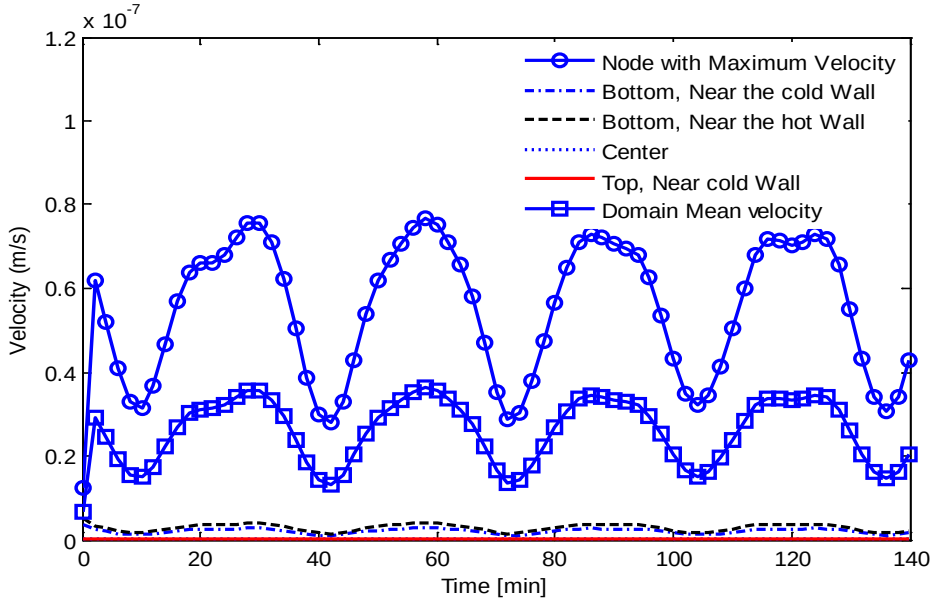

(a) FOTON-M3

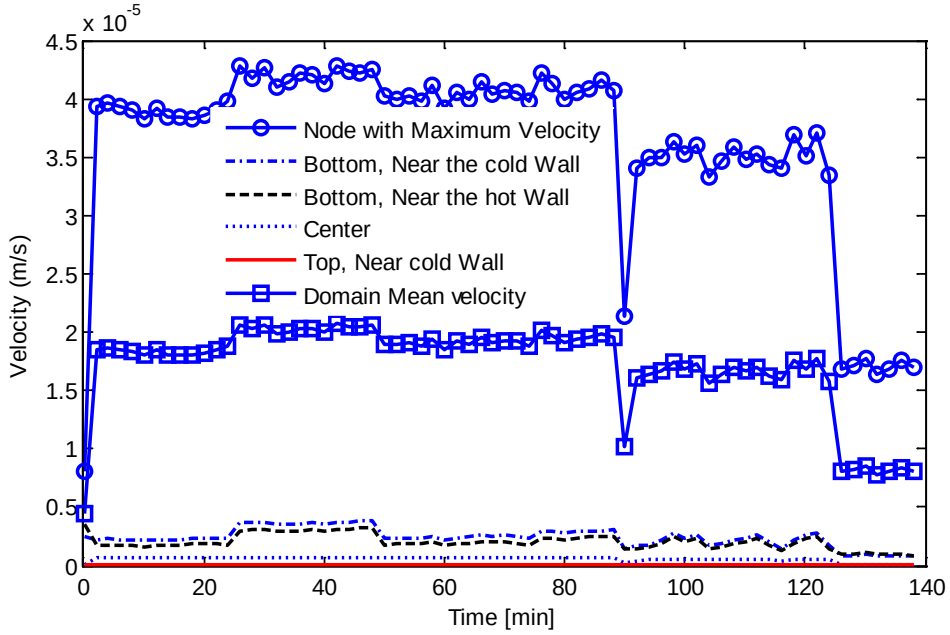

(b) ISS

Figure 4-28 velocity variation over time

To answer these questions, Figure 4-29 is used, of which part (a) shows the x and y directional acceleration as well as induced velocity for FOTON, and part (b) shows y-acceleration and induced velocity as a result of this vibration in the cavity over time for the ISS cases. Acceleration along both directions for ISS was similar, so we just used one of them in this discussion. If one compares x and y acceleration with induced velocity in the cavity over time, one will find this velocity field behaves like acceleration along the y-direction, not the x direction. Therefore, the first important result is that in microgravity environment, the pattern of induced velocity will be quite similar to the pattern of the acceleration along the perpendicular direction of the temperature gradient.

The same process was carried out to find any probable relation to vector summation of these two directional accelerations and the velocity field; however, this process proves again that the induced velocity in the system is close to the y vibrational acceleration, not any summation of other accelerations which were applied to the system.

The frequency of the velocity and its corresponding vibration are not quite the same; however, we can claim that, based on this figure the ratio between theirs frequencies as well as special amount of lead phase on remained constant. However, it requires more investigation and simulation time to determine the steady condition of this phase leading.

It should be noted that we observed the similarity between the induced velocity and vibrational acceleration, as a result of, finding the node with the maximum velocity in the domain as well as choosing the smallest possible time step, which according to our literature review are our contributions in this study.

The similarity between vibrational acceleration and the induced velocity for the ISS cases was more complex in comparison with the FOTON cases because of the high frequency of the ISS vibration. In addition, for ISS cases, some fluctuations exist over time, as a result of crew activity and turning on and off some apparatuses and the refrigerator on board ISS. Like the FOTON cases, the velocity pattern follows the pattern of the average acceleration field along the y-direction with a special shift. The results show that the phase difference between velocity and vibration field in the ISS case is greater than in the FOTON case because of different magnitudes of acceleration between ISS and FOTON. As mentioned before, the magnitude of acceleration for the ISS cases is at least hundred times greater than for FOTON. Consequently, a stronger

induced velocity in the domain of ISS occurred. When the acceleration was applied there was slight time delay between the acceleration and induced velocity in the cavity. As a result of this strong velocity field in the cavity for the ISS cases this slight time delay was greater than that for FOTON cases as shown in Figure 4-30.

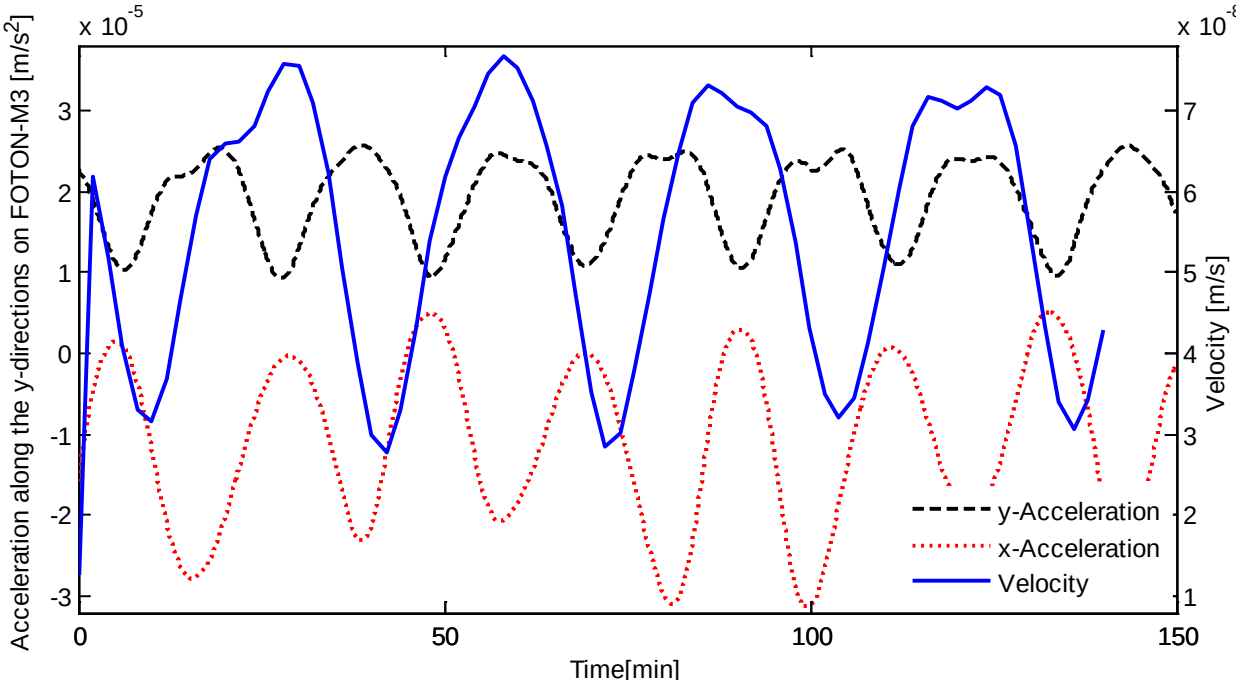

(a) FOTON-M3

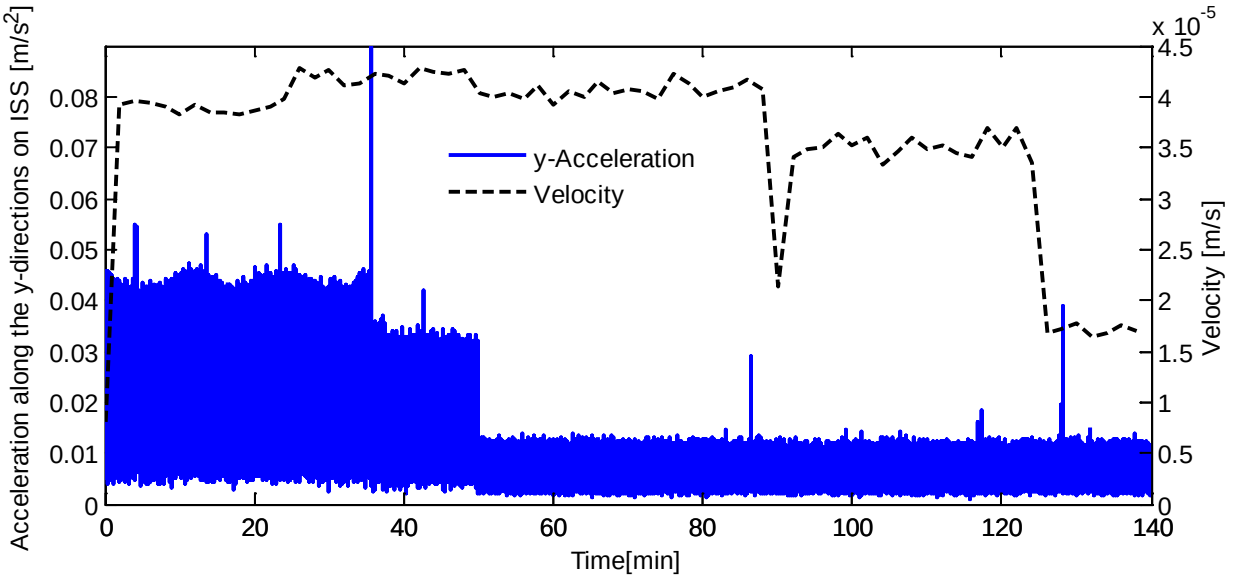

(b) ISS

Figure 4-29 Acceleration and induced velocity over time

Unlike the entire pattern of the acceleration field that is matched with the induced velocity, in Figure 4-29b, there is a jump of about ninety minutes after the beginning of the simulation which needs explanation based on the vibration profile because the reference vibrational acceleration corresponding to this sharp change con not be found in this figure. Thus, the entire vibration over time was searched again with higher resolution and size to find the reference for this behaviour. The result of this search showed the jump which is illustrated in Figure 4-30. This figure is blow-up of a section Figure 4-29b.

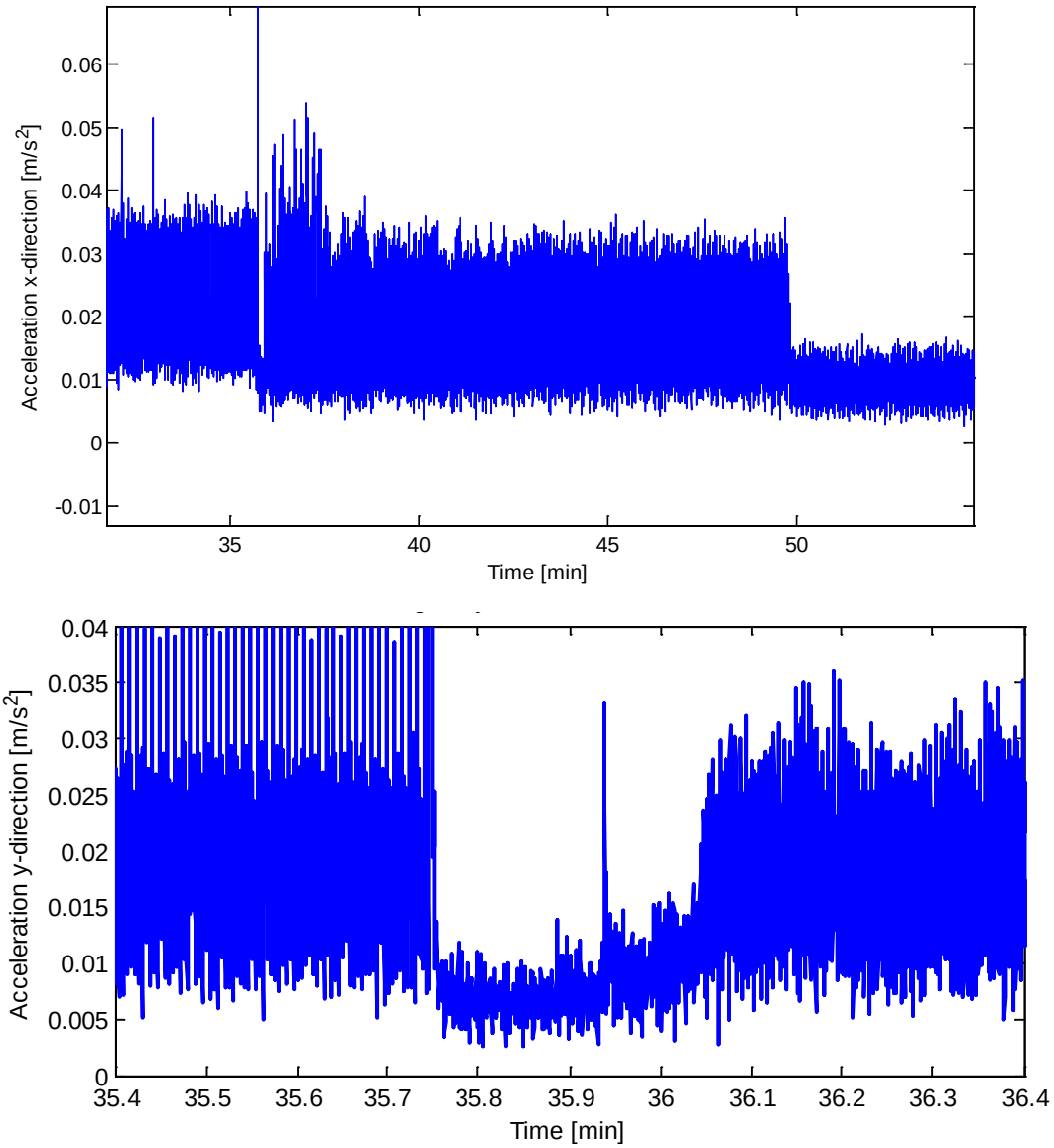

Figure 4-30 Vibrational acceleration between $t = 35.4 \, and \, 36.4$ [min] on board ISS

4.4.5 Cavity size effect

The size effect on convection in a square cavity and vertical and horizontal rectangle was numerically studied in this section. Zeng-Yuan Guo[**70**] discussed the relative importance of three control forces of free convection, inertial-force, viscous-force and buoyancy-force as well as the variations of the three control forces with Rayleigh number. Their results explain that the effect of viscous force compared to the inertial force on the convection increases with diminishing size. In this study three cavity sizes are considered; square cavity, one centimeter each side; rectangular cavity one centimeter by half; and another rectangular cavity, half centimeter by one.

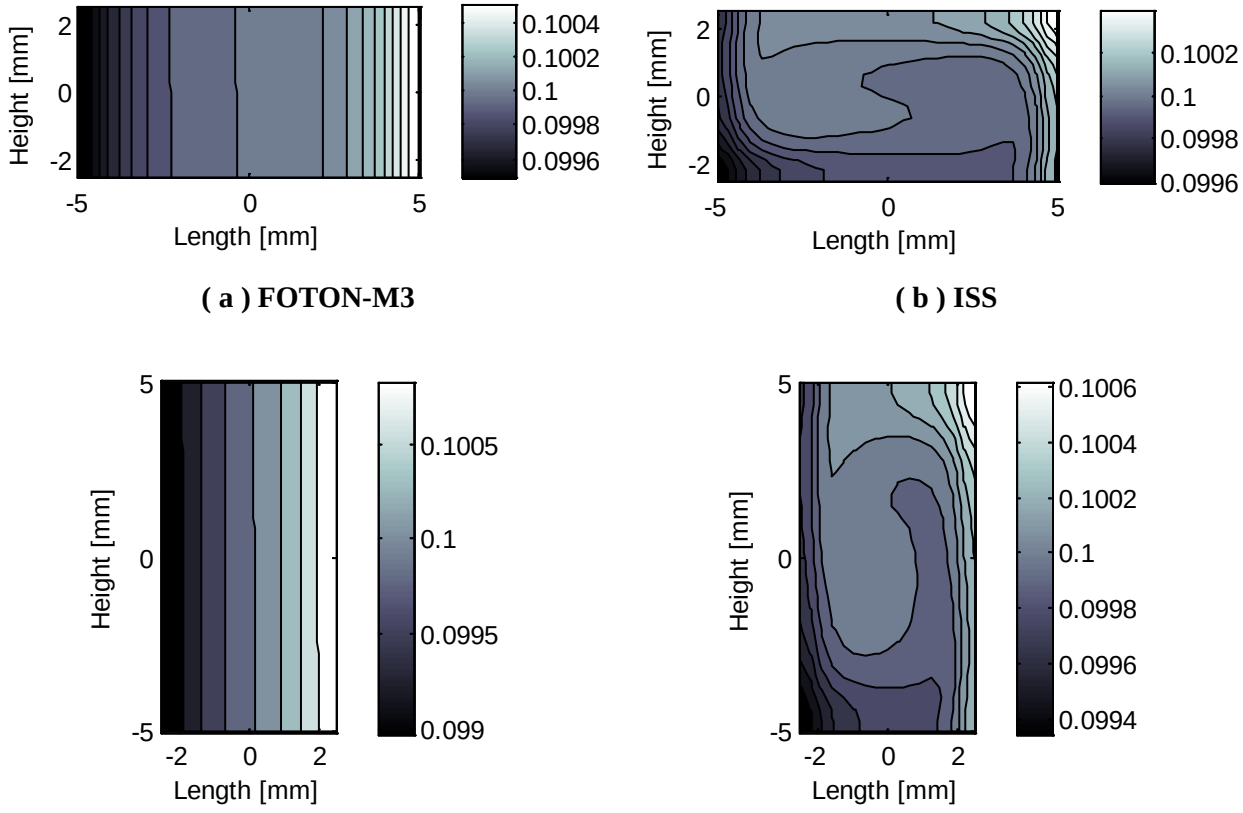

(a) FOTON-M3 **(b) ISS**

(c) FOTON-M3 **(d) ISS**

Figure 4-31 Isopropanol mass fraction distribution in the domain

Figure 4-31 shows the concentration counter for different cavity sizes on board ISS and FOTON. As in the last observation, the linear variation along the temperature gradient was seen for

FOTON cases; however, the variation of these concentrations for the vertical rectangle is a bit greater than for the horizontal one. The same observation can be seen for ISS cases, but the variation as a result of the strong convection cell is not linear. It was observed that by decreasing the length of the cavity, the temperature contour became more linear and more like the FOTON cases. In other words, again we can understand that the effect of thermal diffusion became more effective than the effect of convection when we compare the cavity with the same length and height with the horizontal cavity.

Figure 4-32 shows the temperature contour of different cavity sizes on board ISS and FOTON. It can be seen that by decreasing the length of the cavity, the temperature contour becomes more linear and like the FOTON cases. In other words, we can understand that the effect of thermal diffusion became more pronounced than the convection effect for the cavity with the same height and smaller length.

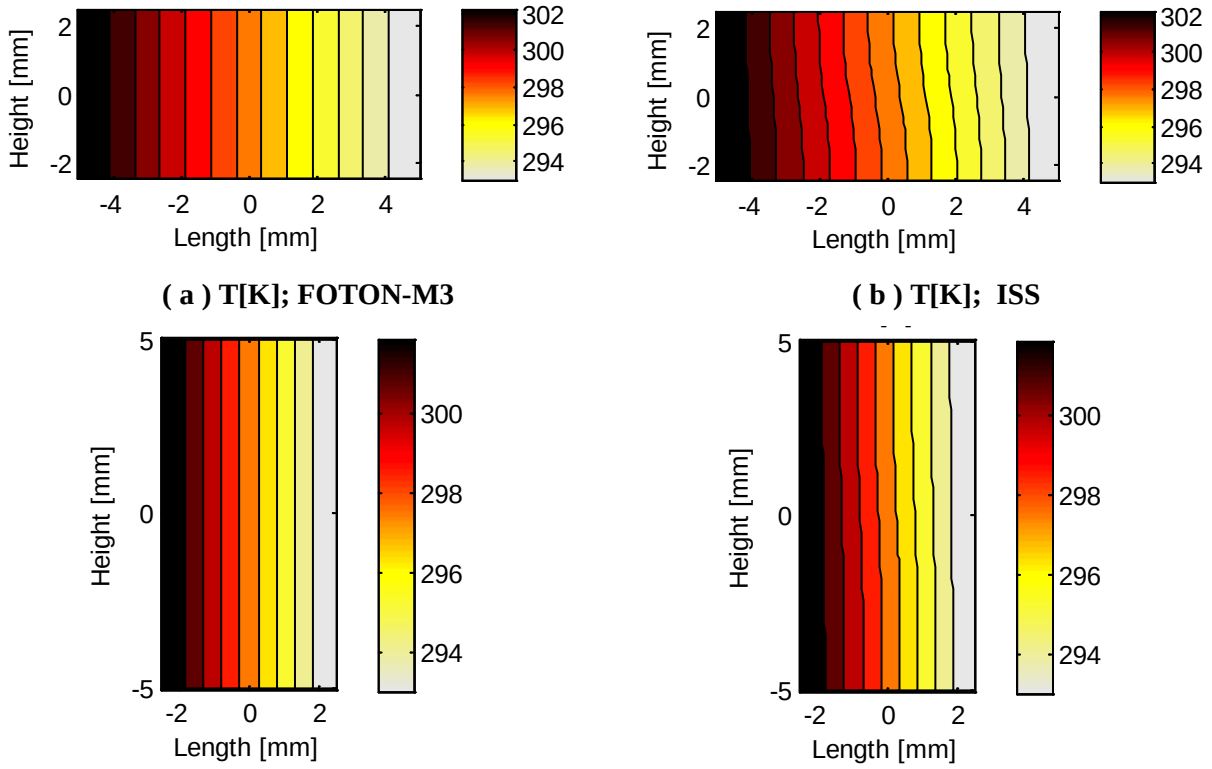

Figure 4-32 Temperature distribution in the cavity

To have better understanding of the cavity size effect, the concentration for three levels along the length of the cavity were plotted for both rectangular cavities in Figure 4-32, in which parts (a) and (c) show this parameter for the unmanned FOTON satellite with quite smooth vibration,

and parts (b) and (d) show that for ISS with a stronger microgravity environment. From comparison between parts (a) and (b), we can conclude that the mass fraction variation along the x-direction at the middle of the cavity is more linear for the cavity with the smaller length. In other words, the curvature line that occurs as a result of the single convection in the cavity could not be observed for the vertical rectangular cavity. It should be added that for both ISS and FOTON cases the stronger separation occurred for the cavity with the smaller distance between the hot and cold wall.

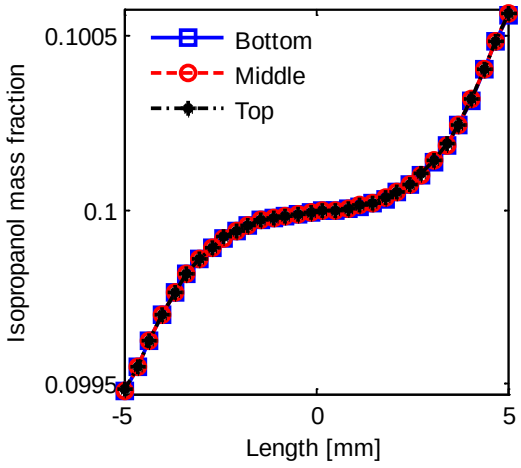

(a) FOTON-M3; L=1.0cm H=0.5cm

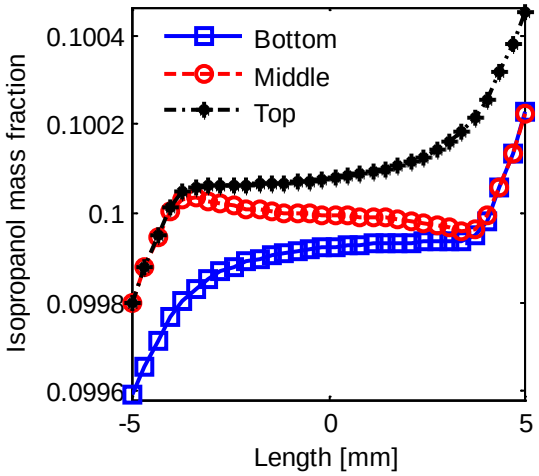

(b) ISS; L=1.0cm H=0.5cm

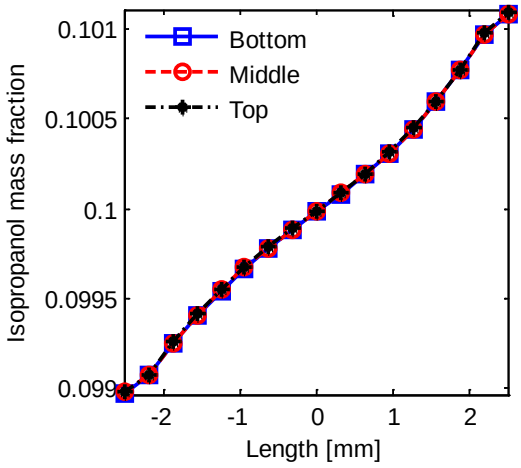

(e) FOTON-M3; L=0.5cm H=1.0cm

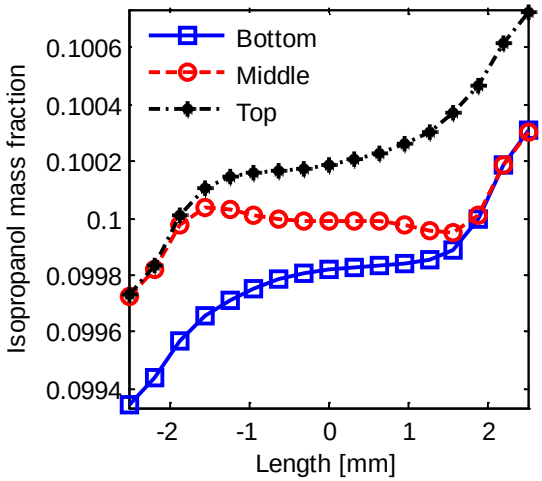

(f) ISS; L=0.5cm H=1.0cm

Figure 4-33 Isopropanol variation along x-direction for different cavity size

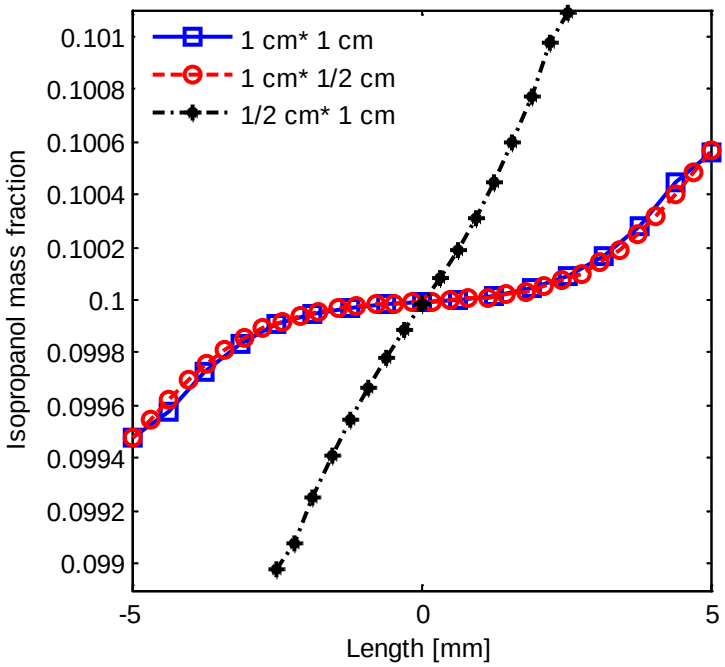

(a) FOTON-M3

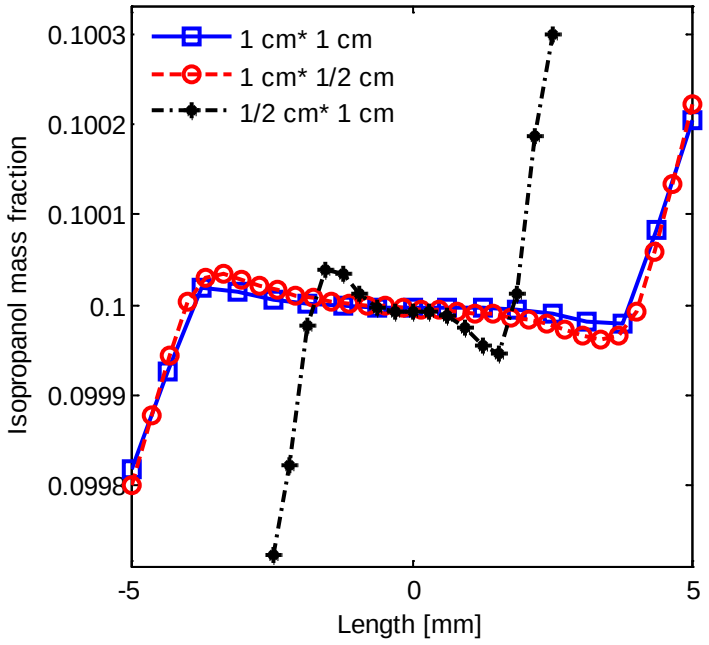

(b) ISS

Figure 4-34 Isopropanol variation along x-direction respect to different cavity size

Figure 4-33 shows isopropanol mass fraction along the direction of the temperature gradient at the middle of the cavity for FOTON and ISS respectively. It is clear that the pure diffusion effects in comparison with the convection effect became more important and even dominant with the size reduction along the direction of the temperature gradient. However, the concentration variations for the cases with the unique height are similar with very small difference. In conclusion, we can claim that for the isopropanol mixture the height of the cavity does not affect the results; however, by increasing the length of the cavity the separation becomes weaker and weaker.

4.4.6 Different initial concentration

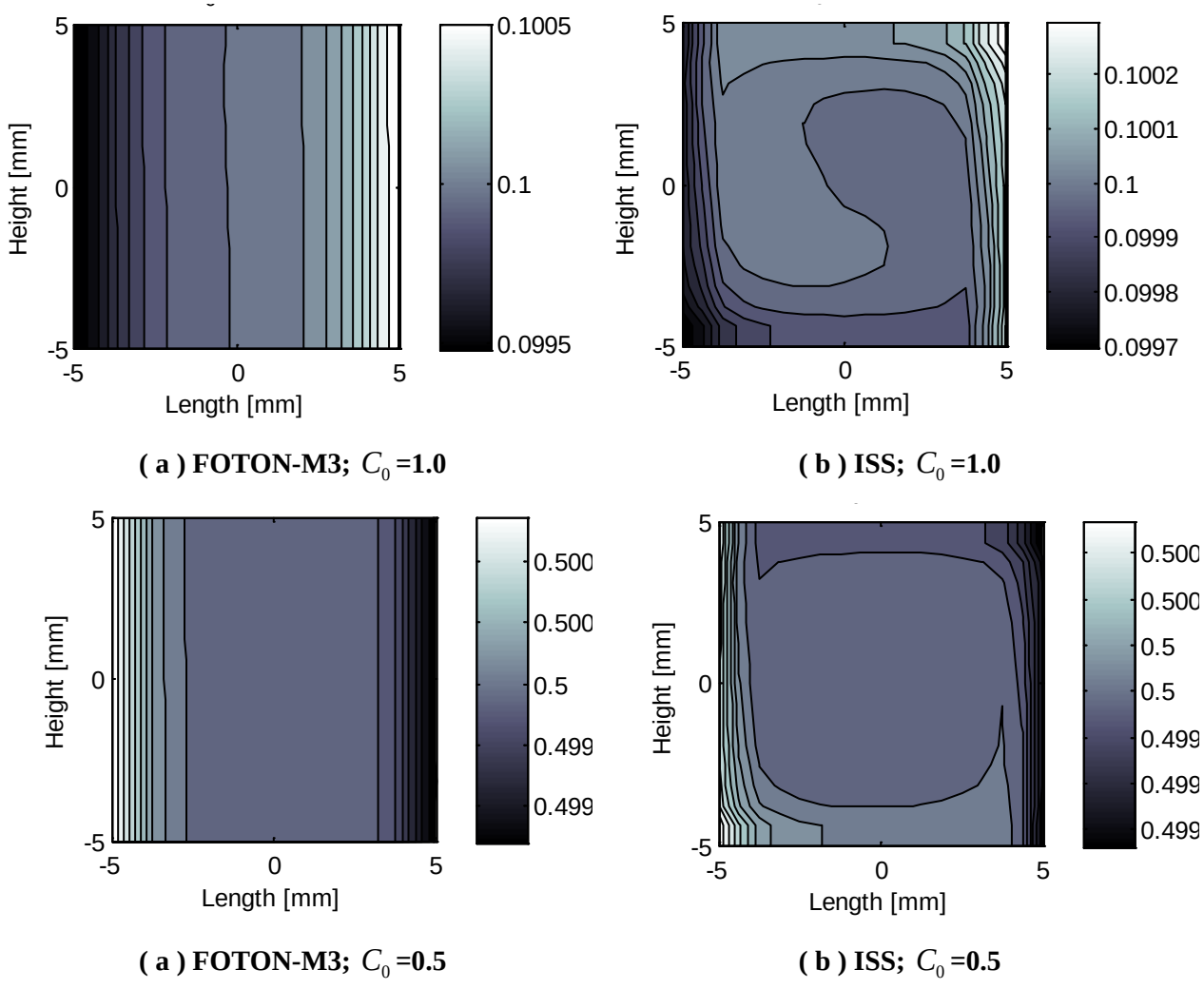

(a) FOTON-M3; C_0 =1.0

(b) ISS; C_0 =1.0

(a) FOTON-M3; C_0 =0.5

(b) ISS; C_0 =0.5

Figure 4-35 Isopropanol mass fraction respect to different initial concentration

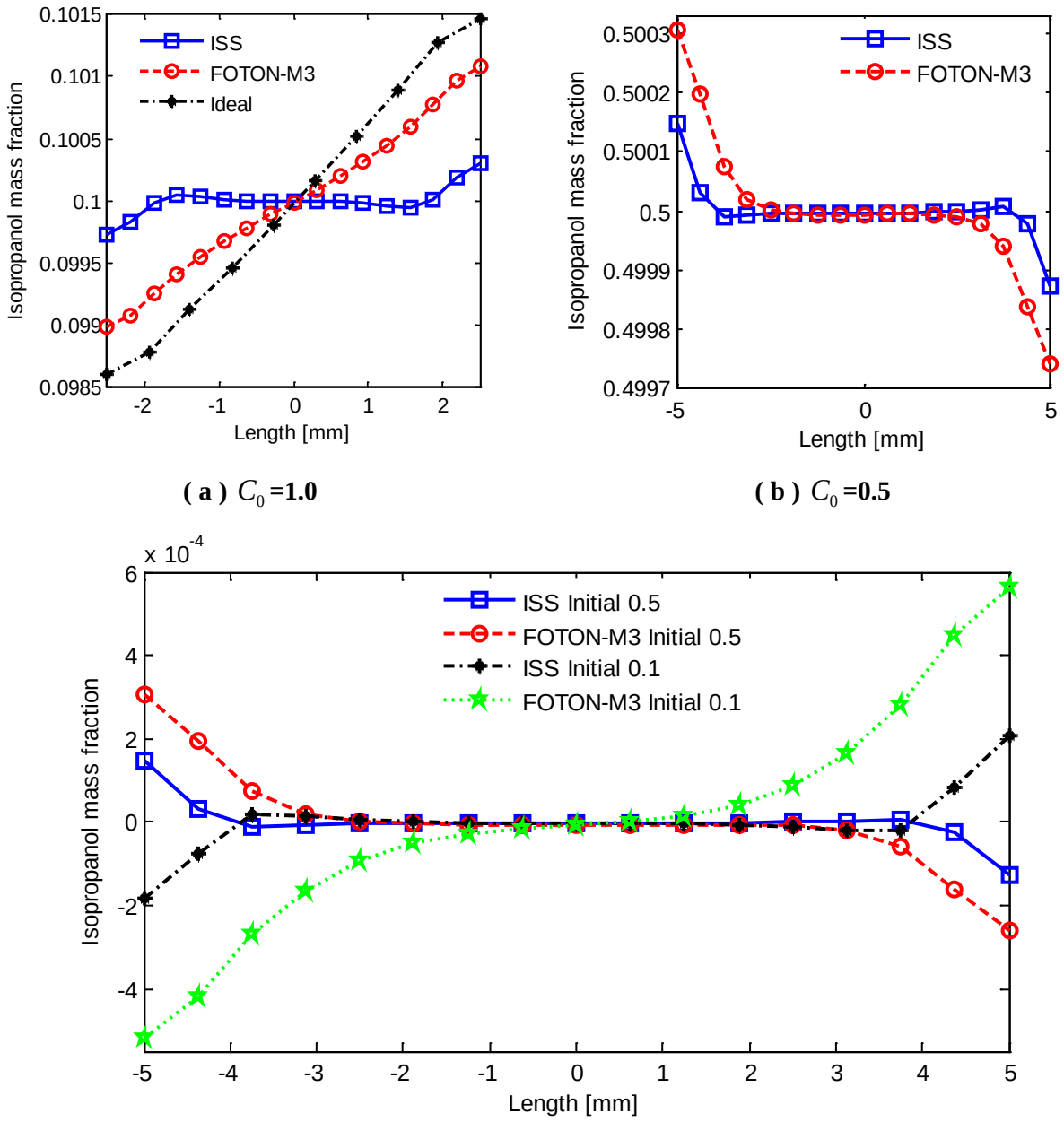

(a) C_0 =1.0

(b) C_0 =0.5

(c) Spatial separation along x direction

Figure 4-36 Isopropanol mass fraction and spatial separation for case 1,2,3,4 and 9

Mixtures five throw nine and mixtures one and two, the domination of water decreases and that of isopropanol increases near the hot wall according to Table 2. Thus, in these mixtures, water drives the thermodiffusion process. Likewise, in mixtures three and four, due to its high mole fraction, isopropanol is likely to dictate the thermodiffusion process. The weaker separation is attributed to the reduced molecular weight inequality that has been observed by Yan *et al* [**70**].

Another important point for comparison between these two different initial concentrations is different amounts of separation, which shows that when water drove the thermodiffusion process, the amount of separation was more than when isopropanol drove this process.

To have a clear understanding of the effect of the negative Soret sign, Figure 4-36 was used, in which part (a) shows the separation versus length of the cavity for positive Soret and part (b) shows this for negative Soret. It is obvious that the concentration gradient magnitude for the positive Soret effect is more than the negative one, see Figure 4-36.

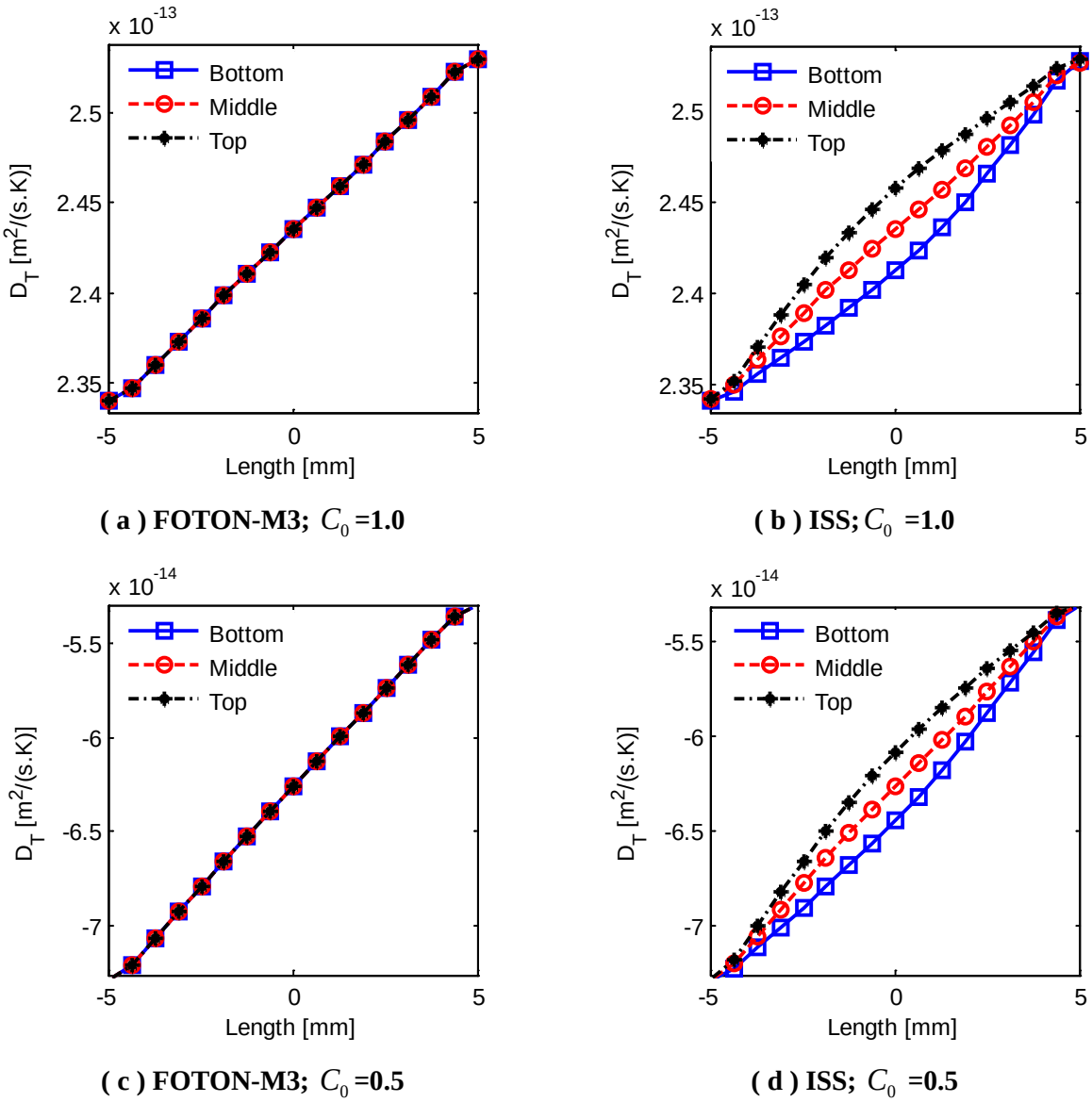

(a) FOTON-M3; C_0 **=1.0**

(b) ISS; C_0 **=1.0**

(c) FOTON-M3; C_0 **=0.5**

(d) ISS; C_0 **=0.5**

Figure 4-37 Thermodiffusion coefficients respect to different initial concentration

The magnitude of this gradient was used because, as a result of negative Soret effect, isopropanol was trapped near the hot wall unlike the cases with positive Soret effect. Consequently, this gradient is negative. Because of different initial concentrations in these two mixtures, it is impossible to compare them at the same scale of mass fraction. Consequently, we had to define a new term that is *concentration difference from its initial value*. In this way, we can plot both positive and negative Soret effect in the same diagram, which is illustrated in part (c). Now, we can make a clear judgment about different ratios of separation in different cases with different experiment environments and Soret signs.

Again the ISS cases have minimum separation along the different levels but are close to each other. For the unmanned FOTON satellite, there is a huge amount of separation for the case with positive and negative Soret coefficients.

This difference is explained as an unsteady condition for the case with negative Soret. In Figure 4-35, the contour illustrates the mixing at the centre of the cavity for both FOTON and ISS cases. This mixing was observed to be stronger for negative Soret diffusion so that there is almost no concentration gradient at the region close to the centre of the cavity.

The thermodiffusion coefficient of mixtures three and four are shown in Figure 4-37 parts (c) and (d), while Figure 4-37 parts (a) and (b) show this coefficient for cases one and two. For all cases, the thermodiffusion coefficient increased from the hot wall to the cold one; however, as mentioned before, for FOTON cases, as a result of pure diffusion, all lines coincided. And the only disagreement is the sign of this coefficient. The negative value of D_T indicates that in these mixtures water tends to moved towards the hot side. On the other hand, all other cases have a positive thermodiffusion coefficient. This change in the sign of D_T shows the movement toward the cold or hot side. Thus, the net result is a change in the direction of separation.

4.4.7 Comparison of FOTON result with Ideal case

In order to understand the contribution of such small velocity disturbances to the thermodiffusion process, simulations were repeated by suppressing these external vibrations. In other words, the mixtures were simulated in an ideal zero-gravity environment. Interestingly, the

results showed that although the variations for FOTON were almost insignificant, they affected the concentration at the final result of the experiments.

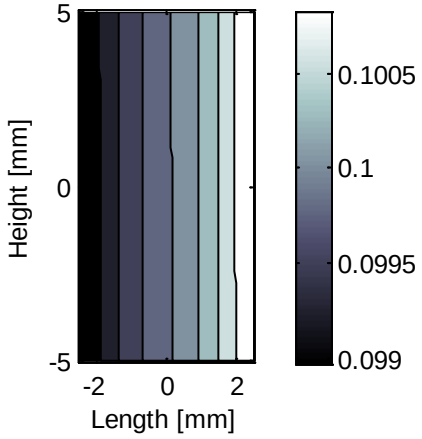

(a) FOTON-M3; Isopropanol mass fraction

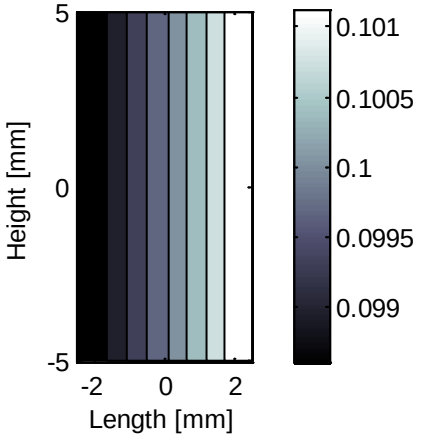

(b) Zero gravity; Isopropanol mass fraction

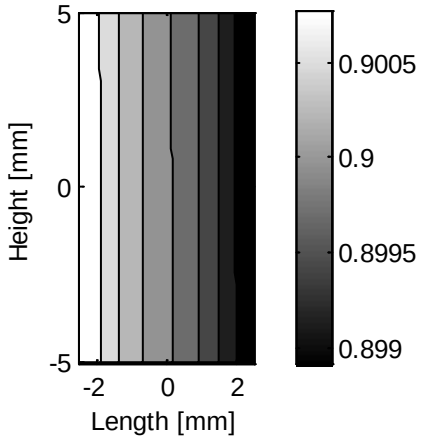

(a) FOTON-M3; Water mass fraction

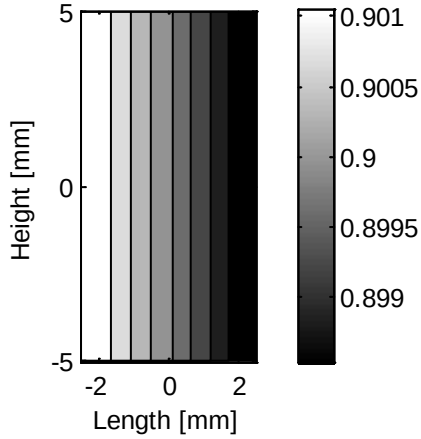

(b) Zero gravity; Water mass fraction

Figure 4-38 Isopropanol and water mass fraction for ideal case and FOTON-M3

Figure 4-38 shows the same pattern of isopropanol and water mass fraction distribution in the cavity; however, by more detection thought the cavity, we found that the separation ratio for the ideal case is greater than for the FOTON case, thus, it is clear that the separation in the ideal case is stronger than that in the ISS cases. To find out details about different amount of separation on board FOTON and in the ideal case, we can use Figure 4-39, which shows isopropanol variation along the x-direction with respect to the different environments.

Table 4-3 Numerical result to compare different cases

Case	Plat Form	Initial Isopropanol Mass Fraction	Maximum Concentration difference	Mass Fraction at half of the cavity near the hot wall	Maximum Concentration gradient per unit length [m^{-1}]
1	ISS	0.10	0.0005564	0.099962	0.038929
2	FOTON-M3	0.10	0.0010835	0.099804	0.108212
3	ISS	0.50	0.0003168	0.500025	-0.027383
4	FOTON-M3	0.50	0.0005655	0.500072	-0.056523
5	ISS	0.10	0.0008027	0.099961	0.042428
6	FOTON-M3	0.10	0.0010855	0.099836	0.108510
7	ISS	0.10	0.0012748	0.099912	0.115717
8	FOTON-M3	0.10	0.0021122	0.099449	0.421952
9	Ideal	0.10	0.0028723	0.099150	0.574476

Once more, this figure shows that although the separation and diffusion in the FOTON case is much stronger than in the ISS case, the separation is not as stronger as in the ideal case. In Table 4-3, three different approaches were used to define a numerical parameter which shows this difference numerically. The first approach was to find the nodes with the maximum and minimum mass fraction and to calculate their difference. The second at steady condition was to find the average concentration at half of the cavity near the hot wall; the last approach was to find the concentration gradient per unit at the centre of the cavity along a horizontal line. One can see that, for all cases, the value of the separation parameter for FOTON is greater than the corresponding value for the ISS case, see Table 4-3.

As mentioned before, the cases which have higher length assign lower value to separation. However, changing the height of the cavity does not affect the result very much. The minus sign for cases three and four means a negative Soret coefficient and unsteady condition; thus, the amount of the separation in these two cases is less than in any of the others. It should be noted that for this entire conclusion, we assumed a lateral thermal gradient.

The last major difference between FOTON and zero gravity or the ideal case was the pattern of their stream lines. As shown in Figure 4-40, there was one strong convection cell in the FOTON case; however, for the ideal case, we observed that there were four weaker convection cells in the cavity. We can claim that this difference occurs as a result of g-jitter vibration.

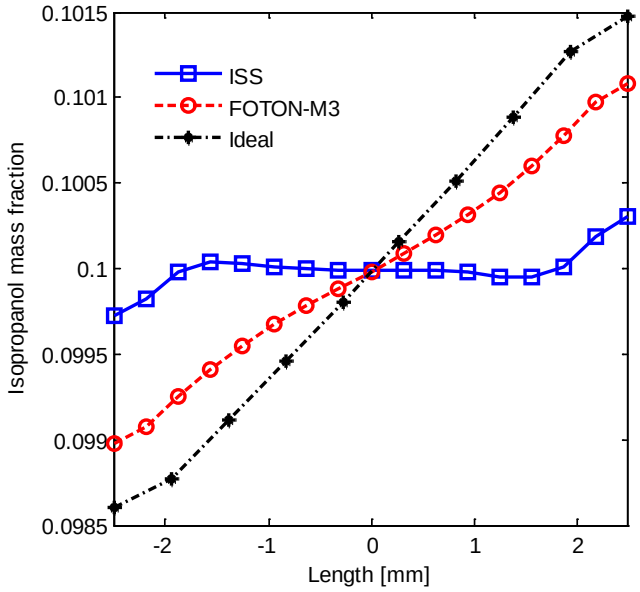

Figure 4-39 Isopropanol variation along x-direction respect to different environment

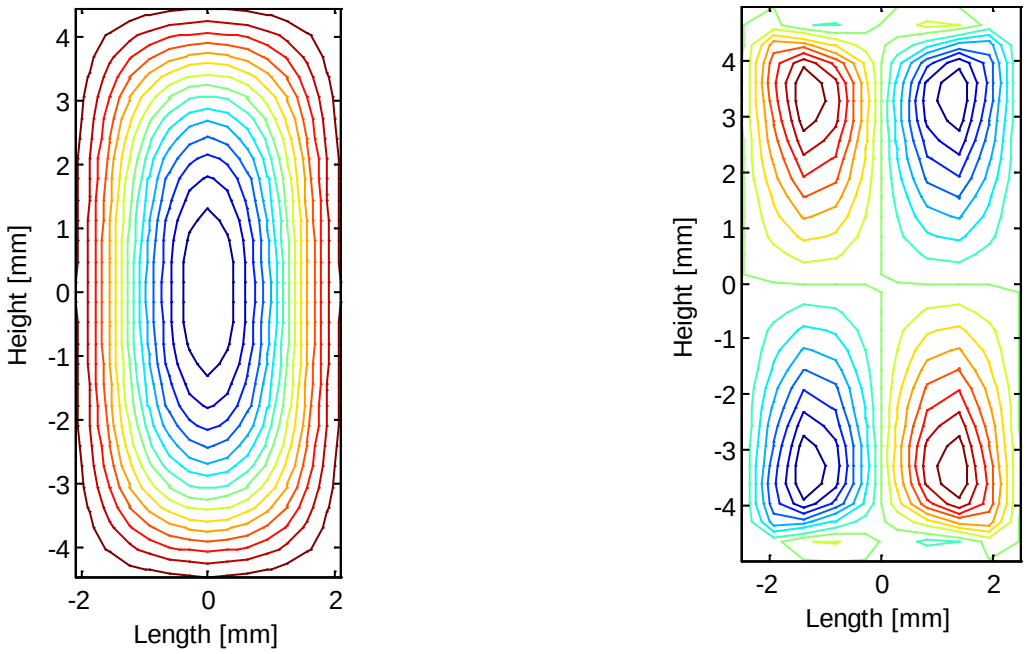

(a) FOTON-M3 **(b) Zero gravity**

Figure 4-40 Cavity stream

The following formula is used to calculate the percentage variation for FOTON and ISS in comparison with the zero-gravity condition.

$$E_{\phi} = \left| \frac{\phi_{Zero-gravity} - \phi_{micro-gravity}}{\phi_{Ideal\ Case}} \right| \times 100 \qquad (4\text{-}1)$$

where $\phi_{Zero-gravity}$ and $\phi_{micro-gravity}$ are the values of the parameter in a zero-gravity and micro-gravity environment, like FOTON or ISS, respectively. Table 4-4 shows these variations for ISS and FOTON-M3, if we assume these to be zero-gravity environments.

4.5 Conclusions

In summary, from our CFD results, it could be concluded that FOTON provides an environment that is conducive to conduct thermodiffusion investigations. In order to understand the behaviour of the mixtures during the course of the experiment, various quantities are examined at five specific locations in the domain, over a period of time. In addition, the mole fraction of the individual species, the temperature, the velocity, the thermodiffusion coefficients and density were studied at different horizontal and vertical levels in the cavity. The locations of nodes that were studied in the transient part are described as follows, Location 1, at the bottom and near the hot wall; Location 2, at the top and near the hot wall, Location 3, at the top and near the cold wall, and Location 4, at the centre of the cavity; and the last one, Location 5, which was the most important node to study, was defined as the node with the maximum velocity in the domain. The transient behaviors of the parameters at these locations are discussed. It must be noted that, based on previous studies of this mixture, the CFD modeling was performed until a time of 8500 seconds. By this time the quasi-steady state has been reached in most of the mixtures. The corresponding temperatures at these locations are given and discussed. As seen in these figures, the mole fraction of water begins to increase at the location near the hot wall for the mixtures with positive Soret effect. Isopropanol experiences a strong separation both for FOTON cases and for the cavities with the smaller length. However, the separation direction is opposite and weak for the mixtures with 0.5 isopropanol mass fraction as a result of negative Soret effect and the unsteady condition.

Table 4-4 Different variation by assuming these two space boards as zero gravity enticements

Case	7	8	9
Plat Form	ISS	FOTON-M3	Ideal
Maximum Concentration difference	0.0012748	0.0021122	0.0028723
Percentage Variation	55.6	26.4	%
Mean Mass Fraction, half of the cavity near the hot wall	0.099912	0.099449	0.421952
Separated Isopropanol, half of the cavity near the hot wall	0.000088	0.00055	0.00085
Percentage Variation	89.6	35.1	%
Maximum Concentration gradient per unit length $\left[m^{-1}\right]$	0.115717	0.421952	0.574476
Percentage Variation	79.8	26.55	%

In this low pressure binary mixture, we notice even higher variations for ISS cases; however, these variations are much smaller for FOTON cases, but it should be mentioned that all the variations are significant and greater than 25 percent. Thus, this kind of investigation should be considered for experiments on board space vehicles. The minimum and maximum variations are about 25 and 35 percent, for the FOTON satellite respectively; however, this variation for ISS is between 55 and 89 percent, which unlike the FOTON case is not negligible. More precisely, the ISS simulation under-predicts the separation of the components by approximately 80%.

However, most effort in this study was allocated to compare the two space vehicles for performing a fluid thermodiffusion experiment; the direct effect of the micro-gravity acceleration on the velocity field was studied. This is the most important parameter and destroys the smooth separation. The result shows that the velocity field is very sensitive to vibration, although the different phase and slightly different frequency between these two fields over time were considered. We think that to find out the exact relation between the velocity and acceleration patterns, more investigation is required; this will perhaps help to predict this result without the three-month-long CFD modeling process.

The other points that made this investigation more accurate than other studies in this field were considering all parameters to be variable over time and position in the cavity. Specifically, diffusion coefficients, density and viscosity were variable in this investigation so that the correctness of assumptions was proved by observing the significant difference of these parameters in the simulation results.

4.6 Future works

For further study, it would be valuable to analyze the thermodiffusion effect for the different cavity sizes, including different binary or turnery mixtures. As mentioned before, studying the effects of the vibration acceleration pattern on the transient induced velocity as well as defining the certain relation between microgravity vibration and induced velocity patterns would be important. And based on these results, predicting the induced velocity in the cavity without any CFD simulation can be a future works based on this study. By following this procedure, the effect of micro-gravity vibration on the mixture in the cavity can be found quickly; however, CFD simulation takes about two months to complete. Finally, a comparison between the numerical simulation result and experimental result, which is provided by Image Processing, can be a valuable future work based on this study.

Appendix

Appendix A: MATLAB code to generate ISS acceleration for main code

This MATLAB Code is developed to generate the RMS and average interval for interested step time;

```
clear
clc
close all

steptime=.1;
PlotTimeSecond=60*35;

TotalSecondInFile=600;
TotalFiles=4;
NumberPointPerSecond=500;
 g0=9.8023;
 NumberPointPerStep=floor(steptime*NumberPointPerSecond);
NumberOfNodeInPlot=PlotTimeSecond/steptime;
NumberPointPerFile=TotalSecondInFile/steptime;
for I=1:TotalFiles
    filename=sprintf('File (%d).es08',I);
    fid = fopen(filename);
    [A b] = fread(fid,'float32');
```

```
time=zeros(b/4,1);

Xacc=zeros(b/4,1);

Yacc=zeros(b/4,1);

Zacc=zeros(b/4,1);

xacc=zeros(b/4,1);

yacc=zeros(b/4,1);

zacc=zeros(b/4,1);


sumX=0;

sumY=0;

sumZ=0;


for i=1:b/4

   time(i)=A(4*i-3);

   xacc(i)=A(4*i-2);

   sumX=sumX+xacc(i);

   yacc(i)=A(4*i-1);

   sumY=sumY+yacc(i);

   zacc(i)=A(4*i-0);

   sumZ=sumZ+zacc(i);

end


meanX=sumX/(b/4);
```

```
meanY=sumY/(b/4);
meanZ=sumZ/(b/4);

for i=1:b/4
    Xacc(i)=(xacc(i)-meanX)*g0;
    Yacc(i)=(yacc(i)-meanY)*g0;
    Zacc(i)=(zacc(i)-meanZ)*g0;
end

counter=1;

for i=1:floor(TotalSecondInFile/steptime)
    Time(i)=steptime*(i-1);
    mX=0;
    mY=0;
    mZ=0;
    rmsX=0;
    rmsY=0;
    rmsZ=0;
    for j=1:NumberPointPerStep
        mX=mX+Xacc(j+(i-1)*NumberPointPerStep);
        mY=mY+Yacc(j+(i-1)*NumberPointPerStep);
        mZ=mZ+Zacc(j+(i-1)*NumberPointPerStep);
        rmsX=rmsX+(Xacc(j+(i-1)*NumberPointPerStep))^2;
```

```
        rmsY=rmsY+Yacc(j+(i-1)*NumberPointPerStep)^2;
        rmsZ=rmsZ+Zacc(j+(i-1)*NumberPointPerStep)^2;
    end
     MXacc(i)=mX/NumberPointPerStep;
    MYacc(i)=mY/NumberPointPerStep;
    MZacc(i)=mZ/NumberPointPerStep;

    RMSXacc(i)=(rmsX/NumberPointPerStep)^.5;
    RMSYacc(i)=(rmsY/NumberPointPerStep)^.5;
    RMSZacc(i)=(rmsZ/NumberPointPerStep)^.5;
     counter=counter+1;
    TotalTime((I-1)*NumberPointPerFile+i)=Time(i)+(I-1)*TotalSecondInFile;

    XacM((I-1)*NumberPointPerFile+i)=MXacc(i);
    YacM((I-1)*NumberPointPerFile+i)=MYacc(i);
    ZacM((I-1)*NumberPointPerFile+i)=MZacc(i);

    XacRMS((I-1)*NumberPointPerFile+i)=RMSXacc(i);
    YacRMS((I-1)*NumberPointPerFile+i)=RMSYacc(i);
    ZacRMS((I-1)*NumberPointPerFile+i)=RMSZacc(i);
  end

%    hold on
%
```

```
    %
plot(time(1:(NumberPointPerSecond*PlotTimeSecond)),Yacc(1:(NumberPointPerSecond*PlotT
imeSecond)));
    %     plot(Time(1:(NumberOfNodeInPlot)),MYacc(1:(NumberOfNodeInPlot)),'c');
    %     plot(Time(1:(NumberOfNodeInPlot)),RMSYacc(1:(NumberOfNodeInPlot)),'m');
    %
    %     xlabel('Acceleration');ylabel('Time(sec)');
    %     legend('real vib','mean','RMS');grid on;

    end
     hold on

    plot(TotalTime(1:(NumberOfNodeInPlot)),YacM(1:(NumberOfNodeInPlot)),'c');
    plot(TotalTime(1:(NumberOfNodeInPlot)),YacRMS(1:(NumberOfNodeInPlot)),'m');

    xlabel('Time(sec)');ylabel('Acceleration');
    legend('mean','RMS');grid on;

    XacRMS=XacRMS';
    YacRMS=YacRMS';
    ZacRMS=ZacRMS';
    XacM=XacM';
    YacM=YacM';
    ZacM=ZacM';
```

```
TotalTime=TotalTime';
VibTime1M3RMS3for2over100sec=[TotalTime,XacM,YacM,ZacM,XacRMS,YacRMS,Zac
RMS];
```

Appendix B: MATLAB code to generate FOTON acceleration for main code

B.1 Curve fitting

Curve fitting is a helpful instrument for representing a data set in a linear or quadratic fashion. MATLAB has two functions, polyfit and polyval, which can quickly and easily fit a polynomial to a set of data points. A first order polynomial is the linear equation that best fits the data. A polynomial can also be used to fit the data in a quadratic sense. As a reminder, the general formula for a polynomial is:

$$f(x) = a_0 x^N + a_1 x^{N-1} + a_2 x^{N-2} + \ldots + a_{N-1} x + a_N \quad (0\text{-}1)$$

The degree of a polynomial is equal to the largest value of the exponents of the independent variable, x.

B.2 Polyfit and Polyval

"Polyfit" is a MATLAB function that computes a least squares polynomial for a given set of data. Polyfit generates the coefficients of the polynomial which can be used to simulate a curve to fit the data, according to the degree specified. A second function, Polyval, evaluates a polynomial for a given set of x values. So, polyval basically generates a curve to fit the data based on the coefficients found using polyfit.

MATLAB's explanations of polyfit and polyval are:

POLYFIT(x,y,n) finds the coefficients of a polynomial p(x) of degree n that fits the data, p(x(i)) is approximately equal to y(i), in a least-squares sense.

POLYVAL(V,s), If V is a vector whose elements are the coefficients of a polynomial, then POLYVAL(V,s) is the value of the polynomial evaluated at s. If s is a matrix or vector, the polynomial is evaluated at all points in s.

B.3 MATLAB code

```
clear
clc
close all
rawdata=[-15.7520000000000,-1.21000000000000,22.7460000000000;-12.4870000000000,-…..
2.51200000000000,21.3760000000000];
rawdata=rawdata'*10^-6;
li=rawdata; %Linear Interpolation
nst=300; %Number of Step Time
rdst=30.6; %Raw Data Step Time
fst=rdst/(30.6*100); %Favorite Step Time
fitstep=5;
totaltime=rdst*max(size(rawdata));
time=0:rdst:totaltime;
 for i=1:nst/fitstep
    px = polyfit(time(1,(i-1)*(fitstep)+1:(i)*(fitstep)+1),rawdata(1,(i-1)*(fitstep)+1:...
      (i)*(fitstep)+1),fitstep);
   newtime=(i-1)*fitstep*rdst:fst:i*fitstep*rdst;
   yfitx = polyval(px,newtime);
    py = polyfit(time(1,(i-1)*(fitstep)+1:(i)*(fitstep)+1),rawdata(2,(i-1)*(fitstep)+1:...
      (i)*(fitstep)+1),fitstep);
   yfity = polyval(py,newtime);
      pz = polyfit(time(1,(i-1)*(fitstep)+1:(i)*(fitstep)+1),rawdata(3,(i-1)*(fitstep)+1:...
      (i)*(fitstep)+1),fitstep);
   yfitz = polyval(pz,newtime);
     Time(1,((i-1)*fitstep*rdst/fst)+1:(i)*fitstep*rdst/fst)=newtime(1,1:fitstep*rdst/fst);
   favdatax(1,((i-1)*fitstep*rdst/fst)+1:(i)*fitstep*rdst/fst)=yfitx(1,1:fitstep*rdst/fst);
   favdatay(1,((i-1)*fitstep*rdst/fst)+1:(i)*fitstep*rdst/fst)=yfity(1,1:fitstep*rdst/fst);
   favdataz(1,((i-1)*fitstep*rdst/fst)+1:(i)*fitstep*rdst/fst)=yfitz(1,1:fitstep*rdst/fst);
end
```

```
FotonVib=[favdatax;favdatay;favdataz]';
 figure (1)
hold on
% plot(Time,favdatax,'--r','LineWidth',2);
plot(time(1,1:nst),li(1,1:nst),'-bs','LineWidth',2,...
                'MarkerEdgeColor','k',...
                'MarkerFaceColor','g',...
                'MarkerSize',3);
xlabel('Time(sec)');ylabel('Acceleration Y');
% legend('Fit','Linear Interpolation');grid on;
figure (2)
hold on
% plot(Time,favdatay,'--r','LineWidth',2);
plot(time(1,1:nst),li(2,1:nst),'-bs','LineWidth',2,...
                'MarkerEdgeColor','k',...
                'MarkerFaceColor','g',...
                'MarkerSize',3);

xlabel('Time(sec)');ylabel('Acceleration Y');
% legend('Fit','Linear Interpolation');grid on;
figure (3)
hold on
plot(Time,favdataz,'--r','LineWidth',2);
plot(time(1,1:nst),li(3,1:nst),'-bs','LineWidth',2,...
                'MarkerEdgeColor','k',...
                'MarkerFaceColor','g',...
                'MarkerSize',3);

xlabel('Time(sec)');ylabel('Acceleration Z');
legend('Fit','Linear Interpolation');grid on;
```

Appendix C Main code structure

This CFD model was developed in FORTRAN based on the Firoozabadi model [redskjfggsdkf]. In this package of software, there are several source and input files. Figure B-1 in Appendix C shows the flowchart of these subroutines. Brief descriptions of these subroutines follow,

Main_show.f

This is the control program. It sets up all variables and data blocks, and calls all other subroutines to conduct the calculation.

data.in

This file includes the initial condition of the mixture such as initial concentration, hot or cold temperature as well as control data.

init.f

This is the subroutine to set the initial condition for a new run based on previous results. This is the subroutine to do coordinate calculation based on a given discretization scheme for a given rectangular domain.

grid_param.in

This file provides the mesh resolution for creating the numerical discretization, so it defines the two-dimensional domain and performs discretization of the domain.

gexp_rms.in

This file provides the vibration data for the main code to apply the real acceleration on the board FOTON or ISS, to have accurate numerical simulation;

coefficients.f

This is the subroutine to calculate all three diffusion coefficients, based on given temperature, pressure and compositions in a mixture.

pcsaft_eos.f

This is the subroutine to calculate density of the mixture at each node, based on given pure properties of the mixture component and using the PC-SAFT equation of state.

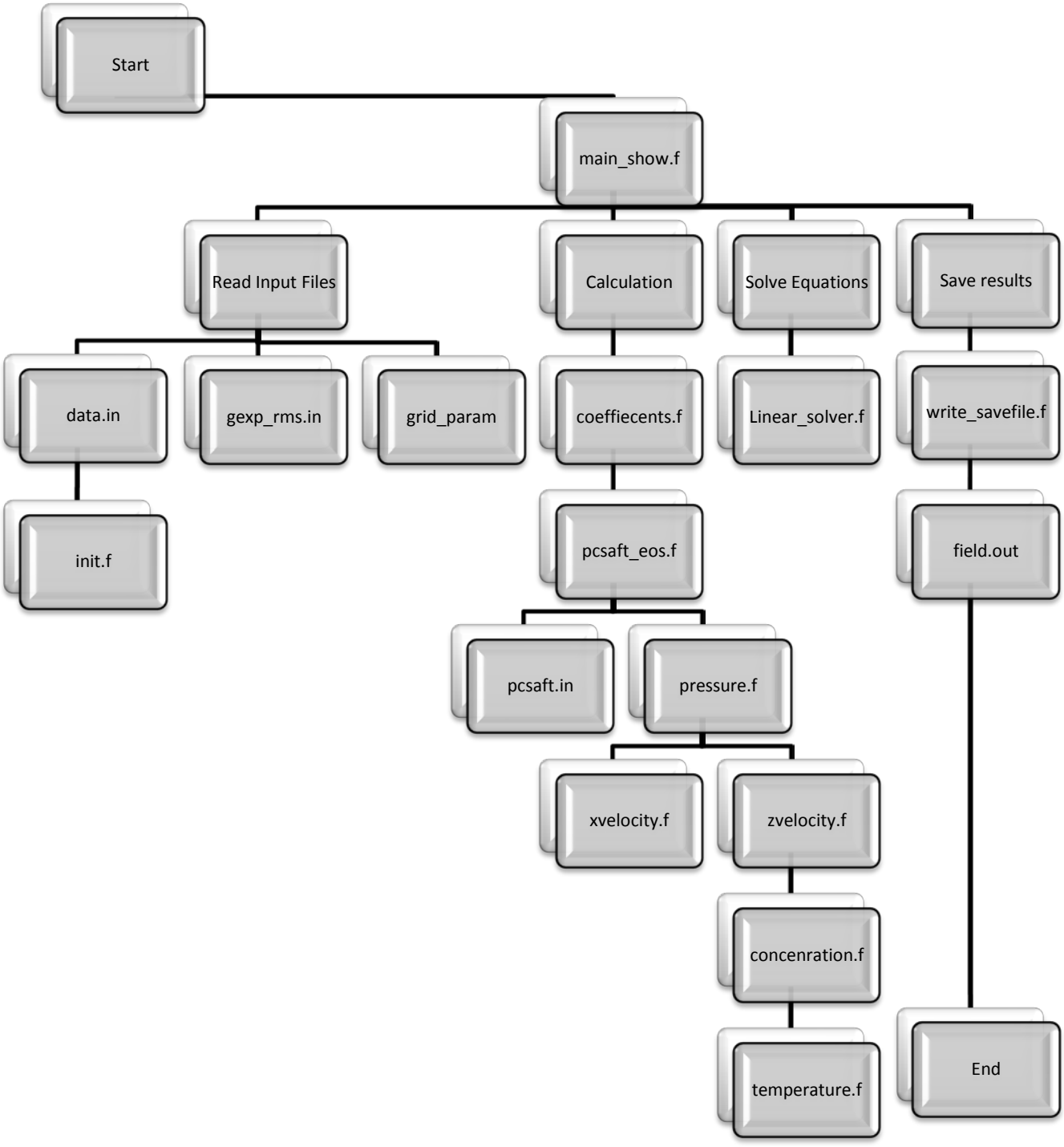

Figure 0-1 Flowchart of FORTRAN code

Appendix D: MATLAB code to show quasi-steady result, plots and diagrams

```
clear
close all
clc
position1=[300,300,310,240];
position2=[300,300,320,270];
position3=[300,300,650,500];
border1=[-2.2,-2.2,14,8];
border2=[-.3,-2.2,-2.7,8];
border3=[-2.5,-2.2,24,8];
aa=.997;
bb=1.003;
filename = sprintf('r115sM');
load(filename);
   S_T=DT./D;

   xvel1 = smooth(xpos*1000,xvelocity(2,:),0.2,'loess');
   xvel2 = smooth(xpos*1000,xvelocity(round(ynode/2),:),0.2,'loess');
   xvel3 = smooth(xpos*1000,xvelocity((ynode-1),:),0.2,'loess');
   minxvel=min([min(xvel1),min(xvel2),min(xvel3)]);
   maxxvel=max([max(xvel1),max(xvel2),max(xvel3)]);

   yvel1 = smooth(xpos*1000,yvelocity(2,:),0.2,'loess');
   yvel2 = smooth(xpos*1000,yvelocity(round(ynode/2),:),0.2,'loess');
   yvel3 = smooth(xpos*1000,yvelocity((ynode-1),:),0.2,'loess');
   minyvel=min([min(yvel1),min(yvel2),min(yvel3)]);
   maxyvel=max([max(yvel1),max(yvel2),max(yvel3)]);

   cc1 = smooth(xpos*1000,massfrac1(2,:),0.2,'loess');
   cc2 = smooth(xpos*1000,massfrac1(round(ynode/2),:),0.2,'loess');
   cc3 = smooth(xpos*1000,massfrac1((ynode-1),:),0.2,'loess');
```

```
mincc=min([min(cc1),min(cc2),min(cc3)]);
maxcc=max([max(cc1),max(cc2),max(cc3)]);

cw1 = smooth(xpos*1000,massfrac2(2,:),0.2,'loess');
cw2 = smooth(xpos*1000,massfrac2(round(ynode/2),:),0.2,'loess');
cw3 = smooth(xpos*1000,massfrac2((ynode-1),:),0.2,'loess');
mincw=min([min(cw1),min(cw2),min(cw3)]);
maxcw=max([max(cw1),max(cw2),max(cw3)]);

TT1 = smooth(xpos*1000,T(2,:),0.2,'loess');
TT2 = smooth(xpos*1000,T(round(ynode/2),:),0.2,'loess');
TT3 = smooth(xpos*1000,T((ynode-1),:),0.2,'loess');
minTT=min([min(TT1),min(TT2),min(TT3)]);
maxTT=max([max(TT1),max(TT2),max(TT3)]);

D1 = smooth(xpos*1000,D(2,:),0.2,'loess');
D2 = smooth(xpos*1000,D(round(ynode/2),:),0.2,'loess');
D3 = smooth(xpos*1000,D((ynode-1),:),0.2,'loess');
minD=min([min(D1),min(D2),min(D3)]);
maxD=max([max(D1),max(D2),max(D3)]);


DT1 = smooth(xpos*1000,DT(2,:),0.2,'loess');
DT2 = smooth(xpos*1000,DT(round(ynode/2),:),0.2,'loess');
DT3 = smooth(xpos*1000,DT((ynode-1),:),0.2,'loess');
minDT=min([min(DT1),min(DT2),min(DT3)]);
maxDT=max([max(DT1),max(DT2),max(DT3)]);

S_T1 = smooth(xpos*1000,S_T(2,:),0.2,'loess');
S_T2 = smooth(xpos*1000,S_T(round(ynode/2),:),0.2,'loess');
S_T3 = smooth(xpos*1000,S_T((ynode-1),:),0.2,'loess');
minS_T=min([min(S_T1),min(S_T2),min(S_T3)]);
maxS_T=max([max(S_T1),max(S_T2),max(S_T3)]);
```

```
vis1 = smooth(xpos*1000,vis(2,:),0.2,'loess');
vis2 = smooth(xpos*1000,vis(round(ynode/2),:),0.2,'loess');
vis3 = smooth(xpos*1000,vis((ynode-1),:),0.2,'loess');
minvis=min([min(vis1),min(vis2),min(vis3)]);
maxvis=max([max(vis1),max(vis2),max(vis3)]);

rho1 = smooth(xpos*1000,rho(2,:),0.2,'loess');
rho2 = smooth(xpos*1000,rho(round(ynode/2),:),0.2,'loess');
rho3 = smooth(xpos*1000,rho((ynode-1),:),0.2,'loess');
minrho=min([min(rho1),min(rho2),min(rho3)]);
maxrho=max([max(rho1),max(rho2),max(rho3)]);



xvel1y = smooth(ypos*1000,xvelocity(:,2),0.2,'loess');
xvel2y = smooth(ypos*1000,xvelocity(:,round(xnode/2)),0.2,'loess');
xvel3y = smooth(ypos*1000,xvelocity(:,(xnode-1)),0.2,'loess');
minxvely=min([min(xvel1y),min(xvel2y),min(xvel3y)]);
maxxvely=max([max(xvel1y),max(xvel2y),max(xvel3y)]);

yvel1y = smooth(ypos*1000,yvelocity(:,2),0.2,'loess');
yvel2y = smooth(ypos*1000,yvelocity(:,round(xnode/2)),0.2,'loess');
yvel3y = smooth(ypos*1000,yvelocity(:,(xnode-1)),0.2,'loess');
minyvely=min([min(yvel1y),min(yvel2y),min(yvel3y)]);
maxyvely=max([max(yvel1y),max(yvel2y),max(yvel3y)]);

cc1y = smooth(ypos*1000,massfrac1(:,2),0.2,'loess');
cc2y = smooth(ypos*1000,massfrac1(:,round(xnode/2)),0.2,'loess');
cc3y = smooth(ypos*1000,massfrac1(:,(xnode-1)),0.2,'loess');
minccy=min([min(cc1y),min(cc2),min(cc3y)]);
maxccy=max([max(cc1y),max(cc2),max(cc3y)]);

cw1y = smooth(ypos*1000,massfrac2(:,2),0.2,'loess');
```

```
cw2y = smooth(ypos*1000,massfrac2(:,round(xnode/2)),0.2,'loess');
cw3y = smooth(ypos*1000,massfrac2(:,(xnode-1)),0.2,'loess');
mincwy=min([min(cw1y),min(cw2y),min(cw3y)]);
maxcwy=max([max(cw1y),max(cw2y),max(cw3y)]);

TT1y = smooth(ypos*1000,T(:,2),0.2,'loess');
TT2y = smooth(ypos*1000,T(:,round(xnode/2)),0.2,'loess');
TT3y = smooth(ypos*1000,T(:,(xnode-1)),0.2,'loess');
minTTy=min([min(TT1y),min(TT2y),min(TT3y)]);
maxTTy=max([max(TT1y),max(TT2y),max(TT3y)]);

D1y = smooth(ypos*1000,D(:,2),0.2,'loess');
D2y = smooth(ypos*1000,D(:,round(xnode/2)),0.2,'loess');
D3y = smooth(ypos*1000,D(:,(xnode-1)),0.2,'loess');
minDy=min([min(D1y),min(D2y),min(D3y)]);
maxDy=max([max(D1y),max(D2y),max(D3y)]);

DT1y = smooth(ypos*1000,DT(:,2),0.2,'loess');
DT2y = smooth(ypos*1000,DT(:,round(xnode/2)),0.2,'loess');
DT3y = smooth(ypos*1000,DT(:,(xnode-1)),0.2,'loess');
minDTy=min([min(DT1y),min(DT2y),min(DT3y)]);
maxDTy=max([max(DT1y),max(DT2y),max(DT3y)]);

S_T1y = smooth(ypos*1000,S_T(:,2),0.2,'loess');
S_T2y = smooth(ypos*1000,S_T(:,round(xnode/2)),0.2,'loess');
S_T3y = smooth(ypos*1000,S_T(:,(xnode-1)),0.2,'loess');
minS_Ty=min([min(S_T1y),min(S_T2y),min(S_T3y)]);
maxS_Ty=max([max(S_T1y),max(S_T2y),max(S_T3y)]);

vis1y = smooth(ypos*1000,vis(:,2),0.2,'loess');
vis2y = smooth(ypos*1000,vis(:,round(xnode/2)),0.2,'loess');
vis3y = smooth(ypos*1000,vis(:,(xnode-1)),0.2,'loess');
minvisy=min([min(vis1y),min(vis2y),min(vis3y)]);
```

```
maxvisy=max([max(vis1y),max(vis2y),max(vis3y)]);

rho1y = smooth(ypos*1000,rho(:,2),0.2,'loess');
rho2y = smooth(ypos*1000,rho(:,round(xnode/2)),0.2,'loess');
rho3y = smooth(ypos*1000,rho(:,(xnode-1)),0.2,'loess');
minrhoy=min([min(rho1y),min(rho2y),min(rho3y)]);
maxrhoy=max([max(rho1y),max(rho2y),max(rho3y)]);

figure('NumberTitle','on','Name',filename,'Position',position2)
set(gca,'Position',get(gca,'OuterPosition')-get(gca,'TightInset').*border2);
axis([-L/2 L/2 -H/2 H/2 ]*1000);
[C,h] = contour(xpos*1000,ypos*1000,stream,15);
set(h,'ShowText','off')
xlabel('Lenght [mm]');ylabel('Height [mm]');
title('Stream line')
axis image

figure('NumberTitle','on','Name',filename,'Position',position2)
set(gca,'Position',get(gca,'OuterPosition')-get(gca,'TightInset').*border2);
% [U,V] = gradient(stream,.2,.2);
quiver(xpos*1000,ypos*1000,xvelocity,yvelocity);axis([-L/2 L/2 -H/2 H/2 ]*1000);
text(-0.4*L*1000,-.45*H*1000,['Average Velocity=', num2str(Meanvel*10^6), ' \mum/s '])
xlabel('Lenght [mm]');ylabel('Height [mm]');
title('Velocity field in the domain at quasi-steady condition          ')
axis image

figure('NumberTitle','on','Name',filename,'Position',position1)
set(gca,'Position',get(gca,'OuterPosition')-get(gca,'TightInset').*border1);

k = [0 0 0];      %# start black
y = [1 1 0];    %# middle1 red
r = [1 0 0];      %#  middle1 yellow
w = [.9 .9 .9];    %#  End whit
```

```
%# colormap of size 64-by-3, ranging from red -> white -> blue
map1 = zeros(20,3); map2 = zeros(20,3); map3 = zeros(20,3);
for i=1:3
    map1(:,i) = linspace(w(i), y(i), 20);
    map2(:,i) = linspace(y(i), r(i), 20);
    map3(:,i) = linspace(r(i), k(i), 20);
end
map = [map1;map2;map3];

contourf(xpos*1000,ypos*1000,T,14)
hold on
contour(xpos*1000,ypos*1000,T,14);
colormap (map);axis([-L/2 L/2 -H/2 H/2 ]*1000);
xlabel('Lenght [mm]');ylabel('Height [mm]');
title('Temperature [K]')
colorbar
axis image

figure('NumberTitle','on','Name',filename,'Position',position1)
set(gca,'Position',get(gca,'OuterPosition')-get(gca,'TightInset').*border1);


contourf(xpos*1000,ypos*1000,massfrac1,18)
hold on
contour(xpos*1000,ypos*1000,massfrac1,18);
axis([-L/2 L/2 -H/2 H/2 ]*1000);
xlabel('Lenght [mm]');ylabel('Height [mm]');
title('Mass fraction of Isopropanol');
colormap copper;
colorbar
axis image
```

```
figure('NumberTitle','on','Name',filename,'Position',position2)
set(gca,'Position',get(gca,'OuterPosition')-get(gca,'TightInset').*border2);
plot(xpos*1000,TT1,'-s',xpos*1000,TT2,'--ro',xpos*1000,TT3,'-.k*','LineWidth',2);
xlabel('Lenght [mm]');ylabel('T [K]');
hleg1=legend('Bottom','Middle','Top','Location','Best');
set(hleg1,'Edgecolor','w');
title('Temperature variation along x-direction');
grid off;
axis square
axis([-L/2*1000 L/2*1000 minTT*0.997 maxTT*1.003])


figure('NumberTitle','on','Name',filename,'Position',position2)
set(gca,'Position',get(gca,'OuterPosition')-get(gca,'TightInset').*border2);
plot(xpos*1000,cc1,'-s',xpos*1000,cc2,'--rO',xpos*1000,cc3,'-.k*','LineWidth',2);
xlabel('Lenght [mm]');ylabel('Isopropanol mass fraction');
hleg1 = legend('Bottom','Middle','Top','Location','Best');grid off;
set(hleg1,'Edgecolor','w');
title('Mass fraction of Isopropanol along x-direction')
axis square
axis([-L/2*1000 L/2*1000 mincc*0.9999 maxcc*1.0001])

figure('NumberTitle','on','Name',filename,'Position',position1)
set(gca,'Position',get(gca,'OuterPosition')-get(gca,'TightInset').*border1);
contourf(xpos*1000,ypos*1000,D,14)
hold on
contour(xpos*1000,ypos*1000,D,14);
colormap bone;axis([-L/2 L/2 -H/2 H/2 ]*1000);
xlabel('Lenght [mm]');ylabel('Height [mm]');
title('   Molecular diff coeff distribution')
```

```
colorbar
axis image


figure('NumberTitle','on','Name',filename,'Position',position1)
set(gca,'Position',get(gca,'OuterPosition')-get(gca,'TightInset').*border1);
contourf(xpos*1000,ypos*1000,DT,14)
hold on
contour(xpos*1000,ypos*1000,DT,14);
colormap pink;axis([-L/2 L/2 -H/2 H/2 ]*1000);
xlabel('Lenght [mm]');ylabel('Height [mm]');
title('   Thermodiff coeff distribution')
colorbar
axis image

figure('NumberTitle','on','Name',filename,'Position',position1)
set(gca,'Position',get(gca,'OuterPosition')-get(gca,'TightInset').*border1);
contourf(xpos*1000,ypos*1000,S_T,14)
hold on
contour(xpos*1000,ypos*1000,S_T,14);
colormap pink;axis([-L/2 L/2 -H/2 H/2 ]*1000);
xlabel('Lenght [mm]');ylabel('Height [mm]');
title('   Soret coeff distribution')
colorbar
axis image


figure('NumberTitle','on','Name',filename,'Position',position2)
set(gca,'Position',get(gca,'OuterPosition')-get(gca,'TightInset').*border2);
plot(xpos*1000,D1,'-s',xpos*1000,D2,'--ro',xpos*1000,D3,'-.k*','LineWidth',2);
xlabel('Lenght [mm]');ylabel('D_M [m^2/K]');
hleg1 = legend('Bottom','Middle','Top','Location','Best');grid off;
set(hleg1,'Edgecolor','w')
```

```
title('            Molecular diff coeff along x-direction')
axis square
axis([-L/2*1000 L/2*1000 minD*0.997 maxD*1.003])

figure('NumberTitle','on','Name',filename,'Position',position2)
set(gca,'Position',get(gca,'OuterPosition')-get(gca,'TightInset').*border2);
plot(xpos*1000,xvel1,'-s',xpos*1000,xvel2,'--ro',xpos*1000,xvel3,'-.k*','LineWidth',2);
xlabel('Lenght [mm]');ylabel('X-Velocity [m/s]');
hleg1 = legend('Bottom','Middle','Top','Location','Best');grid on;
set(hleg1,'Edgecolor','w')
title('     x-velocity along x-direction')
axis square
axis([-L/2*1000 L/2*1000 minxvel*0.997 maxxvel*1.003])

figure('NumberTitle','on','Name',filename,'Position',position2)
set(gca,'Position',get(gca,'OuterPosition')-get(gca,'TightInset').*border2);
plot(xpos*1000,yvel1,'-s',xpos*1000,yvel2,'--ro',xpos*1000,yvel3,'-.k*','LineWidth',2);
xlabel('Lenght [mm]');ylabel('Y-Velocity [m/s]');
hleg1 = legend('Bottom','Middle','Top','Location','Best');grid on;
set(hleg1,'Edgecolor','w')
title('    Y-Velocity along x-direction')
axis square
axis([-L/2*1000 L/2*1000 minyvel*0.997 maxyvel*1.003])

figure('NumberTitle','on','Name',filename,'Position',position2)
set(gca,'Position',get(gca,'OuterPosition')-get(gca,'TightInset').*border2);
plot(xpos*1000,DT1,'-s',xpos*1000,DT2,'--ro',xpos*1000,DT3,'-.k*','LineWidth',2);
xlabel('Lenght [mm]');ylabel('D_T [m^2/K]');
hleg1 = legend('Bottom','Middle','Top','Location','Best');grid off;
set(hleg1,'Edgecolor','w')
title('          Thermodiff coeff along x-direction')
axis square
axis([-L/2*1000 L/2*1000 minDT*0.997 maxDT*1.003])
```

```
figure('NumberTitle','on','Name',filename,'Position',position2)
set(gca,'Position',get(gca,'OuterPosition')-get(gca,'TightInset').*border2);
plot(xpos*1000,S_T1,'-s',xpos*1000,S_T2,'--ro',xpos*1000,S_T3,'-.k*','LineWidth',2);
xlabel('Lenght [mm]');ylabel('S_T');
hleg1 = legend('Bottom','Middle','Top','Location','Best');grid off;
set(hleg1,'Edgecolor','w')
title('     Soret coeff along x-direction')
axis square
axis([-L/2*1000 L/2*1000 minS_T*0.997 maxS_T*1.003])

figure('NumberTitle','on','Name',filename,'Position',position1)
set(gca,'Position',get(gca,'OuterPosition')-get(gca,'TightInset').*border1);
contourf(xpos*1000,ypos*1000,rho,14)
hold on
contour(xpos*1000,ypos*1000,rho,14);
colormap bone;axis([-L/2 L/2 -H/2 H/2 ]*1000);
xlabel('Lenght [mm]');ylabel('Height [mm]');
title('Density distribution in cavity')
colorbar
axis image

figure('NumberTitle','on','Name',filename,'Position',position1)
set(gca,'Position',get(gca,'OuterPosition')-get(gca,'TightInset').*border1);
contourf(xpos*1000,ypos*1000,massfrac2,14)
hold on
contour(xpos*1000,ypos*1000,massfrac2,14);
axis([-L/2 L/2 -H/2 H/2 ]*1000);
xlabel('Lenght [mm]');ylabel('Height [mm]');
title('Water mass fraction in cavity');
colormap gray;
colorbar
axis image
```

```
figure('NumberTitle','on','Name',filename,'Position',position1)
set(gca,'Position',get(gca,'OuterPosition')-get(gca,'TightInset').*border1);
contourf(xpos*1000,ypos*1000,vis,14)
hold on
contour(xpos*1000,ypos*1000,vis,14);
axis([-L/2 L/2 -H/2 H/2 ]*1000);
xlabel('Lenght [mm]');ylabel('Height [mm]');
title('Vicosity  distribution in cavity')
colormap summer;
colorbar
axis image

figure('NumberTitle','on','Name',filename,'Position',position2)
set(gca,'Position',get(gca,'OuterPosition')-get(gca,'TightInset').*border2);
plot(xpos*1000,vis1,'-s',xpos*1000,vis2,'--ro',xpos*1000,vis3,'-.k*','LineWidth',2);
xlabel('Lenght [mm]');ylabel('\mu [kg/(ms)]');
hleg1 = legend('Bottom','Middle','Top','Location','Best');grid off;
set(hleg1,'Edgecolor','w')
title('Viscosity along x-direction')
axis square
axis([-L/2*1000 L/2*1000 minvis*0.9999 maxvis*1.0001])

figure('NumberTitle','on','Name',filename,'Position',position2)
set(gca,'Position',get(gca,'OuterPosition')-get(gca,'TightInset').*border2);
plot(ypos*1000,vis1y,'-s',ypos*1000,vis2y,'--ro',ypos*1000,vis3y,'-.k*','LineWidth',2);
xlabel('Height [mm]');ylabel('\mu [kg/(ms)]');
hleg1 = legend('Near cold wall','middle','Near hot wall','Location','Best');grid off;
set(hleg1,'Edgecolor','w');
title('Viscosity along y-direction')
axis square
axis([-H/2*1000 H/2*1000 minvisy*0.9999 maxvisy*1.0001])
```

```
figure('NumberTitle','on','Name',filename,'Position',position2)
set(gca,'Position',get(gca,'OuterPosition')-get(gca,'TightInset').*border2);
plot(ypos*1000,D1y,'-s',ypos*1000,D2y,'--ro',ypos*1000,D3y,'-.k*','LineWidth',2);
xlabel('Height [mm]');ylabel('D_M [m^2/s]');
hleg1 = legend('Near cold wall','middle','Near hot wall','Location','Best');grid on;
set(hleg1,'Edgecolor','w')
title('            Molecular diff coeff along y-direction')
axis square
axis([-H/2*1000 H/2*1000 minDy*0.997 maxDy*1.003])

figure('NumberTitle','on','Name',filename,'Position',position2) ;
set(gca,'Position',get(gca,'OuterPosition')-get(gca,'TightInset').*border2);
plot(ypos*1000,DT1y,'-s',ypos*1000,DT2y,'--ro',ypos*1000,DT3y,'-.k*','LineWidth',2);
xlabel('Height [mm]');ylabel('D_T [m^2/K.s]');
hleg1 = legend('Near cold wall','middle','Near hot wall','Location','Best');grid on;
set(hleg1,'Edgecolor','w')
title('        Thermodiff coeff along y-direction')
axis square
axis([-H/2*1000 H/2*1000 minDTy*0.997 maxDTy*1.003])

figure('NumberTitle','on','Name',filename,'Position',position2)
set(gca,'Position',get(gca,'OuterPosition')-get(gca,'TightInset').*border2);
plot(ypos*1000,S_T1y,'-s',ypos*1000,S_T2y,'--ro',ypos*1000,S_T3y,'-.k*','LineWidth',2);
xlabel('Height [mm]');ylabel('S_T');
hleg1 = legend('Near cold wall','middle','Near hot wall','Location','Best');grid on;
set(hleg1,'Edgecolor','w')
title('Soret coeff along y-direction in cavity')
axis square
axis([-H/2*1000 H/2*1000 minS_Ty*0.997 maxS_Ty*1.003])

figure('NumberTitle','on','Name',filename,'Position',position2)
set(gca,'Position',get(gca,'OuterPosition')-get(gca,'TightInset').*border2);
plot(ypos*1000,TT1y,'-s',ypos*1000,TT2y,'--ro',ypos*1000,TT3y,'-.k*','LineWidth',2);
```

```
xlabel('Height [mm]');ylabel('T [K]');
hleg1= legend('Near cold wall','middle','Near hot wall','Location','Best');grid on;
set(hleg1,'Edgecolor','w')
title('Temprature variation along y-direction in cavity')
axis square
axis([-H/2*1000 H/2*1000 minTTy*0.997 maxTTy*1.003])

figure('NumberTitle','on','Name',filename,'Position',position2)
set(gca,'Position',get(gca,'OuterPosition')-get(gca,'TightInset').*border2);
plot(ypos*1000,cc1y,'-s',ypos*1000,cc2y,'--ro',ypos*1000,cc3y,'-.k*','LineWidth',2);
xlabel('Height [mm]');ylabel('Isopropanol mass fraction');
hleg1 = legend('Near cold wall','middle','Near hot wall','Location','Best');grid off;
set(hleg1,'Edgecolor','w')
title('   Isopropanol mass fraction along y-direction')
axis square
axis([-H/2*1000 H/2*1000 minccy*0.9999 maxccy*1.0001])

figure('NumberTitle','on','Name',filename,'Position',position2)
set(gca,'Position',get(gca,'OuterPosition')-get(gca,'TightInset').*border2);
plot(xpos*1000,rho1,'-s',xpos*1000,rho2,'--ro',xpos*1000,rho3,'-.k*','LineWidth',2);
xlabel('Lenght [mm]');ylabel('\rho [kg/m^3]');
hleg1 = legend('Bottom','middle','Top','Location','Best');grid off;
set(hleg1,'Edgecolor','w')
title('Density variation along x-direction in cavity')
axis square
axis([-L/2*1000 L/2*1000 minrhoy*0.999 maxrhoy*1.001])

figure('NumberTitle','on','Name',filename,'Position',position2)
set(gca,'Position',get(gca,'OuterPosition')-get(gca,'TightInset').*border2);
plot(ypos*1000,rho1y,'-s',ypos*1000,rho2y,'--ro',ypos*1000,rho3y,'-.k*','LineWidth',2);
xlabel('Height [mm]');ylabel('\rho [kg/m^3]');
hleg1 = legend('Near cold wall','middle','Near hot wall','Location','Best');grid on;
set(hleg1,'Edgecolor','w')
```

```
    title('Density variation along y-direction in cavity')
    axis square
    axis([-H/2*1000 H/2*1000 minrhoy*0.999 maxrhoy*1.001])

    figure('NumberTitle','on','Name',filename,'Position',position2)
    set(gca,'Position',get(gca,'OuterPosition')-get(gca,'TightInset').*border2);
    plot(ypos*1000,xvel1y,'-s',ypos*1000,xvel2y,'--ro',ypos*1000,xvel3y,'-.k*','LineWidth',2);
    xlabel('Height [mm]');ylabel('X-Velocity [m/s]');
    hleg1 = legend('Near cold wall','middle','Near hot wall','Location','Best');grid on;
    set(hleg1,'Edgecolor','w')
    title('    x-velocity along y-direction')
    axis square
    axis([-H/2*1000 H/2*1000 minxvely*0.997 maxxvely*1.003])

    figure('NumberTitle','on','Name',filename,'Position',position2)
    set(gca,'Position',get(gca,'OuterPosition')-get(gca,'TightInset').*border2);
    plot(ypos*1000,yvel1y,'-s',ypos*1000,yvel2y,'--ro',ypos*1000,yvel3y,'-.k*','LineWidth',2);
    xlabel('Height [mm]');ylabel('Y-Velocity [m/s]');
    hleg1 = legend('Near cold wall','middle','Near hot wall','Location','Best');grid on;
    set(hleg1,'Edgecolor','w')
    title('y-velocity along y-direction')
    axis square
    axis([-H/2*1000 H/2*1000 minyvely*0.997 maxyvely*1.003])

% %  print -djpeg -r1400  'filename'
%%
    figure('NumberTitle','on','Name',filename,'Position',position3)
    set(gca,'Position',get(gca,'OuterPosition')-get(gca,'TightInset').*border3);

    [AX1,H11,H12] = plotyy(ypos*1000,cc1y,ypos*1000,DT1y,'plot');

    % set(AX(1),'YTickMode','Auto','XColor','k','YColor','b','ylim',[0
    % .1],'Ytick',0:.02:.1,'Ygrid','on');  ORginal
```

```
set(AX1(1),'YTickMode','Auto','XColor','k','YColor','k','Ygrid','on','ylim',[aa bb].*[minccy maxccy]);
set(AX1(2),'YTickMode','Auto','XColor','k','YColor','k','ylim',[aa bb].*[minDTy maxDTy]);

set(get(AX1(1),'Ylabel'),'String','Mass fraction of Isopropanol') ;
set(get(AX1(2),'Ylabel'),'String','D_T  [m^2/K.s]') ;

set(H11,'LineStyle','--','Marker','p','Color','k','LineWidth',2);
set(H12,'LineStyle','-','Marker','s','Color','k','LineWidth',2);

% set(AX(1),'XGrid','on','Xtick',0:2:20,'XLim',[0 20]);       ORGINAL

set(AX1(1),'XGrid','on');
set(AX1(2));
%     hleg1 = legend('X','Y');

hold on
[AX2,H21,H22] = plotyy(ypos*1000,cc2y,ypos*1000,DT2y,'plot');
hold on
% set(AX(1),'YTickMode','Auto','XColor','k','YColor','b','ylim',[0
% .1],'Ytick',0:.02:.1,'Ygrid','on');  ORginal
set(AX2(1),'YTickMode','Auto','XColor','k','YColor','k','Ygrid','on','ylim',[aa bb].*[minccy maxccy]);
set(AX2(2),'YTickMode','Auto','XColor','k','YColor','k','ylim',[aa bb].*[minDTy maxDTy]);

set(get(AX1(1),'Ylabel'),'String','Mass fraction of Isopropanol') ;
set(get(AX1(2),'Ylabel'),'String','D_T  [m^2/K.s]') ;

set(H21,'LineStyle','--','Marker','o','Color','b','LineWidth',2);
set(H22,'LineStyle','-','Marker','+','Color','b','LineWidth',2);

% set(AX(1),'XGrid','on','Xtick',0:2:20,'XLim',[0 20]);       ORGINAL

set(AX2(1),'XGrid','on');
set(AX2(2));
```

```
%     hleg1 = legend('X1','Y1')

    hold on

    [AX3,H31,H32] = plotyy(ypos*1000,cc3y,ypos*1000,DT3y,'plot');

    % set(AX(1),'YTickMode','Auto','XColor','k','YColor','b','ylim',[0
    % .1],'Ytick',0:.02:.1,'Ygrid','on');  ORginal
    set(AX3(1),'YTickMode','Auto','XColor','k','YColor','k','Ygrid','on','ylim',[aa bb].*[minccy maxccy]);
    set(AX3(2),'YTickMode','Auto','XColor','k','YColor','k','ylim',[aa bb].*[minDTy maxDTy]);

    set(get(AX1(1),'Ylabel'),'String','Mass fraction of Isopropanol') ;
    set(get(AX1(2),'Ylabel'),'String','D_T  [m^2/K.s]') ;

    set(H31,'LineStyle','--','Marker','h','Color','r','LineWidth',2);
    set(H32,'LineStyle','-','Marker','.','Color','r','LineWidth',2);

    % set(AX(1),'XGrid','on','Xtick',0:2:20,'XLim',[0 20]);       ORGINAL

    set(AX3(1),'XGrid','on');
    set(AX3(2));

    HH=[H11,H12,H21,H22,H31,H32];
    xlabel('Height [mm]') ;
    title('Isopropanol mass fraction and Thermodiffusion coefficient along y-direction in cavity');
    hleg1 = legend(HH,'Mass-fraction near hot wall','D_T Near hot wall','Mass-fraction at middle',...
    'D_T at middle','Mass-fraction near cold wall','D_T near cold wall',0);
    set(hleg1,'Edgecolor','w')

%%
    figure('NumberTitle','on','Name',filename,'Position',position3)
    set(gca,'Position',get(gca,'OuterPosition')-get(gca,'TightInset').*border3);
```

```
[AX1,H11,H12] = plotyy(ypos*1000,cc1y,ypos*1000,D1y,'plot');

% set(AX(1),'YTickMode','Auto','XColor','k','YColor','b','ylim',[0
% .1],'Ytick',0:.02:.1,'Ygrid','on');  ORginal
set(AX1(1),'YTickMode','Auto','XColor','k','YColor','k','Ygrid','on','ylim',[aa bb].*[minccy maxccy]);
set(AX1(2),'YTickMode','Auto','XColor','k','YColor','k','ylim',[aa bb].*[minDy maxDy]);

set(get(AX1(1),'Ylabel'),'String','Mass fraction of Isopropanol') ;
set(get(AX1(2),'Ylabel'),'String','D_M  [m^2/s]') ;

set(H11,'LineStyle','--','Marker','p','Color','k','LineWidth',2);
set(H12,'LineStyle','-','Marker','s','Color','k','LineWidth',2);

% set(AX(1),'XGrid','on','Xtick',0:2:20,'XLim',[0 20]);       ORGINAL

set(AX1(1),'XGrid','on');
set(AX1(2));
%     hleg1 = legend('X','Y');

hold on
[AX2,H21,H22] = plotyy(ypos*1000,cc2y,ypos*1000,D2y,'plot');
hold on
% set(AX(1),'YTickMode','Auto','XColor','k','YColor','b','ylim',[0
% .1],'Ytick',0:.02:.1,'Ygrid','on');  ORginal
set(AX2(1),'YTickMode','Auto','XColor','k','YColor','k','Ygrid','on','ylim',[aa bb].*[minccy maxccy]);
set(AX2(2),'YTickMode','Auto','XColor','k','YColor','k','ylim',[aa bb].*[minDy maxDy]);

set(get(AX1(1),'Ylabel'),'String','Mass fraction of Isopropanol') ;
set(get(AX1(2),'Ylabel'),'String','D_M  [m^2/s]') ;

set(H21,'LineStyle','--','Marker','o','Color','b','LineWidth',2);
set(H22,'LineStyle','-','Marker','+','Color','b','LineWidth',2);
```

```
    % set(AX(1),'XGrid','on','Xtick',0:2:20,'XLim',[0 20]);       ORGINAL

    set(AX2(1),'XGrid','on');
    set(AX2(2));
%     hleg1 = legend('X1','Y1')

    hold on

    [AX3,H31,H32] = plotyy(ypos*1000,cc3y,ypos*1000,D3y,'plot');

    % set(AX(1),'YTickMode','Auto','XColor','k','YColor','b','ylim',[0
    % .1],'Ytick',0:.02:.1,'Ygrid','on');  ORginal
    set(AX3(1),'YTickMode','Auto','XColor','k','YColor','k','Ygrid','on','ylim',[aa bb].*[minccy maxccy]);
    set(AX3(2),'YTickMode','Auto','XColor','k','YColor','k','ylim',[aa bb].*[minDy maxDy]);

    set(get(AX1(1),'Ylabel'),'String','Mass fraction of Isopropanol') ;
    set(get(AX1(2),'Ylabel'),'String','D_M  [m^2/s]') ;

    set(H31,'LineStyle','--','Marker','h','Color','r','LineWidth',2);
    set(H32,'LineStyle','-','Marker','.','Color','r','LineWidth',2);

    % set(AX(1),'XGrid','on','Xtick',0:2:20,'XLim',[0 20]);       ORGINAL

    set(AX3(1),'XGrid','on');
    set(AX3(2));

    HH=[H11,H12,H21,H22,H31,H32];
    xlabel('Height [mm]') ;
    title('Isopropanol Mass fraction and Molecular diffusion coefficent along y-direction in cavity');
    hleg1 = legend(HH,'Mass-fraction near hot wall','D_M near hot wall','Mass-fraction at middle',...
    'D_M at middle','Mass-fraction near cold wall','D_M near cold wall',0);
    set(hleg1,'Edgecolor','w');
%%
```

```
figure('NumberTitle','on','Name',filename,'Position',position3)
set(gca,'Position',get(gca,'OuterPosition')-get(gca,'TightInset').*border3);

[AX1,H11,H12] = plotyy(ypos*1000,D1y,ypos*1000,DT1y,'plot');

% set(AX(1),'YTickMode','Auto','XColor','k','YColor','b','ylim',[0
% .1],'Ytick',0:.02:.1,'Ygrid','on');  ORginal
set(AX1(1),'YTickMode','Auto','XColor','k','YColor','k','Ygrid','on','ylim',[aa bb].*[minDy maxDy]);
set(AX1(2),'YTickMode','Auto','XColor','k','YColor','k','ylim',[aa bb].*[minDTy maxDTy]);

set(get(AX1(1),'Ylabel'),'String','D_M  [m^2/s]') ;
set(get(AX1(2),'Ylabel'),'String','D_T  [m^2/K.s]') ;

set(H11,'LineStyle','--','Marker','p','Color','k','LineWidth',2);
set(H12,'LineStyle','-','Marker','s','Color','k','LineWidth',2);

% set(AX(1),'XGrid','on','Xtick',0:2:20,'XLim',[0 20]);       ORGINAL

set(AX1(1),'XGrid','on');
set(AX1(2));
%     hleg1 = legend('X','Y');

hold on
[AX2,H21,H22] = plotyy(ypos*1000,D2y,ypos*1000,DT2y,'plot');
hold on
% set(AX(1),'YTickMode','Auto','XColor','k','YColor','b','ylim',[0
% .1],'Ytick',0:.02:.1,'Ygrid','on');  ORginal
set(AX2(1),'YTickMode','Auto','XColor','k','YColor','k','Ygrid','on','ylim',[aa bb].*[minDy maxDy]);
set(AX2(2),'YTickMode','Auto','XColor','k','YColor','k','ylim',[aa bb].*[minDTy maxDTy]);

set(get(AX1(1),'Ylabel'),'String','D_M  [m^2/s]') ;
set(get(AX1(2),'Ylabel'),'String','D_T  [m^2/K.s]') ;
```

```
    set(H21,'LineStyle','--','Marker','o','Color','b','LineWidth',2);
    set(H22,'LineStyle','-','Marker','+','Color','b','LineWidth',2);

    % set(AX(1),'XGrid','on','Xtick',0:2:20,'XLim',[0 20]);       ORGINAL

    set(AX2(1),'XGrid','on');
    set(AX2(2));
%     hleg1 = legend('X1','Y1')

    hold on

    [AX3,H31,H32] = plotyy(ypos*1000,D3y,ypos*1000,DT3y,'plot');

    % set(AX(1),'YTickMode','Auto','XColor','k','YColor','b','ylim',[0
    % .1],'Ytick',0:.02:.1,'Ygrid','on');  ORginal
    set(AX3(1),'YTickMode','Auto','XColor','k','YColor','k','Ygrid','on','ylim',[aa bb].*[minDy maxDy]);
    set(AX3(2),'YTickMode','Auto','XColor','k','YColor','k','ylim',[aa bb].*[minDTy maxDTy]);

    set(get(AX1(1),'Ylabel'),'String','D_M  [m^2/s]') ;
    set(get(AX1(2),'Ylabel'),'String','D_T  [m^2/K.s]') ;

    set(H31,'LineStyle','--','Marker','h','Color','r','LineWidth',2);
    set(H32,'LineStyle','-','Marker','.','Color','r','LineWidth',2);

    % set(AX(1),'XGrid','on','Xtick',0:2:20,'XLim',[0 20]);       ORGINAL

    set(AX3(1),'XGrid','on');
    set(AX3(2));

    HH=[H11,H12,H21,H22,H31,H32];
    xlabel('Height [mm]') ;
    title('Molecular diffusion and Thermodiffusion coefficient along y-direction in cavity');
    hleg1=legend(HH,'D_M near hot wall','D_T near hot wall','D_M at middle',...
```

```
    'D_T at middle','D_M near cold wall','D_T near cold wall',0);
    set(hleg1,'Edgecolor','w')
%%

    figure('NumberTitle','on','Name',filename,'Position',position3)
    set(gca,'Position',get(gca,'OuterPosition')-get(gca,'TightInset').*border3);

    [AX1,H11,H12] = plotyy(ypos*1000,TT1y,ypos*1000,DT1y,'plot');

    % set(AX(1),'YTickMode','Auto','XColor','k','YColor','b','ylim',[0
    % .1],'Ytick',0:.02:.1,'Ygrid','on');  ORginal
    set(AX1(1),'YTickMode','Auto','XColor','k','YColor','k','Ygrid','on','ylim',[aa bb].*[minTTy maxTTy]);
    set(AX1(2),'YTickMode','Auto','XColor','k','YColor','k','ylim',[aa bb].*[minDTy maxDTy]);

    set(get(AX1(1),'Ylabel'),'String','T [K]') ;
    set(get(AX1(2),'Ylabel'),'String','D_T  [m^2/K.s]') ;

    set(H11,'LineStyle','--','Marker','p','Color','k','LineWidth',2);
    set(H12,'LineStyle','-','Marker','s','Color','k','LineWidth',2);

    % set(AX(1),'XGrid','on','Xtick',0:2:20,'XLim',[0 20]);       ORGINAL

    set(AX1(1),'XGrid','on');
    set(AX1(2));
%     hleg1 = legend('X','Y');

    hold on
    [AX2,H21,H22] = plotyy(ypos*1000,TT2y,ypos*1000,DT2y,'plot');
    hold on
    % set(AX(1),'YTickMode','Auto','XColor','k','YColor','b','ylim',[0
    % .1],'Ytick',0:.02:.1,'Ygrid','on');  ORginal
    set(AX2(1),'YTickMode','Auto','XColor','k','YColor','k','Ygrid','on','ylim',[aa bb].*[minTTy maxTTy]);
    set(AX2(2),'YTickMode','Auto','XColor','k','YColor','k','ylim',[aa bb].*[minDTy maxDTy]);
```

```
    set(get(AX1(1),'Ylabel'),'String','T [K]') ;
    set(get(AX1(2),'Ylabel'),'String','D_T  [m^2/K.s]') ;

    set(H21,'LineStyle','--','Marker','o','Color','b','LineWidth',2);
    set(H22,'LineStyle','-','Marker','+','Color','b','LineWidth',2);

    % set(AX(1),'XGrid','on','Xtick',0:2:20,'XLim',[0 20]);       ORGINAL

    set(AX2(1),'XGrid','on');
    set(AX2(2));
%     hleg1 = legend('X1','Y1')

    hold on

    [AX3,H31,H32] = plotyy(ypos*1000,TT3y,ypos*1000,DT3y,'plot');

    % set(AX(1),'YTickMode','Auto','XColor','k','YColor','b','ylim',[0
    % .1],'Ytick',0:.02:.1,'Ygrid','on');  ORginal
    set(AX3(1),'YTickMode','Auto','XColor','k','YColor','k','Ygrid','on','ylim',[aa bb].*[minTTy maxTTy]);
    set(AX3(2),'YTickMode','Auto','XColor','k','YColor','k','ylim',[aa bb].*[minDTy maxDTy]);

    set(get(AX1(1),'Ylabel'),'String','T [K]') ;
    set(get(AX1(2),'Ylabel'),'String','D_T  [m^2/K.s]') ;

    set(H31,'LineStyle','--','Marker','h','Color','r','LineWidth',2);
    set(H32,'LineStyle','-','Marker','.','Color','r','LineWidth',2);

    % set(AX(1),'XGrid','on','Xtick',0:2:20,'XLim',[0 20]);       ORGINAL

    set(AX3(1),'XGrid','on');
    set(AX3(2));
```

```
    HH=[H11,H12,H21,H22,H31,H32];
    xlabel('Height [mm]') ;
    title('Temperature and Thermodiffusion coefficient along y-direction in cavity');
    hleg1 = legend(HH,'Temperature near hot wall','D_T near hot wall','Temperature at middle',...
    'D_T at middle','Temperature near cold wall','D_T near cold wall',0);%%
    set(hleg1,'Edgecolor','w');

%%
    figure('NumberTitle','on','Name',filename,'Position',position3)
    set(gca,'Position',get(gca,'OuterPosition')-get(gca,'TightInset').*border3);

    [AX1,H11,H12] = plotyy(xpos*1000,cc1,xpos*1000,DT1,'plot');

    % set(AX(1),'YTickMode','Auto','XColor','k','YColor','b','ylim',[0
    % .1],'Ytick',0:.02:.1,'Ygrid','on');  ORginal
    set(AX1(1),'YTickMode','Auto','XColor','k','YColor','k','Ygrid','on','ylim',[aa bb].*[mincc maxcc]);
    set(AX1(2),'YTickMode','Auto','XColor','k','YColor','k','ylim',[aa bb].*[minDT maxDT]);

    set(get(AX1(1),'Ylabel'),'String','Mass fraction of Isopropanol') ;
    set(get(AX1(2),'Ylabel'),'String','D_T  [m^2/K.s]') ;

    set(H11,'LineStyle','--','Marker','p','Color','k','LineWidth',2);
    set(H12,'LineStyle','-','Marker','s','Color','k','LineWidth',2);

    % set(AX(1),'XGrid','on','Xtick',0:2:20,'XLim',[0 20]);       ORGINAL

    set(AX1(1),'XGrid','on');
    set(AX1(2));
%     hleg1 = legend('X','Y');

    hold on
    [AX2,H21,H22] = plotyy(xpos*1000,cc2,xpos*1000,DT2,'plot');
    hold on
```

```
% set(AX(1),'YTickMode','Auto','XColor','k','YColor','b','ylim',[0
% .1],'Ytick',0:.02:.1,'Ygrid','on');  ORginal
set(AX2(1),'YTickMode','Auto','XColor','k','YColor','k','Ygrid','on','ylim',[aa bb].*[mincc maxcc]);
set(AX2(2),'YTickMode','Auto','XColor','k','YColor','k','ylim',[aa bb].*[minDT maxDT]);

set(get(AX1(1),'Ylabel'),'String','Mass fraction of Isopropanol') ;
set(get(AX1(2),'Ylabel'),'String','D_T  [m^2/K.s]') ;

set(H21,'LineStyle','--','Marker','o','Color','b','LineWidth',2);
set(H22,'LineStyle','-','Marker','+','Color','b','LineWidth',2);

% set(AX(1),'XGrid','on','Xtick',0:2:20,'XLim',[0 20]);       ORGINAL

set(AX2(1),'XGrid','on');
set(AX2(2));
%     hleg1 = legend('X1','Y1')


[AX3,H31,H32] = plotyy(xpos*1000,cc3,xpos*1000,DT3,'plot');

% set(AX(1),'YTickMode','Auto','XColor','k','YColor','b','ylim',[0
% .1],'Ytick',0:.02:.1,'Ygrid','on');  ORginal
set(AX3(1),'YTickMode','Auto','XColor','k','YColor','k','Ygrid','on','ylim',[aa bb].*[mincc maxcc]);
set(AX3(2),'YTickMode','Auto','XColor','k','YColor','k','ylim',[aa bb].*[minDT maxDT]);

set(get(AX1(1),'Ylabel'),'String','Mass fraction of Isopropanol') ;
set(get(AX1(2),'Ylabel'),'String','D_T  [m^2/K.s]') ;

set(H31,'LineStyle','--','Marker','h','Color','r','LineWidth',2);
set(H32,'LineStyle','-','Marker','.','Color','r','LineWidth',2);

% set(AX(1),'XGrid','on','Xtick',0:2:20,'XLim',[0 20]);       ORGINAL
```

```
    set(AX3(1),'XGrid','on');
    set(AX3(2));

    HH=[H11,H12,H21,H22,H31,H32];
    xlabel('Lenght [mm]') ;
    title('Isopropanol Mass fraction and Thermodiffusion coefficient along x-direction in cavity');
    hleg1 = legend(HH,'Mass-fraction at Bottom','D_T at Bottom','Mass-fraction at middle',...
    'D_T at middle','Mass-fraction at top','D_T at top',0);
    set(hleg1,'Edgecolor','w');

%%
    figure('NumberTitle','on','Name',filename,'Position',position3)
    set(gca,'Position',get(gca,'OuterPosition')-get(gca,'TightInset').*border3);

    [AX1,H11,H12] = plotyy(xpos*1000,cc1,xpos*1000,D1,'plot');

    % set(AX(1),'YTickMode','Auto','XColor','k','YColor','b','ylim',[0
    % .1],'Ytick',0:.02:.1,'Ygrid','on');  ORginal
    set(AX1(1),'YTickMode','Auto','XColor','k','YColor','k','Ygrid','on','ylim',[aa bb].*[mincc maxcc]);
    set(AX1(2),'YTickMode','Auto','XColor','k','YColor','k','ylim',[aa bb].*[minD maxD]);

    set(get(AX1(1),'Ylabel'),'String','Mass fraction of Isopropanol') ;
    set(get(AX1(2),'Ylabel'),'String','D_M  [m^2/s]') ;

    set(H11,'LineStyle','--','Marker','p','Color','k','LineWidth',2);
    set(H12,'LineStyle','-','Marker','s','Color','k','LineWidth',2);

    % set(AX(1),'XGrid','on','Xtick',0:2:20,'XLim',[0 20]);       ORGINAL

    set(AX1(1),'XGrid','on');
    set(AX1(2));
%     hleg1 = legend('X','Y');
```

```
hold on
[AX2,H21,H22] = plotyy(xpos*1000,cc2,xpos*1000,D2,'plot');
hold on
% set(AX(1),'YTickMode','Auto','XColor','k','YColor','b','ylim',[0
% .1],'Ytick',0:.02:.1,'Ygrid','on');  ORginal
set(AX2(1),'YTickMode','Auto','XColor','k','YColor','k','Ygrid','on','ylim',[aa bb].*[mincc maxcc]);
set(AX2(2),'YTickMode','Auto','XColor','k','YColor','k','ylim',[aa bb].*[minD maxD]);

set(get(AX1(1),'Ylabel'),'String','Mass fraction of Isopropanol') ;
set(get(AX1(2),'Ylabel'),'String','D_M  [m^2/s]') ;

set(H21,'LineStyle','--','Marker','o','Color','b','LineWidth',2);
set(H22,'LineStyle','-','Marker','+','Color','b','LineWidth',2);

% set(AX(1),'XGrid','on','Xtick',0:2:20,'XLim',[0 20]);       ORGINAL

set(AX2(1),'XGrid','on');
set(AX2(2));
%     hleg1 = legend('X1','Y1')

hold on

[AX3,H31,H32] = plotyy(xpos*1000,cc3,xpos*1000,D3,'plot');

% set(AX(1),'YTickMode','Auto','XColor','k','YColor','b','ylim',[0
% .1],'Ytick',0:.02:.1,'Ygrid','on');  ORginal
set(AX3(1),'YTickMode','Auto','XColor','k','YColor','k','Ygrid','on','ylim',[aa bb].*[mincc maxcc]);
set(AX3(2),'YTickMode','Auto','XColor','k','YColor','k','ylim',[aa bb].*[minD maxD]);

set(get(AX1(1),'Ylabel'),'String','Mass fraction of Isopropanol') ;
set(get(AX1(2),'Ylabel'),'String','D_M  [m^2/s]') ;

set(H31,'LineStyle','--','Marker','h','Color','r','LineWidth',2);
```

```
    set(H32,'LineStyle','-','Marker','.','Color','r','LineWidth',2);

    % set(AX(1),'XGrid','on','Xtick',0:2:20,'XLim',[0 20]);       ORGINAL

    set(AX3(1),'XGrid','on');
    set(AX3(2));

    HH=[H11,H12,H21,H22,H31,H32];
    xlabel('Lenght [mm]') ;
    title('Isopropanol Mass fraction and Molecular diffusion coefficent along x-direction in cavity');
    hleg1 = legend(HH,'Mass-fraction at Bottom','D_M at Bottom','Mass-fraction at middle',...
    'D_M at middle','Mass-fraction at top','D_M at top',0);
    set(hleg1,'Edgecolor','w')
%%
    figure('NumberTitle','on','Name',filename,'Position',position3)
    set(gca,'Position',get(gca,'OuterPosition')-get(gca,'TightInset').*border3);

    [AX1,H11,H12] = plotyy(xpos*1000,D1,xpos*1000,DT1,'plot');

    % set(AX(1),'YTickMode','Auto','XColor','k','YColor','b','ylim',[0
    % .1],'Ytick',0:.02:.1,'Ygrid','on');  ORginal
    set(AX1(1),'YTickMode','Auto','XColor','k','YColor','k','Ygrid','on','ylim',[aa bb].*[minD maxD]);
    set(AX1(2),'YTickMode','Auto','XColor','k','YColor','k','ylim',[aa bb].*[minDT maxDT]);

    set(get(AX1(1),'Ylabel'),'String','D_M  [m^2/s]') ;
    set(get(AX1(2),'Ylabel'),'String','D_T  [m^2/K.s]') ;

    set(H11,'LineStyle','--','Marker','p','Color','k','LineWidth',2);
    set(H12,'LineStyle','-','Marker','s','Color','k','LineWidth',2);

    % set(AX(1),'XGrid','on','Xtick',0:2:20,'XLim',[0 20]);       ORGINAL

    set(AX1(1),'XGrid','on');
```

```
    set(AX1(2));
%     hleg1 = legend('X','Y');

    hold on
    [AX2,H21,H22] = plotyy(xpos*1000,D2,xpos*1000,DT2,'plot');
    hold on
    % set(AX(1),'YTickMode','Auto','XColor','k','YColor','b','ylim',[0
    % .1],'Ytick',0:.02:.1,'Ygrid','on');  ORginal
    set(AX2(1),'YTickMode','Auto','XColor','k','YColor','k','Ygrid','on','ylim',[aa bb].*[minD maxD]);
    set(AX2(2),'YTickMode','Auto','XColor','k','YColor','k','ylim',[aa bb].*[minDT maxDT]);

    set(get(AX1(1),'Ylabel'),'String','D_M  [m^2/s]') ;
    set(get(AX1(2),'Ylabel'),'String','D_T  [m^2/K.s]') ;

    set(H21,'LineStyle','--','Marker','o','Color','b','LineWidth',2);
    set(H22,'LineStyle','-','Marker','+','Color','b','LineWidth',2);

    % set(AX(1),'XGrid','on','Xtick',0:2:20,'XLim',[0 20]);       ORGINAL

    set(AX2(1),'XGrid','on');
    set(AX2(2));
%     hleg1 = legend('X1','Y1')

    hold on

    [AX3,H31,H32] = plotyy(xpos*1000,D3,xpos*1000,DT3,'plot');

    % set(AX(1),'YTickMode','Auto','XColor','k','YColor','b','ylim',[0
    % .1],'Ytick',0:.02:.1,'Ygrid','on');  ORginal
    set(AX3(1),'YTickMode','Auto','XColor','k','YColor','k','Ygrid','on','ylim',[aa bb].*[minD maxD]);
    set(AX3(2),'YTickMode','Auto','XColor','k','YColor','k','ylim',[aa bb].*[minDT maxDT]);

    set(get(AX1(1),'Ylabel'),'String','D_M  [m^2/s]') ;
```

```
    set(get(AX1(2),'Ylabel'),'String','D_T  [m^2/K.s]') ;

    set(H31,'LineStyle','--','Marker','h','Color','r','LineWidth',2);
    set(H32,'LineStyle','-','Marker','.','Color','r','LineWidth',2);

    % set(AX(1),'XGrid','on','Xtick',0:2:20,'XLim',[0 20]);       ORGINAL

    set(AX3(1),'XGrid','on');
    set(AX3(2));

    HH=[H11,H12,H21,H22,H31,H32];
    xlabel('Lenght [mm]') ;
    title('Diffusionn and Thermodiffusion coefficient along x-direction in cavity');
    hleg1 = legend(HH,'D_M at Bottom','D_T at Bottom','D_M at middle',...
    'D_T at middle','D_M at top','D_T at top',0);
    set(hleg1,'Edgecolor','w');
%%

    figure('NumberTitle','on','Name',filename,'Position',position3)
    set(gca,'Position',get(gca,'OuterPosition')-get(gca,'TightInset').*border3);

    [AX1,H11,H12] = plotyy(xpos*1000,TT1,xpos*1000,DT1,'plot');

    % set(AX(1),'YTickMode','Auto','XColor','k','YColor','b','ylim',[0
    % .1],'Ytick',0:.02:.1,'Ygrid','on');  ORginal
    set(AX1(1),'YTickMode','Auto','XColor','k','YColor','k','Ygrid','on','ylim',[aa bb].*[minTT maxTT]);
    set(AX1(2),'YTickMode','Auto','XColor','k','YColor','k','ylim',[aa bb].*[minDT maxDT]);

    set(get(AX1(1),'Ylabel'),'String','T [K]') ;
    set(get(AX1(2),'Ylabel'),'String','D_T  [m^2/K.s]') ;

    set(H11,'LineStyle','--','Marker','p','Color','k','LineWidth',2);
    set(H12,'LineStyle','-','Marker','s','Color','k','LineWidth',2);
```

```
    % set(AX(1),'XGrid','on','Xtick',0:2:20,'XLim',[0 20]);       ORGINAL

    set(AX1(1),'XGrid','on');
    set(AX1(2));
%     hleg1 = legend('X','Y');

    hold on
    [AX2,H21,H22] = plotyy(xpos*1000,TT2,xpos*1000,DT2,'plot');
    hold on
    % set(AX(1),'YTickMode','Auto','XColor','k','YColor','b','ylim',[0
    % .1],'Ytick',0:.02:.1,'Ygrid','on');  ORginal
    set(AX2(1),'YTickMode','Auto','XColor','k','YColor','k','Ygrid','on','ylim',[aa bb].*[minTT maxTT]);
    set(AX2(2),'YTickMode','Auto','XColor','k','YColor','k','ylim',[aa bb].*[minDT maxDT]);

    set(get(AX1(1),'Ylabel'),'String','T [K]') ;
    set(get(AX1(2),'Ylabel'),'String','D_T  [m^2/K.s]') ;

    set(H21,'LineStyle','--','Marker','o','Color','b','LineWidth',2);
    set(H22,'LineStyle','-','Marker','+','Color','b','LineWidth',2);

    % set(AX(1),'XGrid','on','Xtick',0:2:20,'XLim',[0 20]);       ORGINAL

    set(AX2(1),'XGrid','on');
    set(AX2(2));
%     hleg1 = legend('X1','Y1')

    hold on

    [AX3,H31,H32] = plotyy(xpos*1000,TT3,xpos*1000,DT3,'plot');

    % set(AX(1),'YTickMode','Auto','XColor','k','YColor','b','ylim',[0
    % .1],'Ytick',0:.02:.1,'Ygrid','on');  ORginal
```

```
set(AX3(1),'YTickMode','Auto','XColor','k','YColor','k','Ygrid','on','ylim',[aa bb].*[minTT maxTT]);
set(AX3(2),'YTickMode','Auto','XColor','k','YColor','k','ylim',[aa bb].*[minDT maxDT]);

set(get(AX1(1),'Ylabel'),'String','T [K]') ;
set(get(AX1(2),'Ylabel'),'String','D_T  [m^2/K.s]') ;

set(H31,'LineStyle','--','Marker','h','Color','r','LineWidth',2);
set(H32,'LineStyle','-','Marker','.','Color','r','LineWidth',2);

% set(AX(1),'XGrid','on','Xtick',0:2:20,'XLim',[0 20]);       ORGINAL

set(AX3(1),'XGrid','on');
set(AX3(2));

HH=[H11,H12,H21,H22,H31,H32];
xlabel('Lenght [mm]') ;
title('Temperature and Thermodiffusion coefficient along x-direction in cavity');
hleg1 = legend(HH,'Temperature at Bottom','D_T at bottom','Temperature at middle',...
'D_T at middle','Temperature at top','D_T at top',0);%%
set(hleg1,'Edgecolor','w')

%%
halfresult=0;
for i=1:floor(xnode/2)
   for j=1:ynode
      halfresult=halfresult+massfrac1(j,i);
   end
end
format long
halfresult=halfresult/(floor(xnode/2)*ynode)
minmincc=min(mincc,minccy);
maxmaxcc=min(maxcc,maxccy);
diiff=maxmaxcc-minmincc
```

```
gradi=(cc2(xnode,1)-cc2(1,1))/L
```

Appendix E: MATLAB code to show transient plots and diagrams

```
clear
close all
clc

% duration=2+1/3; %hours
% H=.01;
% L=.01;
% xnode=17;
%
% steptime=0.008325*150;
% duration=duration*3600;
%
% st=(floor(120/steptime))*steptime; %matlab step time now is near 60 sec
% startshowtime=steptime*4+0.008325*6;
% K=(round(duration/steptime))*steptime+.05;
% digit=floor(log10(K));
position1= [7   400   615   310];
border2=[-1.5,-2.2,6.5,2.5];
filename2 = sprintf('r1s11');

duration=7/3; %hours
H=.01;
L=.01;
xnode=17;

steptime=.0333*150;
 steptime=4;
duration=duration*3600;

st=(floor(120/steptime))*steptime; %matlab step time now is near 60 sec
```

```
 startshowtime=steptime*4;
startshowtime=steptime;
K=(round(duration/steptime))*steptime;%.00001
% K=(round(duration/steptime))*steptime;
digit=floor(log10(K));
k=K/10^digit;
filename = sprintf('data. %.5fE+0%d',k,digit);
result=load(filename);
numberdata=max(size(result));
ynode=numberdata/(18*xnode);



stream=zeros(ynode,xnode);
xvelocity=zeros(ynode,xnode);
yvelocity=zeros(ynode,xnode);
P=zeros(ynode,xnode);
T=zeros(ynode,xnode);
rho=zeros(ynode,xnode);
rhomole=zeros(ynode,xnode);
wtmole=zeros(ynode,xnode);
molarfrac1=zeros(ynode,xnode);
molarfrac2=zeros(ynode,xnode);
massfrac1=zeros(ynode,xnode);
massfrac2=zeros(ynode,xnode);
D=zeros(ynode,xnode);
DT=zeros(ynode,xnode);
DP=zeros(ynode,xnode);
vis=zeros(ynode,xnode);
cp=zeros(ynode,xnode);
K=zeros(ynode,xnode);
xpos=zeros(1,xnode);
ypos=zeros(1,ynode);
```

```
xpos(1)=-L/2;
ypos(1)=-H/2;
for i=2:xnode
   xpos(i)=xpos(i-1)+L/(xnode-1);
end

for i=2:ynode
   ypos(i)=ypos(i-1)+H/(ynode-1);
end

counter=1;
for i=1:ynode
   for j=1:xnode
      stream(i,j)=result(counter);
      counter=counter+1;
   end
end

for i=1:ynode
   for j=1:xnode
      xvelocity(i,j)=result(counter);
      counter=counter+1;
   end
end


for i=1:ynode
   for j=1:xnode
      yvelocity(i,j)=result(counter);
      counter=counter+1;
   end
end
```

```
velocity=(xvelocity.^2+yvelocity.^2).^.5;
sumvel=0;
Mvel=0;
   for i=1:ynode
      for j=1:xnode
         sumvel=sumvel+velocity(i,j);
         if velocity(i,j) > Mvel
            Mvel=velocity(i,j);
            nmc=[i ,j];  %node maximom velocity
         end
      end
   end
Meanvel=sumvel/(ynode*xnode);

for i=1:ynode
   for j=1:xnode
      P(i,j)=result(counter);
      counter=counter+1;
   end
end
for i=1:ynode
   for j=1:xnode
      T(i,j)=result(counter);
      counter=counter+1;
   end
end
for i=1:ynode
   for j=1:xnode
      rho(i,j)=result(counter);
      counter=counter+1;
   end
end
for i=1:ynode
```

```
    for j=1:xnode
        rhomole(i,j)=result(counter);
        counter=counter+1;
    end
end
for i=1:ynode
    for j=1:xnode
        wtmole(i,j)=result(counter);
        counter=counter+1;
    end
end
for i=1:ynode
    for j=1:xnode
        molarfrac1(i,j)=result(counter);
        counter=counter+1;
    end
end
for i=1:ynode
    for j=1:xnode
        molarfrac2(i,j)=result(counter);
        counter=counter+1;
    end
end
for i=1:ynode
    for j=1:xnode
        massfrac1(i,j)=result(counter);
        counter=counter+1;
    end
end
for i=1:ynode
    for j=1:xnode
        massfrac2(i,j)=result(counter);
        counter=counter+1;
```

```
    end
end
for i=1:ynode
    for j=1:xnode
        D(i,j)=result(counter);
        counter=counter+1;
    end
end
for i=1:ynode
    for j=1:xnode
        DT(i,j)=result(counter);
        counter=counter+1;
    end
end
for i=1:ynode
    for j=1:xnode
        DP(i,j)=result(counter);
        counter=counter+1;
    end
end
for i=1:ynode
    for j=1:xnode
        vis(i,j)=result(counter);
        counter=counter+1;
    end
end
for i=1:ynode
    for j=1:xnode
        cp(i,j)=result(counter);
        counter=counter+1;
    end
end
for i=1:ynode
```

```
    for j=1:xnode
        K(i,j)=result(counter);
        counter=counter+1;
    end
end

cc1 = smooth(xpos*1000,massfrac1(2,:),0.2,'loess')*100;
cc2 = smooth(xpos*1000,massfrac1(round(ynode/2),:),0.2,'loess')*100;
cc3 = smooth(xpos*1000,massfrac1((ynode-1),:),0.2,'loess')*100;

c21 = smooth(xpos*1000,massfrac2(2,:),0.2,'loess')*100;
c22 = smooth(xpos*1000,massfrac2(round(ynode/2),:),0.2,'loess')*100;
c23 = smooth(xpos*1000,massfrac2((ynode-1),:),0.2,'loess')*100;
init1=round(cc1(round(xnode/2),1)); %percent
init2=round(c21(round(xnode/2),1)); %percent
mmax1=max(init1-min(cc2),max(cc2)-init1);
mmax2=max(init2-min(c22),max(c22)-init2);

TT1 = smooth(xpos*1000,T(2,:),0.2,'loess');
TT2 = smooth(xpos*1000,T(round(ynode/2),:),0.2,'loess');
TT3 = smooth(xpos*1000,T((ynode-1),:),0.2,'loess');
minT=min(TT1);
maxT=max(TT1);

velmid=zeros(1,floor((duration-steptime)/st));
velmax=zeros(1,floor((duration-steptime)/st));
velhotbottom=zeros(1,floor((duration-steptime)/st));
velcoldtop=zeros(1,floor((duration-steptime)/st));
velhottop=zeros(1,floor((duration-steptime)/st));
Meanvel=zeros(1,floor((duration-steptime)/st));
Tmid=zeros(1,floor((duration-steptime)/st));
Tmax=zeros(1,floor((duration-steptime)/st));
Thotbottom=zeros(1,floor((duration-steptime)/st));
```

```
Tcoldtop=zeros(1,floor((duration-steptime)/st));
Thottop=zeros(1,floor((duration-steptime)/st));

for time=startshowtime:st:duration
   if time > 1000
    time=round(time*100+10^-7)/100;
   end
   digit=floor(log10(time));
   tdigit=time/10^digit-.000001;
   filename = sprintf('data. %.5fE+0%d',tdigit,digit);
   result=load(filename);
   numberdata=max(size(result));
   ynode=numberdata/(18*xnode);

   hour=0;
   min=0;
   if time> (hour+1)*60
      a=floor((time-3600*hour)/60);
      min=min+a;
      if time> (hour+1)*3600
         b=floor(time/3600);
         hour=hour+b;
         min=min-60*hour;
      end
   end



   stream=zeros(ynode,xnode);
   xvelocity=zeros(ynode,xnode);
   yvelocity=zeros(ynode,xnode);
   P=zeros(ynode,xnode);
   T=zeros(ynode,xnode);
```

```
rho=zeros(ynode,xnode);
rhomole=zeros(ynode,xnode);
wtmole=zeros(ynode,xnode);
molarfrac1=zeros(ynode,xnode);
molarfrac2=zeros(ynode,xnode);
massfrac1=zeros(ynode,xnode);
massfrac2=zeros(ynode,xnode);
D=zeros(ynode,xnode);
DT=zeros(ynode,xnode);
DP=zeros(ynode,xnode);
vis=zeros(ynode,xnode);
cp=zeros(ynode,xnode);
K=zeros(ynode,xnode);
xpos=zeros(1,xnode);
ypos=zeros(1,ynode);

indexx=floor((time-steptime)/st)+1;
xpos(1)=-L/2;
ypos(1)=-H/2;
for i=2:xnode
   xpos(i)=xpos(i-1)+L/(xnode-1);
end

for i=2:ynode
   ypos(i)=ypos(i-1)+H/(ynode-1);
end

counter=1;
for i=1:ynode
   for j=1:xnode
      stream(i,j)=result(counter);
      counter=counter+1;
   end
```

```
end

for i=1:ynode
   for j=1:xnode
      xvelocity(i,j)=result(counter);
      counter=counter+1;
   end
end

xvelmid(indexx)=xvelocity(round(ynode/2),round(xnode/2));
xvelmax(indexx)=xvelocity(nmc(1,1),nmc(1,2));
xvelhotbottom(indexx)=xvelocity(2,2);
xvelcoldtop(indexx)=xvelocity(ynode-1,xnode-1);
xvelhottop(indexx)=xvelocity(2,xnode-1);

for i=1:ynode
   for j=1:xnode
      yvelocity(i,j)=result(counter);
      counter=counter+1;
   end
end

yvelmid(indexx)=yvelocity(round(ynode/2),round(xnode/2));
yvelmax(indexx)=yvelocity(nmc(1,1),nmc(1,2));
yvelhotbottom(indexx)=yvelocity(2,2);
yvelcoldtop(indexx)=yvelocity(ynode-1,xnode-1);
yvelhottop(indexx)=yvelocity(2,xnode-1);

velocity=(xvelocity.^2+yvelocity.^2).^.5;
sumvel=0;
for i=1:ynode
   for j=1:xnode
      sumvel=sumvel+velocity(i,j);
```

```
    end
end


Meanvel(indexx)=sumvel/(ynode*xnode);
velmid(indexx)=velocity(round(ynode/2),round(xnode/2));
velmax(indexx)=velocity(nmc(1,1),nmc(1,2));
velhotbottom(indexx)=velocity(2,2);
velcoldtop(indexx)=velocity(ynode-1,xnode-1);
velhottop(indexx)=velocity(2,xnode-1);

for i=1:ynode
    for j=1:xnode
        P(i,j)=result(counter);
        counter=counter+1;
    end
end
for i=1:ynode
    for j=1:xnode
        T(i,j)=result(counter);
        counter=counter+1;
    end
end


Tmid(indexx)=T(round(ynode/2),round(xnode/2));
Tmax(indexx)=T(nmc(1,1),nmc(1,2));
Thotbottom(indexx)=T(2,2);
Tcoldtop(indexx)=T(ynode-1,xnode-1);
Thottop(indexx)=T(2,xnode-1);

for i=1:ynode
    for j=1:xnode
```

```
        rho(i,j)=result(counter);
        counter=counter+1;
    end
end

rhomid(indexx)=rho(round(ynode/2),round(xnode/2));
rhomax(indexx)=rho(nmc(1,1),nmc(1,2));
rhohotbottom(indexx)=rho(2,2);
rhocoldtop(indexx)=rho(ynode-1,xnode-1);
rhohottop(indexx)=rho(2,xnode-1);

for i=1:ynode
    for j=1:xnode
        rhomole(i,j)=result(counter);
        counter=counter+1;
    end
end
for i=1:ynode
    for j=1:xnode
        wtmole(i,j)=result(counter);
        counter=counter+1;
    end
end
for i=1:ynode
    for j=1:xnode
        molarfrac1(i,j)=result(counter);
        counter=counter+1;
    end
end


for i=1:ynode
    for j=1:xnode
```

```
        molarfrac2(i,j)=result(counter);
        counter=counter+1;
    end
end
for i=1:ynode
    for j=1:xnode
        massfrac1(i,j)=result(counter);
        counter=counter+1;
    end
end

frac1mid(indexx)=massfrac1(round(ynode/2),round(xnode/2));
frac1max(indexx)=massfrac1(nmc(1,1),nmc(1,2));
frac1hotbottom(indexx)=massfrac1(2,2);
frac1coldtop(indexx)=massfrac1(ynode-1,xnode-1);
frac1hottop(indexx)=massfrac1(2,xnode-1);
for i=1:ynode
    for j=1:xnode
        massfrac2(i,j)=result(counter);
        counter=counter+1;
    end
end

frac2mid(indexx)=massfrac2(round(ynode/2),round(xnode/2));
frac2max(indexx)=massfrac2(nmc(1,1),nmc(1,2));
frac2hotbottom(indexx)=massfrac2(2,2);
frac2coldtop(indexx)=massfrac2(ynode-1,xnode-1);
frac2hottop(indexx)=massfrac2(2,xnode-1);

for i=1:ynode
    for j=1:xnode
        D(i,j)=result(counter);
        counter=counter+1;
```

```
    end
end

Dmid(indexx)=D(round(ynode/2),round(xnode/2));
Dmax(indexx)=D(nmc(1,1),nmc(1,2));
Dhotbottom(indexx)=D(2,2);
Dcoldtop(indexx)=D(ynode-1,xnode-1);
Dhottop(indexx)=D(2,xnode-1);

for i=1:ynode
    for j=1:xnode
        DT(i,j)=result(counter);
        counter=counter+1;
    end
end

DTmid(indexx)=DT(round(ynode/2),round(xnode/2));
DTmax(indexx)=DT(nmc(1,1),nmc(1,2));
DThotbottom(indexx)=DT(2,2);
DTcoldtop(indexx)=DT(ynode-1,xnode-1);
DThottop(indexx)=DT(2,xnode-1);

for i=1:ynode
    for j=1:xnode
        DP(i,j)=result(counter);
        counter=counter+1;
    end
end
for i=1:ynode
    for j=1:xnode
        vis(i,j)=result(counter);
        counter=counter+1;
    end
```

```
    end

    vismid(indexx)=vis(round(ynode/2),round(xnode/2));
    vismax(indexx)=vis(nmc(1,1),nmc(1,2));
    vishotbottom(indexx)=vis(2,2);
    viscoldtop(indexx)=vis(ynode-1,xnode-1);
    vishottop(indexx)=vis(2,xnode-1);

    for i=1:ynode
        for j=1:xnode
            cp(i,j)=result(counter);
            counter=counter+1;
        end
    end
    for i=1:ynode
        for j=1:xnode
            K(i,j)=result(counter);
            counter=counter+1;
        end
    end



    %%
        cc1 = smooth(xpos*1000,massfrac1(2,:),0.2,'loess')*100;
        cc2 = smooth(xpos*1000,massfrac1(round(ynode/2),:),0.2,'loess')*100;
        cc3 = smooth(xpos*1000,massfrac1((ynode-1),:),0.2,'loess')*100;

        c21 = smooth(xpos*1000,massfrac2(2,:),0.2,'loess')*100;
        c22 = smooth(xpos*1000,massfrac2(round(ynode/2),:),0.2,'loess')*100;
        c23 = smooth(xpos*1000,massfrac2((ynode-1),:),0.2,'loess')*100;
        time
end
```

```
tethemid=atand(yvelmid./xvelmid);
tethemax=atand(yvelmax./xvelmax);
tethehotbottom=atand(yvelhotbottom./xvelhotbottom);
tethecoldtop=atand(yvelcoldtop./xvelcoldtop);
tethehottop=atand(yvelhottop./xvelhottop);

% hleg1 = legend ('Bottom','Middle','Top','Location','Best');grid on;
%     set(hleg1,'Edgecolor','w')

t=steptime:st:duration;
t=t(1,1:max(size(tethemid)))/60;

 figure('NumberTitle','on','Name',filename2,'Position',position1)
plot(t,tethemax,'-bo',t,tethehottop,'-.b',t,tethehotbottom,'--k',...
    t,tethemid,':b',t,tethecoldtop,'-r','LineWidth',2);
% set(gca,'Position',get(gca,'OuterPosition')-get(gca,'TightInset').*border2);
xlabel('Time [min]');ylabel('\theta [deg]');
hleg1 = legend ('Node with Maximum Velocity','Bottom, Near the cold Wall ','Bottom, Near the hot Wall',...
    'Centre','Top, Near cold Wall','Domain Mean velocity',0);
set(hleg1,'Edgecolor','w');
grid off;
title('Velocity angle with time at five locations')

 figure('NumberTitle','on','Name',filename2,'Position',position1)
plot(t,velmax,'-bo',t,velhottop,'-.b',t,velhotbottom,'--k',...
    t,velmid,':b',t,velcoldtop,'-r',t,Meanvel,'-bs','LineWidth',2);
% set(gca,'Position',get(gca,'OuterPosition')-get(gca,'TightInset').*border2);
xlabel('Time [min]');ylabel('Velocity (m/s)');
hleg1 = legend ('Node with Maximum Velocity','Bottom, Near the cold Wall ','Bottom, Near the hot Wall',...
    'Centre','Top, Near cold Wall','Domain Mean velocity',0);
set(hleg1,'Edgecolor','w');
grid off;
title('Variation of velocity with time at five locations')
```

```
% axis([0 ,140 ,0 12*10^-8]);


 figure('NumberTitle','on','Name',filename2,'Position',position1);
plot(t,Tmax,'-bo',t,Thottop,'-.b',t,Thotbottom,':',...
    t,Tmid,'--k',t,Tcoldtop,'-r','LineWidth',2);
% set(gca,'Position',get(gca,'OuterPosition')-get(gca,'TightInset').*border2);
xlabel('Time [min]');ylabel('Temperature [K]');
hleg1 = legend ('Node with Maximum Velocity','Bottom, Near the cold Wall ','Bottom, Near the hot Wall',...
    'Centre','Top, Near cold Wall',0);
set(hleg1,'Edgecolor','w');
grid off;
title('Temprature variation with time at five locations')


 figure('NumberTitle','on','Name',filename2,'Position',position1);
plot(t,Dmax,'-bo',t,Dhottop,'-.b',t,Dhotbottom,':',...
    t,Dmid,'--k',t,Dcoldtop,'-r','LineWidth',2);
% set(gca,'Position',get(gca,'OuterPosition')-get(gca,'TightInset').*border2);
xlabel('Time [min]');ylabel('D_M [m^2/s]');
hleg1 = legend ('Node with Maximum Velocity','Bottom, Near the cold Wall ','Bottom, Near the hot Wall',...
    'Centre','Top, Near cold Wall',0);
set(hleg1,'Edgecolor','w');
grid off;
title('Variation of Molecular Diffusion coefficent with time at five locations')


 figure('NumberTitle','on','Name',filename2,'Position',position1);
plot(t,DTmax,'-bo',t,DThottop,'-.b',t,DThotbottom,':',...
    t,DTmid,'--k',t,DTcoldtop,'-r','LineWidth',2);
% set(gca,'Position',get(gca,'OuterPosition')-get(gca,'TightInset').*border2);
xlabel('Time [min]');ylabel('D_T [m^2/s]');
hleg1 = legend ('Node with Maximum Velocity','Bottom, Near the cold Wall ','Bottom, Near the hot Wall',...
    'Centre','Top, Near cold Wall',0);
set(hleg1,'Edgecolor','w');
```

```
grid off;
title('Variation of Thermodiffusion coefficent with time at five locations')


 figure('NumberTitle','on','Name',filename2,'Position',position1);
plot(t,rhomax,'-bo',t,rhohottop,'-.b',t,rhohotbottom,':',...
    t,rhomid,'--k',t,rhocoldtop,'-r','LineWidth',2);
% set(gca,'Position',get(gca,'OuterPosition')-get(gca,'TightInset').*border2);
xlabel('Time [min]');ylabel('\rho (kg/m^3)');
hleg1 = legend ('Node with Maximum Velocity','Bottom, Near the cold Wall ','Bottom, Near the hot Wall',...
    'Centre','Top, Near cold Wall',0);
set(hleg1,'Edgecolor','w');
grid off;
title('Density variation with time at five locations')


 figure('NumberTitle','on','Name',filename2,'Position',position1);
plot(t,xvelmax,'-bo',t,xvelhottop,'-.b',t,xvelhotbottom,':',...
    t,xvelmid,'--k',t,xvelcoldtop,'-r','LineWidth',2);
% set(gca,'Position',get(gca,'OuterPosition')-get(gca,'TightInset').*border2);
xlabel('Time [min]');ylabel('X-Velocity (m/s)');
hleg1 = legend ('Node with Maximum Velocity','Bottom, Near the cold Wall ','Bottom, Near the hot Wall',...
    'Centre','Top, Near cold Wall',0);
set(hleg1,'Edgecolor','w');
grid off;
title('Variation of velocity along x-direction with time at five locations')
%  axis([0 ,140 ,[-7 10]*10^-9]);

 figure('NumberTitle','on','Name',filename2,'Position',position1);
plot(t,yvelmax,'-bo',t,yvelhottop,'-.b',t,yvelhotbottom,':',...
    t,yvelmid,'--k',t,yvelcoldtop,'-r','LineWidth',2);
% set(gca,'Position',get(gca,'OuterPosition')-get(gca,'TightInset').*border2);
xlabel('Time [min]');ylabel('Y-Velocity (m/s)');
```

```
hleg1 = legend ('Node with Maximum Velocity','Bottom, Near the cold Wall ','Bottom, Near the hot Wall',...
   'Centre','Top, Near cold Wall',0);
set(hleg1,'Edgecolor','w');
grid off;
title('Variation of velocity along y-direction with time at five locations')
%   axis([0 ,140 ,[-8 1]*10^-8]);

 figure('NumberTitle','on','Name',filename2,'Position',position1);
plot(t,frac1max,'-bo',t,frac1hottop,'-.b',t,frac1hotbottom,':',...
   t,frac1mid,'--k',t,frac1coldtop,'-r','LineWidth',2);
% set(gca,'Position',get(gca,'OuterPosition')-get(gca,'TightInset').*border2);
xlabel('Time [min]');ylabel('Isopropanol Mass Fraction');
hleg1 = legend ('Node with Maximum Velocity','Bottom, Near the cold Wall ','Bottom, Near the hot Wall',...
   'Centre','Top, Near cold Wall','Domain Mean velocity',0);
set(hleg1,'Edgecolor','w');
grid off;
title('Mass fraction variation of Isopropanol with time at five locations')
%  axis([0 ,140 ,0.0996 .1008]);

 figure('NumberTitle','on','Name',filename2,'Position',position1);
plot(t,frac2max,'-bo',t,frac2hottop,'-.b',t,frac2hotbottom,':',...
   t,frac2mid,'--k',t,frac2coldtop,'-r','LineWidth',2);
% set(gca,'Position',get(gca,'OuterPosition')-get(gca,'TightInset').*border2);
xlabel('Time [min]');ylabel('Water Mass Fraction');
hleg1 = legend ('Node with Maximum Velocity','Bottom, Near the cold Wall ','Bottom, Near the hot Wall',...
   'Centre','Top, Near cold Wall','Domain Mean velocity',0);
set(hleg1,'Edgecolor','w');
grid off;
title('Mass fraction variation of Water with time at five locations')
%  axis([0 ,140 ,0.0996 .101]);

 figure('NumberTitle','on','Name',filename2,'Position',position1);
plot(t,vismax,'-bo',t,vishottop,'-.b',t,vishotbottom,':',...
```

```
   t,vismid,'--k',t,viscoldtop,'-r','LineWidth',2);
% % set(gca,'Position',get(gca,'OuterPosition')-get(gca,'TightInset').*border2);
xlabel('Time [min]');ylabel('\mu [kg/(ms)]');
hleg1 = legend ('Node with Maximum Velocity','Bottom, Near the cold Wall ','Bottom, Near the hot Wall',...
   'Centre','Top, Near cold Wall','Domain Mean velocity',0);
set(hleg1,'Edgecolor','w');
grid off;
title('Vicosity variation with time at five locations')
% axis([0 ,140 ,1.0353*10^-3 1.038*10^-3]);

quiver(t,0,velmax,yvelmax);
```

References

[1] A Parsa and M. Z. Saghir, "Thermodiffusion ina binary mixture subject on external vibration: Effect of variable physicalproperties," in ASME/JSME, Honolulu, Hawaii, USA, March 2011.

[2] S Duhr and D Braun, "Why molecules move along a temperature gradient ," Proc. Natl. Acad. Sci. U.S.A., vol. 103 (52), no. Bibcode 2006PNAS.10319678D. doi:10.1073/pnas.0603873103. PMC 1750914. PMID 17164337., pp. 19678–82, Dec. 2006.

[3] R Haase,.: Addison-Wesley Publishing Company, 1969, pp. 355-370.

[4] E.L. Dougherty Jr. and H.G Drickamer, "Thermal diffusion and molecular motion in liquids," Jounral of Physics and Chemistry, vol. 59, p. 443.

[5] R. G. r Mortime and H. Eyring, "Elementary transition state theory of the Soret and Dufour effects," Proc. Natl. Acad. Sci. U.S.A., vol. 77, pp. 1728-1731, 19880.

[6] J. M. Kincaid, M. López de Haro, and E.G.D Cohen, "The Enskog theory for multicomponent mixtures II: Mutual diffusion," Joural Chemical Physics, vol. 79-9, p. 45094521, 1983.

[7] L.J.T.M. Kempers, "A thermodynamic theory of the Soret effect in amulticomponent liquid," Journal Chemical Physics, vol. 90(11), pp. 6541-6548, 1989.

[8] G. Z. Gershuni and E. M. Zhukhovitsky, "Convective Instability of a Fluid in a Vibrational Field Under Conditions of Weightlessness," Fluid Dynamics, vol. 16, p. 498, 1981.

[9] G.Z Gershuni and E.Z. Zhukhovitskii, "Vibration induced thermal convection in weightlessness," Fluid Mechanics, vol. 15, pp. 63-84, 1986.

[10] R. Savino, R. Monti, and M. Piccirillo, "Thermovibrational convection in a fluid cell," Computers and Fluids , vol. 27, p. 923, 1998.

[11] M. Chacha, D. Faruque, M. Z. Saghir, and J. C. Legros, "Solutal Thermodiffusion in Binary Mixture in the Presence of G-jitte," International Journal of Thermal Sciences, vol. 41, pp. 899-911, 2002.

[12] G. Z Gershuni, A. K. Kolesnikov, J. C. Legros, and B. L Myznikova, "On the vibrational convective instability of a horizontal binary-mixture layer with Soret effect under transversal high frequency vibration.," International Journal of Heat and Mass, vol. 42, p. 547, 1999.

[13] K. Shukla and A. Firoozabadi, "A new model of thermal coefficients in binary hydrocarbon mixtures," Ind. Engineering. Chemical, vol. 37, p. 3331, 1998.

[14] K. Ghorayeb and A. Firoozabadi, "Ghorayeb, K. and Firoozabadi , A., 2000, “Modeling multicomponent diffusion and convection in porous media," Society of Petroleum Engineers Journal , vol. 5, p. 158, 2000.

[15] H.A. Kooijman and R. Taylor, "Estimation of diffusion coefficients in multicomponent liquid systems," Ind. Engrg. Chem., p. 30, 1991.

[16] D.Y. Peng and D.B. Robinson, "A new two-constant equation of state," Ind. Eng. Chem., vol. 15, no. Fundamental, p. 58, 1976.

[17] Y. Demirel and S.I. Sandler, "Linear-nonequilibrium thermodynamics theory for coupled heat and mass transport," Int. J. Heat Mass Transfer, vol. 44, p. 2439, 2001.

[18] S. Srinivasan and M. Z. Saghir, "Significant Equation of State and Viscosity on the Thermodiffusion Coeffcients of a Ternary Hydrocarbon Mixture.," High Temperatures High Pressures, vol. 39, pp. 65-81, 2010.

[19] S. Srinivasan, M. Dejmeck, and M. Z. Saghir, "Thermo-Solutal-Diffusion in high pressure Liquid Mixtures In the Presence of Micro-Vibrations.," International Journal of Thermal Science, vol. 10, p. 1016, Apr. 2010.

[20] M. Chacha and M. Z. Saghir, "Solutal-Thermo-Diffusion Convection in a Vibrating Rectangular Cavity.," International Journal of Thermal Sciences, vol. 44, pp. 1-10, 2005.

[21] T.C. Jue and B. Ramaswamy, "Numerical analysis of thermosolutal flows in a cavity with gravity modulation effects," Heat Mass Transfe, vol. 38, p. 665, 2002.

[22] G Galliéro, B Duguayb, J. P Caltagirone, and F Montel, "Thermal diffusion sensitivity to the molecular parameters of a binary equimolar mixture, a non-equilibrium molecular dynamics approach," Fluid Phase Equilibria, vol. 208, pp. 171-188, January 2003.

[23] T. Lyubimova, E. Shklyaeva, J.-C. Legros b, V. Shevtsova b, and B. Roux, "Numerical study of high frequency vibration influence on measurement of Soret and diffusion coefficients in low gravity conditions," Advances in Space Research, vol. 36, pp. 70-74, March 2005.

[24] N. V. Gnevanov and B. L. Smorodin, "Convection instability of the flow of a binary mixture under condition of vibration and thermal diffusion," Journal of Applied Mechanics and Technical Physics, Vol. 47, No. 2, pp. 214–220, 2006, vol. 47(2), pp. 214-220, 2006.

[25] C.G. Jiang, M.Z. Saghir, M. Kawaji, and K. Ghorayeb, "Two-dimensional numerical simulation of thermo-gravitational convection in a vertical porous column filled with a binary fluid mixture," International Journal of Thermal Sciences, vol. 43, pp. 1057-1065, March 2004.

[26] F. Herning and L. Zipperer, "Calculation of the viscosity of technical gas mixtures from the viscosity of individual gases," Gas u. Wasserfach, vol. 79, p. 69, 1936.

[27] Y. Yan, S. Pan, K. Jules, and M. Z. Saghir, "Vibrational Effect on Thermal Diffusion Under Different Microgravity Environments.," Microgravity Science and Technology, vol. 19b, pp. 12-25, 2007b.

[28] S. V. Patankar, "Numerical Heat Transfer and Fluid Flow," Taylor and Francis, 1980.

[29] M.Z. Saghir, C.G. Jiang, Derawi2, E.H. Stenby, and M. Kawaji, "Theoretical and experimental comparison of the Soret coeffcieny for water-methanol and water-ethanol binary mixtures," The European Physical Journal E, vol. 15, pp. 241-247, 2004.

[30] J.K. Platten, "In Proceedings of the 5th International Meeting on Thermodiffusion (IMT5)," Philos. Mag., vol. 83, pp. 17-18, 2003.

[31] G. Mathiak, E. Plescher, and R. Willnecker, "Vibrational Effects on Diffusion Experiments," Microgravity sci. technol. , vol. XVI-1 , pp. 295-300, 2005.

[32] D. Langbein, "Quality requirements for microgravity experiments.," Microgravity sci. technol. , vol. III, pp. 138-142, 1990.

[33] Robert J. Asaro, Diana Farkas, and Yashashree Kulkarni, "The Soret effect in diffusion in crystals," Acta Materialia, vol. 56, pp. 1243-1256, 2008.

[34] Y Yan, A Vivianib, and M Z Saghir, "Double diffusion convection under sinusoidal modulations of low-frequency vibrations," Acta Astronautica, vol. 63, pp. 665 – 672, 2008.

[35] A Abbasi, M Z Saghir, and M Kawaji, "Evaluation of the activation energy of viscous flow for the binary mixture in order to estimat the thermodiffusion coefficient," Journal of Non-Equilibrium Thermodynamics, 2008.

[36] A. Abbasi, M. Z. Saghir, and M. Kawaji, "A new proposed approach to estimate the thermodiffusion coefficients for linear chain hydrocarbon binary mixtures," J. Chem. Phys., vol. 131, p. 014502, 2009.

[37] M. Eslamian and M. Z. Saghir, "Microscopic study and modeling of thermodiffusion in binary associating mixtures," Physical Review , vol. 80, p. 061201.

[38] M Eslamian and M. Z Saghir, "Dynamic Thermodiffusion Model for Binary Liguid Mixture," Physical Review E 80, p. 011201, 2009.

[39] M. Eslamian and M. Z. Saghir, "A Critical Review of Thermodiffusion Models:Role and Significance of the Heat of Transport and the Activation Energy of Viscous Flow," J. Non-Equilib. Thermodyn, vol. 34, pp. 97-131, 2009.

[40] M. Eslamian, M. Z. Saghir, and G. Jiang, "On the Role of the Velocity Frame of Reference and Alternative Definitions of the Soret Coefficients in Thermodiffusion," Review.

[41] B. Elhajjar, A. Mojtabi, M. Catherine, and C. Mojtab, "Influence of vertical vibrations on the separation of a binary mixture in a horizontal porous layer heated from below," International Journal of Heat and Mass Transfer, vol. 52, pp. 165-172, 2009.

[42] Y.P. Razi, K. Maliwan, A. Mojtabi, M.C. Charrier Mojtabi, "Influence of vibrations on Soret-driven convection in porous media, Numer.," Heat Transf. A Appl, vol. 10, pp. 981-993, 2004.

[43] F. Grcar, B. Bell, and S. Day, "The Soret effect in naturally propagating, premixed, lean, hydrogen–air flames," Proceedings of the Combustion Institute, vol. 32, pp. 1173-1180, 2009.

[44] H. Bongers and L.P.H. de Goey, "The flat flames study," Combust. Sci. Technol., vol. 175, pp. 1915-1928, 2003.

[45] A, Ern and V. Giovangigli, Combust. Theory Modell, vol. 2, pp. 349-372, 1998.

[46] Bo-Chen Tai and Ming-I Char, "Soret and Dufour effects on free convection flow of non-Newtonian fluids along a vertical plate embedded in a porous medium with thermal radiation," International Communications in Heat and Mass Transfer, vol. 37, pp. 480-483, 2010.

[47] P.A. Lakshmi Narayana and P. Sibanda, "Soret and Dufour effects on free convection along a vertical wavy surface in a fluid saturated Darcy porous medium," International Journal of Heat and Mass Transfer, vol. 53, pp. 3030-3034, 2010.

[48] S. Srinivasan and M. Ziad Saghir, "Experimental Approaches to Study Thermodiffuison".

[49] A. Parsa, S. Srinivasan, and M. Z. Saghir, "Impact of Density Gradients on the Fluid Flow Inside a Vibrating Cavity Subjected to Soret Effect," Physics of Fluids, vol. Submitted, 2010.

[50] S. Srinivasan and M. Z. Saghir, "Impact of the vibrations on Soret separation in binary and ternary mixtures," J. Fluid Mech(Under consideration).

[51] Melissa J.B Rogers, Kenneth Hrovat, and Kevin McPherson, "AccelerACCELEROMETER DATA ANALYSIS AND PRESENTATION TECHNIQUES," 2002.

[52] DeLombard R, R. Hakimzadeh, and Tschen, P, "Experiment Support Requirements Document for Space Acceleration Measurement System-II, PIMS-001," 1995.

[53] "Software Requirements for Processing Microgravity Acceleration Data from the International Space Station PIMS-ISS-001," May 2000.

[54] "Microgravity Control Plan, International Space Station Program," 1998.

[55] "The International Space Station Fact Book," 2000.

[56] "International Space Station PIMS Acceleration Data File Description Document PIMS-ISS-101," Cleveland, Ohio, 2002.

[57] "Microgravity Environment Interpretation Tutorial (MEIT)," 2001.

[58] (2009, Mar.) 1. [Online]. HYPERLINK "http://www.sfu.ca/sonic-studio/handbook/index.html" http://www.sfu.ca/sonic-studio/handbook/index.html

[59] 1. [Online]. HYPERLINK "http://femci.gsfc.nasa.gov" http://femci.gsfc.nasa.gov

[60] (2000, Feb.) [Online]. HYPERLINK "http://www.spaceflight.esa.int/users/index.cfm?act=default.page&level=11&page=392" http://www.spaceflight.esa.int/users/index.cfm?act=default.page&level=11&page=392

[61] Baglioni P, Demets R, and Verga A, "ESA Payloads and Experiments on the Foton-12 Mission," ESTEC, Noordwijk, The Netherlands, Feb 2000.

[62] (2007, Nov.) [Online]. HYPERLINK "http://www.asc-csa.gc.ca/eng/sciences/scco.asp" http://www.asc-csa.gc.ca/eng/sciences/scco.asp

[63] Olubusola Thomas, Reservoir analysis based on copositional gradients.: stanford university, 2007.

[64] Tannehill , John C;Anderson , Dale A; Pletcher ,Richard H;, Coumputational Fuid Mechanics and heat Transfer. London: Taylor & Francis Ltd, 1997.

[65] J Lienhard and J Lienhard, A Heat Tranfer Textbook. Massachusetts, U.S.A: Cambridge Massachusetts, 2008.

[66] S. Srinivasan and M. Z. Saghir, "Experimental Data on Thermodiffusion in Ternary Hydrocarbon Mixtures.," Journal of Chemical Physics, vol. 131, 124508, 2009.

[67] Peng Ding-Yu and B. Robinson Donald, "A New Two-Constant Equation of State," vol. 15, pp. 59–64.

[68] G Joachim and S Gabriele, "Perturbed-Chain SAFT: An Equation of State Based on a Perturbation Theory for Chain Molecules," Ind. Eng. Chem. Res, vol. 40, pp. 1244-1260, 2001.

[69] Y. Yan, K. Jules, and M. Z. Saghir, "A Comparative Study of G-jitter Effect on Thermal Diffusion Aboard the International Spacestation.," Fluid Dynamics and Material Processing Journal, vol. 3 (3), pp. 231-245.

[70] Y Yan, P Blanco, M. Z Saghir, and M. M. Bou-Ali, "An improved theoretical model for thermodiffusion coefficient in liquid hydrocarbon mixtures: Comparison between experimental and numerical results," J. Chem. Phys. 129, p. 194507, 2008.

[71] De Groot and Mazur S.R., Non-Equilibrium Thermodynamics. New York: Dover, 1984.

[72] R. Monti, R. Savino, and M Lappa, "On the Convective Disturbances Induced by G-jitters on the Space Station," Acta Astronautica, vol. 48(5-12), p. 603, 2001.

[73] S. Srinivasan, Eslamian, and M. Z. M. & Saghir, "Estimation of the Thermodiffusion Coefficients for n-Dodecane/n-Butane/Methane Mixtures and Comparison with Experimental Data from Foton M3 Mission.," IAC, vol. (IAC-09-A2.3.1)., 2009.

[74] Van VaerenberghS., S. Srinivasan, and M. Z. Saghir, "Thermodiffusion in Multicomponent Hydrocarbon Mixtures: Experimental Investigations and Computational Analysis.," Journal of Chemical Physics, vol. 114505, p. 131.

[75] "International Space Station User's Guide Release 2.0, NASA.,".

[76] "Expedition Two (Press Kit): Open for Business- Shuttle Press kit," 2001.

[77] "The Joint Architecture For Unmanned System," 2004.

[78] G Zeng-Yuan, L Zhi-Xin, and L Xiao-Bing, "Size effect on free convection in a square cavity," 2002.

[79] N. V. Gnevanov and B. L. Smorodin, "Convective instability of the floe of a binary mixture under conditions of vibrations and thermaldiffusion," Journal of Applied Mechanics and Technical Physics, vol. 47-2, pp. 214-220, 2006.